NATURAL FRACTURE CHARACTER AND DISTRIBUTION ADJACENT TO THE NENANA BASIN, CENTRAL ALASKA

By

Alec J. Rizzo

RECOMMENDED:

Dr. Elisabeth Nadin

Dr. Paul McCarthy

Dr. Catherine Hanks
Advisory Committee Chair

Dr. Paul McCarthy
Chair, Department of Geosciences

APPROVED:

Dr. Paul Layer
Dean, College of Natural Science and Mathematics

Dr. John Eichelberger
Dean of the Graduate School

14 July 2015
Date

NATURAL FRACTURE CHARACTER AND DISTRIBUTION ADJACENT TO THE NENANA BASIN, CENTRAL ALASKA

A

THESIS

Presented to the Faculty

of the University of Alaska Fairbanks

in Partial Fulfillment of the Requirements for the Degree of

MASTER OF SCIENCE

By

Alec J. Rizzo, B.A.

Fairbanks, Alaska

August 2015

ABSTRACT

The NE-trending Nenana basin is a Cenozoic-aged basin located in central Alaska between the Denali and Tintina fault systems. The narrow, deep basin is a current exploration target for oil and gas resources in Interior Alaska. Natural fractures were analyzed to further understand larger structural features such as faults and folds related to the structural evolution of the Nenana basin and surrounding areas. Fracture sets were measured and described on the margin of the basin at four field locations: the Fairbanks area, along the Parks Highway between Fairbanks and Nenana, and in outcrop around the Nenana and Healy areas. In addition to measuring fracture sets in outcrop and collecting oriented samples, statistical and thin section analyses were used to further analyze fracture characteristics. Calcite twin thermometry and apatite fission track analysis were used to constrain the timing and thermal evolution of the field area.

Based on the orientations of observed map-scale faults, folds, and fracture sets, I divided the four field locations into two structural domains. Domain I is characterized by NE-striking faults and associated active seismicity while Domain II is dominated by E-W striking folds and faults related to the late Cenozoic development of the Northern Foothills fold-and-thrust belt. I interpret that fracture sets in Domain I are related to the evolution of high angle faulting between the Nenana basin and the Fairbanks area during Cenozoic time. In Domain II, I interpret fracture sets are related to the evolution of the fold-and-thrust belt north of the Alaska Range. By combining fracture characteristics and apatite fission track analyses I provide constraints for the timing and shear sense of larger structural features related to the opening history of the Nenana basin. Furthermore, I propose that the evolution of the Nenana basin took place in three distinct tectonic phases during the Cenozoic. The three phases represent the transition from a pure extensional setting in the Late Paleocene to oblique-extensional faulting from the Late Miocene to present day.

Table of Contents

Page

Page

List of Figures

Page

Page

Page

Page

Page

Page

Page

Page

List of Tables

Page

Page

Page

Page

Page

Page

List of Appendices

Page

ACKNOWLEDGMENTS

I would like to recognize my advisor Dr. Catherine Hanks for her support and encouragement throughout the duration of my research. She provided me with the guidance necessary to complete my research and I could not have asked for a better advisor and mentor. I would also like to thank my committee members Dr. Elisabeth Nadin, Dr. Paul McCarthy, and Dr. Wesley Wallace for their knowledge and advice throughout the past 4 years. I would like to thank the U.S. Air Force Office of Scientific Research for providing the Award no. FA9550-11-1-0006 that funded the majority of my research. In addition, I would like to thank the UAF Department of Geosciences, the UAF Geophysical Institute, and BP Exploration Alaska, Inc. for providing teaching assistantships and the remaining funds to allow me to complete my thesis work. Finally, I would like to thank my friends, family, and colleagues for making my time in Fairbanks so enjoyable.

CHAPTER 1: INTRODUCTION

Natural fractures develop in many different complex structural environments, and understanding their character and distribution throughout a field area can provide insight into the stresses responsible for their formation. Many basins undergo multiple tectonic events that cause different generations of faults and folds. The relationship of mesostructures such as natural fractures to folds and faults can aid in understanding the much larger question of how these intracratonic basins evolve through time.

Central Alaska is a broad region bounded by two right-lateral fault systems (Fig. 1). This region contains several intracratonic basins, inactive and active complex fault systems, and evolving thrust belts. Understanding the timing, mechanisms, and relationship of natural fractures to the regional geology will aid in understanding the stresses responsible for the evolution of these prominent structural features.

This project focuses on one of these intracratonic basins: the northeast trending, Cenozoic-aged Nenana basin located southwest of Fairbanks (Fig. 1; Riehle, 1997; Dixit and Hanks, 2014). The Nenana basin is a narrow, deep intracratonic basin whose geometry and evolution is governed by multiple episodes of faulting. The basin is estimated to be ~25,000 feet deep and is predominantly filled with non-marine sediments containing coal-bearing sequences (Van Kooten et al., 2012). The Nenana basin is currently being explored for its oil, gas, and coal bed methane potential, and is being evaluated as a reservoir for CO_2 sequestration.

The Nenana basin has been the focus of episodic hydrocarbon exploration over the past 30 years, and is actively being explored by Doyon, Ltd., an Alaska Native corporation. The petroleum

system for the Nenana basin consists of coals and coaly shales from the Usibelli Group as source rocks, with numerous reservoir types (Doyon, Ltd., 2012). Doyon, Limited (2012) interpreted that the deeper parts of the basin are mature enough with type I/II kerogens for the production of oil & gas. The true oil and gas potential of the basin, as well as its promise for CO_2 sequestration, will be better understood through a thorough investigation of the basin's formation and evolution.

Natural fractures can also provide further information pertaining to reservoir characterization. Studying fracture orientation and extent of fracture cement, as well as fracture density and spacing, are important steps to take when evaluating a potential reservoir. Natural fractures can act as migration pathways for fluids and gases and can greatly increase the permeability and secondary porosity of a reservoir. In contrast, the connectivity of fracture networks can greatly decrease seal integrity and cause problems for developing or isolating natural resources.

This study is therefore aimed at establishing the distribution, character and timing of fractures in and adjacent to the Nenana basin; the potential relationship of these fractures to faulting in the region; and the implications of these fractures for principal stress orientations throughout the basin's history. In order to achieve these goals, my study included the following objectives:

1) Identify the fracture sets in the field area and understand their relative timing

2) Understand fracture morphology in both outcrop and thin section.

3) Utilize apatite fission track and thin section analyses to further constrain the timing, thermal history, and thermal deformation of the observed fracture sets.

4) Perform statistical analyses of fracture characteristics, such as density, spacing, height, and length, to investigate how fractures change spatially across the field area.

5) Relate fracture sets to larger structural features, such as faults and folds, and generate a conceptual model of the evolution of stresses that caused basin formation.

This study of natural fractures throughout the basin and surrounding areas in central Alaska is one part of a larger project funded by the Department of Energy and the U.S. Air Force that is investigating the potential of using the Nenana basin for CO_2 sequestration.

CHAPTER 2: BACKGROUND

2.1 Regional Tectonic/Geologic Setting

The tectonic evolution of southern and central Alaska is controlled by the North American-Pacific plate convergence (Fig. 2; Haeussler, 2008). The subduction of the Yakutat microplate is postulated to have caused counterclockwise rotation and northwest movement of south-central Alaska (Haeussler, 2008; Bemis, 2010). Deformation caused by this convergence can be seen up to 600 km inland, and right-lateral displacement and contraction continues along the Denali fault and within the Alaska Range (Bemis, 2010).

2.2 Interior Alaska Tectonic Setting and Active Seismicity:

Central Alaska is bounded by two primary right-lateral strike-slip faults-- the Tintina fault system in the north and the Denali fault system in the south (Fig. 2; Haeussler, 2008). Rocks in the intervening Yukon-Tanana terrane, a highly deformed terrane of Precambrian-early Paleozoic rocks, are cut by a series of Cenozoic northeast-striking lineaments and left-lateral strike-slip faults (Ridgway et al., 2007; Ratchkovski and Hansen, 2002; Ruppert et al., 2008). These lineaments and northeast-striking faults are associated with northeast-trending zones of seismicity that include the Minto Flats seismic zone, the Fairbanks seismic zone, and the Salcha seismic zone (Fig. 3; Ruppert et al., 2008; Ratchkovski & Hansen, 2002).

In order to explain the observed seismicity, Page et al. (1995) proposed a model for Interior Alaska in which the Tintina and Denali right-lateral strike-slip faults bound a dextral shear zone which is deforming internally via clockwise crustal block rotation (Fig. 4). In their model, NE-striking left-lateral strike-slip faults within the shear zone act as subsidiary slip surfaces that help accommodate this clockwise rotation of crustal blocks. This is the best known, and most widely

cited, model explaining the NE-striking seismic zones in interior Alaska, but it does not mean it is the only explanation for them.

The model proposed by Page et al. (1995) is based upon slip on both the Denali and Tintina fault systems. There is evidence that there has been significant motion along both major dextral faults that could promote clockwise motion in Interior Alaska (Gabrielse et al., 1985, 2006; Nokleberg et al. 1985, 1994; Plafker and Berg, 1994; Page et al., 1995; Benowitz et al. 2012, Koehler, 2013). Based on displacement of plutons and metamorphic rocks, Benowitz et al. (2012) suggested that there was 100 km of dextral slip along the Denali fault from 51 Ma to 25 Ma, and another 300 km since 25 Ma. In addition, from fault reconstructions based on K-Ar ages of deformed and metamorphosed igneous and sedimentary rocks of the Maclaren terrane, there has been 400 km of right-lateral displacement since 56 Ma (Fig. 5; Nokleberg et al. 1985; 1994). Along the Tintina fault, based on restorations of thrust offset, it is estimated that there was 400-430 km of right-lateral displacement between Late Cretaceous and Early Tertiary time (Gabrielse et al., 1985, 2006). Recent motion along the Tintina fault is limited to a 14 km-long Holocene scarp within a 90 km- long zone of suspected Quaternary or Neogene offset (Plafker and Berg, 1994; Page et al., 1995; Koehler, 2013). Compared to the interpreted displacement between the Late Cretaceous to Early Tertiary, not much motion has been recorded along the modern-day active portion of the Tintina fault.

2.3 Major Geologic Elements of Interior Alaska

The highly deformed Yukon-Tanana terrane, the Nenana basin, the Tanana basin, and the northern Alaska Range foothills fold-and-thrust belt are all located in the zone between the Denali and Tintina fault systems (Fig. 1). In the sections below, each geologic element will be described in terms of timing, formation, and stratigraphy.

2.3.1 The Yukon-Tanana Terrane

The Yukon-Tanana terrane underlies a large portion of east-central Alaska and is a "broad band" of metamorphic rocks between the Denali and Tintina fault systems (Fig. 5; Goldfarb et al., 2000; Hansen, 1991). Latest Cretaceous to Early Tertiary right-lateral motion along the Tintina fault displaced the Yukon-Tanana composite terrane 450 km into Alaska from the Yukon Territory (Pavlis and Sisson, 1993). The terrane is highly deformed and is separated into lineated and foliated tectonites that record multiple deformation events (Hansen and Dusel-Bacon, 1998). On the basis of kinematic, pressure, temperature and thermochronometric data, the Yukon-Tanana terrane can be divided into allochthonous and parautochthonous tectonites (Hansen and Dusel-Bacon, 1998). According to Hansen and Dusel-Bacon (1998), the geologic history of the tectonites can be described in three deformation events.

1) Pre-Jurassic to Early Jurassic (>212 Ma) NE-oriented contraction that deformed oceanic rocks (Hansen and Dusel-Bacon, 1998);

2) Early to Middle Jurassic (>188–185 Ma) NW-oriented contraction that resulted in the repositioning of both types of tectonites (Hansen and Dusel-Bacon, 1998); and

3) Early Cretaceous (135–110 Ma) SE-oriented crustal extension that exposed the parautochthonous continental rocks,

The complex deformational history of the Yukon-Tanana terrane is recorded in the rocks throughout east-central Alaska (Fig. 5). The exposed metamorphosed sedimentary and igneous rocks of the composite terrane are found in the geologic elements of east-central Alaska discussed in section 2.3.

2.3.2 The Nenana Basin

The Nenana basin is a long, narrow, NE-SW trending basin that covers ~5200 square miles in the western part of Interior Alaska (Fig. 1; Riehle, 1997; Dixit and Hanks, 2014; Van Kooten et al., 2012). The Nenana basin has been interpreted to be a result of crustal extension and right-lateral strike-slip along the Denali and Tintina fault systems (Van Kooten et al., 2012, Dixit and Hanks, 2014). According to Van Kooten et al. (2012), the basin developed on plutonic and metamorphic basement rocks of the Yukon-Tanana terrane, and is a structural half graben with a basin bounding normal fault, the Minto fault, on its southeast margin (Fig. 6; Doyon Limited, 2009).

Bouguer gravity and gravity inversion maps indicate that the deepest part of the basin is to the north with an estimated depth of ~25,000 feet (Van Kooten et al., 2012). Based on wells drilled in the basin, the sediments filling the basin are predominantly sedimentary non-marine Usibelli Group overlying Late Paleocene strata. Based on published well data by Doyon, Ltd., there could be rocks older than Late Paleocene in the deeper parts of the basin (Fig. 7; Van Kooten et al., 2012; Doyon Limited, 2012). Overlying the Late Paleocene sediments, the Usibelli Group consists of coal-bearing fluvial and lacustrine sedimentary rocks and is divided into five separate formations: the Healy Creek, Sanctuary, Suntrana, Lignite Creek, and Grubstake formations. Overlying the Usibelli Group is the Nenana Gravel, which consists of conglomerate associated with alluvial fan and braided river deposits (Ridgway et al., 2007).

Ongoing work in the Nenana basin incorporates 2D seismic lines acquired by ConocoPhillips in 2005 as part of a land seismic survey, as well as additional 2D and 3D seismic data acquired by Doyon Limited in 2005 and 2014, respectively. In addition to these surveys, exploration wells drilled into the basin have been interpreted to determine the subsurface

distribution and thicknesses of the Cenozoic sedimentary successions (Van Kooten et al., 2012; Dixit and Hanks, 2014). Recent research has shown that more than one active fault controls basin extension; this basin can thus be interpreted as a pull-apart basin. It may have been such since sometime after ≤6 Ma, but several lines of evidence indicate it has not been a pull-apart basin through most of its evolution. From the published geohistory model provided by Van Kooten et al. (2012), the initial subsidence of the Nenana basin began in the Late Paleocene and it continues to the present. In combination with published seismic profiles and structure maps provided by Doyon Limited and available interpreted seismic lines, Dixit and Hanks (2014) interpret the following structural evolution of the Nenana basin since the late Paleocene:

Late Paleocene (pre-Healy unconformity)

The Late Paleocene represents the initiation of the Nenana basin, but not necessarily the NE-trending basin of today. During this time period there was rapid tectonic subsidence and deposition of Paleocene sediments (Dixit and Hanks, 2014).

The generation of faults sub-parallel to the proto-Minto fault characterizes the first phase of basin evolution. Based on seismic interpretation by Doyon Limited (2014), and Dixit and Hanks (2014), the major NE-striking normal faults were active during this time period. These NE-striking normal faults accommodated extension in a NW-SE direction. A subsidiary set of NW-striking normal faults was active at this time as well (Fig. 8; Dixit and Hanks, 2014; written

Late Miocene-Pliocene (Lignite Creek Formation)

This time period represents the reactivation of the pre-existing NE-striking faults with oblique slip. Both NE-striking and NW-striking fault patterns continue to have an extensional dip-slip component, but there is left-lateral shear along the NE-striking faults and possibly pure dip-slip motion along the NW-striking faults (written commun., N. Dixit, 2014; Dixit and Hanks, 2014).

This is supported by seismic interpretation (Doyon Limited, 2014; Dixit and Hanks, 2014). The basin continues to extend in the NW-SE direction (Fig. 8).

Another important aspect of this stage in basin evolution is the formation of E-W striking, southeasterly dipping reverse faults (Fig. 8). The reverse dip-slip motion along these faults is interpreted from positive flower structures seen in 2D seismic lines (written commun., N. Dixit, 2014; Dixit and Hanks, 2014). These E-W striking reverse faults are located between the NE-striking lineaments of the Minto flats seismic zone. The zone of reverse faults may indicate a restraining bend in a left-lateral fault system (Fig. 8) (written commun., N. Dixit, 2014; Dixit and Hanks, 2014).

Pliocene-Present Day

The final phase of basin evolution involves rapid tectonic subsidence from Pliocene to present day. There is a significant strike-slip component with a minor normal slip component along major NE-striking faults (written commun., N. Dixit, 2014; Dixit and Hanks, 2014). The NW-striking faults are pure dip-slip with an extensional component, and NE-striking faults to the northwest continue to widen the basin (Fig. 8).

2.3.3 The Tanana Basin

The Tanana basin is a broad, shallow basin located south of Fairbanks and east of the Nenana basin (Fig. 1). The basin stratigraphy consists of metamorphosed rocks overlain by packages of the Usibelli Group and Nenana Gravel (Kirschner, 1994). The Tanana basin is interpreted to have formed during Neogene time due to crustal loading as the frontal thrusts of the Alaska Range propagated northward (Ridgway et al., 2007).

2.3.4 The Northern Foothills Fold-and-Thrust Belt

The northern foothills fold-and-thrust belt, south of the Nenana basin, is characterized by a series of east-west striking thrust faults and folds (Fig. 1; Bemis and Wallace, 2007 and Bemis et al., 2012). The arcuate fold-and-thrust belt lies north of the main axis of the Alaska Range and separates the Alaska Range from the broad Tanana basin to the north (Bemis and Wallace, 2007). The foothills are ~350 km long and 100 km wide and gradually lose structural relief northwards towards the Tanana basin (Ridgway et al., 2007).

Thrust structures pervade the basement metamorphic rocks, the Miocene Usibelli Group, and the latest Miocene and younger Nenana Gravel. These east-west striking thrust faults dip both north and south, and are accompanied by east-west trending folds (Fig. 9). Previous studies suggest that the late Cenozoic orogeny that uplifted this region ended prior to 2.6 Ma (Wahrhaftig, 1958), but recent work on the geologic relationships and topography of the region suggests that these structures are still actively forming (Bemis and Wallace, 2007; Bemis, 2010; Bemis et al., 2012).

The structural changes along strike displayed in map view can be attributed to along-strike variations in shortening, perhaps due to strike-slip motion along pre-existing faults in the area, changes in lithology (bed units), and influences from pre-existing basement structures (Bemis and Wallace, 2007). Deformed sedimentary rocks and geomorphic studies throughout the series of folds and thrust faults indicate that the deformation front of the fold and thrust belt has migrated northward over time (Bemis and Wallace 2007; Ridgway et al., 2007). Deformation began just north of the Hines Creek fault and has moved northward to the present day northern foothills thrust (Fig. 1; Bemis and Wallace 2007). The recent deformation and close proximity of the foothills to the Nenana basin may have caused some compressional features in the southern part of the basin.

2.4 Natural Fractures

The study area is pervasively fractured due to the prolonged and pervasive deformation described above. Natural fractures are defined as "discontinuities in rocks caused by brittle failure of the host rock (Narr and Suppe, 1991). There are three failure mechanisms for fracture formation (Pollard and Segall, 1987; Scholz, 2002; Bons et al., 2012) (Fig. 10; Bons et al., 2012):

1) Mode I

In mode 1 fractures, displacement of joints are perpendicular to the fracture wall. These are also known as 'extension fractures.' They are characterized by an opening mode displacement normal to the fracture wall, and open parallel to the maximum and perpendicular to the minimum compressive stresses (Fig. 11; Ramsey and Chester, 2004). On a Mohr circle, extension fractures form under low differential stress ($\sigma_1 - \sigma_3$) and σ_3 can be negative (Davis and Reynolds, 1996) (Fig. 11; Ramsey and Chester, 2004).

2) Mode II

In mode 2, failure occurs parallel to the fracture plane. These are also known as 'sliding shear fractures'. Shear fractures form under a compressive stress state with displacement parallel to the fracture face (Fig. 11; Ramsey and Chester, 2004). According to Ramsey and Chester (2004), shear fractures form at 20° to 40° angles to the maximum principal compressive stress direction (Fig. 11; Ramsey and Chester, 2004). On a Mohr circle, shear fractures form under greater differential stress than extension fractures (Fig. 11; Ramsey & Chester, 2004).

3) Mode III

Displacement for mode 3 fractures is parallel to the fracture plane and perpendicular to the direction of fracture propagation. These are also known as 'tearing shear fractures'. Like mode 2 fractures, mode 3 fractures form under a compressive stress and at acute angles to the maximum

principal compressive stress direction. On a Mohr circle, shear fractures form under greater differential stress than extension fractures (Fig. 11; Ramsey & Chester, 2004).

Apart from extension and shear, a transitional stress condition forms hybrid fractures, which are a mix of compressive and tensile fractures at acute angles to the maximum compressive stress (Fig. 11; Engelder, 1987; Ramsey and Chester, 2004; Bons et al., 2012).

A fracture 'set' is a group of parallel fractures with similar characteristics such as orientation, while a fracture 'system' contains more than one fracture set to form an interconnected network for increased permeability and porosity in a reservoir (Narr and Suppe, 1991). Natural fracture/vein networks are important geologic structures for understanding the stress, strain, pressure, and temperature during their initial formation (Bons et al., 2012). In addition, with their relationships to local faults, fracture sets can demonstrate the evolution of a particular fault, providing insight on how the tectonic setting in which that fault formed evolved over a time.

The type of fracture formed at any given location is strongly dependent not only on the local stresses, but also the stress of the overall structural regime. Natural fractures are a result of the total history a body of rock has undergone; studying natural fractures can reveal previous local and regional stress fields of a particular area. Apart from the three types of fractures, shear fractures can form as conjugate sets. A set of conjugate shear fractures forms at acute angles from the maximum principal stress (Fig. 12; Twiss and Moores, 1992). The conjugate fractures have opposite senses of shear and the angle bisecting the fractures corresponds with the orientation of an extension fracture. In addition, the angle bisecting the conjugate shears is the maximum compressional stress responsible for fracture formation (Twiss and Moores, 1992).

Apart from fracture formation occurring due to increasing differential stress, pore fluid pressure can be responsible for fracture set formation at significant depths in the subsurface. At

depths above 3 km in the subsurface, the pore fluid pressure is "typically normal to the hydrostatic pressure", which ultimately restricts fluid flow (Twiss and Moores, 1992; Davis and Reynolds, 1996). Below this depth, fluid pressure becomes greater than hydrostatic pressure as temperature rises in the subsurface. The rise in temperature can cause pore fluid pressure to exceed lithostatic pressures at depth (Davis and Reynolds, 1996). On a Mohr diagram, increasing pore fluid pressure results in the stress circle hitting the failure envelope and fractures forming due to tensile or transitional tensile failure (Davis and Reynolds, 1996). Pore fluid pressure can have a significant impact on fracture set formation depending on the relationship between the various pressures that exist in the subsurface.

Natural fractures can occur as veins (filled with a mineral) or with open apertures in the outcrop. Tectonic veins, in particular, represent phases of geologic activity that occurred after the host rock was formed (Bons et al., 2012). By looking at their shape, internal structure, and orientation they can reveal information about paleo-stress fields and the amount of deformation and fluid pressure a body of rock underwent (Bons et al., 2012). In addition, the mineralogy of the vein can also indicate the metamorphic conditions (pressure and temperature) that the body of rock underwent during vein formation (Bons et al., 2012). This can be important for understanding the approximate depth of vein formation, which in turn can lead to a better understanding of the evolution of the individual fracture sets.

Understanding the microstructures of a vein in thin section can provide insight on the characteristics of the overall fracture set that cannot be observed in outcrop. Crack seal events are repeated cracks in the vein caused by repeated deformation, which are then resealed due to additional fluid flow (Ramsay, 1980, Bons et al., 2012). It is possible that multiple crack seal events in a vein can yield insight into the evolution of that particular fracture or fracture set if the

identified trend is common. The fracture fill is also important when looking at how the fracture opened. If the crystals are perpendicular to the fracture wall, that indicates that the vein opened with little or no shear (Engelder, 1987; Passchier and Trouw, 2005).

2.5 Natural Fractures Related to Faulting

Fractures that form in relation to faults can form as both extension and shear fractures. The orientation of fractures will change depending upon the orientation of *in situ* stresses. For normal faulting, the principal stress, σ_1 is vertical, σ_2 is oriented parallel to the intersection of the conjugate fault planes, and σ_3 is oriented perpendicular to the acute bisector of conjugate fault planes (Figure 13a; Narr and Suppe, 1991). These local stresses result in fractures forming sub-parallel to parallel to the fault plane and the σ_2 stress (Fig. 13a; Stearns, 1968). For thrust faulting, σ_1 is oriented perpendicular to the obtuse bisector of the conjugate fault planes, σ_2 is oriented parallel to the intersection of the conjugate fault planes, and σ_3 is vertical (Fig. 13b). Both shear fractures and extension fractures can form parallel to the fault plane (Twiss and Moores, 1992). In addition, conjugate shear fractures can form at acute angles to the maximum compressive stress.

In fault systems, a pattern of shear fractures called 'riedel shears' can also form due to reoriented stress vectors along normal, thrust and strike-slip faults if there is significant shearing in a zone around the fault plane. The orientation of riedel shears is dependent on the type of shear on the master fault (Fig. 14; Davis and Reynolds, 1996). The formation and timing of riedel shears are described for a left-lateral master fault in the numbered steps below:

1) The first shears to form are the R shears, and they form at an acute angle 15° anticlockwise from the master fault. R shears form en echelon arrays with individual faults synthetic to the shear of the master fault.

2) The next set to form are called R' shears. R' shears are antithetic to the master fault and usually form at a high angle, 75°, counterclockwise from the master fault. R' shears can form separately or with R shears. They are antithetic to the principal fault motion (Fig. 14; Davis and Reynolds, 1996).

3) The next set to form are called P shears. P shears are synthetic to the master fault and form en echelon arrays with individual faults at acute angles clockwise to the principle fault. P' shears are antithetic conjugates to P shears and both are less common than R and R' shears because they may require significant displacement in order to form (Fig. 14; Davis and Reynolds, 1996).

Fault-related fractures can form as extension, shear, conjugate shears, and in a riedel shear geometry in normal, thrust, and strike-slip systems. The orientation of natural fractures will change depending upon the orientation of the *in situ* stresses present. Observing fracture orientations in relation to dominant fault trends can help determine the evolution of local stress over time.

2.6 Natural Fractures Related to Folding

According to Twiss and Moores (1992), fracture orientations associated with folds are described as "conjugate shear fractures with or without a set of extension fractures." When interpreting fold-related fractures it is important to understand what fractures may have formed before, during, and after the folding process. Natural fractures that formed during a folding event will match the orientations of the stress axes that caused the deformation (Jäger et al., 2008). The two most common extension fracture sets to form are both orthogonal and parallel to the fold axes (Figure 15; Hayes and Hanks, 2008; Engelder, 1987; Twiss and Moores, 1992; Jäger et al., 2008; Wentz, 2014). Deformational events such as folding not only control the orientation of the fracture sets, but also the type of fractures that form throughout the event. Different orientations of fracture sets can form if there are multiple layers of stratigraphy. This is due to tangential longitudinal

strain and it commonly occurs in rocks that are actively deforming (Ramsay and Huber, 1987; Hayes and Hanks, 2008; Wentz, 2014)). The outer arc of the fold commonly deforms due to layer parallel extension, while the inner arc deforms from layer parallel contraction (Davis and Reynolds, 1996; Wentz, 2014). This can create separate stress regimes in different parts of the fold. Four unique types of fracture combinations can form across a fold due to these stresses and contain combinations of both conjugate shears and extension fractures (Fig. 15; Hayes and Hanks, 2008).

Different fracture types may form in different parts of the fold due to varying regional and local stress orientations. In complex fold geometries, both extension fractures and conjugate shear fractures can form in the compressive state. Extension fractures may form parallel to the maximum principal stress orientation while conjugate shear fractures may form at acute angles to σ_1 (Twiss and Moores, 1992). The orientations of both conjugate shears and extension fractures are dependent on the location they form on the fold due to tangential longitudinal strain (Fig.15; Hayes and Hanks, 2008).

2.7 Apatite Fission Track Thermochronology

Low temperature thermal histories of the rocks in the field area can be constrained using apatite fission track analysis (Donelick et al., 2005). Apatite is an abundant mineral found in many sedimentary, igneous and metamorphic rocks, which makes it ideal for obtaining data in crustal rocks. In addition, the abundance of uranium and thorium in apatite allows for relative ages to be calculated. Data is based on fission tracks, or damage "trails", in the apatite caused by radiation or fission due to uranium in the mineral (Donelick et al. 2005). The number and length of fission tracks relative to the amount of uranium is used to calculate the age of the sample.

Fission tracks in apatite are produced by the fission of Uranium-238 and the rate that they form is dependent on the concentration of the isotope in the system (Donelick et al. 2005). The process consists of a nucleus splitting into two particles that are repelled by each other. This creates

a linear damage zone in the crystal lattice displayed by chemical etching (Dusel-Bacon and Murphy, 2001). After the tracks are formed, they anneal, or heal at a rate directly related to the temperature that they are exposed to (Gleadow et al. 1986). In a closed system, younger tracks tend to be longer due to the shorter amount of time they have been exposed to temperature (Donelick et al., 2005). The track lengths can be used to determine the rate of cooling a certain body of rock has undergone. The tracks heal in the partial annealing zone, or "PAZ", which is defined between 110 °C - 60 °C (Gleadow et al., 1986). This zone represents the range at which tracks can anneal; they heal effectively at temperatures ≥110 °C and not effectively at temperatures ≤60°C. The age of the sample is related to the amount the tracks have annealed which is related to the amount of uranium-238 in the sample. As the tracks anneal, the age of the sample decreases; the age approaches zero as the tracks anneal (Gleadow et al., 1986). The decay rate of uranium-238 and track density within the crystal grain is interpreted to reveal the time since cooling (Dickin, 1995). Once the samples cool below the partial annealing zone, the tracks will no longer anneal and the age of the sample is sealed.

CHAPTER 3: METHODS

The majority of geological study of the Nenana basin has been through a private corporation, but data from two drilled wells, seismic lines across the length and width of the basin (provided by Doyon, Limited and ConocoPhillips), and fieldwork on the margins of the basin, are integrated into this study. The first approach was to measure natural fractures in outcrops exposed along the basin margin as far north as Fairbanks and as far south as Healy. Fracture characteristics such as orientation, fracture lengths and heights, and shear sense in the metamorphosed basement, in the Miocene-aged Usibelli Group, and in the Early Tertiary basalt in the Fairbanks area were measured to establish a fracture history of both the basin and Interior Alaska. In addition, thin-section analysis, apatite fission-track data, and fracture statistics (fracture density, spacing, height, and length values) were used to generate a model for the initiation of fracture sets related to the formation and evolution of the Nenana basin.

3.1 Fieldwork

It is necessary to collect detailed field measurements to determine the fracture character and distribution throughout a basin. The distribution, character and relative timing of fractures were determined in outcrops along the Parks Highway from Fairbanks to Healy. Host rocks varied from metamorphic basement rocks of the Yukon-Tanana terrane in the Fairbanks and Nenana areas, local basalt quarries in the Fairbanks area, and Tertiary sedimentary rocks in the Healy area. Fieldwork was conducted throughout the summers of 2012 and 2013 at 25 field sites along the margin of the Nenana basin and within interior Alaska (Fig. 17).

3.2 Fracture Analysis Techniques

Detailed fracture data was collected at outcrops using the straight scan-line fracture survey method with an open-reel measuring tape (Fig. 16) (Shackleton, 2003) (Appendix A). An open-

reel measuring tape was placed perpendicular to fracture sets at an outcrop, and every fracture that intersected the tape was measured and described with respect to:

a. Fracture orientation

b. Fracture spacing

c. Lengths of individual fractures along transect

d. Fracture heights perpendicular to layering

e. Aperture width of fractures

f. Nature of termination where observable

g. Fracture type

If possible, ≥25 fractures for each transect were measured. Fracture sets throughout the study were classified using the following characteristics (based on work by Shackleton, 2003; Hayes, 2004; Duncan, 2007; Loveland, 2010):

a. Fracture orientation

b. Morphology

c. The presence or absence of fill (quartz or calcite)

d. Relative age relationships governed by where the fractures terminate (cross-cutting relationships)

In addition, visible heights and lengths of individual fractures were measured with separate measuring tapes in outcrop. Relative age was determined by abutting relationships--if one fracture set terminated against another, it was interpreted as younger (Twiss and Moores, 1992).

Fracture data were collected at 25 locations along the margin of the basin (Fig. 17) (Appendix A). Fractures measured across field localities on the margin of the basin range in vein

fill and shear sense (Table 1). In addition to measuring fracture characteristics, oriented samples were collected for thin section analysis of veins for additional analysis of fracture sets (Fig. 18).

3.3 Spatial Fracture Characteristics

Statistical fracture analysis techniques were used to understand how fracture characteristics such as density, spacing, length, and height change between fracture sets and to analyze the data in a more spatial sense. A number of statistical techniques were used to analyze and present the data (Appendix B). For fracture density and spacing, box plots were used to see how the mean values and the ranges of values differ between possible sets. For fracture height and length, histograms were used to see how these values change between each fracture set. Box plots were not used for fracture height and length because *visible* heights and lengths were measured for these values, not *actual* total height and length.

In order to understand how the fracture sets change spatially, measurements were made at varying distances from the basin. Fracture density and spacing were analyzed to see if fracture characteristics vary systematically with distance from the basin. The measurements for fracture density and spacing for each fracture set were plotted on a map with their distance from the basin margin. In addition, if measured fracture sets from separate field areas share common characteristics such as orientation, fill, and shear sense, a comparison of means was done on the data to determine if the fracture sets were statistically different; one-way analysis of variance tests (anova tests) were performed to see if the values for density and spacing are similar.

The density and spacing data allow for fracture sets with similar characteristics to be compared, while height and length data can serve as proxies for permeability and will give a better understanding of how the dimensions of the sets change across study areas (Singhal & Gupta, 2010).

3.4 Thin Section Analysis

Oriented samples were taken of well-preserved cement-filled fractures. Samples were made into double-polished thin sections by National Petrographic, Inc. Thin sections were analyzed and interpreted in terms of vein composition, extent of vein deformation, and the direction of shear as determined from crystal orientation. If the vein was composed of calcite, calcite temperature gauges were used to determine deformation temperatures.

3.4.1 Calcite Twin Paleothermometry

How an individual vein formed can indicate the type and extent of deformation the rock has undergone (Bons et al., 2012). Depending on the thickness and extent of deformation of the individual sets of calcite twins, they can show a relative temperature of formation (Fig. 19; Burkhard, 1993; Bons et al., 2012). The higher the temperature at which the twins form, the thicker and more deformed they appear. Using this methodology and a geothermal gradient for the field area of 32 °C/km determined from the Eielson test hole in central Alaska (Dusel-Bacon and Murphy, 2001), estimated depth of vein formation can be calculated. Thin sections not only help determine vein character on a micro scale, but will aid in determining approximate age and depth constraints for vein formation by correlating them with apatite fission track time-temperature curves.

3.5 Apatite Fission Track Analysis

During the summer of 2012, samples of metamorphic rocks of the Yukon-Tanana terrane were collected across faults at varying distances from the Nenana basin (Fig. 20; Frohman, 2014). Fourteen apatite fission track samples were collected around the Fairbanks area and from wells within the Nenana basin and analyzed for cooling ages and thermal histories (Appendix C). From the fourteen AFT samples that were datable, only eight samples had enough grains and fission

tracks to compute a reliable age. Samples lacking apatite grains with fewer fission tracks have greater error ranges and are considered lower quality samples (Fig. 20).

Apatite fission-track samples were sent to Apatite to Zircon, Inc., and analyzed and modeled by Paul B. O'Sullivan. Inverse modeling was used and it predicts the evolution of the thermochronometric system based on thermal relationships (annealing behavior), chemical characteristics (parent-daughter decay rates), and assumed conditions (present day and starting conditions of sample) (Ketcham, 2005). The program HeFty was used to model the samples and many time-temperature curves were generated by Paul O'Sullivan and interpreted in Frohman (2014). Initial inputs to constrain the time-temperature histories of samples for the models include the age of the samples, the present day geothermal gradient of the field area, and the sample depth. I describe the interpretations made by Frohman (2014), and utilize the time-temperature curves and basic trends to further understand the timing and thermal evolution of the observed fracture sets. For this thesis, only the time-temperature paths from the Late Paleocene onwards were analyzed. This is because the time periods important for the evolution of the Nenana basin are from the Late Paleocene onwards (Dixit and Hanks, 2014).

In order to further analyze the AFT data, Frohman (2014) utilized time-temperature curves to calculate cooling rates of samples through the partial annealing zone. This was done by taking the slope of the weighted mean curve from each thermal model. Five points were picked within the partial annealing zone (PAZ) (between 60°-120 °C) that had a temperature and a corresponding age and were used to calculate the slope (Frohman, 2014). To obtain the exhumation rate for all the samples, the cooling rate was divided by the geothermal gradient and then multiplied by 1000 to get the exhumation rate in m/Ma. Both the cooling and exhumation rates were used to understand the rates at which samples cooled at varying distances from the basin.

CHAPTER 4: OBSERVATIONS/ RESULTS

4.1 Fracture Sets

By examining the fracture characteristics from the 25 field locations, I observed ten different fracture sets on the margin of the Nenana basin. The fracture sets are categorized by numbers and letters depending on where they were measured. Fracture sets F1-F6 are found in the Fairbanks area, along the Parks Highway, and in the Nenana area while fracture sets A-D are only found in the Healy area. Thin sections for each fracture set are interpreted and characterized by dominant vein fill, shear sense, and crystal character. Thin sections cut horizontally (parallel to the strike of the vein) as well as cut vertically (parallel to the dip of the vein) were both used to understand the overall shear character of the vein (Fig. 21).

Fracture Set 1 (F1)

Fracture set F1 ranges in strike from 285°-300° and has an average dip of 54° NE +/- 30° (Fig. 22; Table 1). The fracture set consists of shear fractures with right-lateral motion in both outcrop and in thin section. Vein fill is primarily quartz with secondary calcite. The oldest fracture set measured commonly terminates internal to compositional layering or against other F1 fractures (Fig. 23). In metamorphic rocks, the average density of F1 is 5.89 fractures/meter while average spacing is 0.27 meters (Table 1). Visible heights range from 0.004 to 5.8 meters and visible lengths vary from 0.0014 to 1.65 meters in outcrop (Table 1). In basalt, the average density is 8.19 fractures/meter and average fracture spacing is 0.28 meters. Fracture height ranges from 0.14 to 5.8 meters and length varies from 0.14 to 0.18 meters (Table 1).

Veins of fracture set F1 contain quartz with secondary calcite (Fig. 24). Quartz crystals range in shape from blocky to elongate blocky, while secondary calcite tends to be fibrous. The crystals vary in orientation from 40°-50° (70° NE on the horizontal plane) with respect to the vein wall (295°) in thin sections cut both horizontal and vertical parallel to the dip of the vein (Fig. 21).

Orientation of both calcite and quartz crystals throughout the vein varies: some crystals are sub-perpendicular to the vein wall, others are at low angles from the vein wall, suggesting both an extensional and right-lateral shear component throughout vein history. The angles with respect to the vein wall provide slip vectors for the opening of the vein. Combining the orientation of crystals in the vein from thin sections cut parallel to the strike and dip provides a slip vector for the opening history of the vein (Fig. 24). For F1, the opening history shows a strong normal dip-slip component with a right-lateral shear sense (Fig. 25a). No calcite twins were visible in thin section for fracture set F1.

Fracture Set 2 (F2)

Fractures in F2 range in strike from 300°-320° and have average dip of 75° SW +/- 30° (Fig. 22; Table 1). Fracture set F2 fractures are found in the Fairbanks area, along the Parks Highway, and at the Nenana outcrop (Table 1). F2 fractures are dominantly shear fractures with right-lateral motion visible in outcrop (Fig. 26). Vein fill is calcite and is only found in metamorphic rocks. F2 commonly terminates against F1, internal to compositional layering, and against other F2 fractures (Fig. 23; Fig. 27). Across the three areas, average density for F2 is 7.19 fractures/meter while average spacing is 0.186 meters (Table 1). F2 varies in height from 0.002 to 2 meters and varies in length from 0.004 to 10 meters (Table 1).

In thin section, calcite crystals are dominant with subsidiary quartz (Fig. 28). Calcite crystals tend to be blocky to fibrous in shape, while secondary quartz forms in blocky to elongate blocky crystals (Fig. 28). The horizontal thin sections of F2 veins display right-lateral shear. Orientation of calcite crystals throughout the vein varies, some crystals are sub-perpendicular while others are at low angles to the vein wall (Fig. 28). The crystals interpreted in the horizontal thin section are oriented at 40°-50° angles to the right (91° NE) with respect to the vein wall (316°)

(Fig. 28, Nen11a). These oriented crystals show right-lateral shear. Vertical and parallel to the dip of the vein, the crystals are oriented at 30° angles to the left from the vein wall (Fig. 28, Nen11b). Combined slip vectors indicate that this fracture set opened obliquely with a right-lateral shear sense with a strong normal dip-slip component (Fig. 25b).

Two sets of calcite twins are present in thin section and range in thickness from 1-5 μ and 10-15 μ (Fig. 25). The thicker set of calcite twins shows minor curvature while the other set shows no clear signs of deformation. From the morphology and thickness of the calcite twins, it is interpreted that both type I (<200 °C) and type II (150-300 °C) calcite twins are present in thin sections for F2.

Fracture Set 3 (F3)

Fractures in F3 are categorized into two subsets based on the varying degrees of dip. Both subsets range in strike from 265°-285° and range in dip from 18° S +/- 20° (Subset A) to 65° N +/- 20° (Subset B) (Fig. 22; Table 1). Both subsets are shear fractures with right-lateral motion (Fig. 22). This fracture set is only found in the Fairbanks area in both the metamorphic rocks and basalt (Table 1). F3 commonly terminates against older fracture sets (F1 and F2), internal to compositional layering, and against itself (Fig. 27). In the metamorphic rocks, average density is 4.91 fractures/meter and average fracture spacing is 0.23 meters (Table 1). Fracture set F3 heights range from 0.056 to 0.19 meters, while fracture lengths vary from 0.094 to 9.09 meters (Table 1). In basalt, average density is 2.36 fractures/meters and fracture spacing is 0.71 meters. Heights and lengths vary from 0.09 to 9.1 and 0.06 to 0.19 meters, respectively (Table 1).

In thin section, F3 veins are filled with calcite (Fig. 29). The length of crystals varies, but the majorities of crystals have a blocky shape and extend the entire width of the vein. The orientation of crystals relative to the vein wall suggests a right-lateral shear component to the

opening of the vein. The horizontal thin section of the vein shows a strong right-lateral movement with crystals oriented at 45°-60° (47° NE) with respect to the vein wall (277°) (Fig. 29, LH1a). The vertical thin section parallel to the dip of the vein shows crystals oriented from 50°-70° with respect to the vein wall showing a normal dip-slip component (Fig. 29, LH1b). Combined slip vectors show that the vein opened obliquely with extensional dip-slip motion with a strong right-lateral motion. There is a normal dip-slip component to the opening projection of the vein but it is subsidiary to the strike-slip component (Fig. 25c).

Interpretation of calcite twin morphology shows two distinct sets of twins ranging in thickness from 1-5 μ and 15-20 μ (Fig. 29). The thicker set shows signs of deformation with patchy and curved twins while the other set shows no apparent signs of deformation (Fig. 29). Both type I (<200 °C) and type II (150-300 °C) calcite twins are present in F3 thin sections.

Fracture Set 4 (F4)

Fracture set F4 ranges in strike from 240°-260° and has an average dip of 73° SE +/- 30° (Fig. 22; Table 1). F4 is found in the Fairbanks area, along the Parks Highway, and at the Nenana outcrop in metamorphic rocks (Table 1). Fractures belonging to F4 are interpreted as shear fractures with left-lateral shear sense observed from en echelon fractures (Fig. 30). In addition, horizontal slickenfibres observed in outcrop show a left-lateral component with little to no dip-slip movement (Fig. 31). F4 consists of both quartz- and calcite-filled veins and commonly terminates against older fracture sets (F1-F3), internal to compositional layering, or against other fractures within F4 (Fig. 32). In addition, F4 is generally seen in outcrop crosscutting F5, so the age relationship between the two sets is indeterminate (Fig. 33). Average density for F4 across the three field areas is 10.57 fractures/meter and average fracture spacing is 0.31 meters (Table 1).

Fracture height ranges from 0.014 to 2 meters and fracture length varies from 0.012 to 10 meters (Table 1).

Set F4 fractures contain mostly calcite, or a combination of calcite and secondary quartz (Figs. 34-36). Calcite tends to be fibrous to blocky while secondary quartz is blocky to elongate blocky in shape. However, the morphology of vein fill is highly variable in this fracture set. Extensional veins are dominated by quartz, while shear veins are dominated by calcite. The thin sections from the Birch Hill locality (Fig. 36) contain veins with quartz crystals perpendicular to the vein wall. At other sites on the margin of the basin, the calcite-dominated veins show a strong sense of left-lateral motion. In the horizontal thin section, there are two sets of calcite crystal angles. The first group of crystals are oriented from 65°-75° (311° NW), while the second one ranges from 40°-50° (286° NW) and both show left-lateral movement with respect to the vein wall (241°) (Fig. 34, Nen6a). In addition, in the thin section cut parallel to the dip of the vein, crystals are oriented both at 20° and 40° angles (Fig. 34, Nen6b). Combined slip vectors show that the opening projection of the vein has both a minor and strong normal dip-slip component with a left-lateral shear sense (Fig. 25d).

Interpretation of calcite twins in F4 thin sections shows two distinct sets of twins ranging in thickness from 1-10 μ and 15-20 μ (Fig. 34, 36). The thicker calcite twins show signs of deformation with patchy and curved twins while the other set shows no signs of deformation (Fig. 36). It is interpreted that both type I (<200 °C) and type II (150-300 °C) calcite twins are present in F4 thin sections.

Fracture Set 5 (F5)

Fracture set F5 ranges in strike from 340°-360° and has an average dip of 81° E +/- 30° (Fig 22; Table 1). Fractures belonging to F5 are found in the Fairbanks area, along the Parks

Highway, and at the Nenana outcrop (Table 1). F5 fractures are interpreted as shear fractures with right-lateral shear sense visible in outcrop and in thin section. Measured in both basalt and metamorphic rocks across field areas, vein fill for fracture set F5 is primarily calcite with secondary quartz. F5 commonly terminates against older fracture sets (F1-F4), internal to compositional layering, and against other F5 fractures (Fig. 32). F5 and F4 commonly cross-cut each other, showing no clear indication of relative age (Fig. 33). In metamorphic rocks, average fracture spacing is 7.22 fractures/meter and 0.21 meters. Fracture heights and lengths vary significantly ranging from 0.002 to 4 meters and 0.23 to 5 meters, respectively (Table 1). In basalt in the Fairbanks area, fracture density and spacing are 3.53 fractures/meter and 0.10 meters (Table 1). Fracture height varies from 0.32-0.55 meters, and not enough data was obtained for fracture lengths in basalt (Table 1).

In thin section, F5 fractures are calcite-filled with secondary quartz (Fig. 37). Calcite crystals appear to have grown at a 45°- 60° angle (~125°- 140° SE) with respect to the vein wall (~170°), indicating that there is a right-lateral shear component to the veins. There are two distinct sets of calcite twins present in thin section. The twins tend to range in thickness from 1-5 μ and 10-15 μ. The thicker set of calcite twins is defined by patchy and curvy morphology. It is interpreted that both type I (<200 °C) and type II (150-300 °C) calcite twins are present in thin section (Fig. 34).

Fracture Set 6 (F6)

Fractures belonging to F6 range in strike from 200°-220° and have an average dip of 74° NW +/- 30° (Fig. 22; Table 1). Set F6 fractures are found in the Fairbanks area, along the Parks Highway, and at the Nenana outcrop (Table 1). The fracture set is interpreted as shear fractures with a left-lateral shear sense and they are commonly filled with both quartz and calcite (Fig. 38).

F6 fractures are measurable in both basalt and metamorphic rocks across the field area. Fractures of F6 commonly terminate against older fracture sets (F1-F5), internal to compositional layering, or against other F6 fractures (Fig. 32). In the metamorphic rocks, average density is 6.44 fractures/meter and average fracture spacing is 0.29 meters (Table 1). Visible heights range from 0.002 to 2.76 meters and lengths vary from 0.011 to 10.0 meters (Table 1). In basalt, average density is 10.11 fractures/meter and average spacing is 0.15 meters. Heights and lengths vary from 0.16 to 2.05 and 0.03 to 0.13 meters, respectively (Table 1).

Set F6 fractures have veins containing calcite with minor quartz (Figs. 39-40). Veins show a crack-seal texture with calcite crystals appearing to have grown from previously precipitated calcite. Calcite crystals vary in shape from fibrous to blocky. Both calcite and quartz crystals appear to have grown perpendicular to (~300° NW) and at 45°-60° (~340° NW) with respect to the vein wall (~210°), indicating that there are extensional and left-lateral shear components to the veins.

Interpretation of calcite twin morphology shows a set of twins ranging from 1-5 μ in thickness with little to no deformation visible and a thicker set ranging from 10-15 μ. Both type I (<200 °C) and type II (150-300 °C) calcite twins are present in thin section (Figs. 39-40).

Fracture Set A (Fa)

Fractures in Fa range in strike from 355°-25° and have an average dip of 74° W +/- 20° (Fig. 41; Table 2). The fracture set only occurs in metamorphic rocks around the Healy field area. The vein fill is quartz with no observed shear sense in outcrop. The oldest fracture set in the Healy area, it commonly terminates internal to compositional layering or upon other Fa fractures (Fig. 42). Average fracture density is 11.87 fractures/meter while average spacing is 0.10 meters (Table

2). Fractures belonging to Fa tend to be less extensive than other measured sets with visible heights ranging from 0.004-0.12 meters and lengths ranging from 0.06-0.33 meters (Table 2).

Fa fracture fill consists of quartz (Fig. 43). Crystals tend to be elongate blocky to blocky in shape and appear to have precipitated from the wall inward. In addition, these veins appear to have a crack-seal texture, showing more than one crack seal event in its history. No calcite twins were measurable in thin section for Fa.

Fracture Set B (Fb)

Fractures in set Fb range in strike from 240°-270° with an average dip of 74° S +/- 20° (Fig. 41; Table 2). The fracture set occurs in both metamorphic and sedimentary rocks around the Healy field area (Table 2). Set Fb fractures are both quartz- and calcite-filled shear fractures with right-lateral shear sense (Fig. 44). The set commonly terminates against Fa, internal to compositional layering in metamorphic rocks, within bedding in sedimentary rocks, or on other Fb fractures in outcrop (Fig. 42). In metamorphic rocks, average density and spacing is 11.48 fractures/meter and 0.12 meters (Table 2). Fb fracture heights vary from 0.004-0.49 and lengths range from 0.013-1.83 meters (Table 2). In sedimentary rocks, fracture density and spacing is 2.69 fractures/meter and 0.37 meters (Table 2). Visible heights and lengths range from 0.51-2.5 meters and 0.024-1.0 meters, respectively (Table 2).

In thin section, the fracture cement of this fracture set is quartz with minor calcite (Fig. 45). Quartz crystals range in shape from elongate blocky to blocky while calcite crystals are blocky to fibrous. In addition, visible fluid inclusions throughout the quartz crystals are present. Orientations of both quartz and calcite crystals indicate a right-lateral sense of shear (Fig. 45).

Both type II (150-300 °C) and type III (>200 °C) twins are identified in thin section (Fig. 45). Type II thicknesses range from 5-15 μ and are thick and tabular in shape. Type III twins are thicker and contain a slightly more curved, patchy morphology (Fig. 45).

Fracture Set C (Fc)

Fc fractures range in strike from 325°-350° with an average dip of 78° W +/- 20° (Fig. 41; Table 2). The fracture set is measurable in both metamorphic and sedimentary rocks throughout the Healy field area (Table 2). At the Fox Creek field locality (farthest south locality on figure 17), fracture set Fc is a quartz-filled fracture set with observed left-lateral shear sense in outcrop (Fig. 46). Fc commonly terminates against older fracture sets (Fa and Fb), internal to compositional layering in metamorphic rocks, within bedding in sedimentary rocks, or upon other Fc fractures (Fig. 47). In metamorphic rocks, fracture density and spacing is 8.79 fractures/meter and 0.15 meters (Table 2). Heights and lengths range from 0.002-1.94 meters and 0.012-2.17 meters, respectively (Table 2). In sedimentary rocks average density is 5.42 fractures/meter while average fracture spacing is 0.26 meters (Table 2). Fracture heights and lengths vary from 0.073-2.5 meters and 0.01-0.5 meters (Table 2).

Thin section analysis shows this fracture set is filled with quartz (Fig. 48). Crystals tend to be elongate blocky to blocky in shape and range in size from 100-500 μm, and can extend from vein wall to vein wall. A thin section from the Suntrana Creek field locality shows crystals oriented perpendicular to the vein wall, indicating that there is little to no shear movement. This contrasts with outcrop observations at the Fox Creek and Bison Gulch field localities (both show left-lateral shear), so I hypothesize the pure extension seen in thin section may be due to local stresses or no shear occurred in the Suntrana creek field area. No calcite twins were measurable in thin section for Fc due to lack of calcite crystals present in the vein.

Fracture Set D (Fd)

The youngest set measureable in the Healy area, Fd ranges in strike from 300°-320 with an average dip of 70° SW +/- 20° (Fig. 41; Table 2). In outcrop, fracture set Fd has remnant quartz fill observed on fracture faces. Found in both metamorphic and sedimentary rocks, Fd commonly terminates against all other fracture sets in the Healy area, against itself, and internal to compositional layering in metamorphic rocks, and within bedding for sedimentary rocks with no observed shear sense (Fig. 49). In metamorphic rocks, average fracture density is 13.64 fractures/meter while average spacing is 0.064 meters. Fractures belonging to Fd have visible heights ranging from 0.003-0.23 meters and lengths ranging from 0.032-1.38 meters. In the sedimentary rocks, average density and spacing is 4.65 fractures/meter and 0.24 meters. Ranges in visible heights and lengths vary from 0.011-2.0 meters and 0.019-1.02 meters.

4.2 Fracture Characteristics vs. Distance from the Basin

To see if the fracture characteristics are dependent on distance from the Nenana basin, each field site was measured to see how far it was from the Minto fault and then plotted against the characteristic (i.e. Distance from basin vs. Density) (Figs. 50-51). Only fracture density and spacing were analyzed in this manner because true height and length measurements were limited by the exposures. No graphs for fracture spacing are shown because it is inversely proportional to the fracture density. For some fracture sets, the values for the mean densities increase as they grow nearer to the basin (F3 and F4). For other fracture sets, there is no clear trend in fracture density displayed by the graphs. One reason for the lack of trend associated with the dataset is because Central Alaska is comprised of rigid blocks separated by active NE-striking faults. No clear trend exists because many of my observed fractures were measured close to NE-striking faults and I interpret that this caused an increase in fracture density at certain field localities. Due to the

pervasive faulting and complex geology of Central Alaska, this method is not important to understand the fracture character and distribution along the basin margin.

4.3 Apatite Fission Track Analysis

The AFT samples range in error due to differing grain counts and fission tracks present in samples (Fig. 20). The observations below are based on the higher quality samples.

The apatite fission track data from field locations show distinct differences. In the Fairbanks area, there were 5 samples taken with ages ranging from 25.9 Ma to 84.7 Ma. Three of these ages are greater than 45 Ma. Samples along the Parks Highway and the Nenana area range from 7.8 Ma to 69.7 Ma; of the 9 samples collected in these areas, 6 of them are younger than 40 Ma (Table 3).

Cooling age results from AFT dating reveal that the metamorphic basement rocks of Interior Alaska attained temperatures between 60 °C and 170 °C. The majority of sample ages fall into the age range of 26-40 Ma (σ_1 +/- 3-8 Ma), which suggests that there was a regional episode of exhumation and uplift that is responsible for cooling of the samples during this time period (Frohman, 2014). The older sample ages from the AFT analysis generally are located in Fairbanks (84.7 Ma), while the younger ages fall along the basin margin to the south (7.8 Ma).

The data suggest that, for the majority of samples, the onset of rapid cooling began around 40-60 Ma (Frohman, 2014) (Table 4) (Appendix C). For samples 12 and 17, onset of rapid cooling began around 30 Ma and 15 Ma, respectively (Table 4). Exhumation rates from the samples suggest that periods of faster exhumation are linked to younger onset of rapid cooling. Rates from samples with ages ranging from 40-60 Ma tend to have slower exhumation rates than samples with younger ages (Table 4).

Track lengths for AFT samples range from 13.9 to 15.2 μ with standard deviations ranging from 1-6.8 (Table 3). The track lengths are relatively long, suggesting that they did not spend a

long time in the partial annealing zone. The track lengths for all samples are similar in length and suggest a regional episode of exhumation and uplift that allowed the samples to spend similar amounts of time annealing in the partial annealing zone.

CHAPTER 5: DISCUSSION

5.1 Structural Domains Based on Fracture Characteristics

The area surrounding the Nenana basin can be separated into two structural domains based on the fracture character, apatite fission track analysis, and mapped folds and faults (Fig. 52). Domain I consists of the Fairbanks, Parks Highway and the Nenana areas, while Domain II consists of the Healy area.

Domain I: Fairbanks, Parks Highway, and Nenana Areas

Domain I is characterized by high-angle NE- and NW-striking faults on the margin and interior to the Nenana basin. According to AFT analysis, samples from across Domain I share a regional uplift event that resulted in the majority of sample ages ranging from 26-40 Ma (Fig. 20). From the interpretation of AFT time-temperature curves, slower exhumation rates are present farther away from the basin (Frohman, 2014). On the basin margin, faster exhumation rates and younger sample ages are present.

Six observed fracture sets are measureable in Domain I across the Fairbanks, Parks Highway, and Healy areas. Fracture sets F2, F4, F5, and F6 share common characteristics including field observations, thin section observations, and statistical analyses. With these four regional fracture sets present in Domain I, I interpret that the Fairbanks, Parks Highway and Nenana areas evolved under similar tectonic regimes. Due to the strike, dip, and shear sense of the fracture sets, I interpret that they are related to the evolution of the NE- and NW-striking faults present interior to, and on the margin of, the Nenana basin.

Domain II: Healy, Alaska Area

Domain II has low angle E-W-striking thrust faults and E-W-trending folds of the Northern Foothills (Fig. 52). Fracture transects were taken on the fold limbs and axes of the Northern Foothills fold and thrust belt (Fig. 53). Calcite twins from Domain II have undergone higher deformation temperatures (<200 °C) than Domain I.

Four fracture sets were measured within the Northern Foothills fold-and-thrust belt. Due to the differences in faulting and stress regimes, the four fracture sets measurable in Domain II are significantly different in shear sense and orientation and are unrelated to Domain I fracture sets (Table 2). I propose that the fracture sets measured in Domain II are related to the Late Cenozoic evolution of the Northern Foothills fold-and-thrust belt.

5.2 Petrographic and AFTA Constraints on Thermal Evolution

Apatite fission-track data and thin section analyses help constrain the relative timing and temperature of deformation of the Nenana basin and exposed parts of Domain I.

5.2.1 AFT Results--Regional Tectonic Setting

To better understand the regional exhumation event that resulted in the modeled sample ages in Domain I (26-40 Ma), it is important to look at large-scale structures like the Denali and Tintina fault systems. It is estimated from restoring thrust faults and Eocene magmatic rocks in central and western Yukon Territory, that there has been 400-430 km of right-lateral displacement along the Tintina fault in the middle to late Eocene (48-41 Ma) (Gabrielse et al., 2006). It is estimated that the Denali fault has had ~400 km of right-lateral displacement since 51 Ma (Benowitz et al., 2012). By restoring offset syn-magmatic plutons and metamorphic rocks that are cut by the Denali fault, Benowitz et al. (2012) estimated that there has been ~100 km of

displacement between ~51-25 Ma and ~300 km of displacement since ~25 Ma. The modeled sample ages of 26-40 Ma in Domain I overlap with the period when these two right-lateral faults were most active, suggesting that these ages are related to motion on these two regional faults.

CHAPTER 6: MODELS FOR FRACTURE FORMATION

In order to understand the evolution of fractures on the margin and interior to the Nenana basin, it is important to tie them to other known regional and local events. Conversely, fracture character, distribution and conditions of formation provide important information on the local and regional deformation conditions during their formation. In this chapter, I will discuss the preferred model for the formation of fractures in Domain I and Domain II taking into consideration the distribution of fracture sets, regional and local structures and the current understanding of the timing of evolution of the Nenana basin. I will then combine this conceptual model with the thermal history model into an integrated model of deformation, burial history and uplift for the area.

6.1 Domain I

Domain I is characterized by high angle NE- and NW-oriented fault patterns. Domain I evolution coincides with the evolution of the Nenana basin. The Late Paleocene is characterized by the onset of normal faulting along both NE- and NW-oriented fault patterns. The Late Miocene-Pliocene is characterized as the onset of oblique faulting (normal and strike-slip components) along both fault patterns. The final period of basin evolution is characterized by continued oblique faulting along both fault patterns. All six observed fracture patterns will be discussed with respect to their timing. Fracture sets F2, F4, F5, and F6 are interpreted to be regional sets while F1 and F3 are interpreted as local sets and are only observed in the Fairbanks area.

6.1.1 Overall conceptual model

The fracture sets in Domain I can be incorporated into a conceptual model of the structural and stratigraphic evolution of the Nenana basin (Dixit and Hanks, 2014) and the nearby Fairbanks area (Frohman, 2014). Several other conceptual models were evaluated (e.g., formation as riedel shears related to various observed faults) and are discussed in more detail in Appendix D. However, these alternate interpretations had too many deficiencies. For the sake of clarity, only the preferred conceptual model for fracture formation is discussed in this section (Fig. 54).

In the proposed model, the regional sets (F2, F4, F5, and F6) are placed in the context of the three main phases of Nenana basin evolution as proposed by Dixit and Hanks (2014)--early growth of the basin during Late Paleocene time, the activation of oblique faulting from the Late Miocene to Pliocene, and then continued oblique slip from Pliocene to present day. I then discuss possible causes for fracture sets only observed in the Fairbanks area (F1 and F3).

Late Paleocene (pre-Healy unconformity)

Late Paleocene evolution is characterized by the onset of normal faulting (Fig. 55; Dixit and Hanks, 2014). Both NE-SW and NW-SE-oriented normal faults within and on the margin of the Nenana basin are active during this phase. In this model, any fractures associated with this time period have been overprinted by fracture sets that form in later time periods in basin evolution.

Late Miocene-Pliocene

Phase II is characterized by oblique dip-slip faulting both within and on the margins of the Nenana basin. The dominant active faults in phase II are NE-striking normal faults with a left-lateral strike-slip component and NW-striking normal faults with right-lateral slip (Fig. 56). I

interpret that fracture sets F1, F2, F3, F4, F5, and F6 all formed during this period of oblique faulting and strike-slip motion throughout the basin.

F2 formed parallel to NW-striking faults

I interpret the regional fracture set F2 formed as shear fractures synchronously with the NW-striking fault pattern when it was activated with oblique dip-slip in the Late Miocene (Fig. 56). Fracture set F2 and the NW-striking faults have a similar average orientation (320°/74 SW vs. 325°/70 SW) and share a common right-lateral shear sense (Fig. 57).

F4 and F5 formed as conjugate shear fractures related to a NE-oriented maximum stress

In this interpretation, F4 and F5 formed simultaneously in response to compressive stress in the NE-SW direction (Fig. 58). The NE-oriented maximum stress would bisect the acute angle of the conjugate shear fractures.

To further support that F4 and F5 formed from a NE-oriented stress, other features in the basin can form under similar stress vectors. The NE-oriented principal stress can also result in WNW-trending thrust structures and faults (Fig. 56). It is interpreted by Dixit and Hanks (2014) that these structures formed from the left-stepping character of the Minto fault, specifically as structures belonging to a restraining bend on a left-stepping strike-slip fault. From this additional evidence, I propose that F4 and F5 formed simultaneously from the NE-oriented maximum stress, and the presence of WNW-striking reverse faults interior to the basin provides supporting evidence for this formation model.

F6 formed parallel to the NE-striking faults

I interpret that F6 fractures are related to normal, left-lateral strike-slip oblique motion on NE-striking faults during Late Miocene time (Fig. 56). Fracture set F6 and the NE-striking faults have the same average orientation (30° NE) and share a left-lateral shear sense (Fig. 59).

Local Fracture Sets F1 and F3

Both fracture sets F1 and F3 are only found in the Fairbanks area. Fracture set F1 is very similar to the regional F2 fracture set. Both have a right-lateral shear sense and differ in orientation by 10°-15° (Fig. 60). I interpret F1 to have formed under similar stress conditions as F2 formation. Fracture set F1 is related to the Cretaceous-aged NW-oriented thrust faults in the Fairbanks area. The difference in orientation of the two sets is due to local variations in stresses in the Fairbanks area.

Fracture set F3 is only observed in a few locations in the Fairbanks area (Figure 60). This fracture set shows evidence of right-lateral shear and parallels an E-W striking set of faults that occur in fault blocks bounded by prominent NE-striking faults. I interpret that these NE-striking faults experienced a significant amount of left-lateral strike-slip during the Late Miocene, which resulted in the formation of new and/or reactivated pre-existing EW-striking faults linking thrust faults with a right-lateral strike-slip component (Fig. 60). The F3 fracture set formed parallel to these Cretaceous-aged EW-striking linking faults (Fig. 60).

Pliocene- Present Day

Left-lateral and normal oblique slip along the NE-striking faults continued from Pliocene time to the present day (Fig. 61). By this time, the amount of normal fault motion along existing faults has decreased and has become subsidiary to the strike-slip motion (Dixit and Hanks, 2014). NE-striking left-lateral oblique faults paralleling the Minto fault continue to form and account for the continued NW-SE growth of the basin.

Fracture set F6 is oriented NE-SW, has a left-lateral shear sense, and is the youngest fracture set (Fig. 59). I propose that F6 fractures continued to form during the Pliocene and are

related to the generation of new NE-SW-striking oblique (normal and left-lateral strike-slip components) faults (Fig. 59).

Deficiencies

Fracture Sets F4 and F5

The above scenario does not take into account the lack of tangible evidence for E-W trending thrust structures within the basin. Dixit and Hanks (2014) identified thrust structures interior to the basin, but their density and exact orientation are not fully understood. This is due to lack of seismic data throughout the entire basin and a lack of publicly available data.

Even though the orientation of the thrust structures is not fully understood, it is interpreted that they formed from a NE-oriented stress. The NE-oriented stress can create thrust structures that correlate to the orientation of thrust structures from a restraining bend in a multi-strand strike-slip fault system such as the Minto fault.

6.1.2 Implication of AFT results and calcite paleothermometry for burial history of the Fairbanks-Nenana basin area

There are two specific trends of cooling/exhumation rates in Domain I. On the margin of the basin, the Late Paleocene evolution occurred during a burial period, while the Late Miocene to Pliocene period occurred during a transitional phase from burial to exhumation. The Pliocene to present day is characterized by rapid exhumation (Fig. 62a). Farther away from the basin margin, the three time periods of basin evolution occurred during periods of exhumation (Fig. 62b). Tying this in with calcite thermometry, fracture formation on the margin of the basin occurred in either one or two very similar tectonic events. This can be related to the transition of a pure extensional phase of basin evolution or a period of oblique faulting (both normal dip-slip and strike-slip components).

AFT time-temperature curves (Appendix C) and the morphology of calcite twins constrain the timing of fracture formation and deformation temperatures. The calcite twins observed in thin section from the Fairbanks, Parks Highway, and Nenana areas are interpreted to be type I and type II. Using a geothermal gradient of 32°C/ km provided by Dusel-Bacon and Murphy (2001) for central Alaska, type I twins develop at a depth of ~5.3 km and type II develop at a range from 4.68 km- 9.38 km below the surface. After integrating the calcite thermal indicators, AFT time-temperature curves, and the Dixit and Hanks (2014) model, additional timing constraints that support the formation of the fracture sets from the Late Miocene to present day are apparent.

According to Dixit and Hanks (2014), the basin began to form in the Late Paleocene and has since evolved in three phases. Stages (separated by age) in basin evolution, AFT time-temperature curves, fracture set formation, and calcite twin thermometry are integrated and described below. In order to integrate the data sets, a sample on the margin of the basin and a sample in the Fairbanks area were selected that demonstrate the two trends in exhumation and cooling found in the field area (Fig. 62). The first trend based on the time-temperature curve is linked to younger sample ages and is from a sample located on the Nenana basin margin. The second trend from an AFT time-temperature curve is located in the Fairbanks area and is representative of older sample ages and slower exhumation and cooling rates.

Late Paleocene (pre-Healy unconformity)

The Late Paleocene is characterized by rapid tectonic subsidence interior to the basin. It is interpreted that no observed fracture sets were formed during the Late Paleocene due to the lack of strike-slip motion on faults. From interpreting the time-temperature curves, samples during this time period underwent different thermal histories depending on their proximity to the basin (Fig.

62). On the basin margin during the Late Paleocene, burial is occurring (Fig. 62a) while at greater distances from the basin margin, rocks are being exhumed at a steady rate (Fig. 62b).

Late Miocene-Pliocene

The observed tectonic subsidence is slower compared to the Late Paleocene. The Late Miocene-Pliocene represents the activation of oblique faulting along the NW- and NE-striking faults. All observed fracture sets in Domain I are interpreted to have formed during this time. Not only do all the observed fracture sets have a component of shear, but calcite in thin section for Domain I fracture sets is dominated by type I and type II twins. Shear along faults and temperatures that allow the formation of type I and type II twins are present in this time period in basin evolution. This further supports the hypothesis that the observed shear fracture sets formed during the Late Miocene- Pliocene time period in basin evolution.

Pliocene- Present Day

Rapid tectonic subsidence and continued generation of NE-striking faults characterize the final phase in basin evolution. It is interpreted that F6 is the only fracture set that continues to form in this time period of basin evolution. Some F6 thin sections contain both type I and II twin types, while other F6 thin sections only contain type I twins. Type I twins are only present from the Pliocene to present day because the temperatures necessary for type II twins are not present during the final phase of basin evolution (Fig. 62). This further supports the hypothesis that F6 is the only fracture set that continued to form in the final phase of basin evolution.

6.2 Domain II

The four fracture sets observed in Domain II are oriented both parallel and perpendicular to the thrust system (Table 2). The fracture transects are on fold limbs and axes throughout Domain II (Fig. 53). Based on their relative timing, orientation and sense of shear, these fracture sets can be incorporated into a model for the evolution of Domain II.

6.2.1 Fractures Related to the Evolution of the Northern Foothills Fold-and-Thrust Belt

Stage 1: Late Cenozoic

Fracture set Fa

The earliest fracture set, Fa, is a regional set of NS-striking extension fractures only found in basement rocks in the Healy area. Fa fractures are oriented perpendicular to the strike of major faults and folds in the fold-and-thrust belt.

These fractures are interpreted as forming in response to regional stresses early in the evolution of the fold and thrust belt (Fig. 63). Fa fractures are interpreted to have formed prior to folding and before the Usibelli Group was lithified, (Fig. 63). The fracture set was formed in response to a maximum principal stress oriented N-S.

Stage 2:

This stage represents the onset of folding and thrusting in the Northern Foothills fold-and-thrust belt. Regional stress orientations stay the same, but the differential stresses increase as folding commences.

Fracture set Fb

The orientation of Fb fractures parallels the dominant fault and fold orientation in the domain. In addition fracture cement in Fb veins displays some evidence of right-lateral shear in thin section.

I interpret that Fb fractures formed on the fold hinges as folding commenced in the domain (Fig. 64). The right-lateral shear suggests that not only is the fracture set forming parallel to the fold hinges, but also it is displaying the same motion as much larger structures such as the Denali fault (Fig. 64). This can be interpreted to indicate that the slip along the Denali fault is contributing to the deformation in Domain II.

Fracture Sets Fc and Fd

Fracture sets Fc and Fd are the youngest fracture sets observed and are oriented sub-perpendicular to the dominant fault trends (Fig. 64). Fc ranges from 330°-350° while Fd is oriented from 300°-320° degrees. Fc has a left-lateral shear sense observed in outcrop while Fd has no observed shear.

These late fractures are interpreted as conjugate shear fractures related to the development of the folds. Both fracture sets Fc and Fd are interpreted to be one fracture in a conjugate shear set, where the second NNE-oriented conjugate shear is nonexistent or has not formed. NE and NW-oriented conjugate shears are common structures that form on the hinges of folds (Fig. 15, #2). I propose that either the second conjugate shear did not form or the outcrops were in too poor condition to measure the missing set. I propose that the lack of observed shear in fracture set Fd is due to the condition of the outcrops. The changes in strike (~20°) of these two fracture sets could be due to the same reasons why there are variations in strike along the fault traces throughout the field area. The changes in orientation between the two sets is a result of variation in shortening

along the length of the fault; a component of strike-slip motion along the faults; local changes in lithologies; or influence by pre-existing basement structures (Bemis and Wallace, 2007).

6.3 Implications on the Evolution of Domain I and II and Their Relation to the Nenana Basin

The evolution of Domain I and II are unrelated. Domain I fractures are related to a different set of structures that do not match the orientation or the shear sense on observed structures in Domain II. Domain II fracture sets show no relation to the NE-oriented and NW-oriented fault patterns in Domain I. From my interpretation, the four observed fracture sets in Domain II are unrelated to the formation of the Nenana Basin. There are no observed structures interior to the basin that can cause the formation or shear sense present along fracture sets Fa, Fb, Fc or Fd.

CHAPTER 7: CONCLUSIONS

The Nenana basin is a Cenozoic-aged basin governed by the active tectonics in central Alaska since Late Paleocene time. The area surrounding the basin can be separated into two structural domains with different fracture and fault characteristics and uplift/subsidence histories.

Domain I consists of the exposed areas immediately adjacent to the basin, and continues east along the Parks Highway to the Fairbanks area. Since Late Paleocene time, Domain I evolution is related to the activation of NE and NW-striking faults located interior to and on the margin of the Nenana basin. Domain II is located north of the Alaska Range near Healy, Alaska, and its evolution is tied to the Late Cenozoic development of the Northern Foothills fold-and-thrust belt.

The fracture sets observed in the area near the Nenana basin can be tied to the evolution of larger structural elements on the margin of the basin, and interpretations can be projected into the Nenana basin. The fractures tell a story of a complex structural evolution of the faults in the basin, but provide insight on the large-scale deformational history of Interior Alaska.

Fairbanks, the Parks Highway, and Nenana areas are characterized by NE-striking oblique faults with a left-lateral component and E-W proto-thrust faults that are interpreted to be have been reactivated due to the continued deformation in central Alaska. Six fracture sets with varying shear indicators are present in Domain I. I interpret that regional fracture sets F2, F4, F5, and F6 are tied to the evolution of faulting documented by Dixit and Hanks (2014) as the basin continues to extend in the NW-SE direction since Late Paleocene time. The regional fracture sets are related to the activation of NE-striking and NW-striking faults that originated as normal faults and evolved into oblique faults by Late Miocene time. On a local scale in the Fairbanks field area, fracture sets F1 and F3 formed from the evolution of local Cretaceous-aged thrust faults. By integrating AFT time-temperature curves, calcite twin thermometry, and the time constraints from Dixit and Hanks

(2014), the timing of the observed fracture sets in Domain I is placed from the Late Miocene to Present day.

Domain II consists of the Healy area in the Northern Foothills fold-and-thrust belt, located north of the Alaska Range and the Denali fault system. Four separate fracture sets unrelated to the stresses experienced by Domain I are present in Domain II. Fracture set Fa formed prior to the development of the fold and thrust belt and reflects a N-S-oriented maximum horizontal *in situ* stress. Later fractures sets are interpreted as forming during Miocene and younger folding and thrust faulting.

7.1 Implications for Hydrocarbon Exploration.

Some lithologies in the Nenana basin are potential reservoirs for oil and gas. It is important to understand the timing and orientation of structural features that can affect the risk associated with developing a highly faulted basin. Some common risks from faults can include lack of seals that can lead to oil and gas migrating and not being trapped (Selley, 1997). Other production risks along active faults include loss of well integrity, resulting in blowouts in the subsurface (Selley, 1997).

The Nenana basin is a narrow basin dominated by both NE and NW-oriented faults. Regional fracture sets related to active faulting and formation of the basin could impact migration pathways or the ability of either faults or adjacent shales to act as seals for hydrocarbons and other fluids. The majority of fractures measured in the field were filled with either quartz or calcite and if this is true in the subsurface, the fractures would be acting more as seals rather than promoting fluid flow. If the fracture sets are not filled in the subsurface, areas near faults would have increased permeability and secondary porosity due to increase in fracture density. In addition, from my

observed shear vectors on the fracture sets (normal dip slip and strike-slip components), I would expect to see structural traps caused by the oblique faults juxtaposing the reservoirs and seal rocks.

Overall, the Nenana basin has a high potential for untapped energy resources. More data acquisition to further understand rock properties and the role faults and fractures play in either sealing hydrocarbon accumulations or providing migration pathways must be done to further understand the basin's potential for containing economic amounts of hydrocarbons.

CHAPTER 8: FUTURE WORK

Future studies that would help support the conclusions of my thesis would be more field analysis, thin section analysis, measuring fractures in core, and fluid inclusion analysis. These data would provide additional information on the depth and temperature of fracture formation and cementation and provide insight on what fluids and gases were present during the evolution of the area. Additionally, since the Nenana basin is being actively explored for hydrocarbons I propose performing additional petroleum system analyses to further understand how the observed fracture sets impact the reservoir characteristics interior to the basin.

Fieldwork and Thin Section Analysis

Additional data and samples acquired in the field would allow for additional shear indicators on fracture sets that couldn't be observed initially. Acquiring thin sections for Fd fracture set in the Healy area and thin sections cut parallel to both the strike and dip of all fracture sets would help further constrain the opening history of the veins.

Fluid Inclusion Analysis

Fluid inclusion data will help constrain fluid flow history throughout the fractures. Fluid inclusions are bubbles of liquid that were trapped upon the formation of mineral or fracture cement. If the fluid inclusions remain intact after they are formed, they can provide information on temperatures, pressures, and the chemical environment during the crystal or vein growth (Bakker and Jansen, 1991; Bons et al. 2012). Specifically, heating and freezing measurements of fluid inclusions trapped in the cements can provide data about the temperature, pressure, and fluid composition conditions of the cement formation (Hanks et al. 2006). By understanding the temperature at which the liquid crystallized or the inclusion homogenizes it is possible to

determine the identity of the fluid such as the salinity, amount of CO_2, and H_2O (Bons et al. 2012). This information can help determine if the Nenana basin is a prime target for oil and gas exploration.

Analyzing Fractures in Core

Analyzing fractures in core taken from the Nenana basin would help determine if there are any changes in the orientations of fracture sets due to the difference in local stresses across the basin. In addition, the character of fracture fill at depth can aid in understanding the extent of vein fill and provide implications on permeability and secondary porosity of the Nenana basin.

Petroleum System Analysis

Since the Nenana basin is being actively explored for its oil and gas potential, it would be interesting to understand the effect of the observed fracture sets on reservoir properties such as porosity and permeability.

On a much larger scale, it would be ideal to identify the active petroleum systems throughout the basin. There are potential source rocks and reservoir rocks in the Miocene Usibelli Group, but further characterization of their trap styles and their potential risk is necessary in order to understand the basin's potential and provide further information on key targets to pursue in the near future.

CHAPTER 9: REFERENCES

Bakker, R.J., Jansen, J.B.H., 1991. Experimental post-entrapment water-loss from synthetic CO2-H2O inclusions in natural quartz. Geochimica et Cosmochimica Acta 55, 2215-2230.

Bemis, S.P., 2010, Moletrack scarps to mountains: Quaternary tectonics of the central Alaska Range [Ph.D. thesis]: University of Alaska Fairbanks, 137 p.

Bemis, S.P., and Wallace, W.K., 2007, this volume, Neotectonic framework of the north-central Alaska Range foothills, *in* Ridgway, K.D., Troop, J.M., Glen, J.M.G., and O'Neill, J.M., eds., Tectonic Growth of a Collisional Continental Margin: Crustal Evolution of Southern Alaska: Geological Society of America Special Paper 431, p. 549-572.

Bemis, S.P., Carver, G.A., and Koehler, R.D., 2012, The Quaternary thrust system of the Northern Alaska Range: Geosphere, v. 8, no. 1, p. 196–205, doi:10.1130/GES00695.1.

Benowitz, J., Vansant, G., Roeske, S., Layer, P.W., Hults, C., and O'Sullivan, P.B., 2012, Eocene to present slip rate history of the eastern Denali Fault System: American Geophysical Union, Abstracts, T11A-2547, 1 p

Bons, P.D., Elburg, M.A., and Gomez-Rivas, E., 2012, A review of the formation of tectonic veins and their microstructures: Journal of Structural Geology, v. 43, p. 33-62.

Burkhard, M., 1993. Calcite twins, their geometry, appearance and significance as stress–strain. markers and indicators of tectonic regime: a review. Journal of Structural Geology 15, 351–368.

Davis, G.H., and Reynolds, S.J., 1996, Structural geology of rocks and regions: New York, John Wiley & Sons, Inc., 776 p.

Dickin, A.P., 1995, Radiogenic Isotope Geology: Cambridge, United Kingdom, Cambridge University Press, 490 p.

Dixit, N.C. and Hanks, C.L., 2014. Tectono-Thermal History of the Southern Nenana Basin, Interior Alaska: Implications for Conventional and Unconventional Hydrocarbon Exploration: Poster.

Donelick, R.A., O'Sullivan, P.B., Ketcham, R.A., 2005, Apatite fission-track analysis: Reviews in Mineralogy & Geochemistry V. 58, p 49-94.

Doyon, Limited, 2009, Interior Alaska natural gas exploration. Alaska Miners Association, Fairbanks Chapter. http://www.arcticminers.org/presentations/Jim_Mery.pdf.

Doyon, Limited, 2012, Interior oil & gas exploration, nenana and yukon flats basins. http://alaskaalliance.com/files/alliance_presentations/8_Jim%20Mery.pdf

Doyon, Limited, 2014, Nenana basin seismic survey Autumn 2014. http://www.doyonoil.com/Content/pdfs/NenanaBasin3DSeismic.pdf

Duncan, A.S., 2007, Evolution of fractures and Tertiary fold-and-thrust deformation in the Central Brooks Range foothills, Alaska [M.S. thesis]: Fairbanks, University of Alaska Fairbanks, 122 p.

Duncan, A.S., Hanks, C.L., Wallace, W.K., O'Sullivan, P.B., and Parris, T.M., 2007, Fracture distribution, thermal history and structural evolution of the central Brooks Range Foothills, Alaska [abs.]: Geological Society of America Abstracts with Programs, v. 38, no. 5, p. 89.

Dusel-Bacon, C., and Murphy, J.M., 2001, Apatite fission-track evidence of widespread Eocene heating and exhumation in the Yukon– Tanana Upland, interior Alaska: Canada Journal of Geoscience, V. 38, p. 1191- 1204

Engelder, T., 1987. Joints and shear fractures in rock. In: Atkinson, B.K. (Ed.), Fracture Mechanics of Rock. Academic Press, London, pp. 27e69.

Frohman R.A., 2014, Identification and evolution of tectonic faults in the greater Fairbanks area, Alaska: [M.S. thesis] Fairbanks, University of Alaska Fairbanks, 248 p.

Gabrielse, H., 1985, Major dextral transcurrent displacements along the northern Rocky Mountain Trench and related lineaments in north-central British Columbia: Geological Society of America Bulletin, v. 96, no. 1, p. 1–14.

Gabrielse, H., Murphy, D.C., and Mortensen, J.K., 2006, Cretaceous and Cenozoic dextral orogen-parallel displacements, magmatism, and paleogeography, north-central Canadian Cordillera, in Haggart, J.W., Enkin, R.J., and Monger, J.W.H., eds., Paleogeography of the North American Cordillera; Evidence for and against large-scale displacements: Geological Association of Canada Special Paper 46, p. 255–276.

Gleadow, A.J.W, Duddy, I.R., Green, P.R., and Hegarty, K.A., 1986, Fission track lengths in the apatite annealing zone and interpretation of mixed ages: Earth and Planetary Science Letters, v. 78, p. 245-254.

Goldfarb, R., Hart, C., Miller, M., Miller, L., Farmer, G.L., Groves, D., 2000, The Tintina gold belt – a global perspective, in The Tintina Gold Belt: Concepts, Exploration, and Discoveries, British Columbia and Yukon Chamber of Mines, Cordilleran Roundup Special Volume 2, p. 5-31.

Haeussler, P. J., 2008, An overview of the neotectonics of Interior Alaska: Far-field deformation from the Yakutat Microplate collision: Geophysical monograph 179, p. 83-108.

Hanks, C.L., Parris, T.M., Wallace, W.K., 2006, Fracture paragenesis and microthermometry in Lisburne Group detachment folds: implications for the thermal and structural evolution of the northeastern Brooks Range, Alaska: AAPG Bulletin 90 (1), p 1-20.

Hansen, V.L., and Dusel-Bacon, C., 1998, Structural and kinematic evolution of the Yukon-Tanana upland tectonites, east-central Alaska: A record of late Paleozoic to Mesozoic crustal assembly: Geological Society of America Bulletin, v. 110, no. 2, p. 211-230.

Hayes, M.R., 2004, The influence of mechanical stratigraphy on the development of detachment folds and associated mesoscopic structures:an example from the Lisburne Group carbonates, Northeastern Brooks Range, Alaska [M.S. thesis]: Fairbanks, University of Alaska Fairbanks, 134 p.

Hayes, M.R., and Hanks, C.L., 2008, Evolving mechanical stratigraphy during detachment folding: Journal of Structural Geology, v. 30, p. 548-564.

Jäger, P., Schmalholz, S.M., Schmid, D.W., and Kuhl, E., 2008, Brittle fracture during folding of rocks: a finite element study: Philosophical Magazine, v. 88, nos. 28-29, p. 3245-3263.

Ketcham, R., 2005, Forward and inverse modeling of low temperature thermochronology data, *in* Reiners, P.W., and Ehlers, T.A., eds., Thermochronology: Reviews in Mineralogy and Geochemistry, v. 58, p. 275-314.

Kirschner, C.E., 1994, Interior basins of Alaska, in Plafker, G., and Berg, H.C., eds., The geology of Alaska: The Geology of North America, Geological Society of America, Boulder, Colorado, v. G1, p. 469-493.

Koehler, R.D., 2013, Quaternary Faults and Folds (QFF): Alaska Division of Geological & Geophysical Surveys Digital Data Series 3. http://maps.dggs.alaska.gov/qff/. doi:10.14509/24956.

Lacazette, A., 2000, Technical Presentations. http://www.naturalfractures.com/technical.htm.

Loveland, A.M., 2010, Fracture evolution in a fold-and-thrust belt and the adjacent foreland basin: An example from the northeastern Brooks Range, Alaska: University of Alaska Fairbanks, M.S. thesis, 168 p.

Narr, W., and Suppe, J., 1991, Joint spacing in sedimentary rocks: Journal of Structural Geology, v. 13, p. 1037-1048.

Newberry, R.J., Bundtzen, T.K., Clautice, K.H., Combellick, R.A., Douglas, T., Laird, G.M., Liss, S.A., Pinney, D.S., Reifenstuhl, R.R., and Solie, D.N., 1996, Preliminary geologic map of the Fairbanks mining district, Alaska: Alaska Division of Geological & Geophysical Surveys Public Data File 96-16, 17 p., 2 sheets, scale 1:63,360.

Nokleberg, W.J., Jones, D.L., and Silberling, N.J., 1985, Origin and tectonic evolution of the Maclaren and Wrangellia terranes, eastern Alaska Range, Alaska: Geological Society of America, Bulletin, v. 96, no. 10, p. 1251-1270.

Nokleberg, W.J., Plafker, G., and Wilson, F.H., 1994, Geology of south-central Alaska, in Plafker, G., and Berg, H.C., eds., The Geology of Alaska: Geological Society of America, p. 311-364.

Page, R.A., Plafker, G., and Pulpan, H., 1995, Block rotation in east-central Alaska: A framework for evaluating earthquake potential?: Geology, v. 23, no. 7, p. 629–632.

Passchier, C.W., Trouw, R.A.J., 2005. Microtectonics, second ed. Springer Verlag, Berlin

Pavlis, T.L., and Sisson, V.B., 1993, Mid-cretaceous extensional tectonics of the Yukon-tanana terrane, trans-Alaska crustal transect (TACT), east-central Alaska: Tectonics, v. 12, p. 103-122.

Plafker, G., and Berg, H.C., 1994, Review of the geology and tectonic evolution of Alaska, *in* Plafker, George, and Berg, H.C., eds., The Geology of Alaska: Boulder, Colorado, Geological Society of America, The Geology of North America, v. G-1, p. 989–1,021.

Pollard, D.D., Segall, P., 1987. Theoretical displacements and stresses near fractures in rocks: with applications to faults, joints, dikes and solution surfaces. In: Atkinson, B.K. (Ed.), Fracture Mechanics of Rock. Academic Press, London, p. 277-348.

Ramsey, J.M., and Chester, F.M., 2004, Hybrid fracture and the transition from extension fracture to shear fracture: Nature, v. 428, p. 63-65.

Ramsay, J.G., 1980. The crack-seal mechanism of rock deformation. Nature 284, 135e139.

Ramsay, J.G., and Huber, M.I., 1987, The techniques of modern structural geology, volume 2: Fold and fractures, p. 309-700. London, Academic Press.

Ratchkovski, N. A., and Hansen, R., 2002, New Constraints on Tectonics of Interior Alaska: Earthquake Locations, Sources Mechanisms, and Stress Regime, Bulletin of the Seismological Society of America 92 (3): p. 998-1014.

Ridgway, K.D., Thoms, E.E., Layer, P.W., Lesh, M.E., White, J.M., and Smith, S.V., 2007, Neogene transpressional foreland basin development on the north side of the central Alaska Range, Usibelli Group and Nenana Gravel, Tanana basin, *in* Ridgway , K.D., Trop, J.M., Glen, J.M.G., and O'Neill, J.M., eds., Tectonic Growth of a Collisional Continental Margin: Crustal Evolution of Southern Alaska: Geological Society of America Special Paper 431, p. 507–547.

Riehle, J.R., Fleming, M.D., Moliniam B.F., Dover, J.H., Keley, J.S., Miller, M.L., Nokleberg, W.J., Plafker, G., and Till, A. B. 1997. Digital-shaded relief image of Alaska: U.S.

Geological Survey Miscellaneous Investigations Map I- 2585, Scale: 1:250,000.

Ruppert, N.A., 2008, Stress map for Alaska from earthquake focal mechanisms, *in* Freymueller, J.T., Haeussler, P.J., Wesson, R., and Ekström, G., eds., Active Tectonics and Seismic Potential of Alaska: Washington, D.C., American Geophysical Union Geophysical. Monograph Series 179, p. 351–367.

Ruppert, N.A., Ridgway, K.D., Freymueller, J.T., Cross, R.S., and Hansen, R.A., 2008, Active tectonics of Interior Alaska—Seismicity, GPS geodesy, and local geomorphology, *in* Freymueller, J.T., Haeussler, P.J., Wesson, R.L., and Ekström, G., eds., Active Tectonics and Seismic Potential of Alaska: Washington, D.C., American Geophysical Union, Geophysical Monograph 179, p. 109–133.

Scholz, C.H., 2002. The Mechanics of Earthquakes and Faulting, second ed. Cambridge University Press, Cambridge.

Selley, R., 1997, Elements of petroleum geology: San Diego, Academic Press, 470 p.

Shackleton, J.R., 2003, The relationship between fracturing, asymmetric folding, and normal faulting in Lisburne Group carbonates: Porcupine Lake valley, northeastern Brooks Range, Alaska [M.S. thesis]: Fairbanks, University of Alaska Fairbanks, 189 p.

Singhal, B.B.S., Gupta, R.S., 2010, Fractures and Discontinuities, Applied Hydrogeology of Fractured Rocks: New York, Springer Science + Business Media, 408 p.

Stearns, D.W., 1968, Certain aspects of fractures in naturally deformed rocks, *in* Reiker, R.E., National Science Foundation Advanced Science Seminar in Rock Mechanics: Special Report, Air Force Cambridge Research Laboratories, Bedford, MA, v. AD66993751, p. 97-118.

Twiss, R.J., and Moores, E.M., 1992, Structural Geology, San Francisco, W. H. Freeman & Co., 532 p.

Van Kooten, G.K., Richter, M., Zippi, P.A., 2012, Alaska's Interior rift basins: A new frontier for discovery, Oil and Gas journal, 10 p. http://www.doyon.com/lands/oil_gas/DoyonNenanaOGJ.pdf.

Wahrhaftig, C., 1958, Quaternary geology of the Nenana River valley and adjacent parts of the Alaska Range: U.S. Geological Survey Professional Paper 293-A, p. 1–68.

Wentz, R., 2014, Fracture characteristics and distribution in exposed Cretaceous rocks near the umiat anticline, north slope of Alaska [M.S. thesis]: Fairbanks, University of Alaska Fairbanks, 163 p.

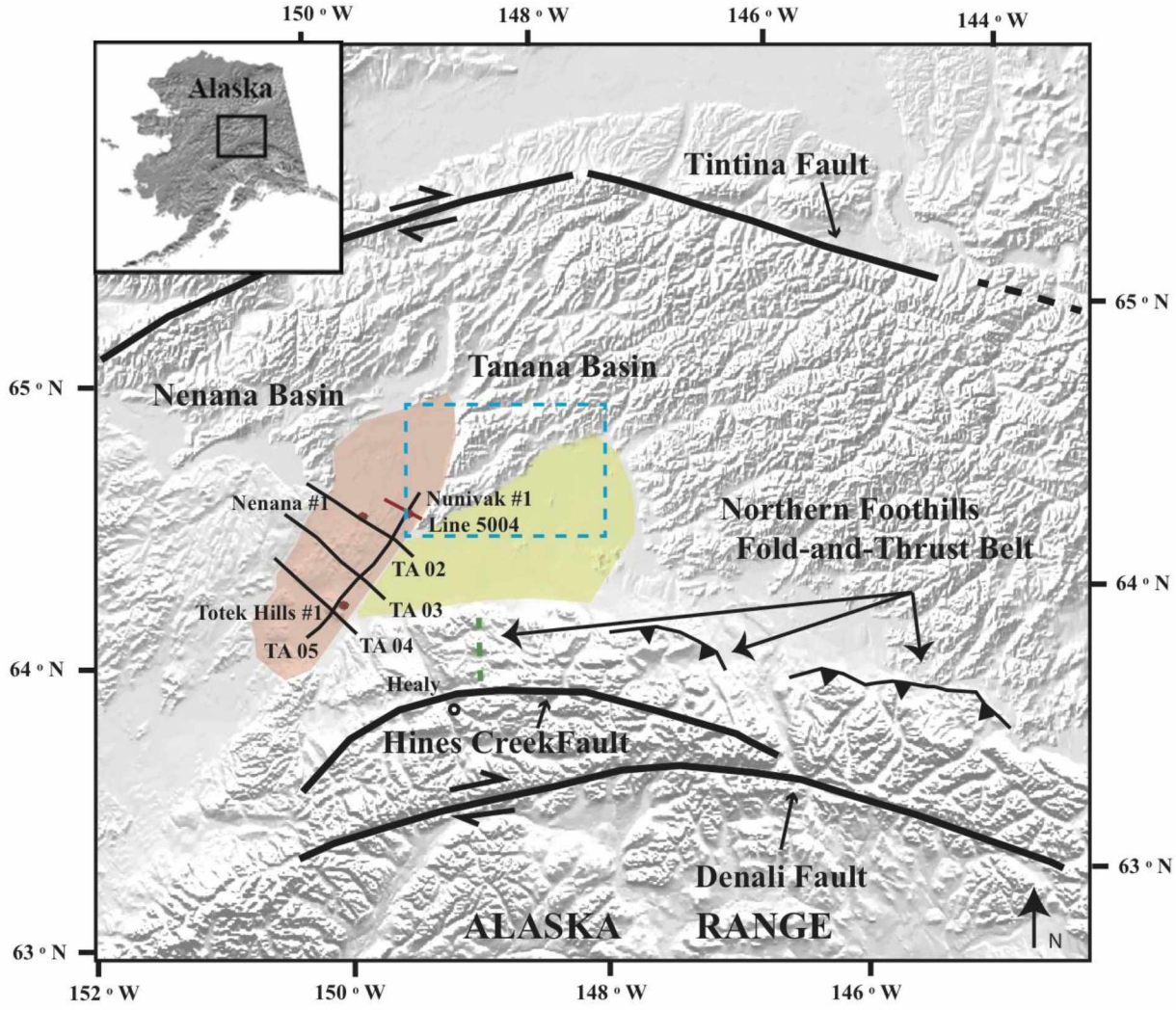

Figure 1: Major geologic elements of central Alaska. The Nenana basin (red) is located between the Tintina and Denali fault systems in central Alaska. The extent of AFT sample collection discussed in this thesis is outlined in the blue box. Other prominent geologic features include the northern hills fold-and-thrust belt; and the Tanana basin (yellow). Interior to the Nenana basin, the Nenana #1, Totek Hills #1 and Nunivak #1 are three drilled wells. In addition to the drilled wells, seismic lines used in this thesis are present on the map. The inset in the upper left corner shows the approximate location of the figure in central Alaska. A geologic interpretation of line 5004 is present in figure 6. Map modified from Riehle, 1997; Dixit amd Hanks, 2014.

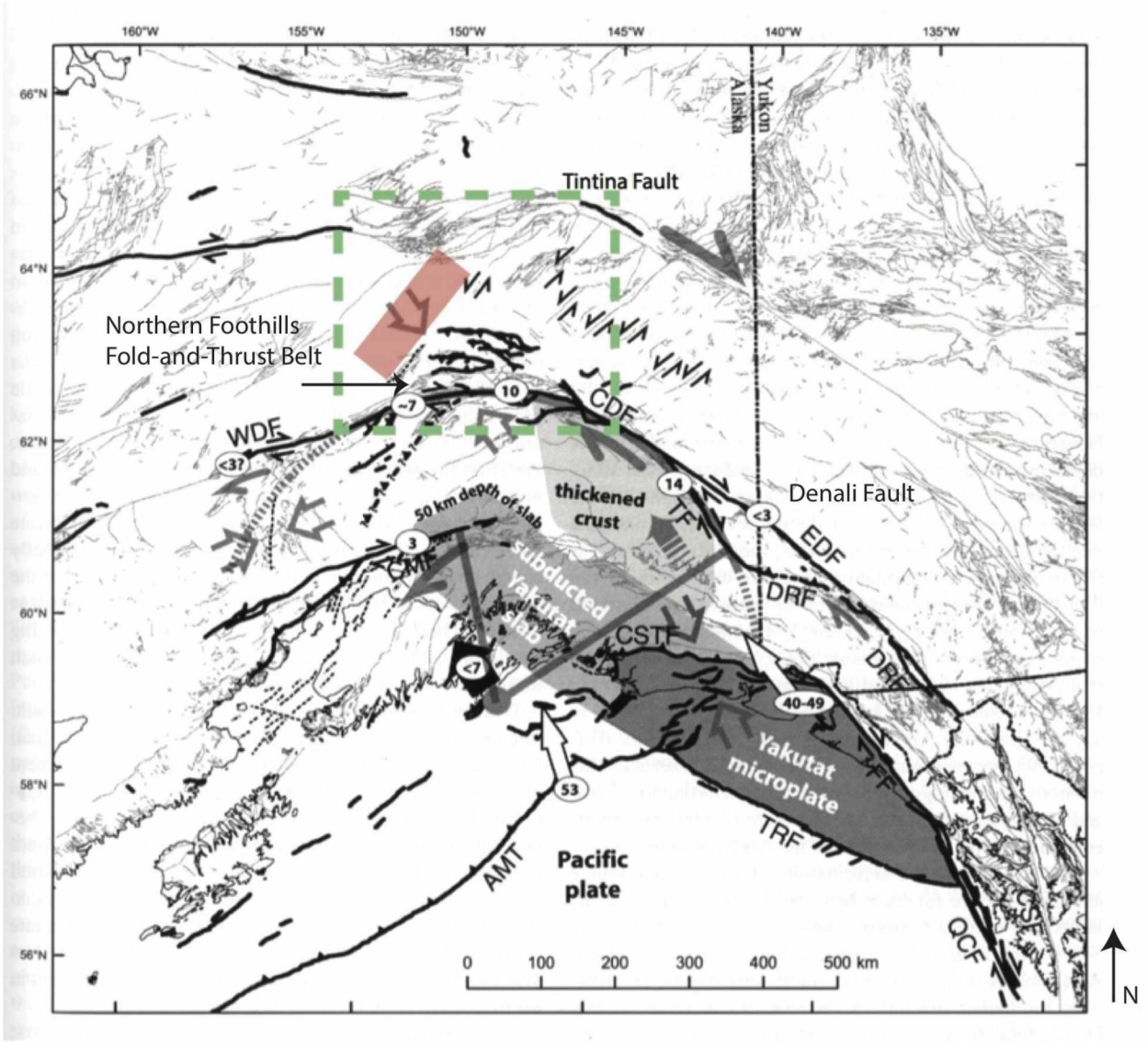

Figure 2: Geologic setting of southern and central Alaska. The tectonics of southern and central Alaska are influenced by the North American-Pacific plate convergence and the subduction of the Yakutat Microplate. It is interpreted that the northwestern convergence of both prominent features resulted in counterclockwise rotation in southern Alaska.
In addition, the Yakutat Microplate is a major cause of the right-lateral displacement along and contraction of the Denali fault system. Compression related to these events is hypothesized to have transferred across the Denali fault system and resulted in the Northern Foothills fold- and-thrust belt. The approximate location of the Nenana basin is outlined by the red box. The green box represents the outline of figure 1. Fault block and slip rates are shown in white ovals in mm/yr; faults are shown with solid/dashed black lines; WDF=West Denali fault, CDF= Central Denali fault, EDF= East Denali fault; TF= Totschunda fault; DRF= Duke River fault; LCF= Lake Clark fault; CMF= Castle Mountain fault; CSTF= Chugach-St. Elias thrust fault; AMT= Aleutian megathrust; QCF= Queen Charlotte fault; FF= Fairweather fault; TRF= Transition fault; CSF= Chatham fault. Figure modified from Haeussler, 2008.

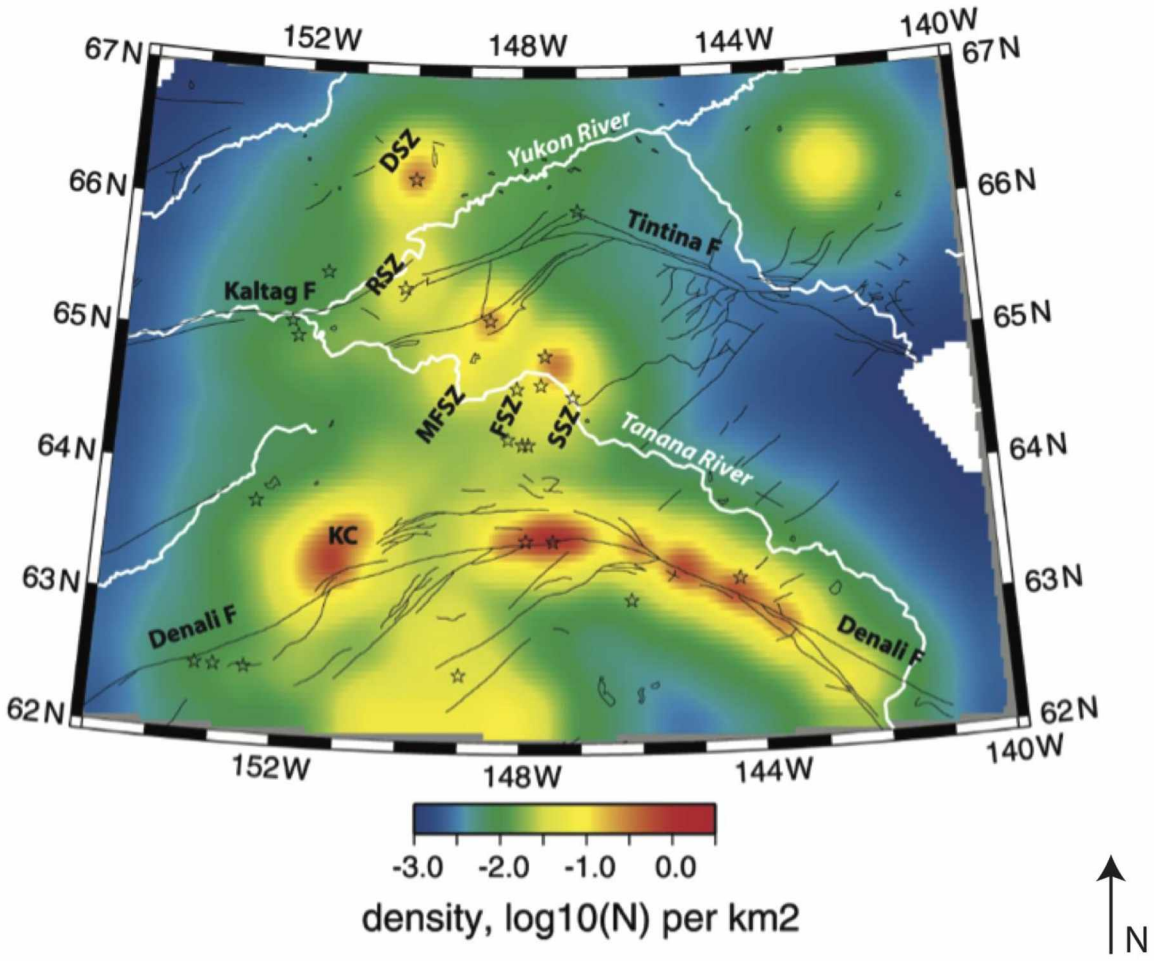

Figure 3: Pattern and density of seismicity in central Alaska. A detailed map showing the NE-oriented pattern of active seismic zones in central Alaska between the Denali and Tintina fault systems. The colors signify the density of earthquakes with the color red signifying high density. MFSZ= Minto Flats Seismic Zone, FSZ= Fairbanks Seismic Zone, SSZ= Salcha Seismic Zone, KC= Kantishna Cluster, RSZ= Rampart Seismic Zone, DSZ= Dall City Seismic Zone. Figure modified From Ruppert et al., 2008.

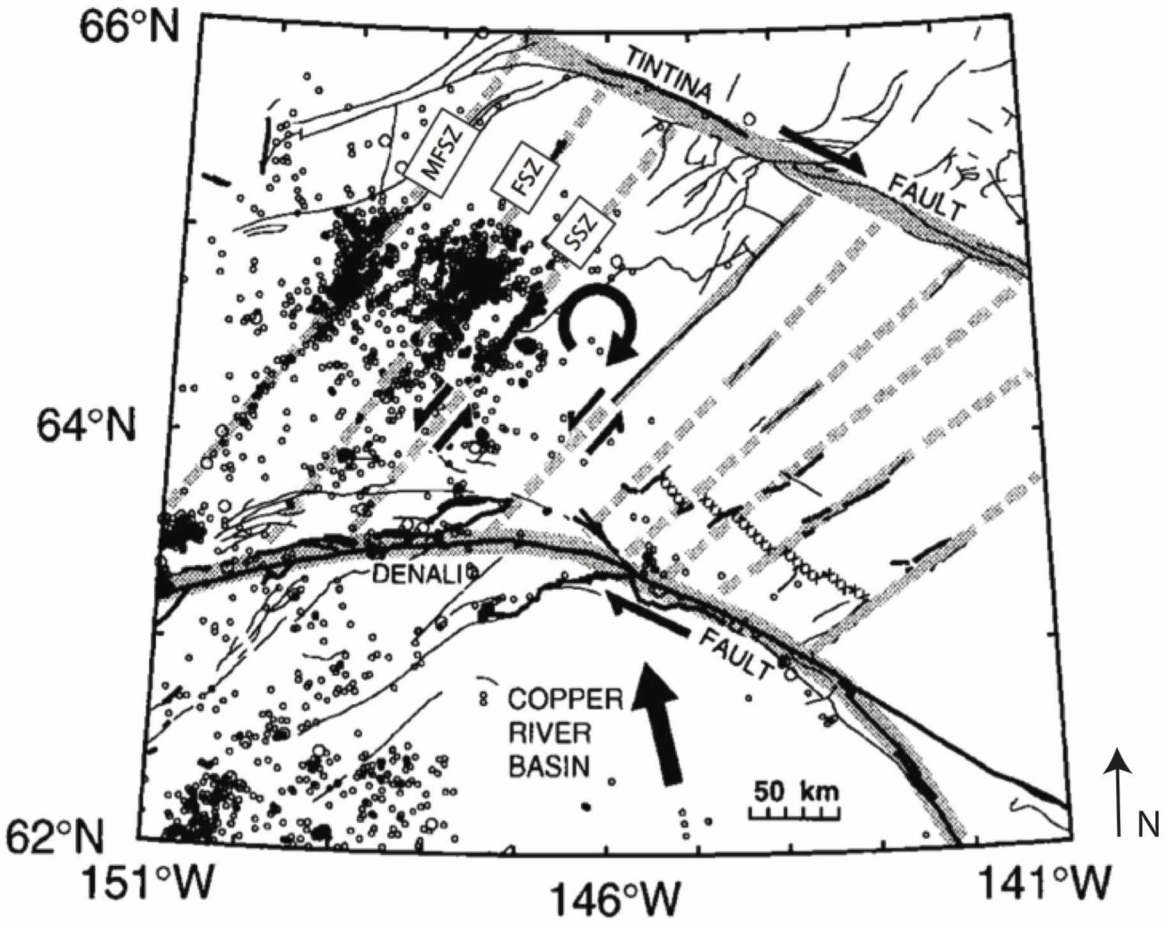

Figure 4: Clockwise crustal block rotation model for east-central Alaska. One explanation of the northeast-oriented seismic zones in central Alaska involves crustal blocks rotating in a dextral shear zone (Page et al., 1995). Dashed lines show inferred locations of block boundaries between the Denali and Tintina fault systems. In this model, faults within the shear zone have a left-lateral strike-slip component and act as subsidiary slip surfaces that aid in block rotation. MFSZ= Minto Flats Seismic Zone, FSZ= Fairbanks Seismic Zone, SSZ= Salcha Seismic Zone. Figure modified from Page et al., 1995.

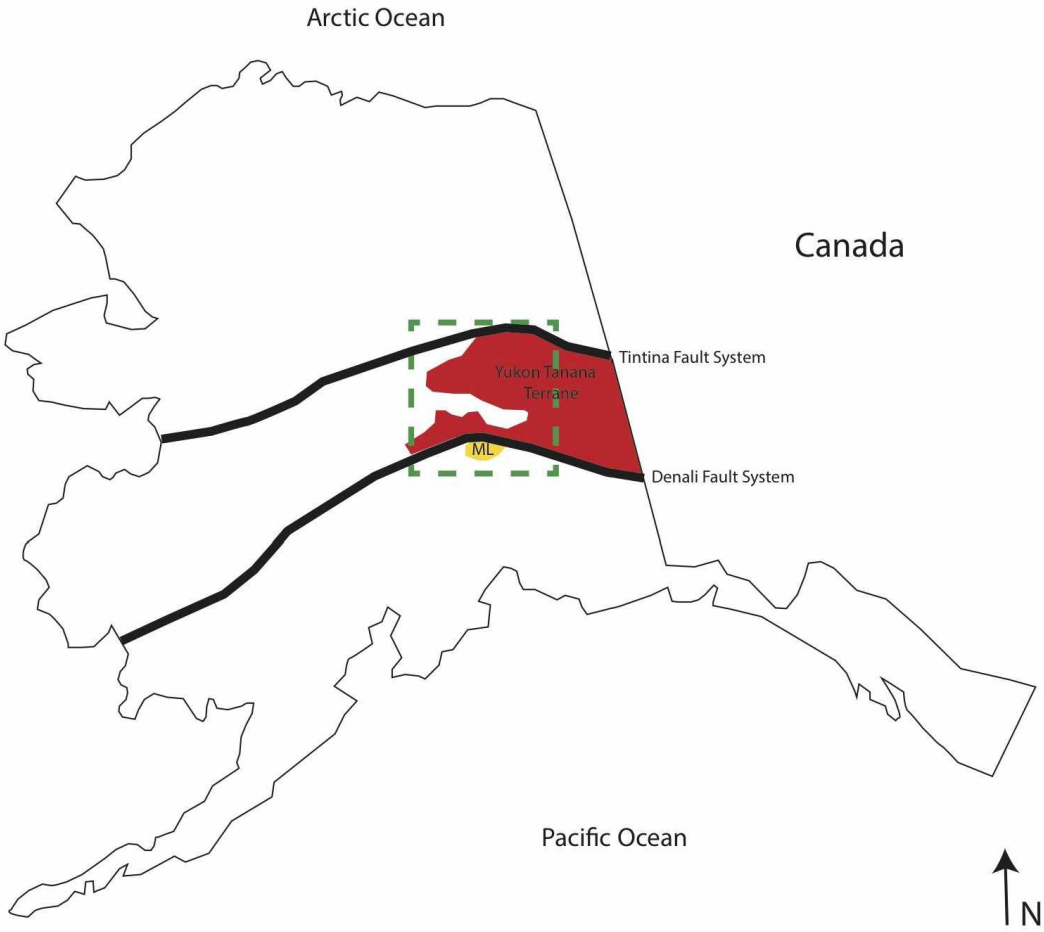

Figure 5: Location of the Yukon-Tanana and the Maclaren terranes. Location of the Yukon-Tanana (shown in red) and the Maclaren (ML, shown in yellow) terranes with respect to central Alaska. The Yukon Tanana terrane is located between the Denali and Tintina fault systems and is primarily composed of metamorphosed sedimentary and igneous rocks. The Maclaren terrane is located south of the Denali fault and consists of both igneous and metamorphosed sedimentary rocks. The green box represents the outline of figure 1. Figure modified from Goldfarb et al., 2000.

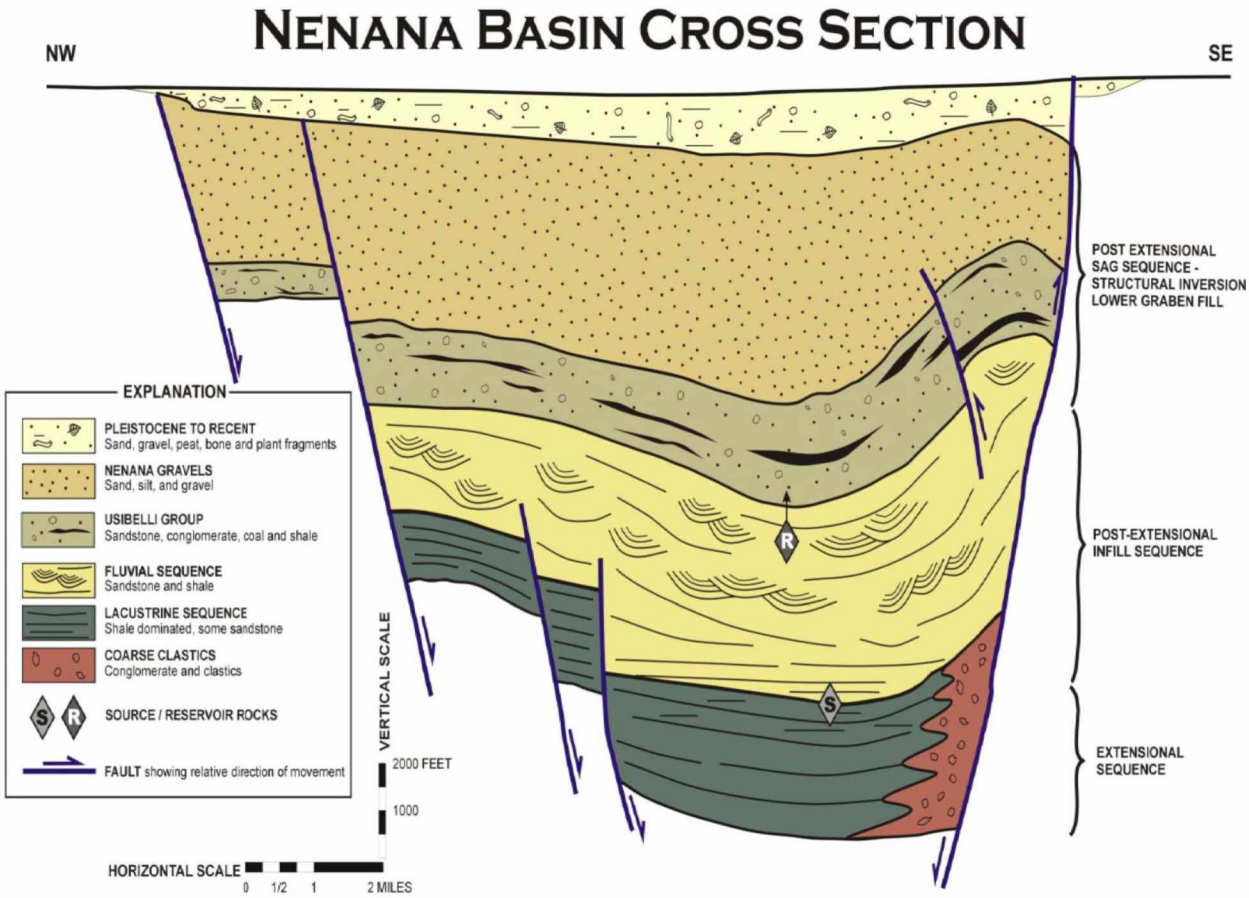

Figure 6: Geologic interpretation of line 5004 from the Nenana basin. This northwest-southeast oriented cross-section shows the present-day geometry of the Nenana basin. The Nenana basin is a half-graben with predominately normal faulting. It is bounded on the southeast side by the Minto fault, a normal fault with left-lateral component. The location of this seismic line is shown in figure 1. Interpretation by Doyon, Limited, 2009.

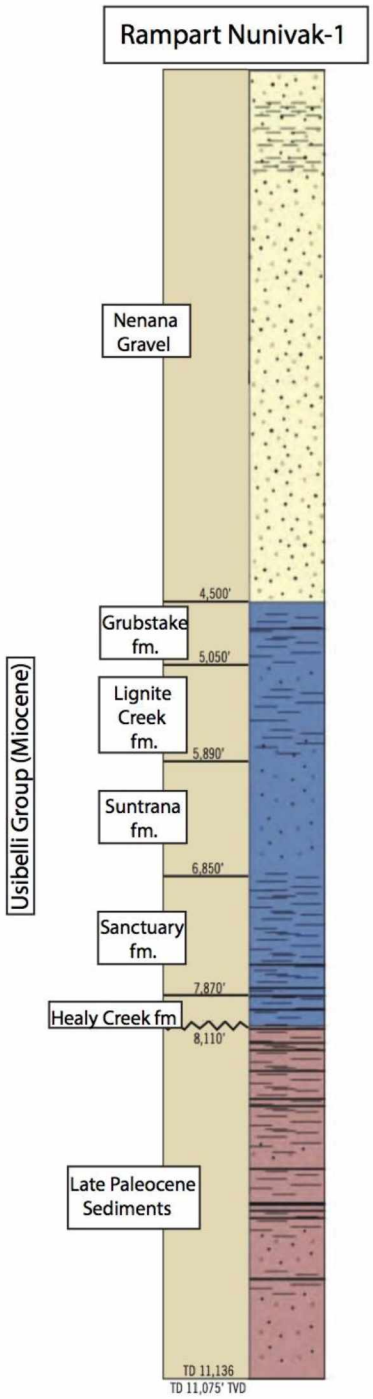

Figure 7: Nunivak-1 lithostratigraphy. A stratigraphic column based on well cuttings and gamma ray logs from the Nenana basin showing deposits of the Nenana Gravel and the Usibelli Group overlying Late Paleocene sediments. Sediments are predominately non-marine, coal-bearing sequences. Location of this well is seen on figure 1. Figure modified from Van Kooten et al., 2012.

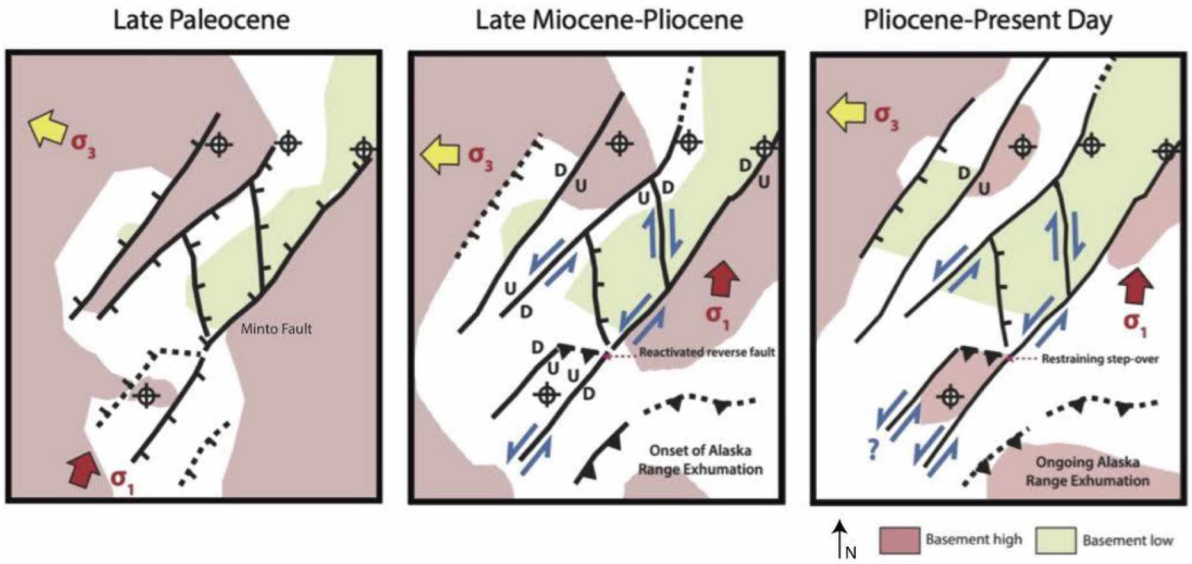

Figure 8: Structural evolution of the Nenana basin. Maps generated by Dixit and Hanks (2014), showing the evolution of the Nenana basin based on seismic data. Maps were generated by flattening on a specific horizon (Healy Unconformity, Lignite Creek Formation, and present day) and restoring faults to their position at that particular time.
Late Paleocene (Healy Unconformity): At this time, the basin is extending in the NW-SE direction. Two dominant normal fault patterns are present during this phase. Both NW and NE-striking dip-slip normal faults are active in this time period.
Late Miocene-Pliocene (Lignite Creek Formation): The second time period is characterized by the onset of oblique slip faulting throughout the basin. The NE-striking faults have a left-lateral shear sense while the NW-striking faults have a proposed right-lateral shear sense. It is interpreted that the left-stepping Minto fault in the basin formed thrust structures at its restraining bend. Both fault orientations are oblique slip faults with a normal component during this time period.
Pliocene-Present Day: The final stage is characterized by continued oblique slip motion (normal dip-slip with strike-slip) but the dip-slip component is subsidiary to the strike-slip component during this time period. The basin continues to open in the NW-SE orientation.

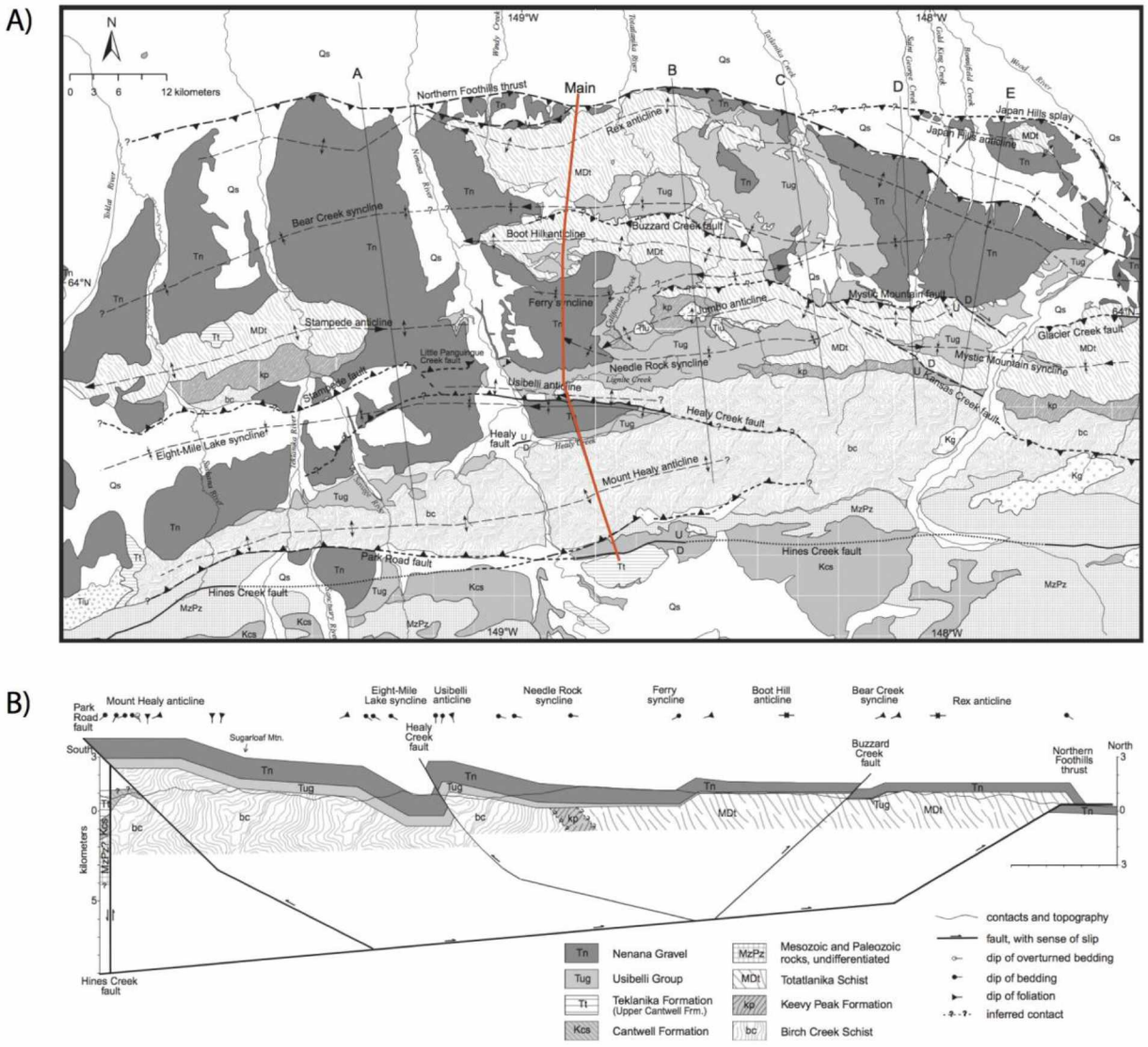

Figure 9: Map view and north-south structural cross-section of the Northern Foothills field area.
A) Map view of faults and folds in the Northern Foothills fold-and-thrust belt. Red line represents the line of transect for the balanced cross-section.
B) Balanced cross-section displaying north and south dipping thrust faults and east-west trending folds. In addition to this local scale map, the location of the cross-section is shown on figure 1 with a green dotted line. Modified from Bemis and Wallace, 2007.

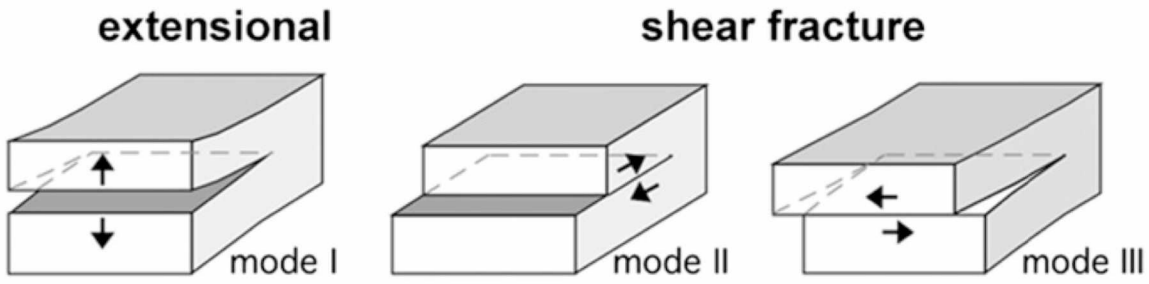

Figure 10: Fracture failure modes. Mode I forms extension fractures while mode II and mode III form as shear fractures. For mode I fractures, displacement occurs perpendicular to the fracture face. Mode II and III, displacement occurs parallel to the fracture face. Figure from Bons et al., 2012.

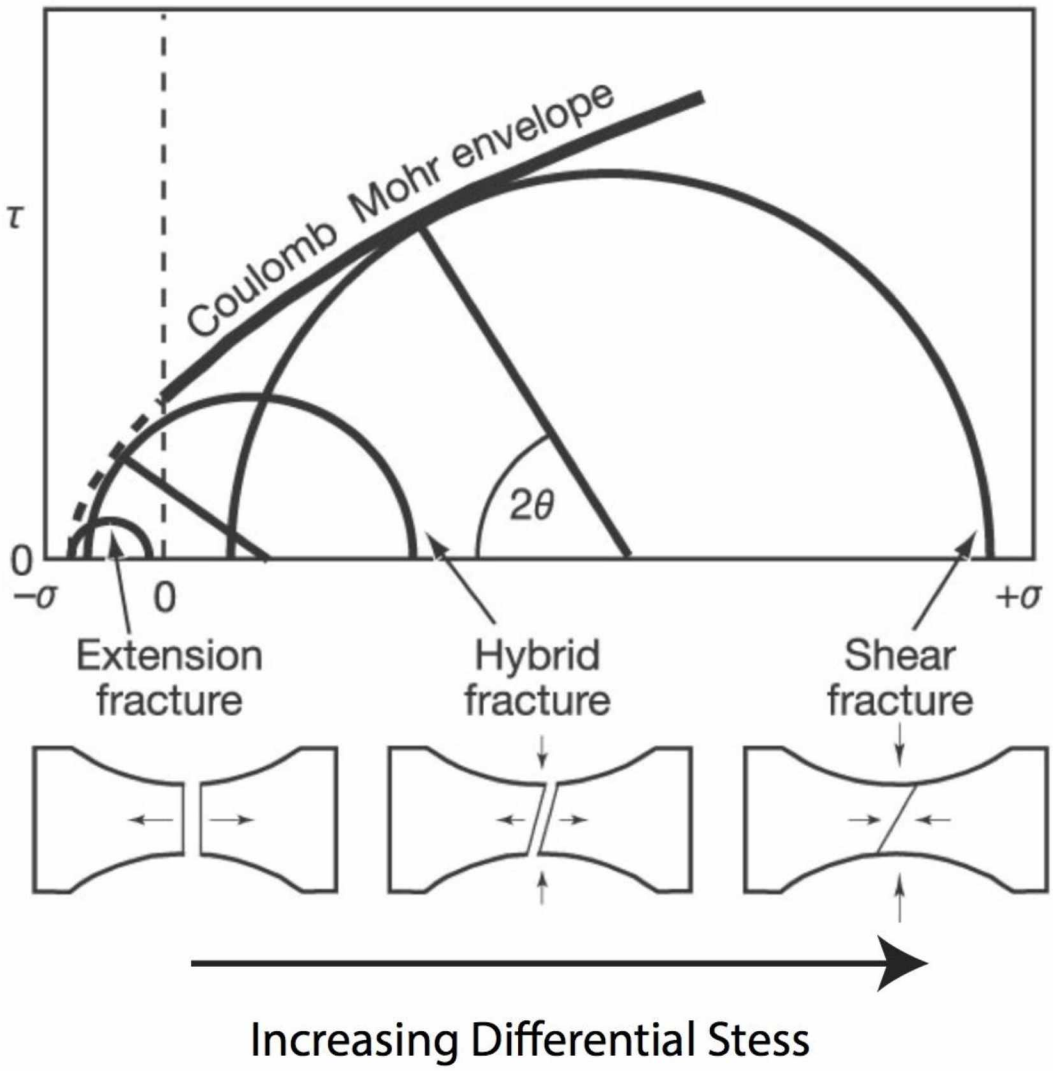

Figure 11: Schematic mohr circle diagram. The diagram displays the stress conditions necessary to generate extension, shear, and hybrid fractures. Extension fractures form at low differential stresses, while shear and hybrid fractures form at greater amounts of differential stress. Figure modified from Ramsay and Chester, 2004.

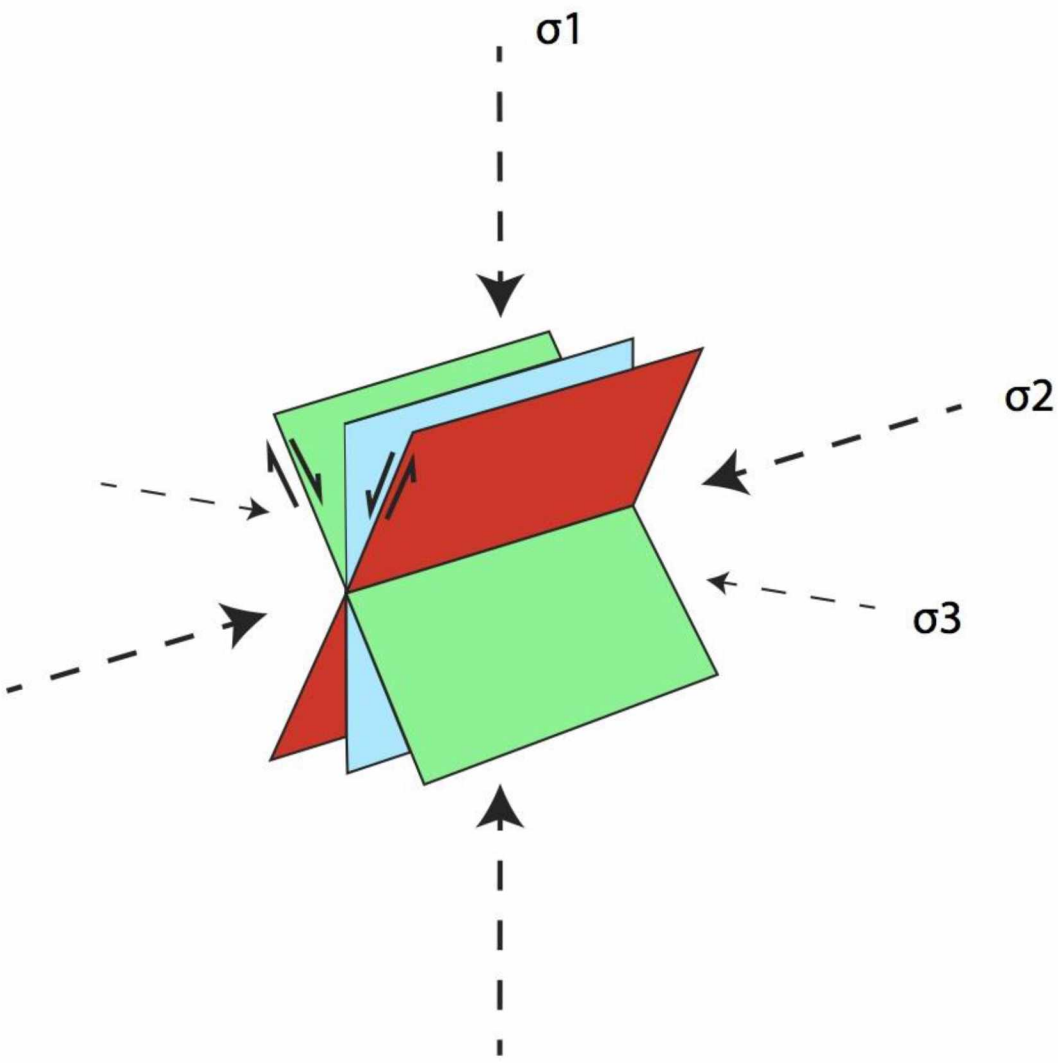

Figure 12: Orientation of conjugate shear fractures and extension fractures with respect to principle stresses. Conjugate shear fractures are shear fractures with opposite senses of shear and are separated by an acute angle (~60°). Conjugate shears (red and green) are interpreted as forming due to a maximum principle stress (σ1) oriented so that it bisects the acute angle between the conjugate shears. In contrast, extension fractures (blue) form parallel to σ1 and perpendicular to σ3. The conjugate shears and extension fractures form at separate times in history of the host rock. Figure modified from Twiss and Moores, 1992.

-

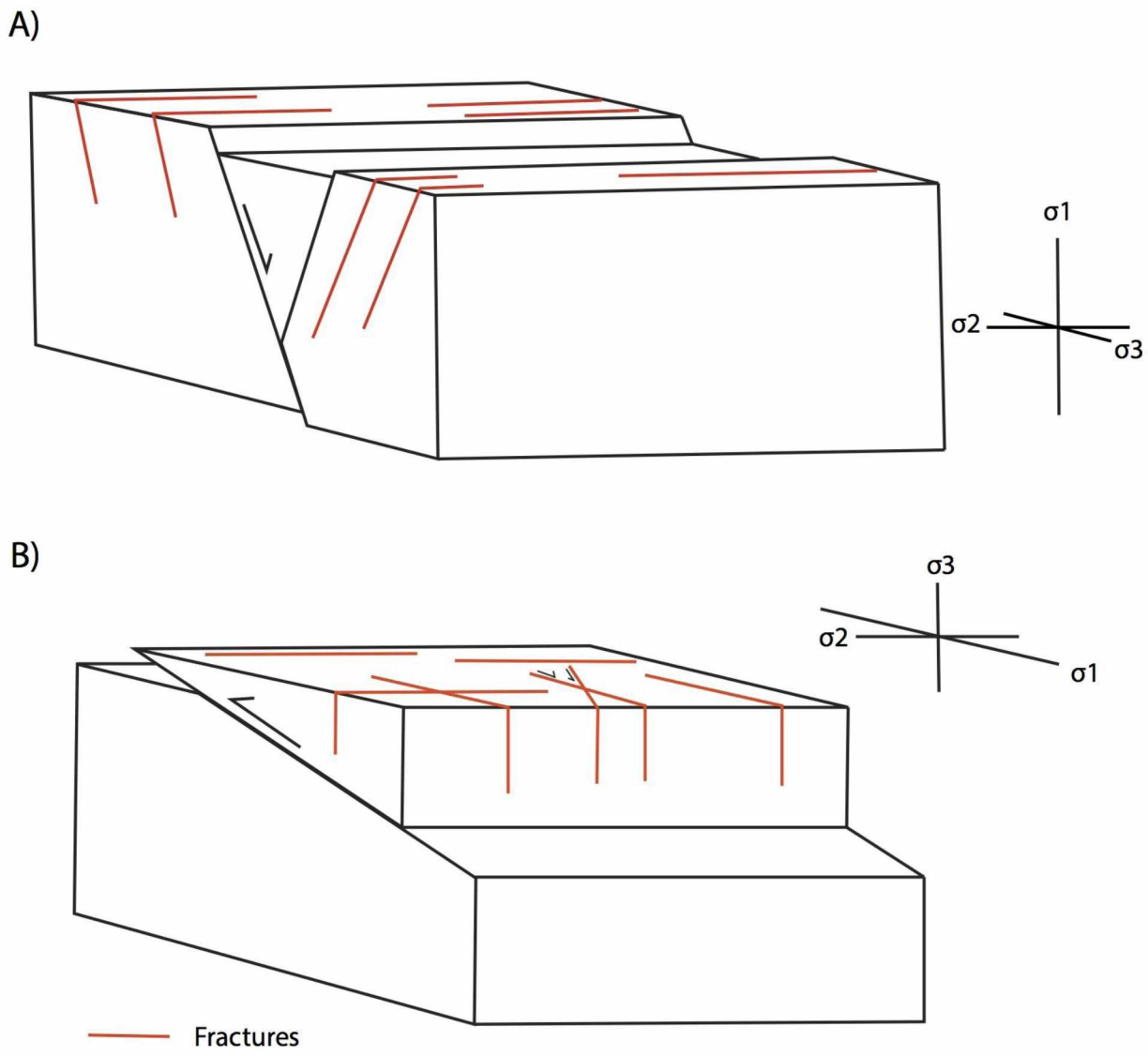

Figure 13: Fractures related to faulting.

A) Fractures Related to Normal Faulting.
Fractures that form in relation to extensional faults form with a strike sub-parallel or parallel to the fault plane. Figure modified from Lacazette, 2000.

B) Fractures that form in relation to thrust faults can form with a strike parallel or orthogonal to the fault plane. In addition, conjugate shear fractures form at acute angles to the maximum principle stress. Figure modified from Lacazette, 2000.

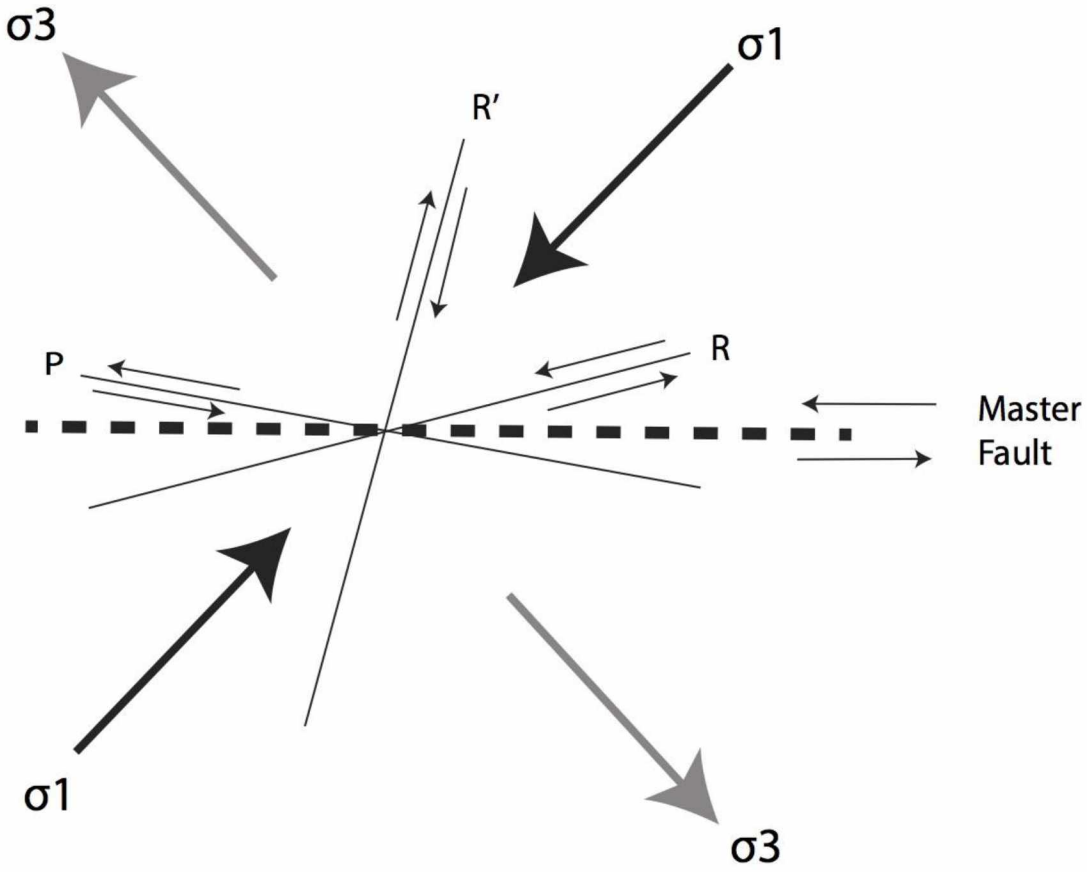

Figure 14: Riedel shears. Riedel shears are fractures that form as subsidiary features to a master fault. R and R' are conjugate shears with opposite senses of shear that can either form simultaneously or separately. R shears form at acute angles to the master fault and have the same sense of shear as the master fault; R' shears form at higher angles to the master fault and have an opposite sense of displacement. The angle bisecting the R and R' shears represents the maximum principle stress within the shear zone. P shears form at an acute angle clockwise to the master fault and they are not as common as R and R' shears. Figure modified from Davis and Reynolds, 1996.

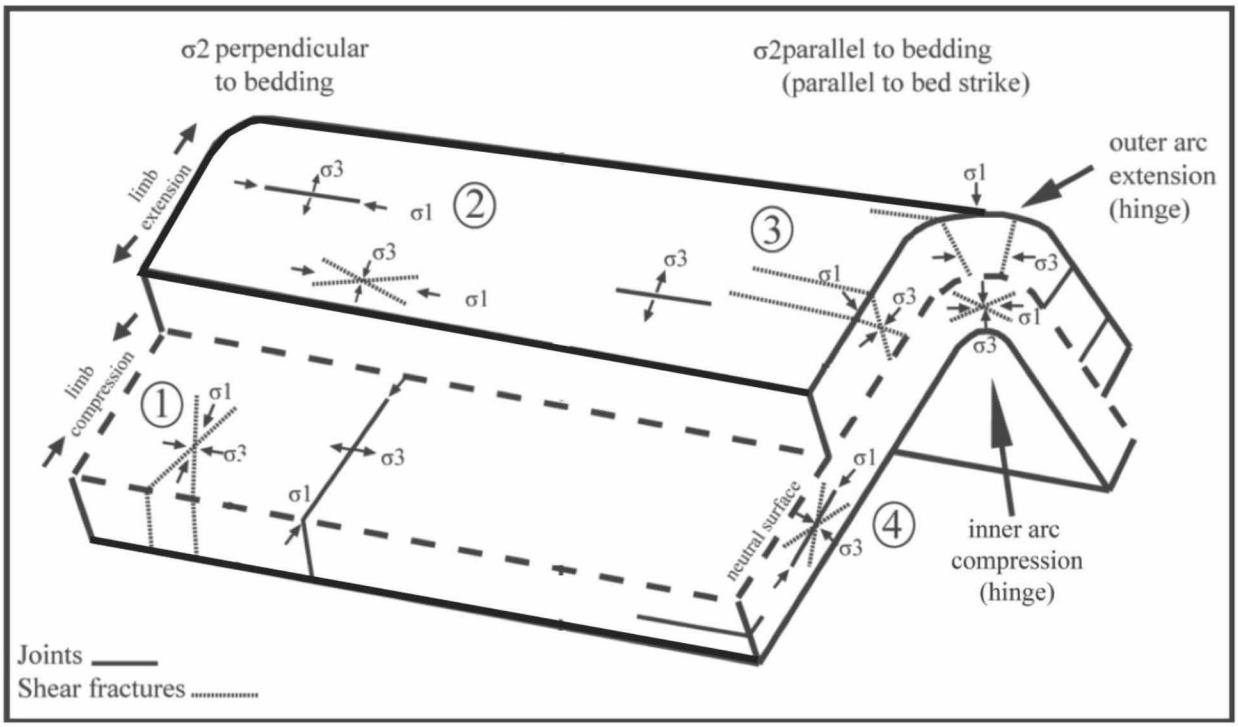

Figure 15: Fractures related to folding. Both extension fractures and conjugate shear fractures form as structural folds develop. Fractures both orthogonal and parallel to the fold axis may be present. If a fold has multiple mechanical layers, the outer layer deforms due to limb extension and the inner arc deforms due to limb compression. Four sets are formed due to the differing orientations of stresses depending on their location with respect to the fold hinge and limb. Figure modified from Hayes, 2004 and Wentz, 2014.

1) *A set of conjugate shear fractures and an extension fracture*. The shear fractures form at acute angles to the σ1 plane while the extension fracture forms parallel to the σ1 plane (Stearns, 1968).
2) *A set of conjugate shear fractures and an extension fracture*. The extension fracture forms parallel to the σ1 plane while the conjugate shear fractures form at acute angles to the σ1 plane. Fractures form due to shortening parallel to the fold axis and extension parallel to the dip of the fold (Stearns, 1968).
3) *A set of conjugate shear fractures and an extension fracture oriented parallel to the fold axis*. Extension occurs parallel to the dip while compression is normal to the fold axial plane (Stearns, 1968).
4) *An extension fracture parallel to bedding and low angle shear fractures*. The σ1 plane is parallel to dip and extension occurs normal to bedding (Stearns, 1968).

Figure 16: Scan-line fracture survey methodology. Natural fractures were measured by placing an open-reel measuring tape on an outcrop perpendicular to the fracture set and the location and orientation of each fracture was recorded. Each fracture was then measured in terms of height, length, and the width of the aperture. The last step was to record age relationships and shear sense if observable.

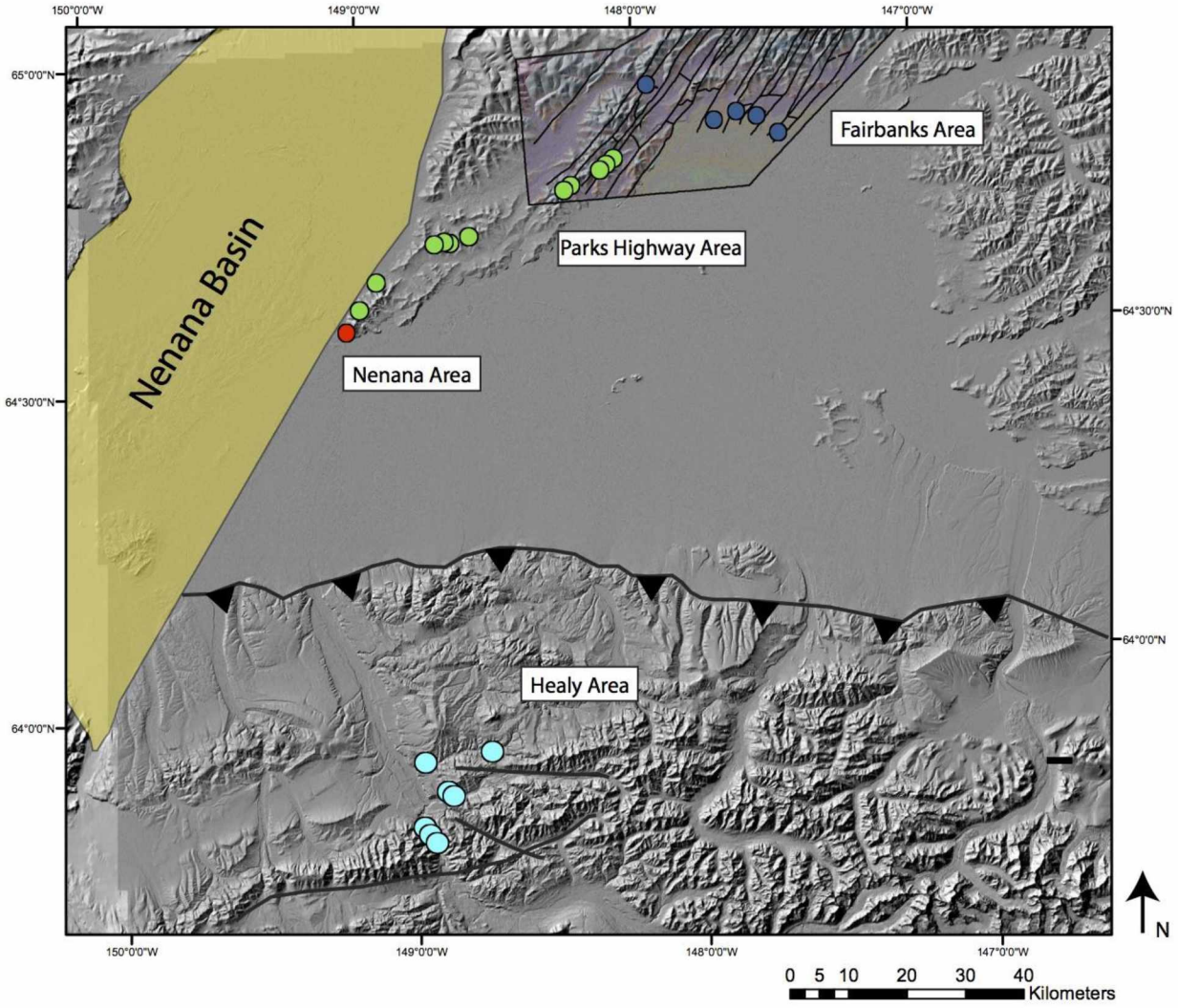

Figure 17: Fieldwork locations. Outcrop locations sampled for fracture character and distribution are on the northeast, east, and southeast margins of the Nenana basin (shown in yellow). Locations included Fairbanks (dark blue dots), along the Parks Highway (green dots), in Nenana (red dots), and in Healy, Alaska (light blue dots). The NE-striking faults in the Fairbanks area were mapped by Newberry et al. (1996).

Figure 18: Collection of oriented samples. Oriented samples of fractures were collected for thin section analyses. The strike, dip, and north direction were marked on the samples prior to removal from the outcrop.

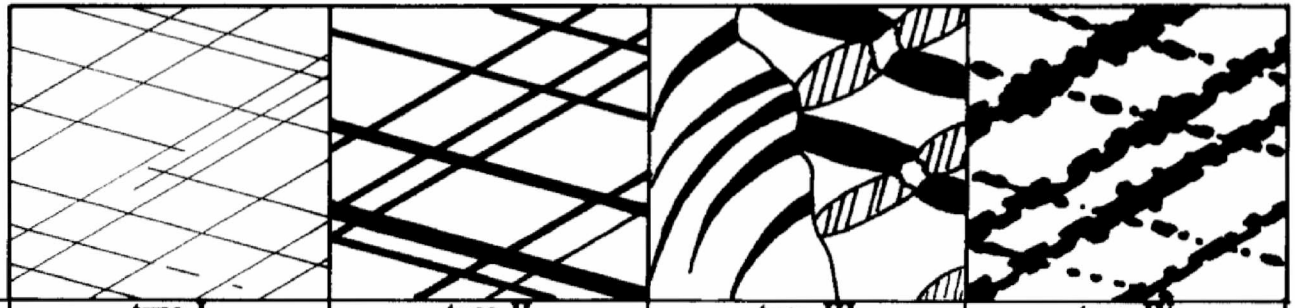

	type I	type II	type III	type IV
Geometry **Description**	- thin twins - straight - rational - 1, 2 or 3 sets per grain	- thick (>>1μm) - straight - slightly lense shaped - rational	- curved thick twins - twins in twins - completely twinned - irrational	- thick, patchy - sutured twin boundaries - trails of tiny grains - irrational
Interpretations	- little deformation - little cover - very low temperature - (post-metamorphic) - (late tectonic)	- considerable deformation - completely twinned grains are possible - syn- or post-metamorphic deformation	- large deformation -intracrystalline deformation mechanisms (r-& f-glide) - syn-metamorphic deformation.	- large deformation - dynamic recrystallization (grain boundary migration) - pre- or syn-metamorphic deformation
Temperature	**< 200°C**	**150-300°C**	**> 200°C**	**>250°C**

Figure 19: Calcite thermometry. The geometry of calcite twins reflects the temperature of deformation. Four types of twins have been documented; with increasing temperature, calcite twins become thicker, curved and patchy. Figure from Burkhard, 1993.

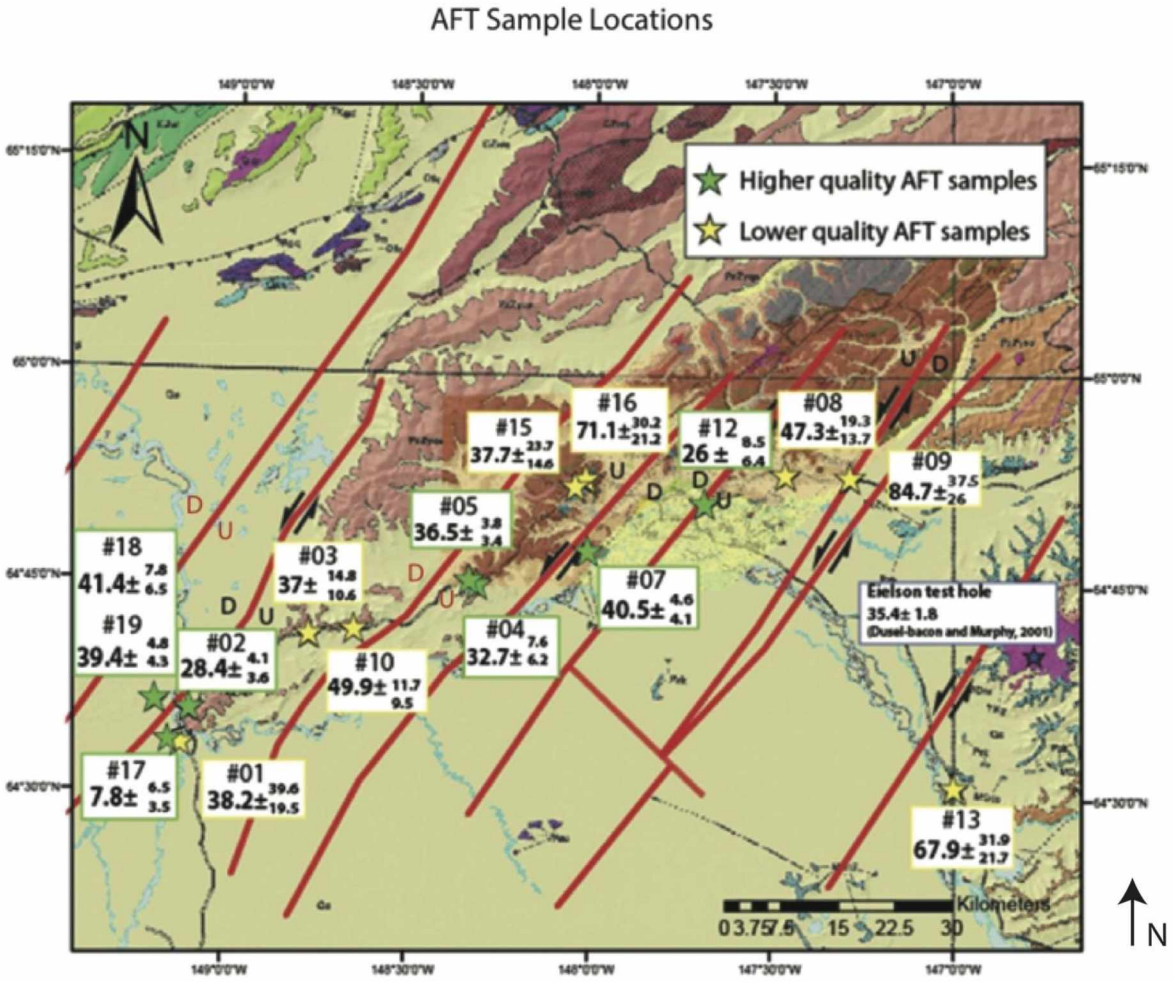

Figure 20: Apatite fission track sample locations. Apatite fission track samples incorporated into this study were collected by N. Dixit, R. Frohman and A. Rizzo. Samples were collected from both the hanging wall and footwall of the NE-SW striking faults in the Fairbanks area. Samples lacking apatite grains and that have fewer fission tracks have greater error ranges and are considered lower quality samples. Higher quality samples are shown in green while lower quality samples are shown in yellow. Figure from Frohman, 2014.

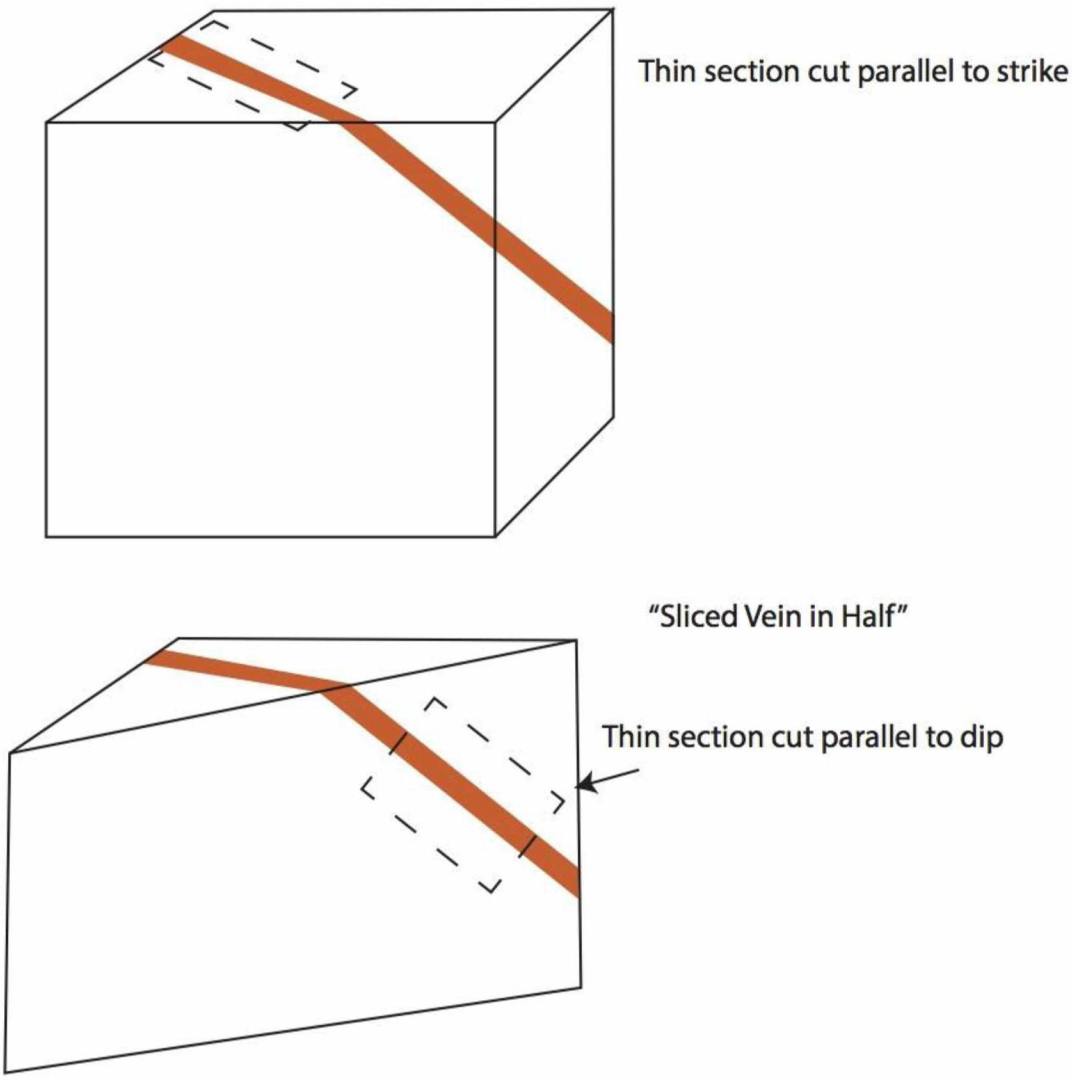

Figure 21: Thin section orientations. Two orientations of thin sections are used in this project.
A) Cut in a horizontal plane parallel to the strike of the vein
B) Cut parallel to the dip of the fracture.

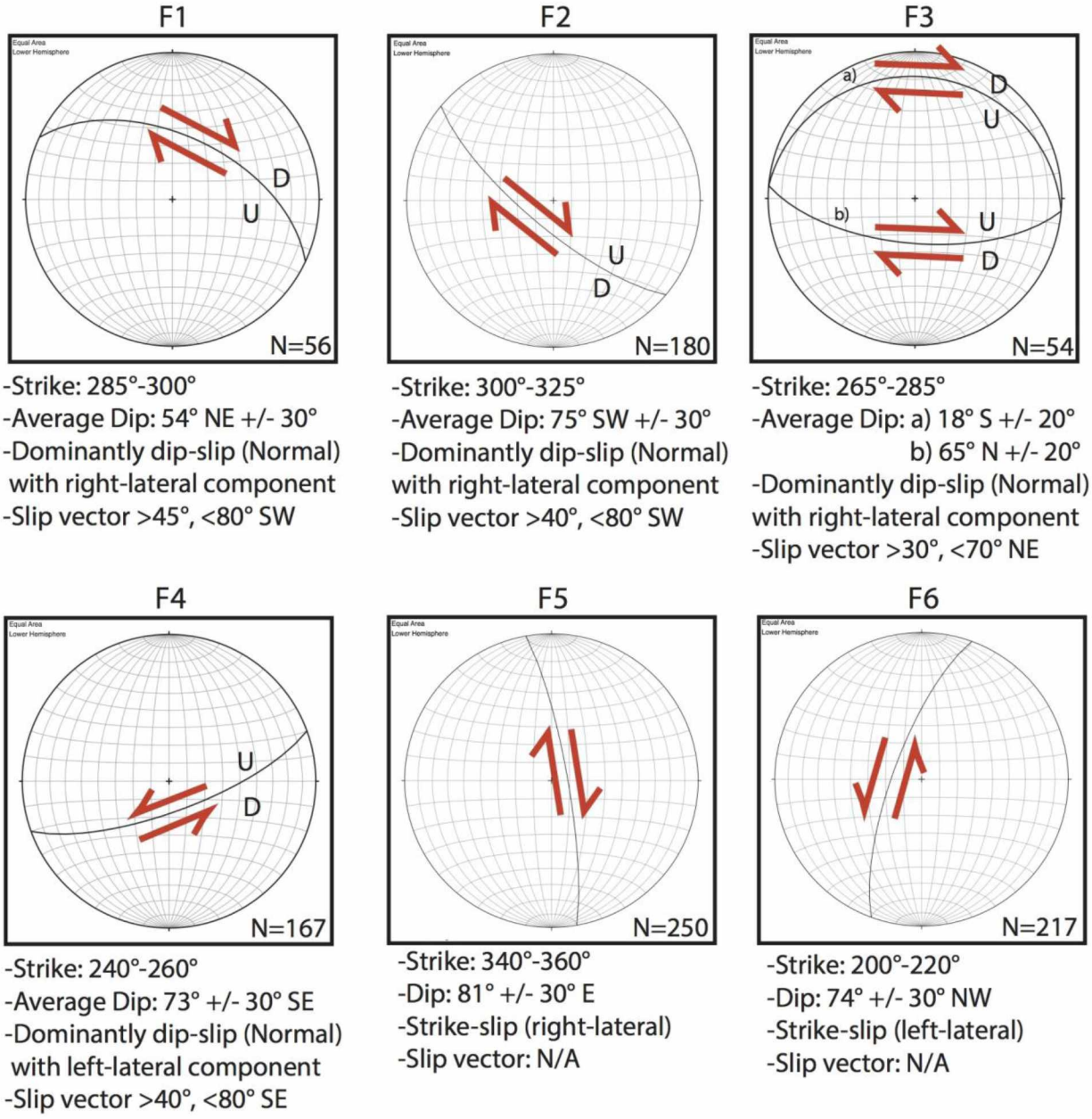

Figure 22: Summary of fracture sets in Domain I. Equal area, lower hemisphere stereonets of each fracture set illustrate average fracture orientation, dip direction, and sense of movement. Slip vectors for fracture sets 1-4 are documented and pictured in figure 25, but are not shown here because they are for individual samples, not average orientations. Red arrows document observed slip from both field and thin section data for each set.

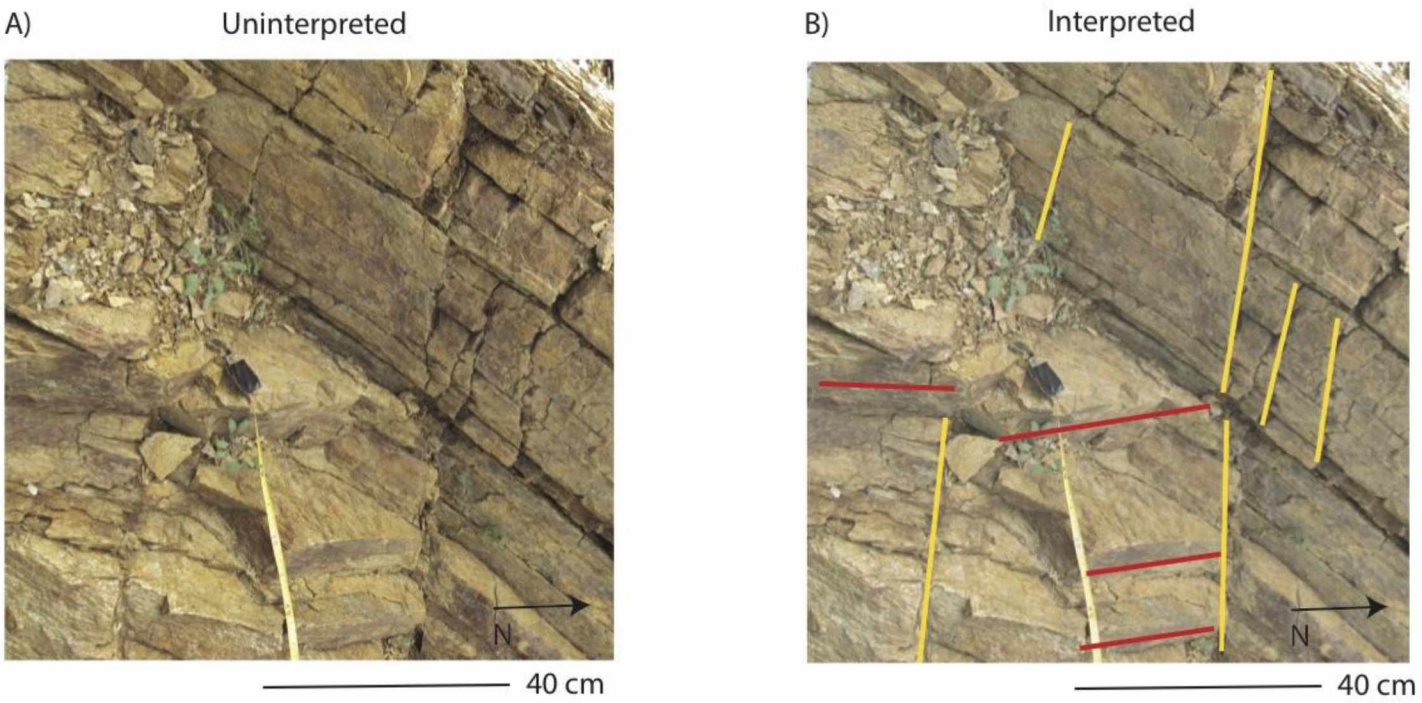

Figure 23: Crosscutting relationships of fracture Sets (F1 + F2)
A) Uninterpreted outcrop showing fracture sets at the Murphy Dome outcrop near Fairbanks.
B) Age relationships of fracture sets F1 (yellow) and F2 (red). Interpretation shows F2 terminating against F1 in outcrop

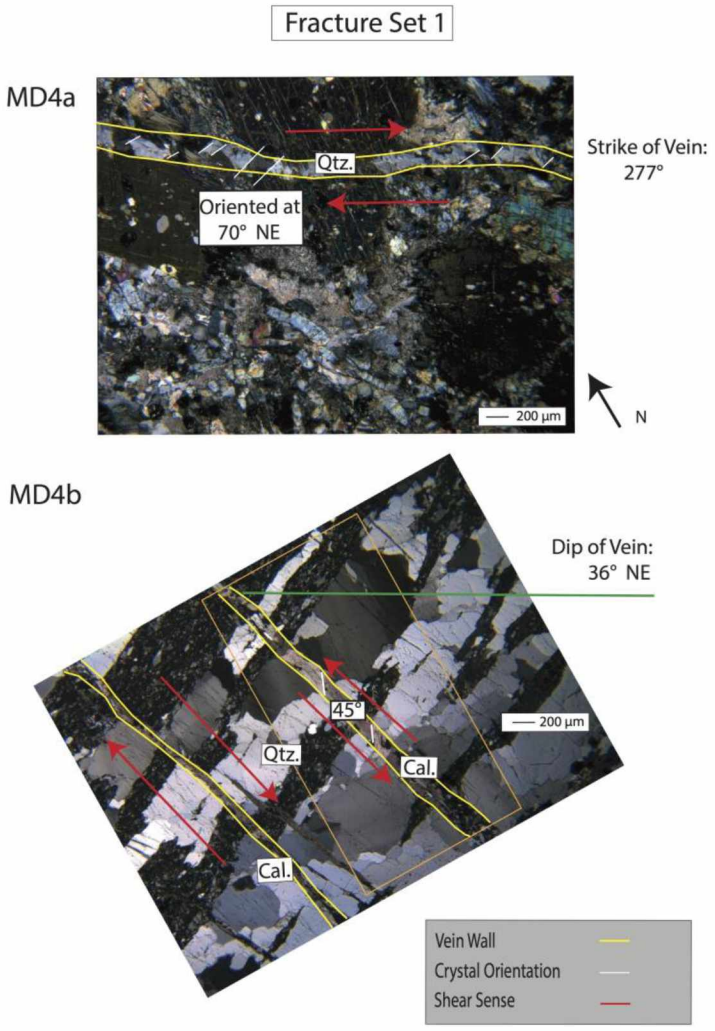

Figure 24: Thin section analysis of F1 filled fracture from the Murphy Dome outcrop. An example of a F1 quartz-filled fracture with secondary calcite. Crystals are oriented oblique to the vein wall showing that the veins have a shear origin. No calcite twins were observed in thin section. In both figures, yellow lines signify vein walls; red lines signify observed shear; white lines signify crystal orientations. Cross polarized light.

MD4a: Thin section oriented parallel to the strike of the quartz vein. Quartz crystals are angled at 40°-50° with respect to the vein wall and there is a right-lateral shear sense.

MD4b: Thin section oriented parallel to the dip of the vein. Quartz crystals are oriented 40°-50° with respect to the vein wall. There is a dip-slip component showing offset of crystals. Two different fracture sets are pictured, the F1 vein is outlined in the orange box.

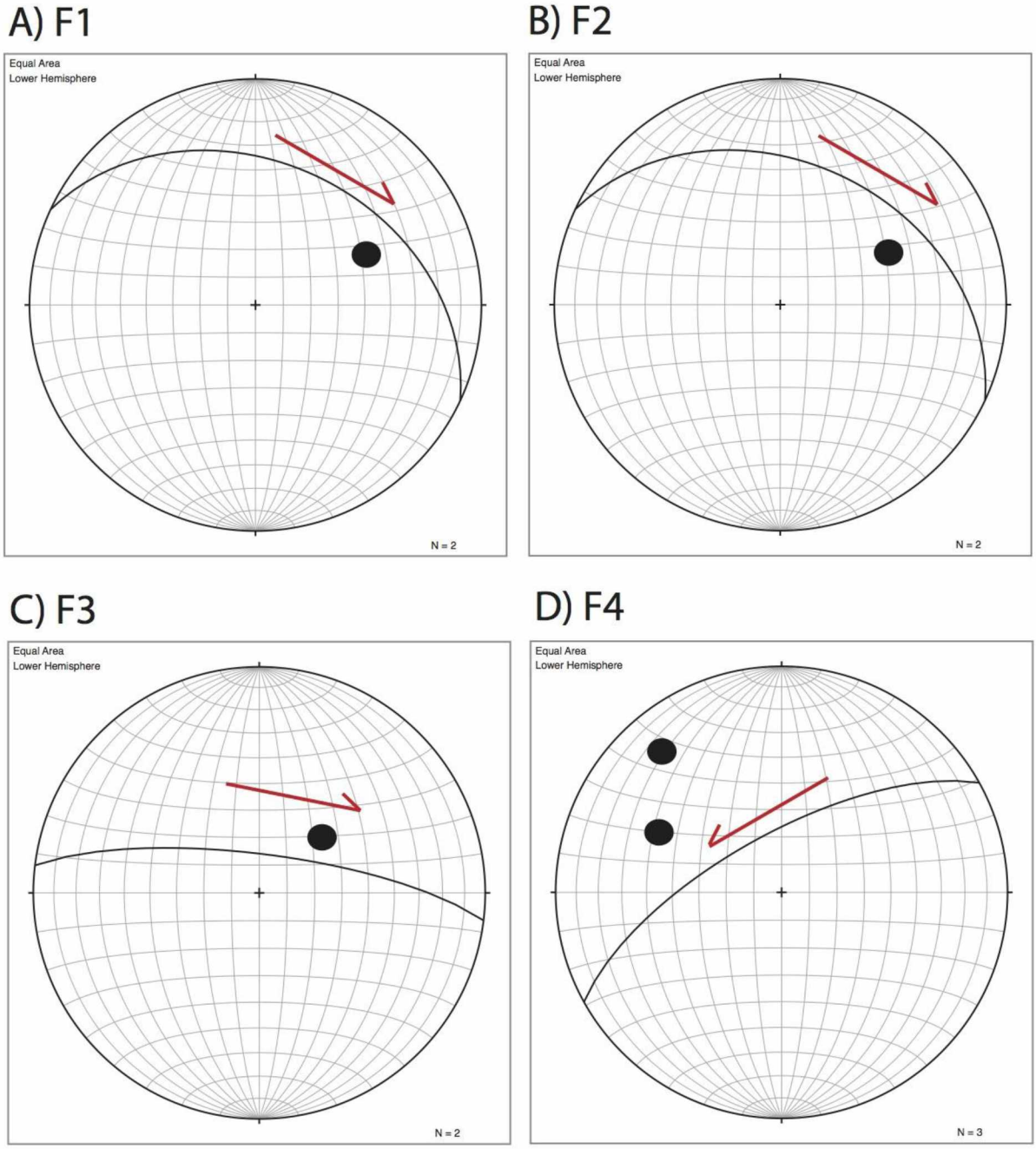

Figure 25: Opening projections of fracture sets F1, F2, F3, and F4. Equal area, lower hemisphere stereonets showing the combined trend and plunge of crystal orientations parallel to the strike and dip of the vein. Both quartz and calcite crystals were measured depending on what was present in the filled fracture. Red arrows represent observed slip for each fracture set,

A) F1 has a right-lateral opening projection with a strong dip-slip component
B) F2 has a right-lateral opening projection with a strong dip-slip component
C) F3 has a right-lateral opening projection with a strong dip-slip component
D) F4 has a left-lateral opening projection with both a strong and minor dip-slip component (two lines).

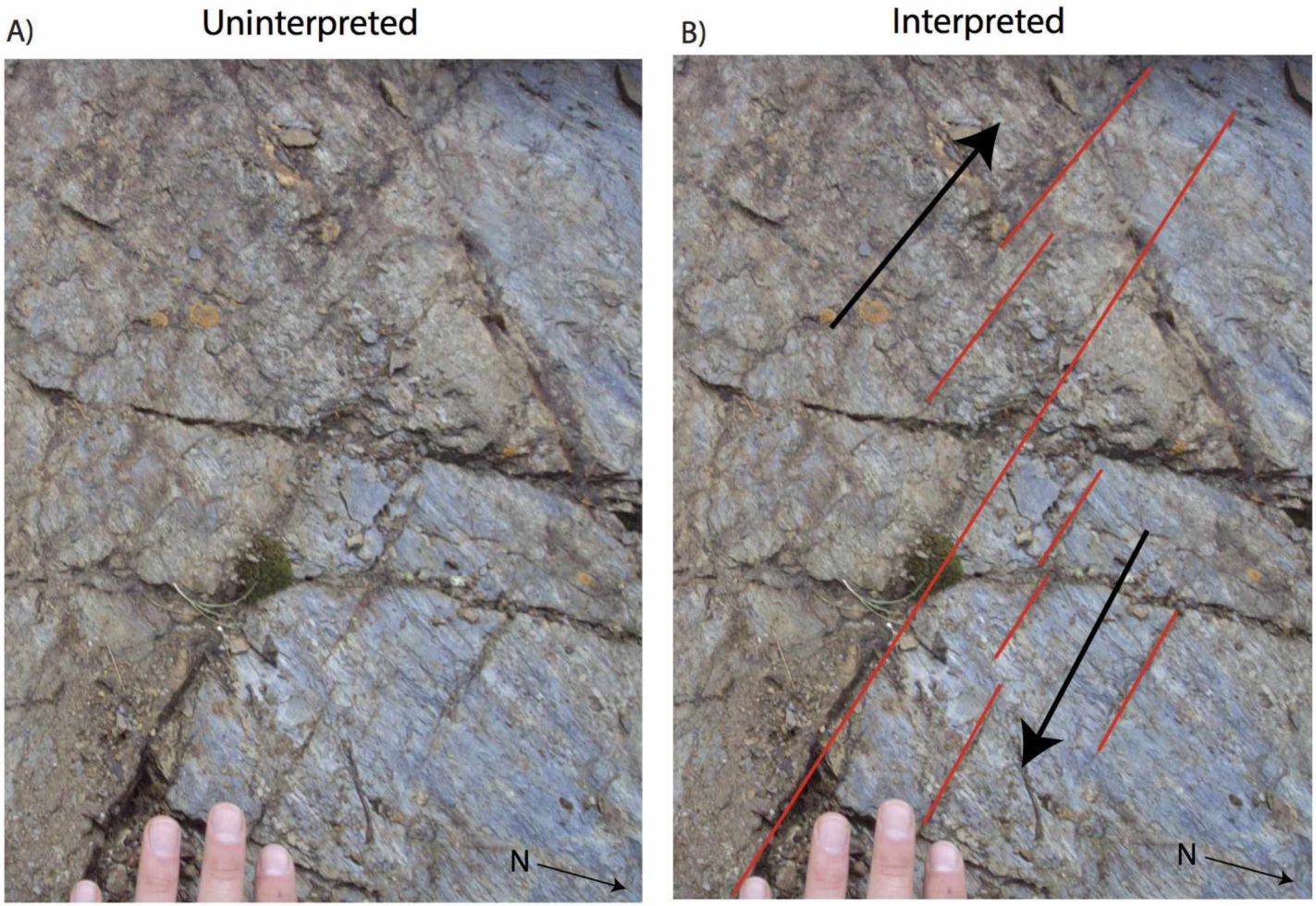

Figure 26: Shear indicators, F2 fractures, Nenana outcrop
A) Uninterpreted F2 fractures at the Nenana outcrop
B) Extensive shear fractures showing right-lateral shear sense in outcrop

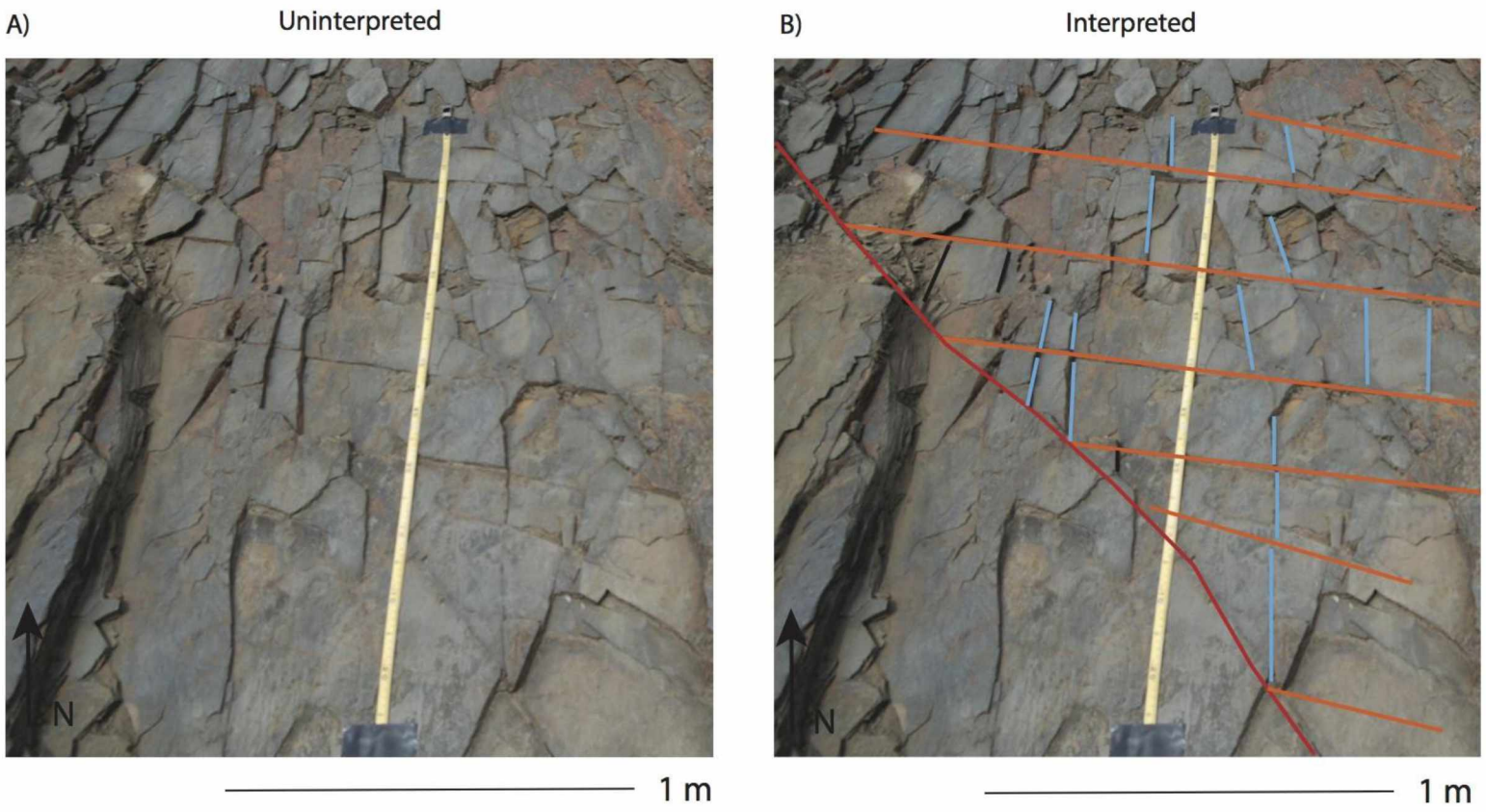

Figure 27: Cross-cutting relationships of fracture sets F2, F3 and F5 observed in Fairbanks area outcrops.
A) Uninterpreted outcrop showing age relationships between fracture sets at the Birch Hill outcrop in Fairbanks.
B) Age relationships of fracture sets 2 (red), 3 (orange), and 5 (blue). F5 terminates against both other sets, while F3 is interpreted to terminate against F2.

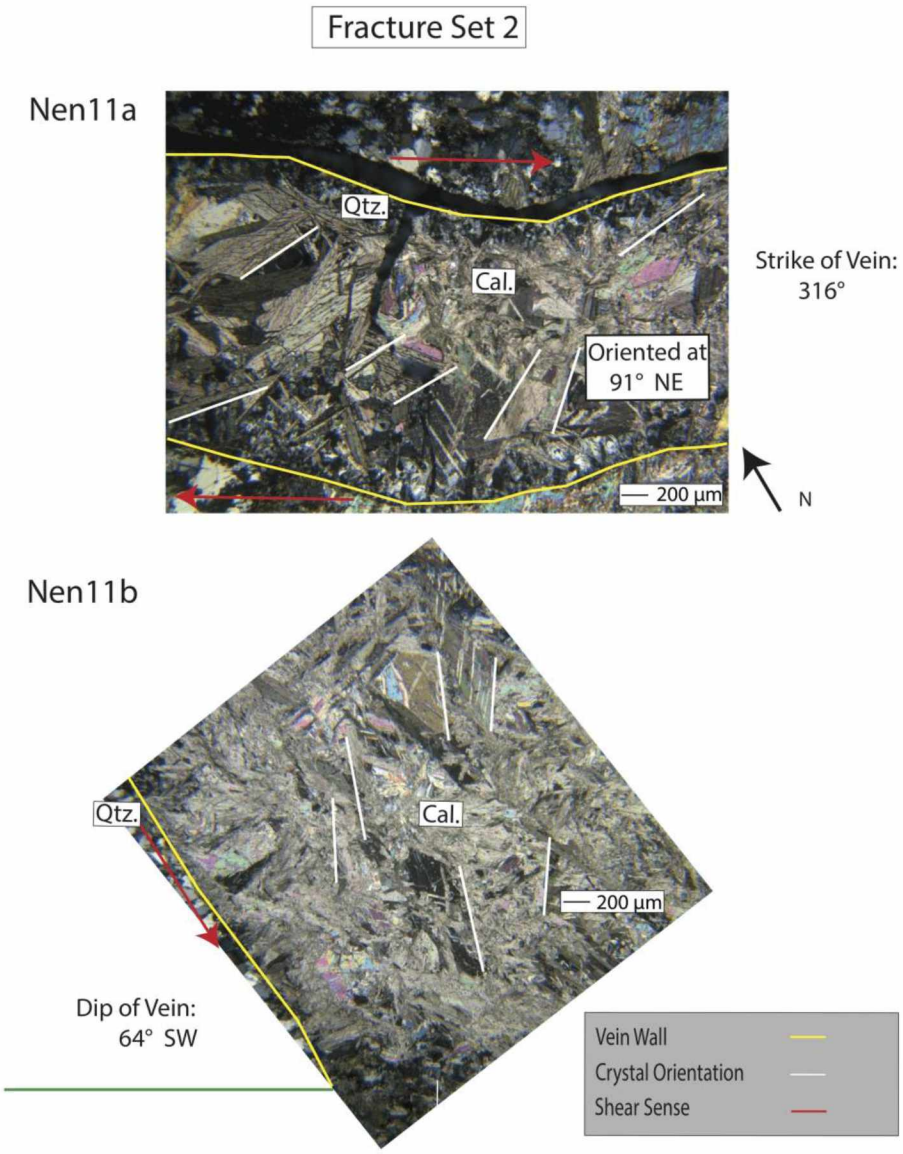

Figure 28: Thin section analysis of a F2 filled fracture from the Nenana outcrop. Thin sections for F2 show calcite shear veins with secondary quartz. Parallel to the strike of the vein, there is a right-lateral shear sense shown by the angles of crystals with respect to the vein wall. In both figures, yellow lines signify vein walls; red lines signify observed shear; white lines signify crystal orientations. Cross polarized light.

Nen11a: Thin section is oriented parallel to the strike of the vein. Crystals are angled at 40°-50° with respect to the vein wall displaying right-lateral shear.

Nen11b: Thin section is oriented parallel to the dip of the vein, crystals are chaotically oriented with some indication of dip-slip component. Crystals are angled at 30° with respect to the vein. Both type I and type II twins are present

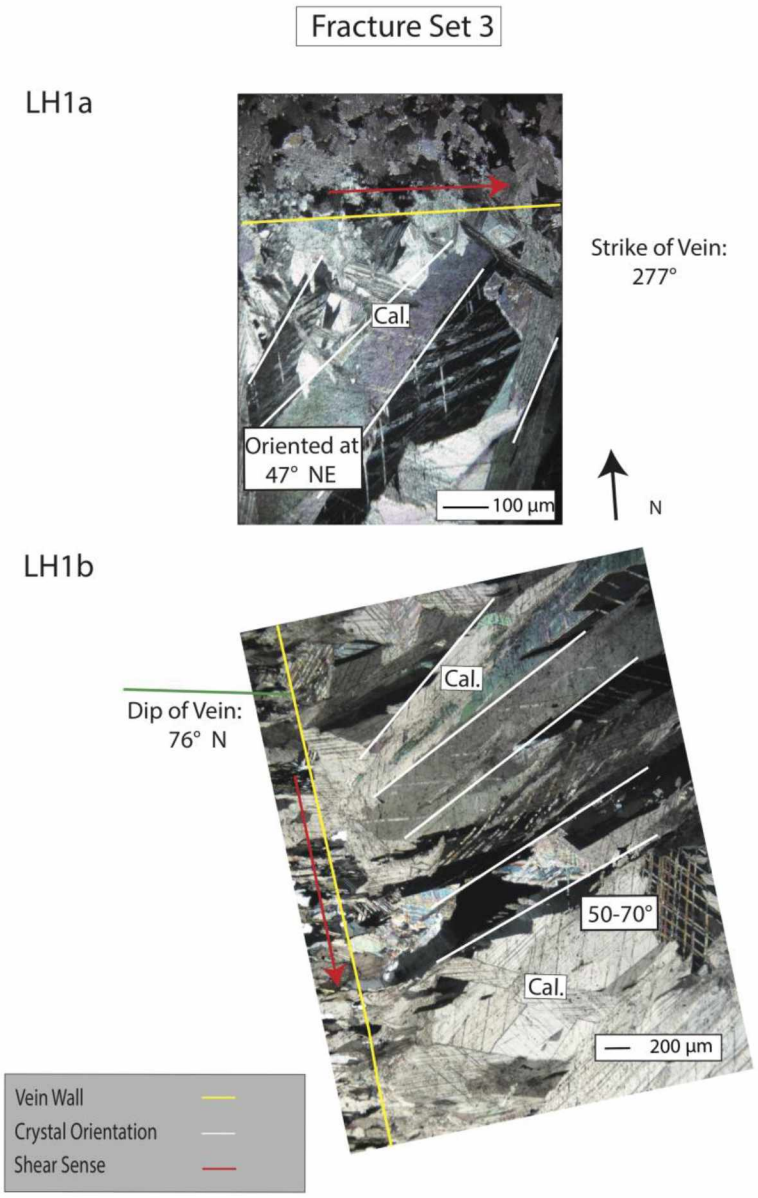

Figure 29: Thin section analysis of a F3 from the Lakloey Hill outcrop in the Fairbanks area. F3 veins are dominated by calcite crystals. In both figures, yellow lines signify vein walls; red lines signify observed shear; white lines signify crystal orientations. Cross polarized light.

LH1a: Thin section is oriented parallel to the strike of the vein. Crystals are angled at 40°-60° to the vein with right-lateral shear sense.

LH1b: Thin section is oriented parallel to the dip of the vein, crystals are angled at 50°-70° with respect to the vein wall with a dip slip component.
Both type I and type II calcite twins are present.

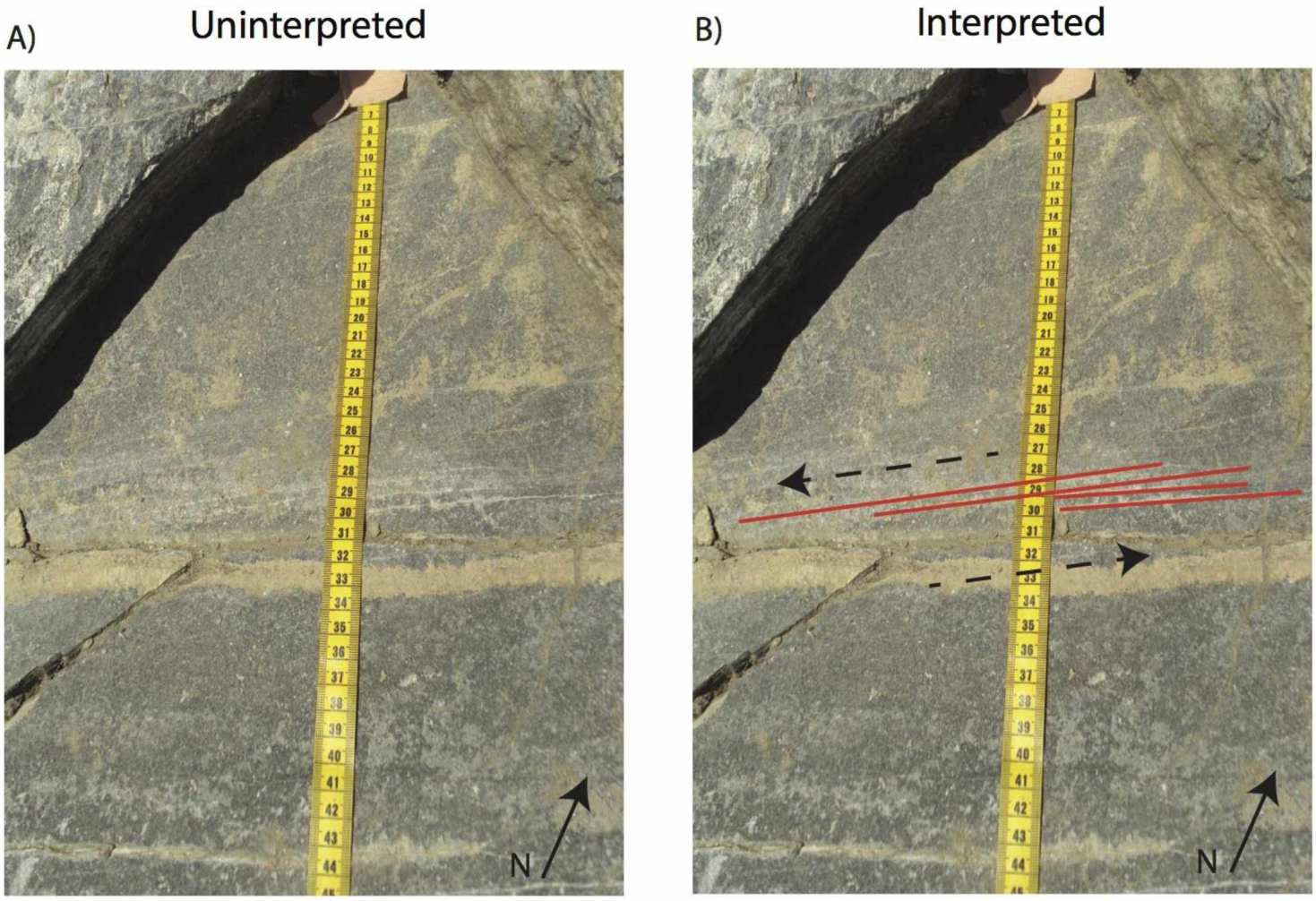

Figure 30: Shear indicators, fracture set F4 fractures, Nenana outcrop.
A) Uninterpreted F4 fractures at the Nenana outcrop
B) Interpreted en echelon fractures showing left-lateral shear sense
Scale in the figure is in cm.

Figure 31: Slickenfibres in metamorphic rock on F4 fracture faces along the Parks Highway. Slickenfibres with interpreted left-lateral shear sense on fracture faces located at the Monderosa Grill outcrop along the Parks Highway. The black arrows signify the direction of shear (left-lateral).

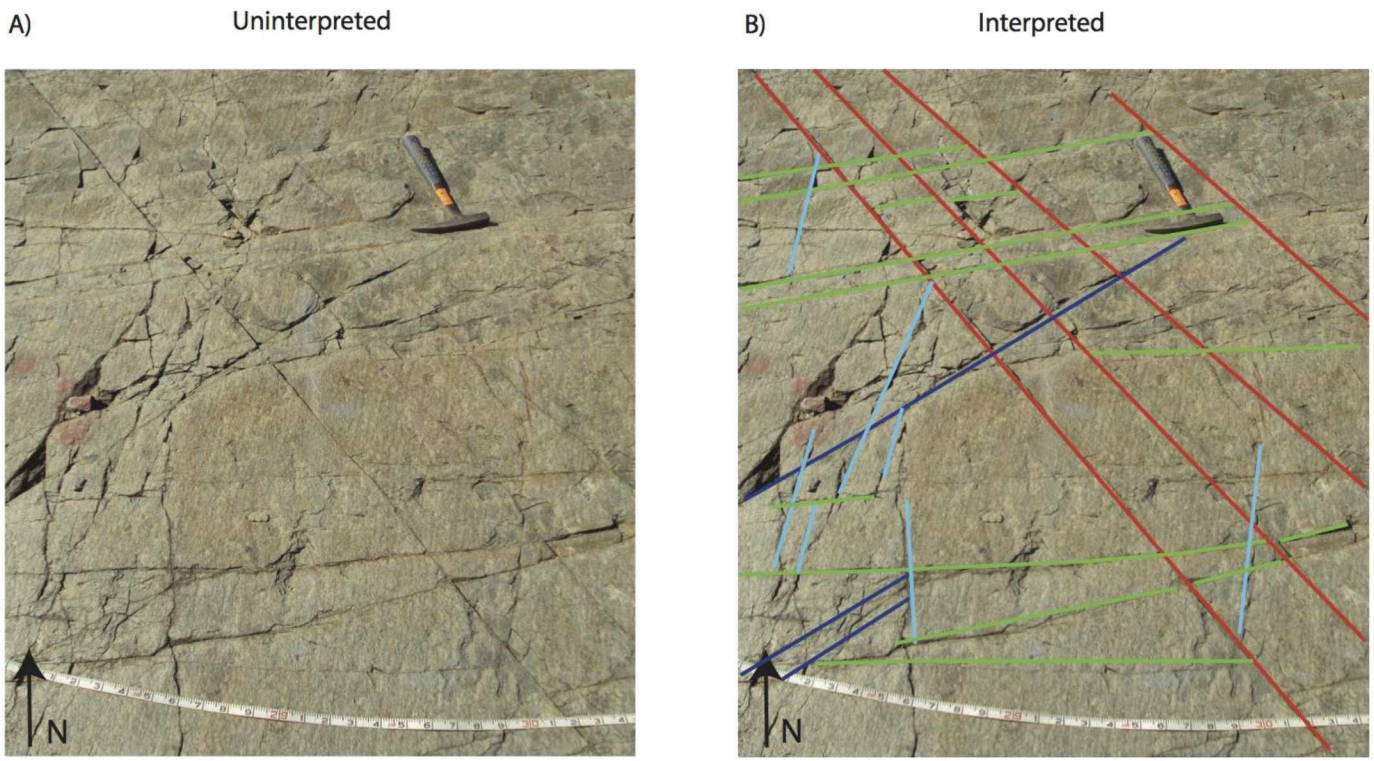

Figure 32: Cross-cutting relationships of fracture sets F2, F4, F5 and F6 at the Nenana outcrop.
A) Uninterpreted outcrop showing age relationships between fracture sets
B) Age relationships of fracture sets F2 (red), F4 (green), F5 (light blue), and F6 (dark blue).
1) F2 crosscuts all fracture sets (oldest set)
2) F4 terminates against F2
3) F5 terminates against F2 and commonly crosscuts F4

There is a rock hammer for scale.

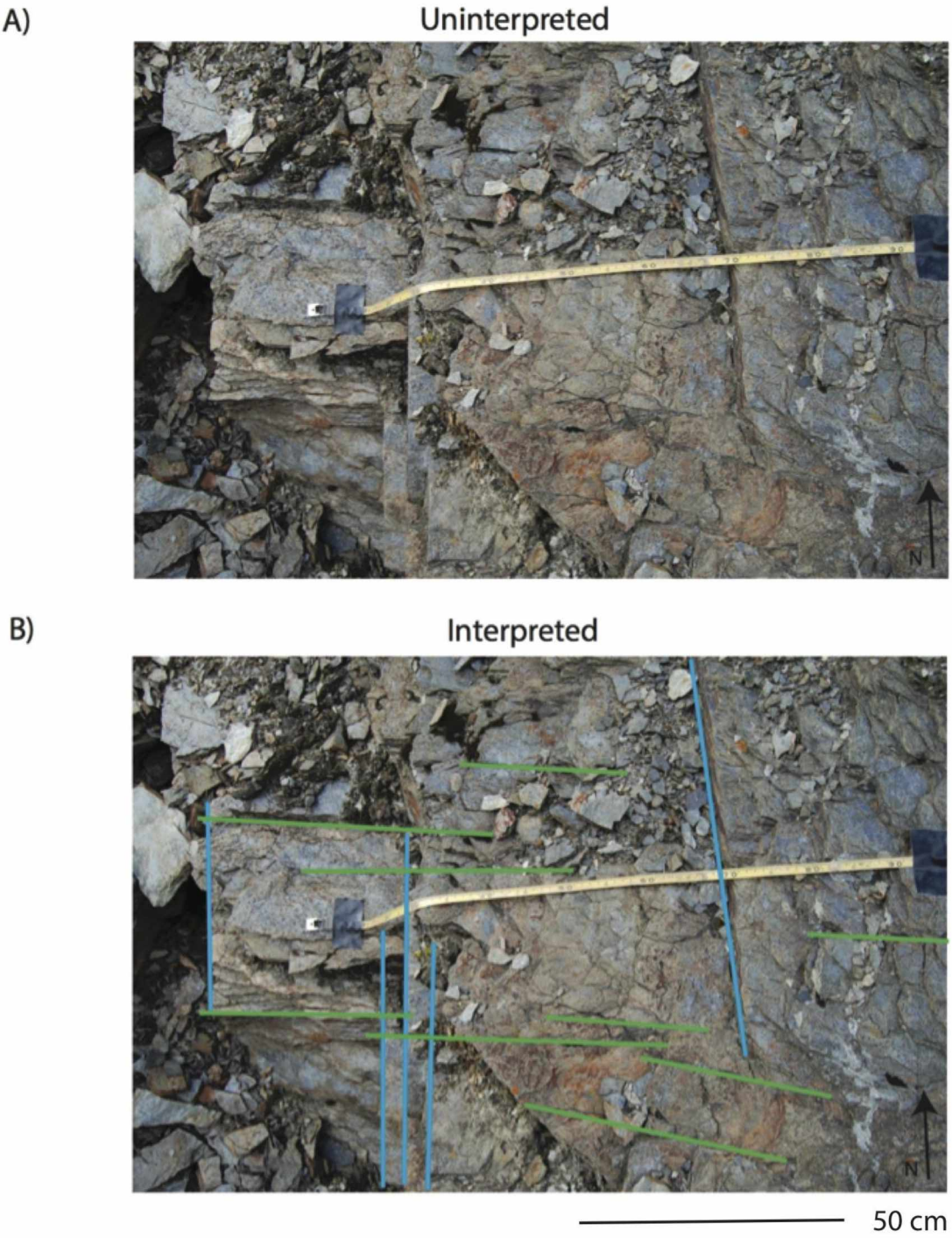

Figure 33: Cross-cutting relationships of fracture sets F4 and F5 at outcrop at MP 313 on the Parks Highway.
A) Uninterpreted outcrop showing fracture sets F4 and F5.
B) Age relationships of fracture sets F4 (green) and F5 (light blue). No clear age relationship is visible; they cross-cut each other, which is interpreted as simultaneous formation of the two sets.

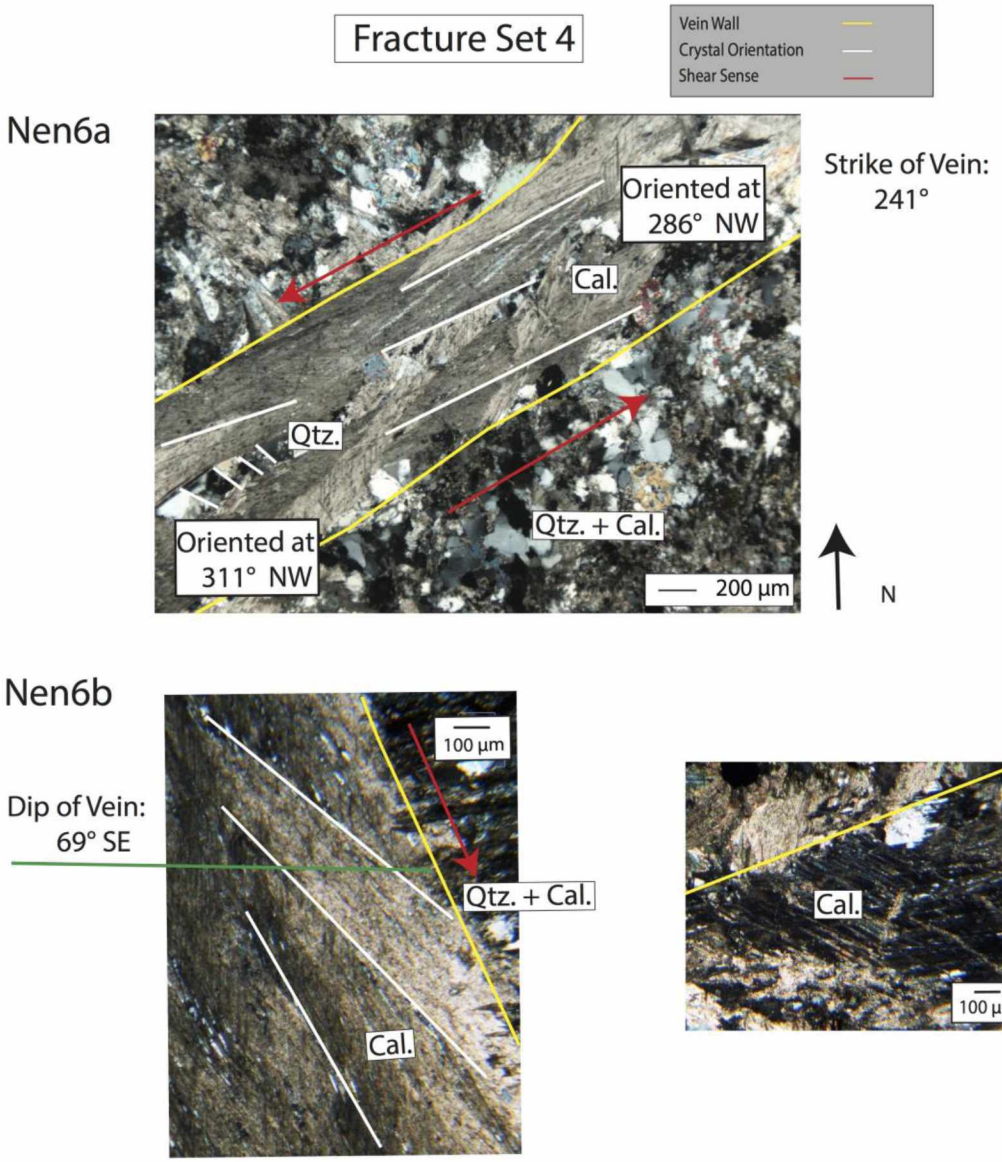

Figure 34: Thin section analysis of a F4 filled fracture from the Nenana outcrop. F4 veins are filled with calcite and secondary quartz. In both figures, yellow lines signify vein walls; red lines signify observed shear; white lines signify crystal orientations. Cross polarized light.

Nen6a: The thin section is oriented parallel to the strike of the vein. Crystals show a left-lateral shear sense. Crystals are angled at two orientations, 65°-°70, and 40°-50 with respect to the vein wall.

Nen6b: Thin section is oriented parallel to the dip of the vein. Crystals are angled at 50°-70° with respect to the vein wall and show a dip-slip component.

Both type I and type II calcite twins are present in thin section for F4.

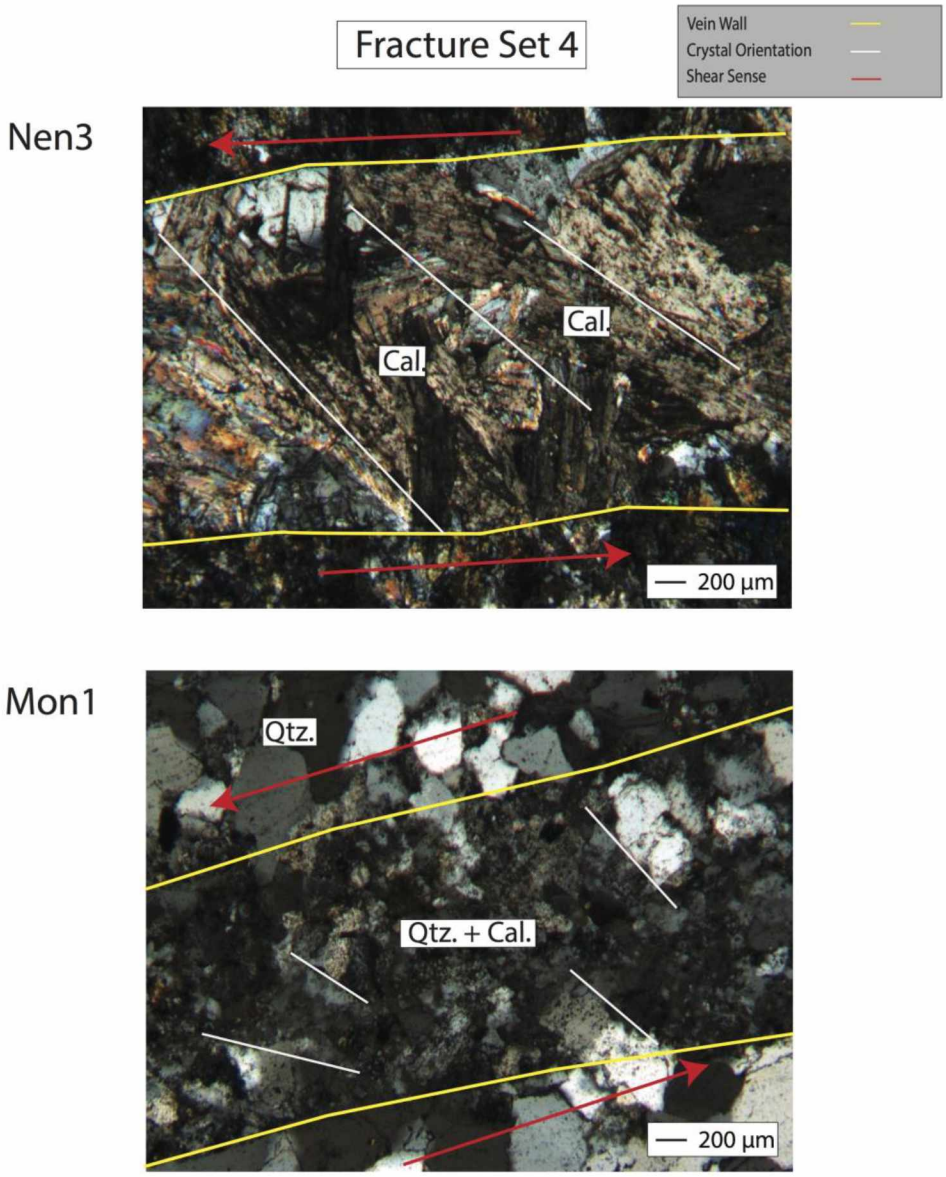

Figure 35: Thin section analysis of F4 filled fractures from the Nenana and Monderosa grill outcrops**.** Veins are characterized as calcite veins with secondary quartz. Crystals are angled with respect to the vein wall. In both figures, yellow lines signify vein walls; red lines signify observed shear; white lines signify crystal orientations. Cross polarized light.

Nen3: The thin section is oriented parallel to the strike of the vein. Crystals show a left-lateral shear sense. Crystals are angled at 40°-50° with respect to the vein wall.

Mon1= The thin section is oriented parallel to the strike of the vein. Crystals show a left-lateral shear sense and are angled at 40°-50° with respect to the vein wall.

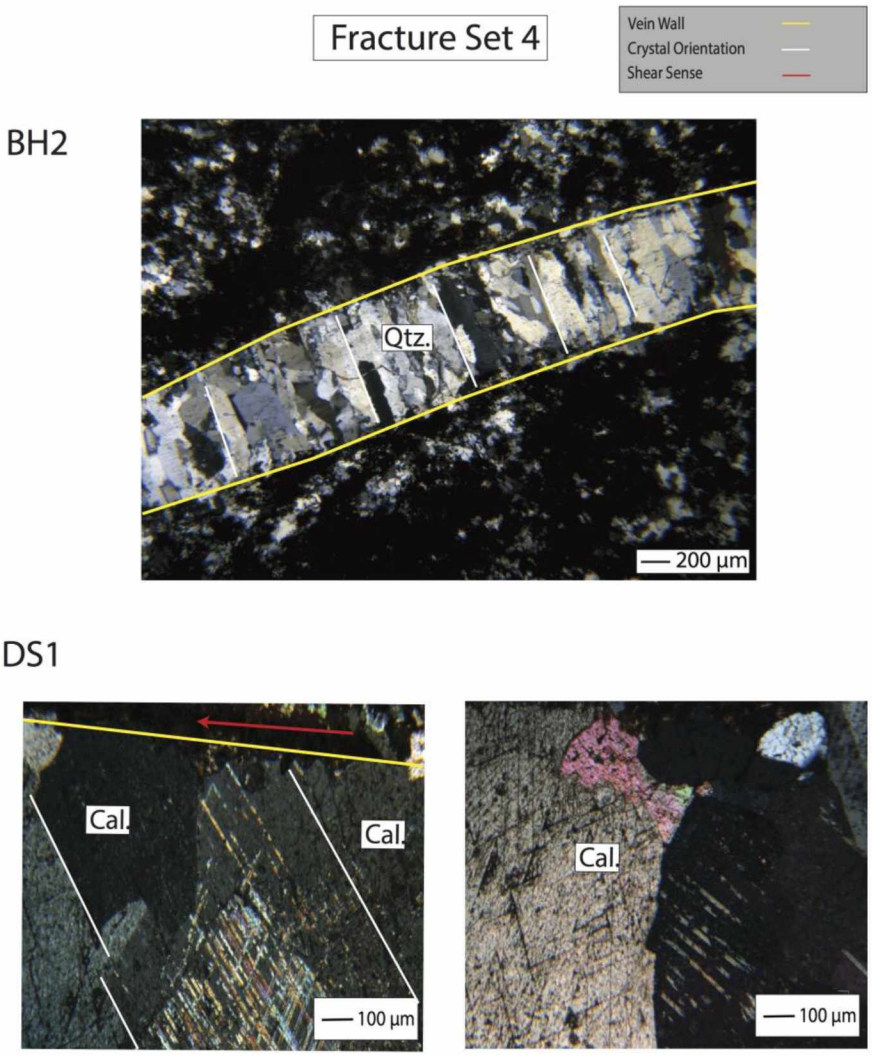

Figure 36: Thin section analysis of F4 filled fractures from the Birch Hill and Duckering Stairs outcrops. Veins are characterized as calcite veins with secondary quartz. In both figures, yellow lines signify vein walls; red lines signify observed shear; white lines signify crystal orientations. Cross polarized light.

BH2: The thin section is oriented parallel to the strike of the vein. Pictured is a quartz vein from the Birch Hill outcrop showing an extensional history to the vein wall with crystals perpendicular to the vein wall.

DS1: The thin section is oriented parallel to the strike of the vein. A calcite vein from the Duckering Stairs outcrop shows crystals oriented with respect to the vein wall. Crystals show a left-lateral shear sense.

Both type I and II calcite twins are present in F4 veins.

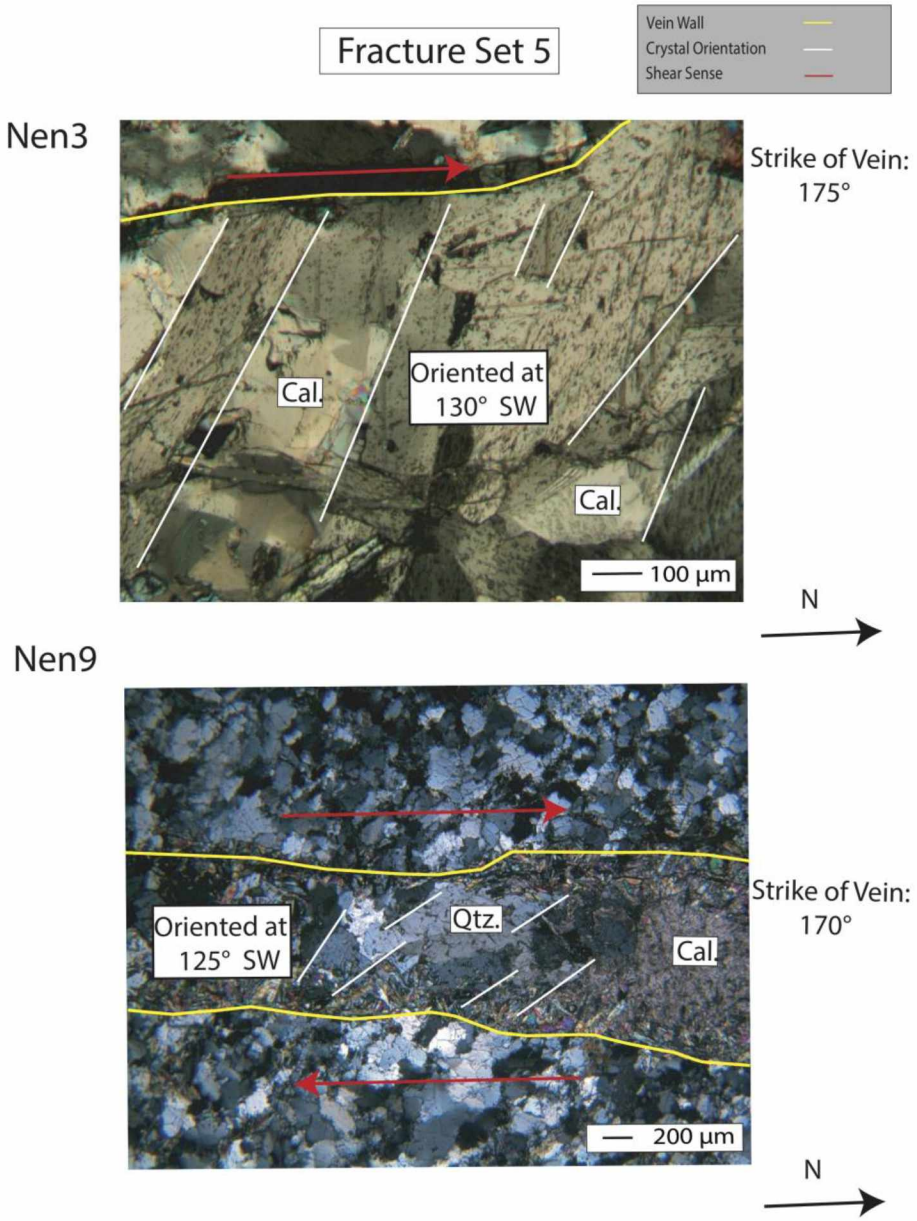

Figure 37: Thin section analysis of F5 filled fractures at the Nenana outcrop. Veins are characterized as calcite veins with secondary quartz. In both figures, yellow lines signify vein walls; red lines signify observed shear; white lines signify crystal orientations. Cross polarized light.

Nen3: The thin section is oriented parallel to the strike of the vein. Crystals are oriented at an angle with respect to the vein wall. Crystals are showing a right-lateral shear sense.

Nen9: The thin section is oriented parallel to the strike of the vein. Crystals are oriented at an angle with respect to the vein wall and show a right-lateral shear sense.

In F5 filled fractures, both type I and II calcite twins are present.

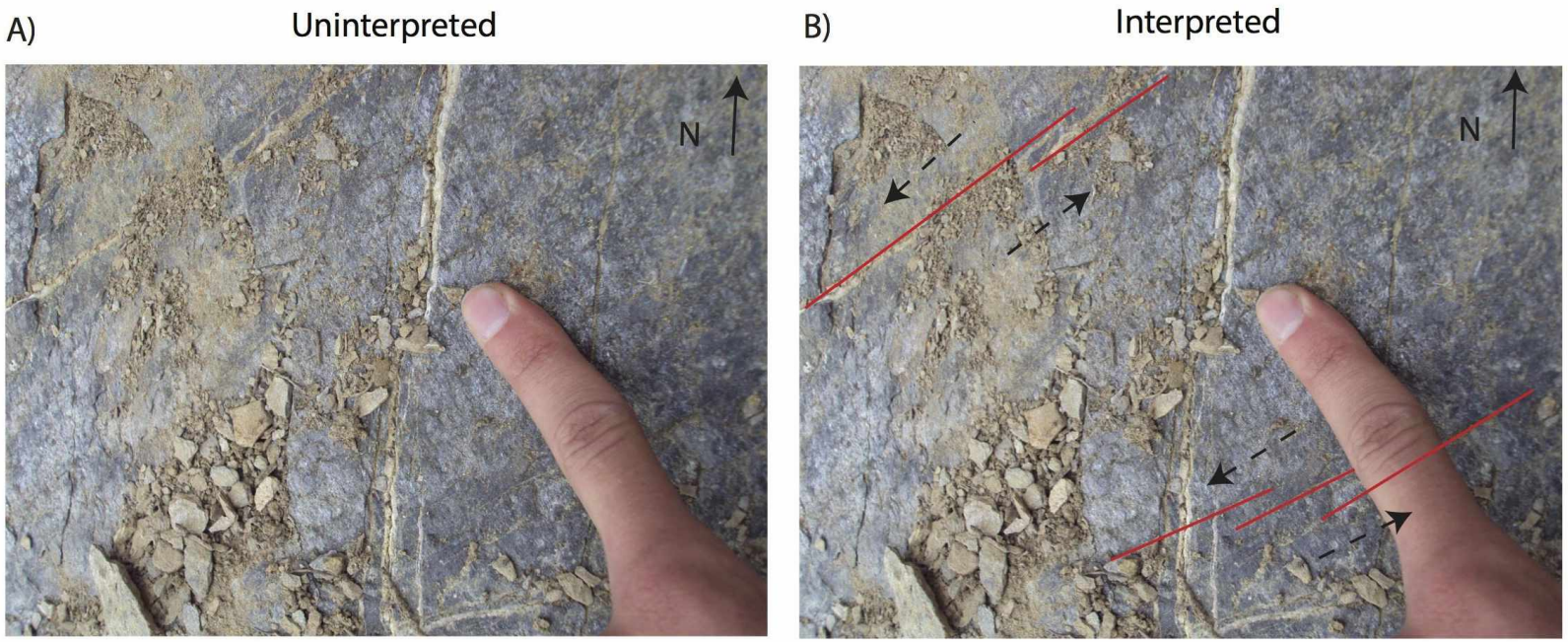

Figure 38: Shear indicators, F6 fractures, Nenana outcrop
A) Uninterpreted F6 fractures
B) Interpreted en echelon fractures showing left-lateral shear. In addition, an example of fracture set F5 is shown (N-striking fracture).

The finger is used for scale.

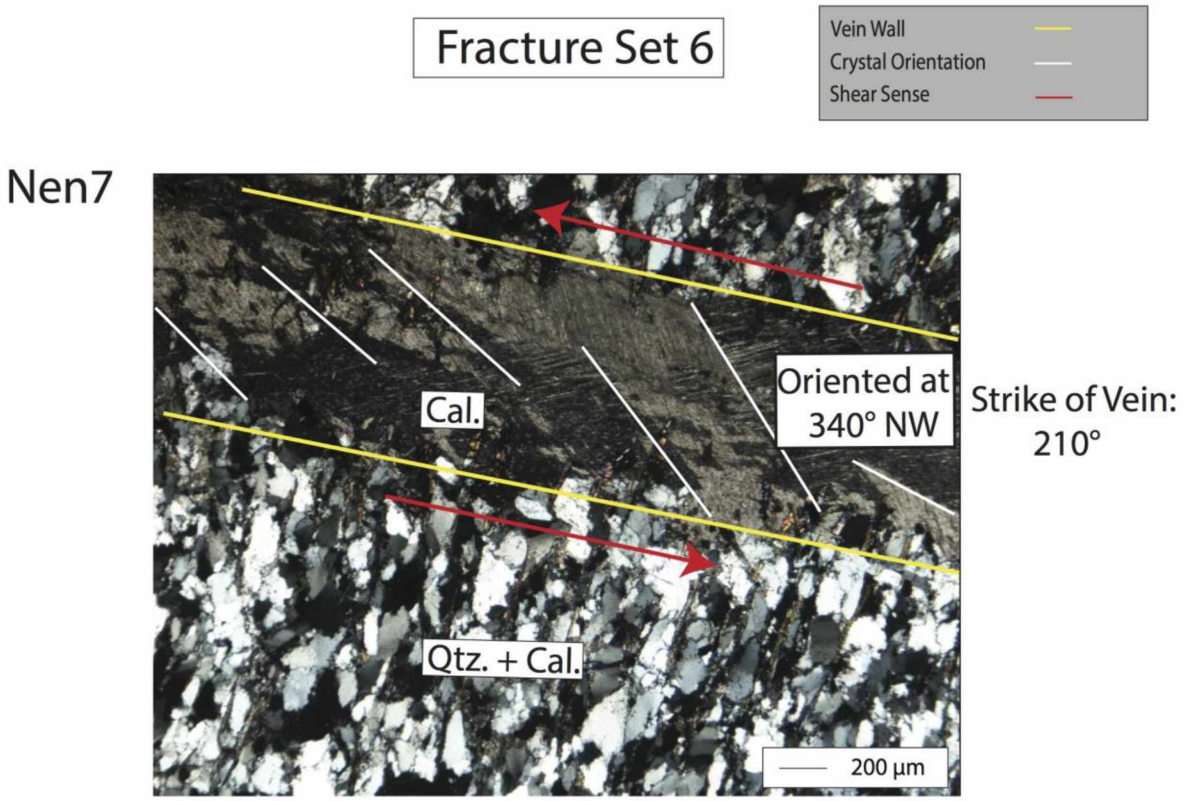

Figure 39: Thin section analysis of a F6 filled fracture at the Nenana outcrop. Calcite crystals dominate F6 veins with a left-lateral shear sense parallel to the strike of the vein. Only type I twins are present in this thin section. Yellow lines signify vein walls; red lines signify observed shear; white lines signify crystal orientations. Cross polarized light.

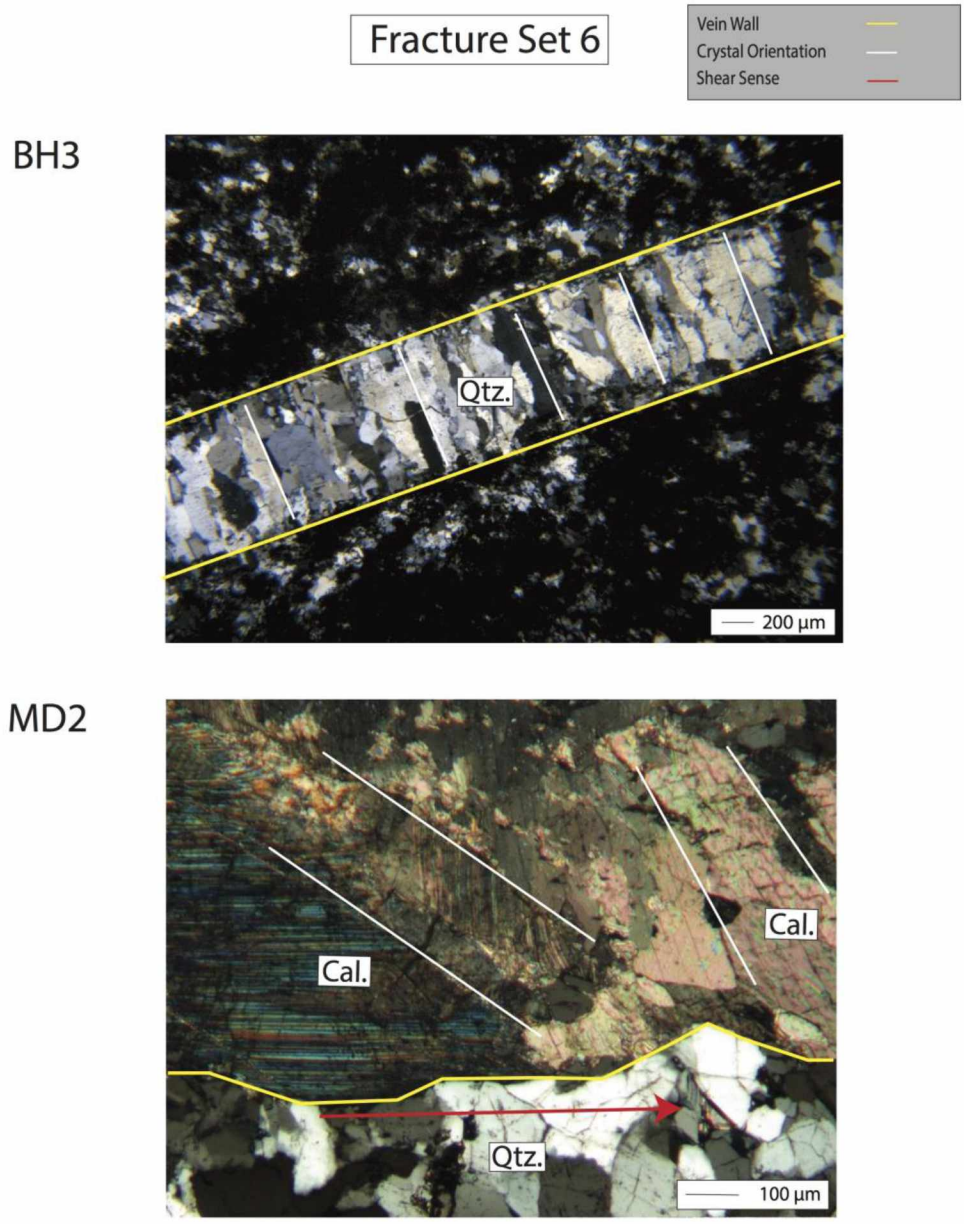

Figure 40: Thin section analysis of F6 filled fractures from the Birch Hill and Murphy Dome outcrops. In both figures, yellow lines signify vein walls; red lines signify observed shear; white lines signify crystal orientations. Cross polarized light.

BH3: The thin section is oriented parallel to the strike of the vein. The vein is from the Birch Hill outcrop and shows a strong extensional component with crystals perpendicular to the vein wall.

MD2: The thin section is oriented parallel to the strike of the vein. The sample is from the Murphy Dome outcrop and calcite crystals dominate veins and show a left-lateral shear sense.

Both type I and type II twins are present

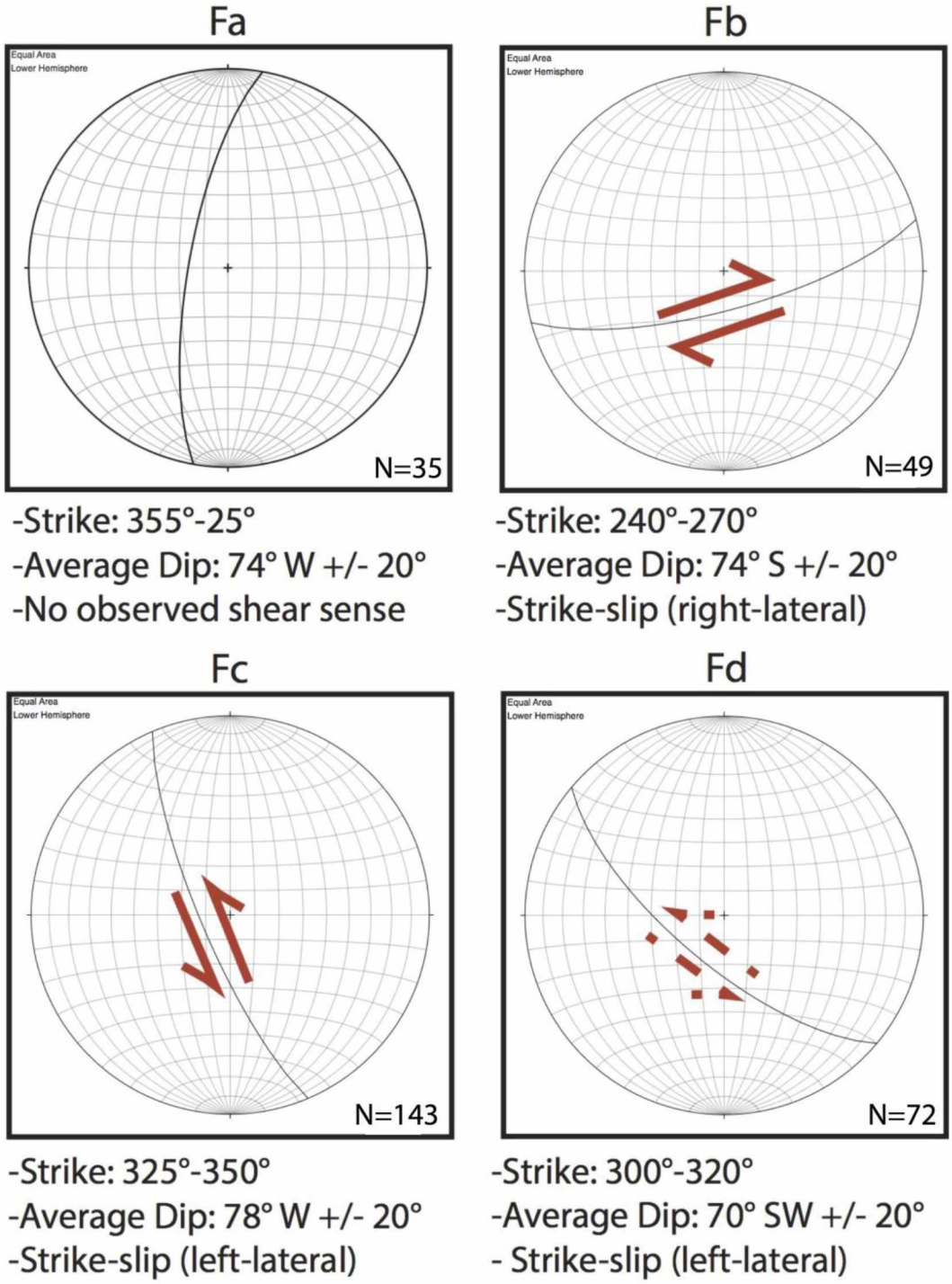

Figure 41: Summary of fracture sets in Domain II. A summary of fracture orientations, dip directions, and sense of movement for fracture sets in the Healy area. Red arrows document observed slip from both field and thin section data for each set.

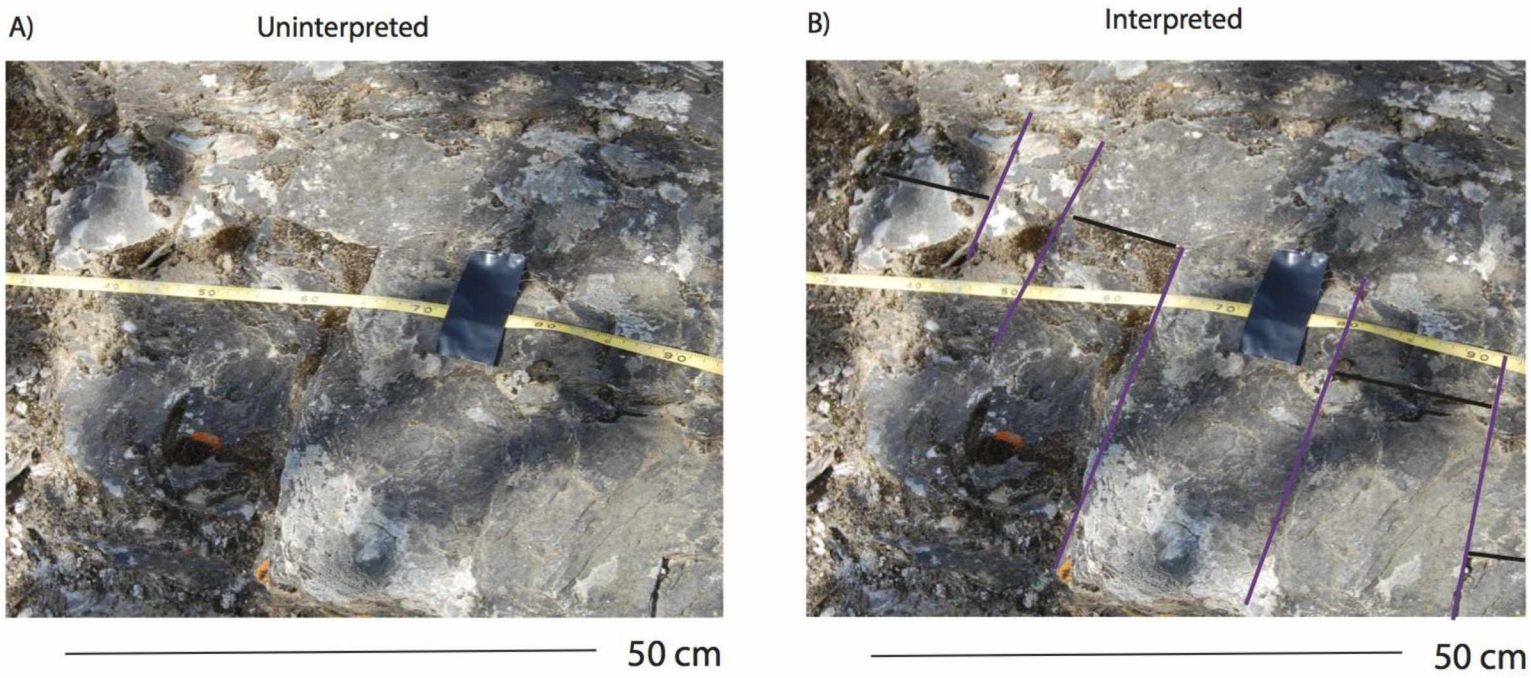

Figure 42: Cross-cutting relationships of Healy area fracture sets (Fa + Fb).
A) Uninterpreted picture taken at the Dragonfly Creek outcrop near Healy
B) Fa (purple) and Fb (black) are both found at this location. Fb terminates against Fa

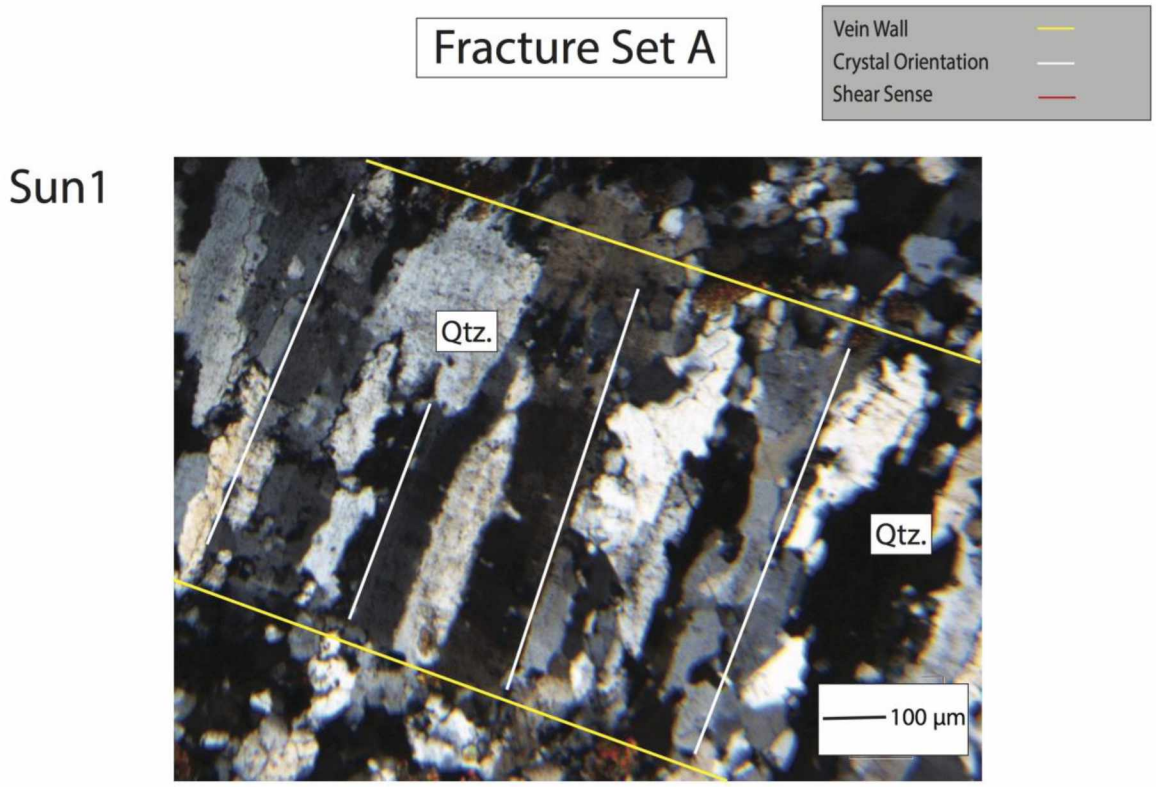

Figure 43: Thin section analysis of a Fa filled fracture from the Suntrana outcrop. Vein character is extensional with quartz crystals perpendicular to the vein wall showing no clear shear indictors. Crystals are blocky-elongate in shape and may extend across the entire vein. Thin section Sun1 is oriented parallel to the strike of the vein. Yellow lines signify vein walls; red lines signify observed shear; white lines signify crystal orientations. Cross polarized light.

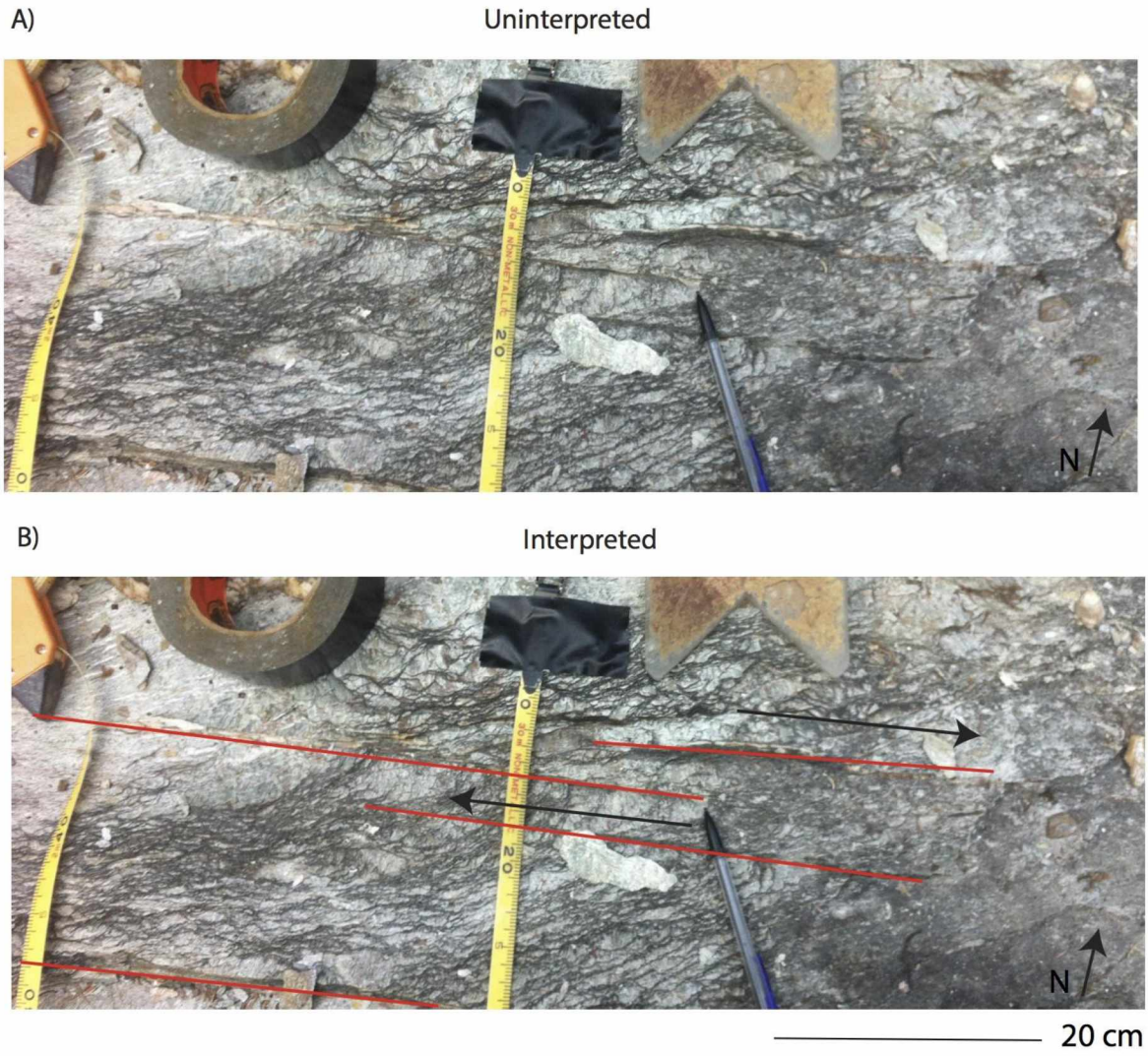

Figure 44: Shear indicators of Fb fracture sets at the Fox Creek outcrop in the Healy area. Red lines signify natural fractures and black arrows show interpreted shear.
A) Uninterpreted Fb fractures
B) En echelon fractures (red) interpreted as showing right-lateral shear sense

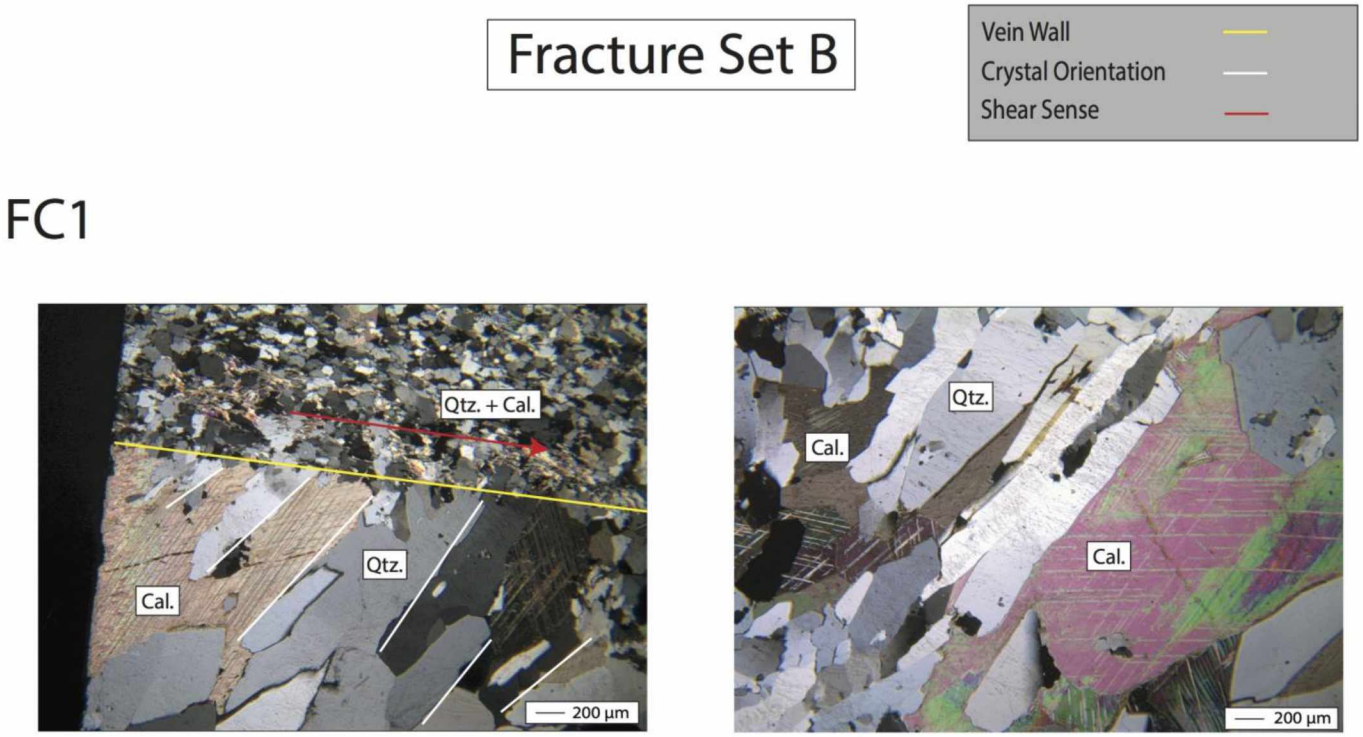

Figure 45: Thin section analysis of an Fb filled fracture from the Fox Creek outcrop in the Healy area. The thin section is oriented parallel to the strike of the vein. Fb veins have both quartz and calcite crystals angled with respect to the vein wall showing a right-lateral shear sense. Both type II and III calcite twins are present in thin section. Cross polarized light.

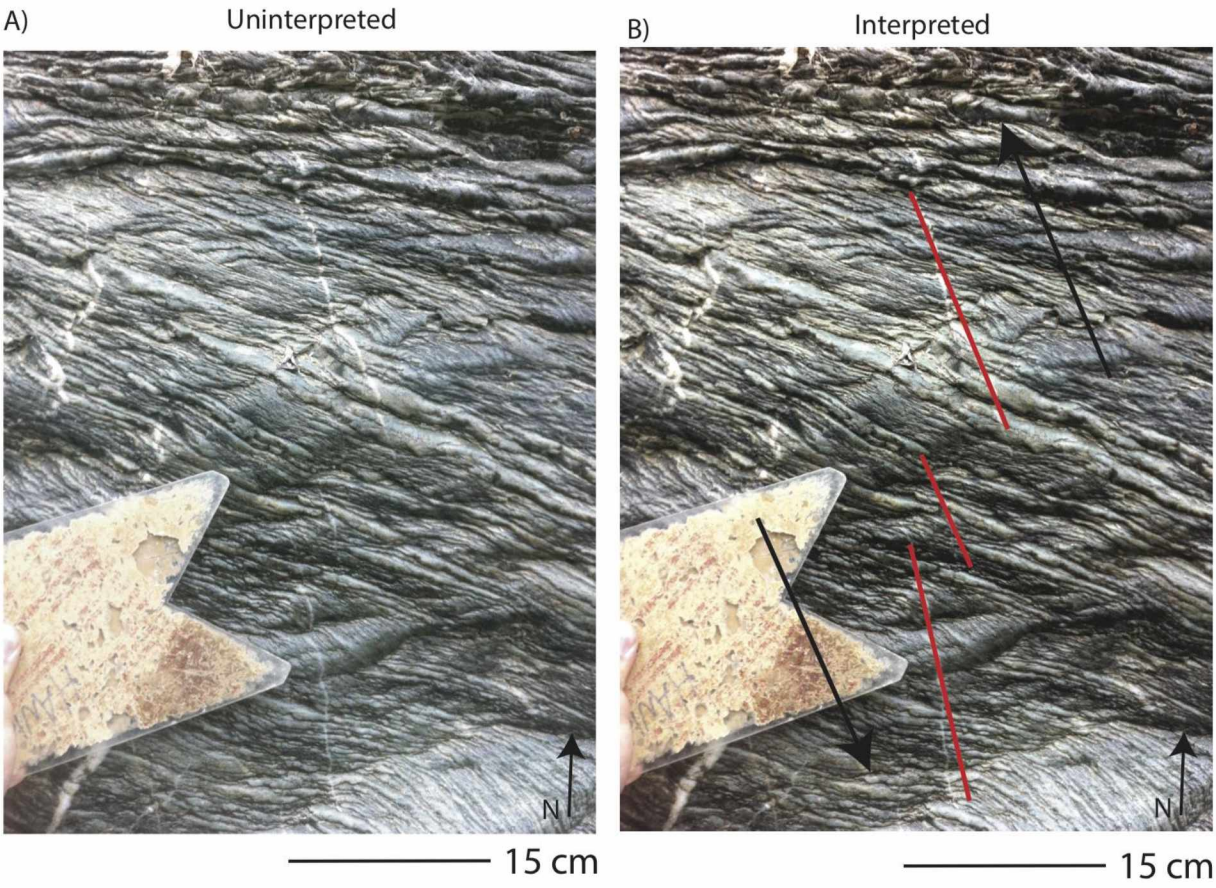

Figure 46: Shear indicators of Fc fractures from the Fox Creek outcrop in the Healy area. Red lines signify natural fractures while black arrows show interpreted shear sense.
A) Uninterpreted Fc fractures at the Fox Creek outcrop in the Healy area
B) En echelon fractures interpreted as showing left-lateral shear sense

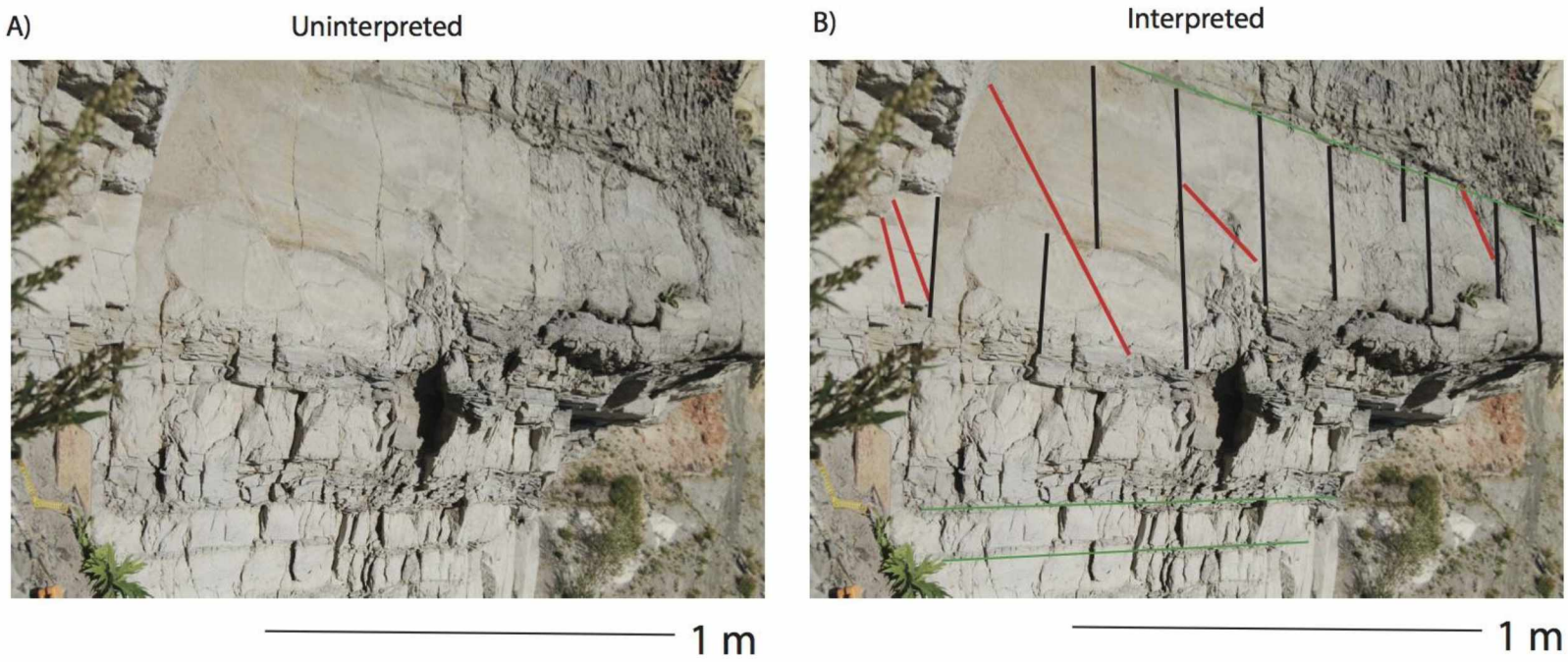

Figure 47: Cross-cutting relationships of Healy area fracture sets (Fb + Fc) at the Suntrana outcrop.
A) Uninterpreted siltstone outcrop at the Suntrana outcrop near Healy (Fig. 17)
B) Fb (black) and Fc (red) are both found at this location. Fc terminates against Fb. Some bedding planes are shown with green lines

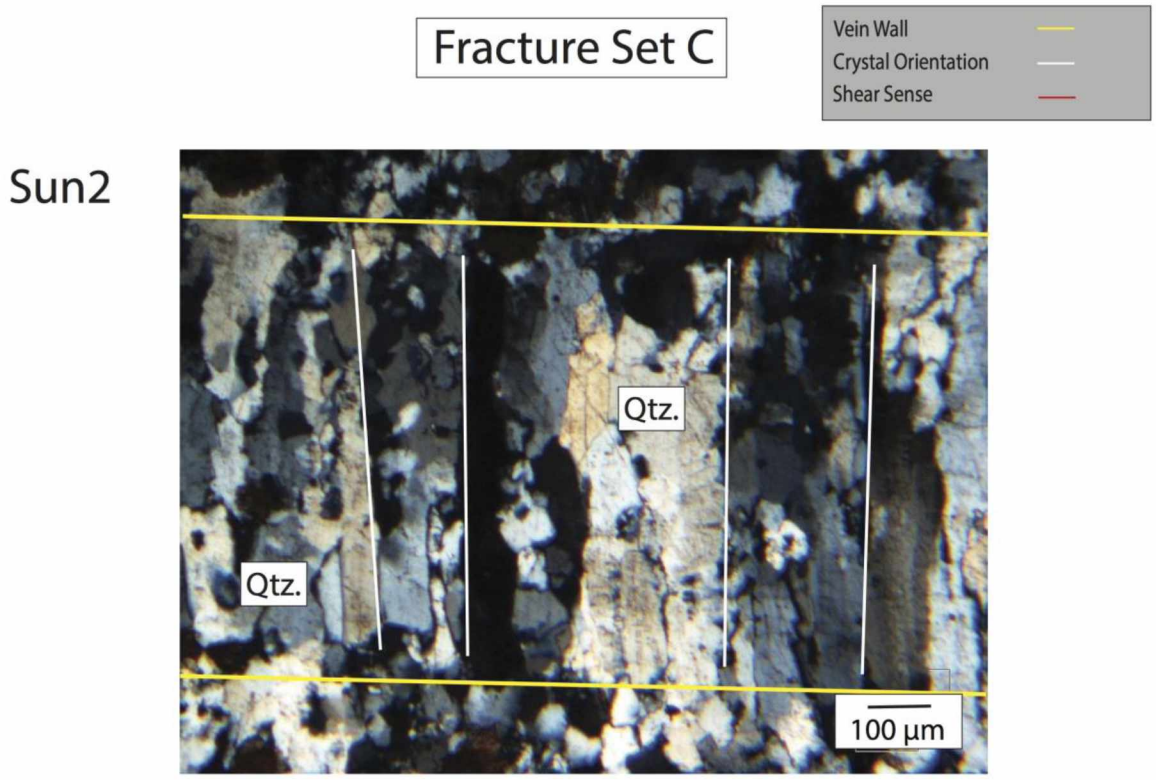

Figure 48: Thin section analysis of an Fc filled fracture from the Suntrana outcrop in the Healy area. Thin section Sun2 is oriented parallel to the strike of the vein. Fc veins can be characterized as extension veins with quartz crystals perpendicular to the vein wall showing no clear shear indictors. Crystals are blocky-elongate in shape and can extend across the entire vein. Cross polarized light.

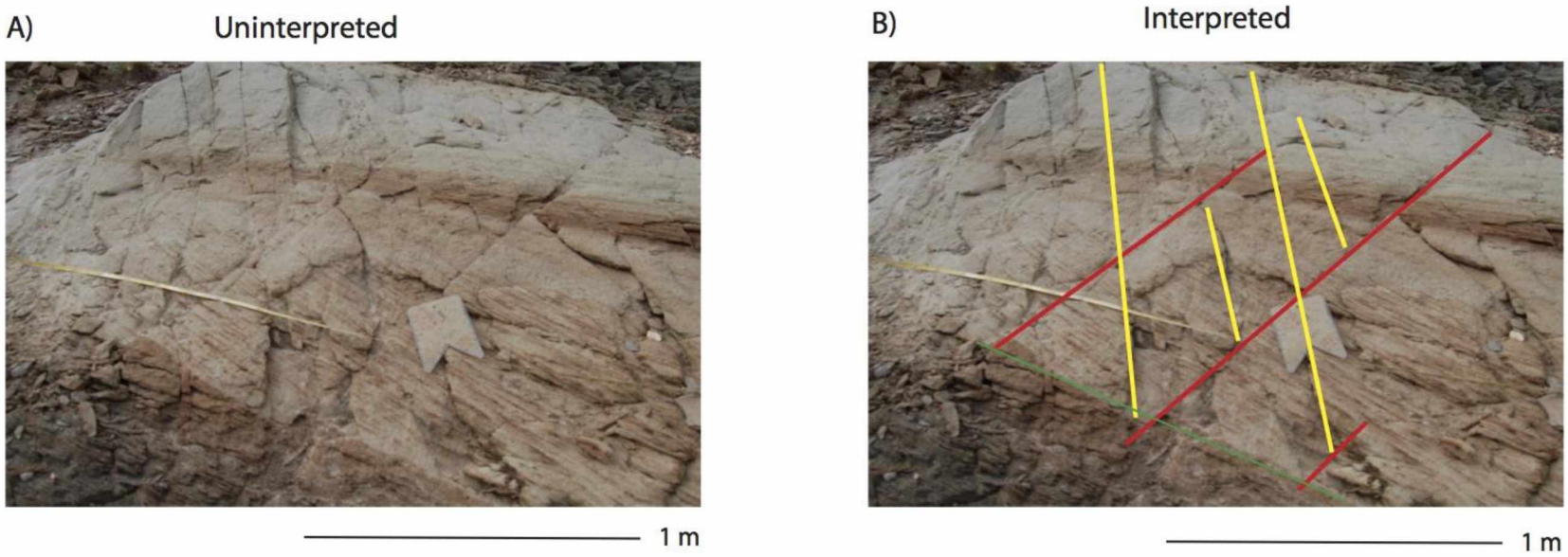

Figure 49: Cross-cutting relationships of Healy area Fracture Sets (Fc + Fd) at the Suntrana outcrop.
A) Uninterpreted outcrop located at the Suntrana outcrop near Healy
B) Fc (red) and Fd (yellow) in cross-bedded, oxidized sandstone. Fd is interpreted to terminate against Fc. The green line represents average bedding plane.

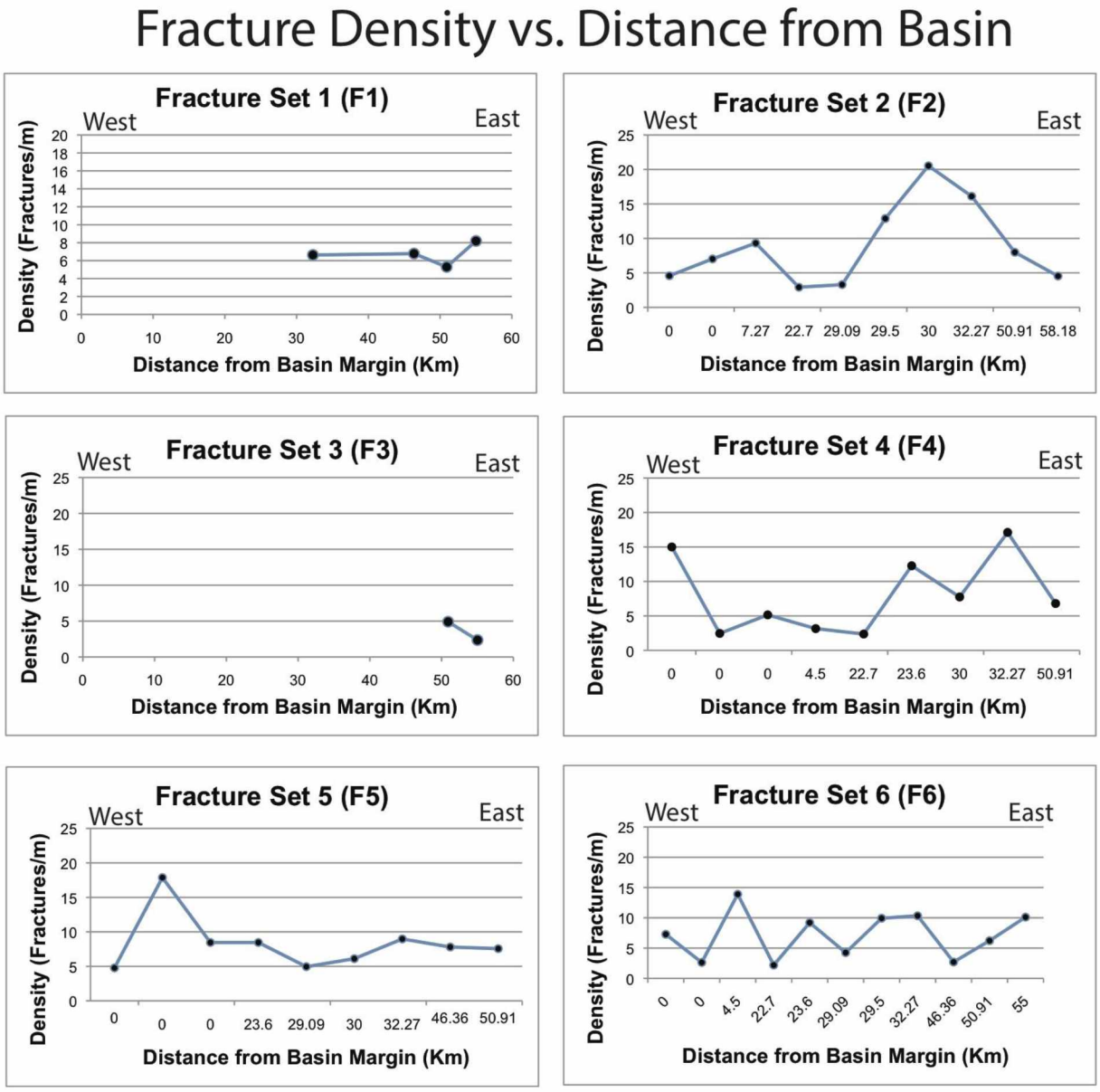

Figure 50: Density of fractures within fracture sets F1, F2, F3, F4, F5 and F6 vs. distance from eastern margin of Nenana basin. The density of fractures within each of the six fracture sets observed in the Fairbanks, Parks Highway and Nenana areas are plotted with respect to the distance from the eastern margin of the Nenana Basin, as defined by the Minto fault. For fracture sets F3 and F4, fracture density increases toward the margin of the basin.

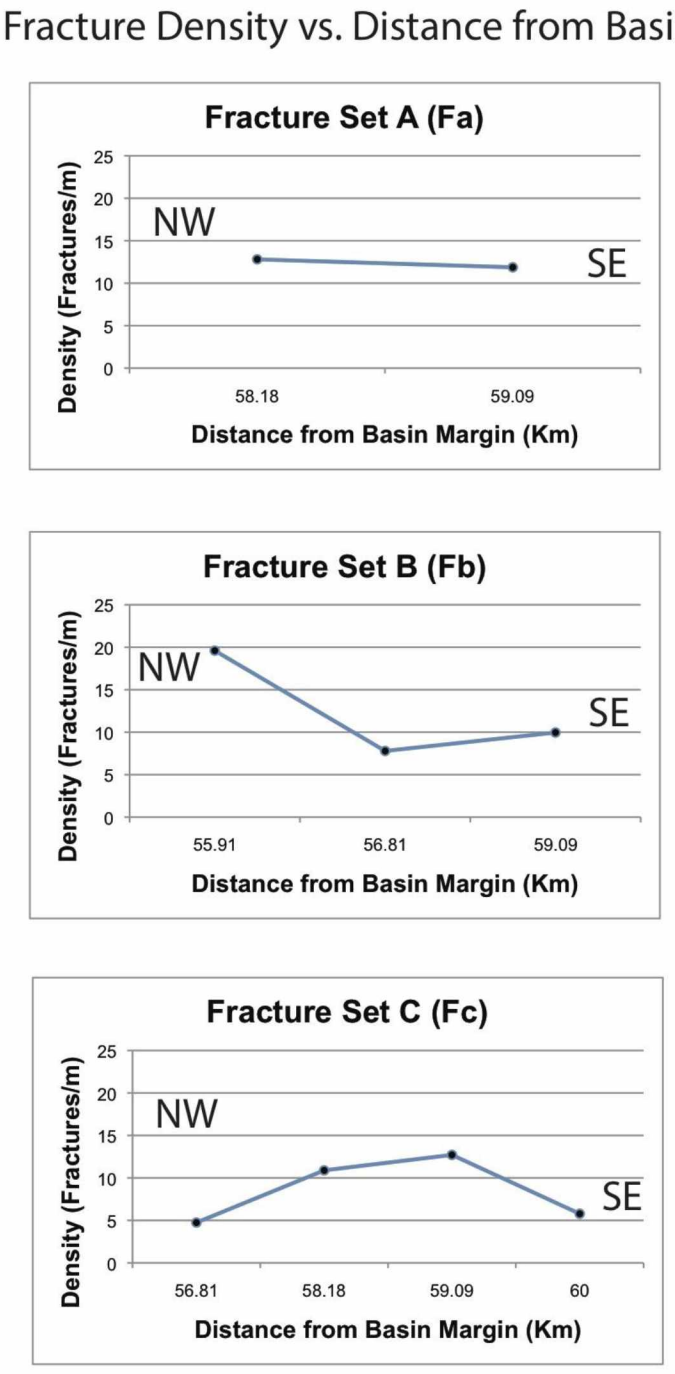

6

Figure 51: Density of fractures within fracture sets Fa, Fb, Fc, and Fd, vs. distance from eastern margin of Nenana Basin. The density of fractures within each of the four fracture sets observed in the Healy area are plotted with respect to the distance from the eastern margin of the Nenana Basin, as defined by the Minto fault. The distances are represented in a NW-SE transect. For some fracture sets (Fa and Fb), fracture densities increase toward the margin of the basin and northward.

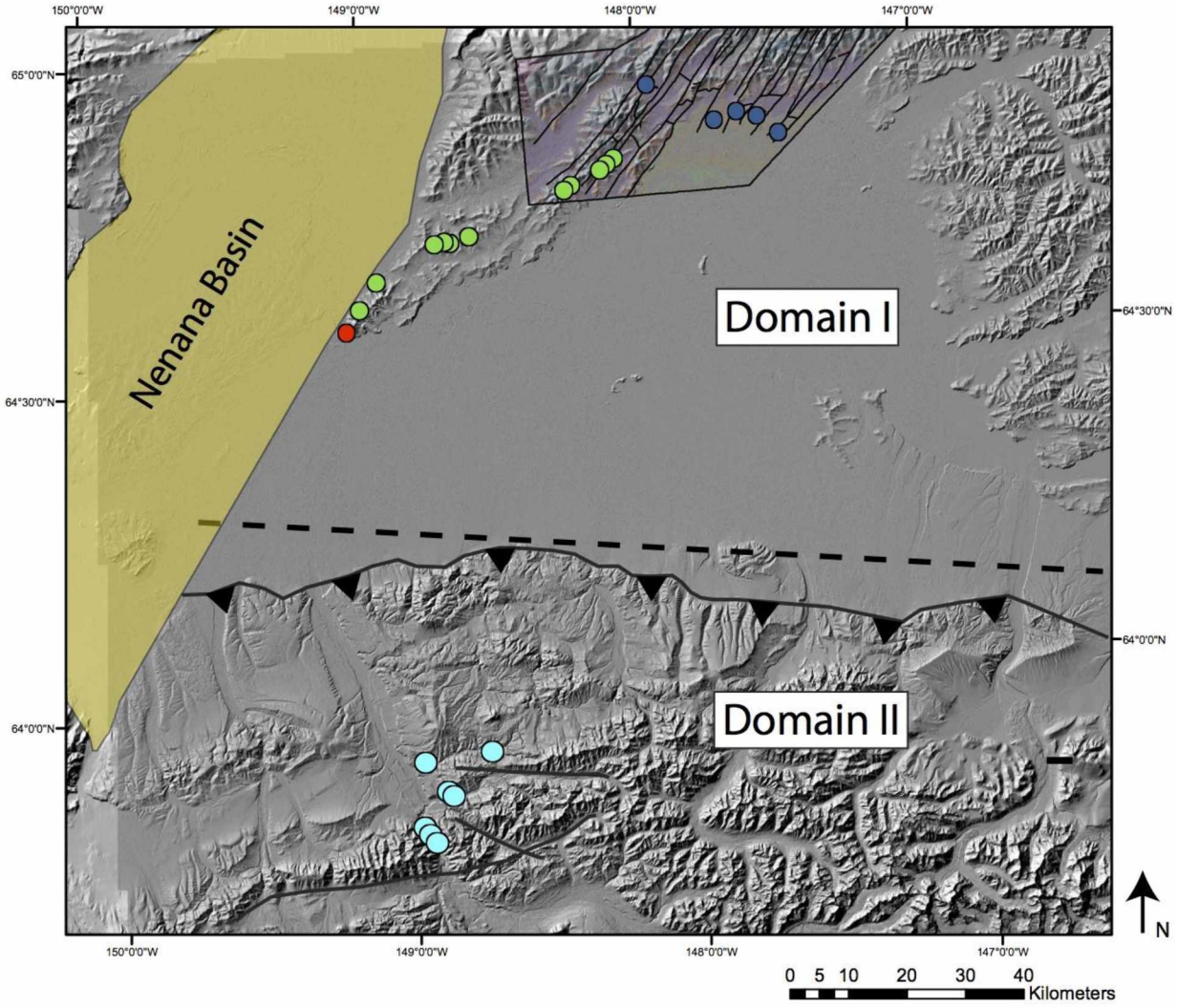

Figure 52: Structural domains. Domain I= Fairbanks, Parks Highway and Nenana areas; Domain II= Healy Area. Domains were defined by the structural elements and fracture characteristics. Domain I is characterized by NE-SW striking high-angle faulting and active seismicity. Its limit to the south is constrained by active seismicity. Domain II is characterized by the Northern Foothills fold-and-thrust belt and its extent northward is bounded by the Tanana basin and active seismicity of Domain I.

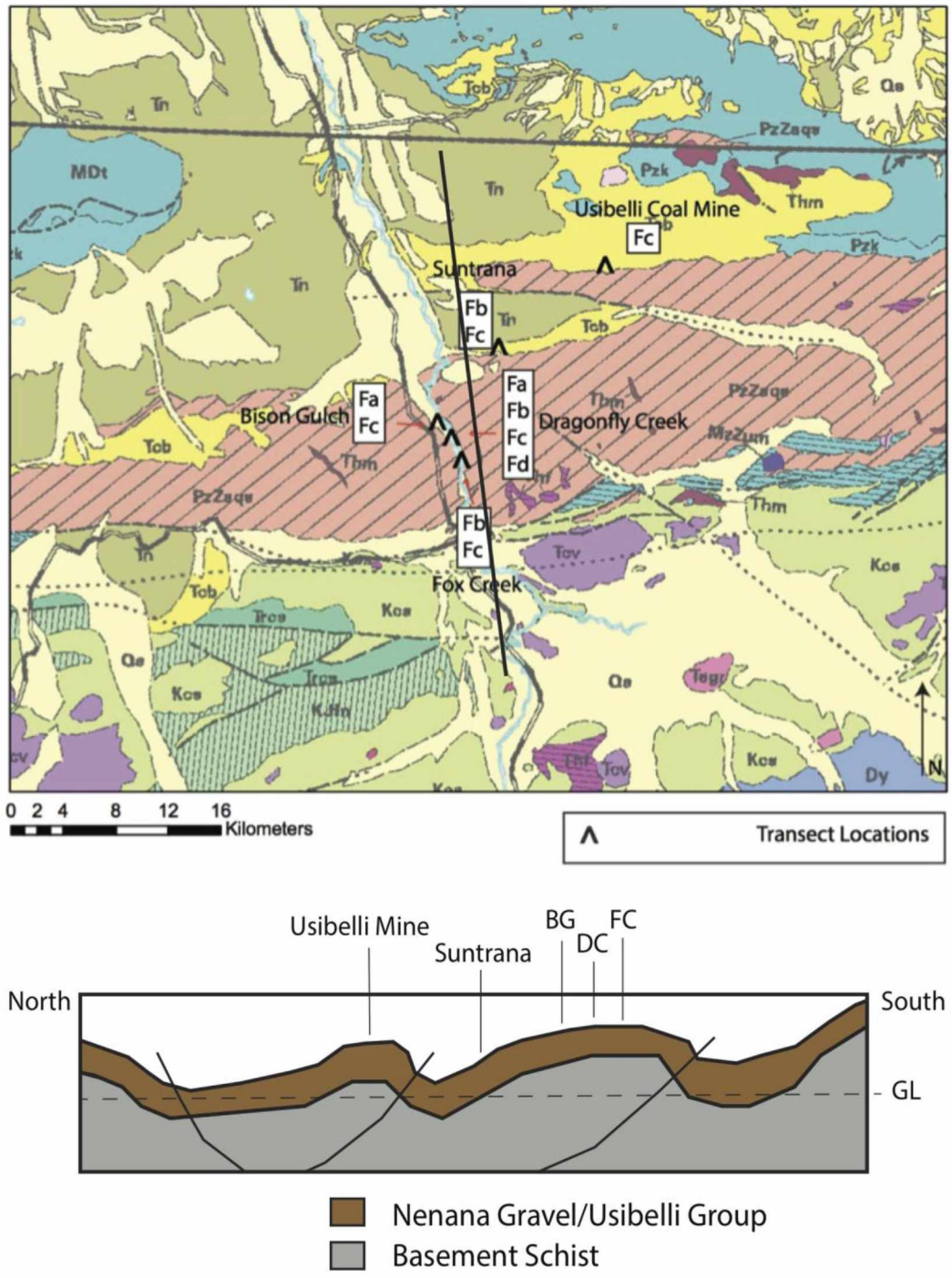

Figure 53: Cross-section of the Northern Foothills fold-and-thrust belt in the Healy Area. The line of transect is shown in black on the map. Field locations are on the fold axes and limbs of the E-trending folds in Domain II, in both sedimentary and basement rocks. BG= Bison Gulch; DC= Dragonfly Creek; FC= Fox Creek.

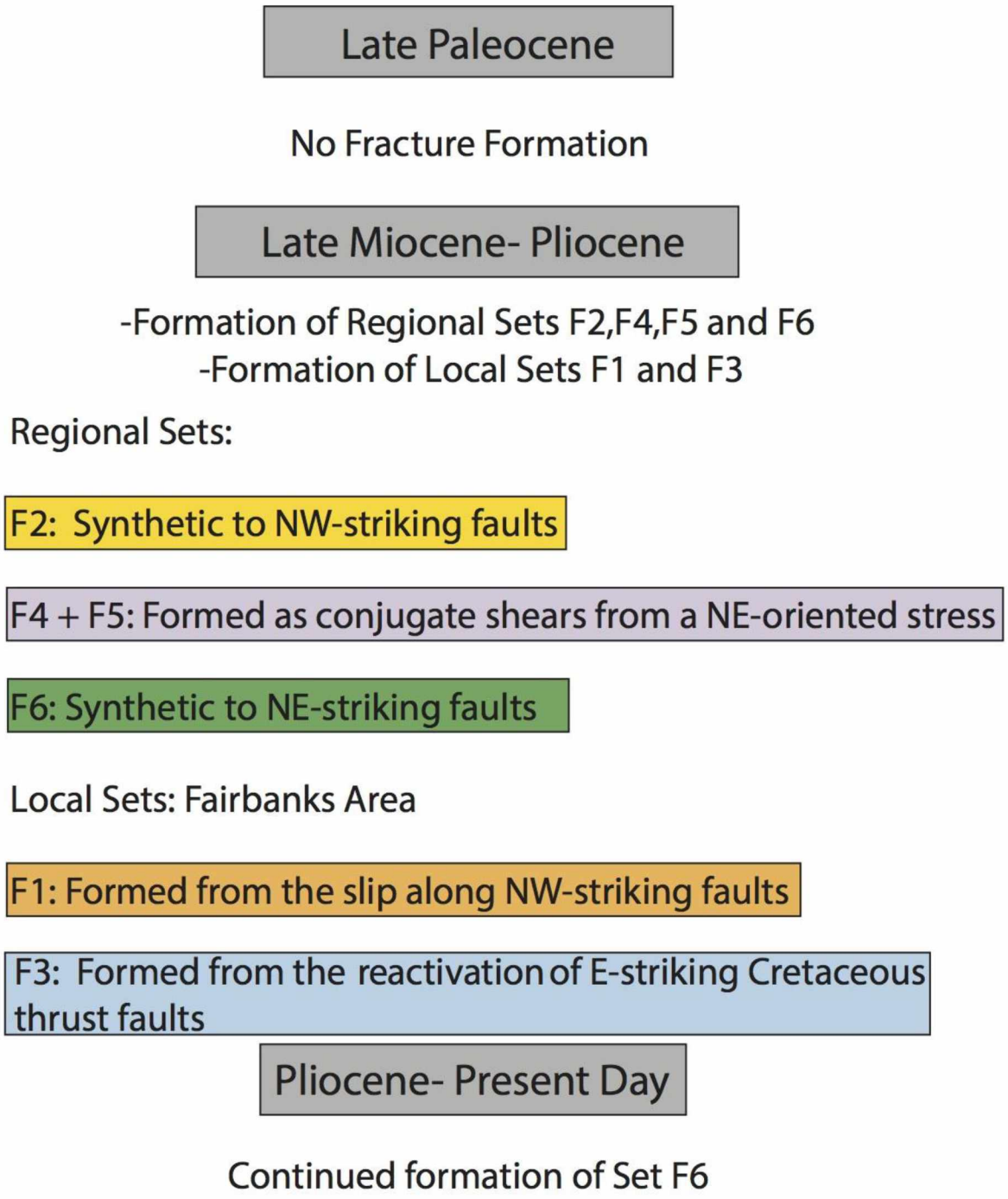

Fig 54: Summary of fracturing history in Domain I.

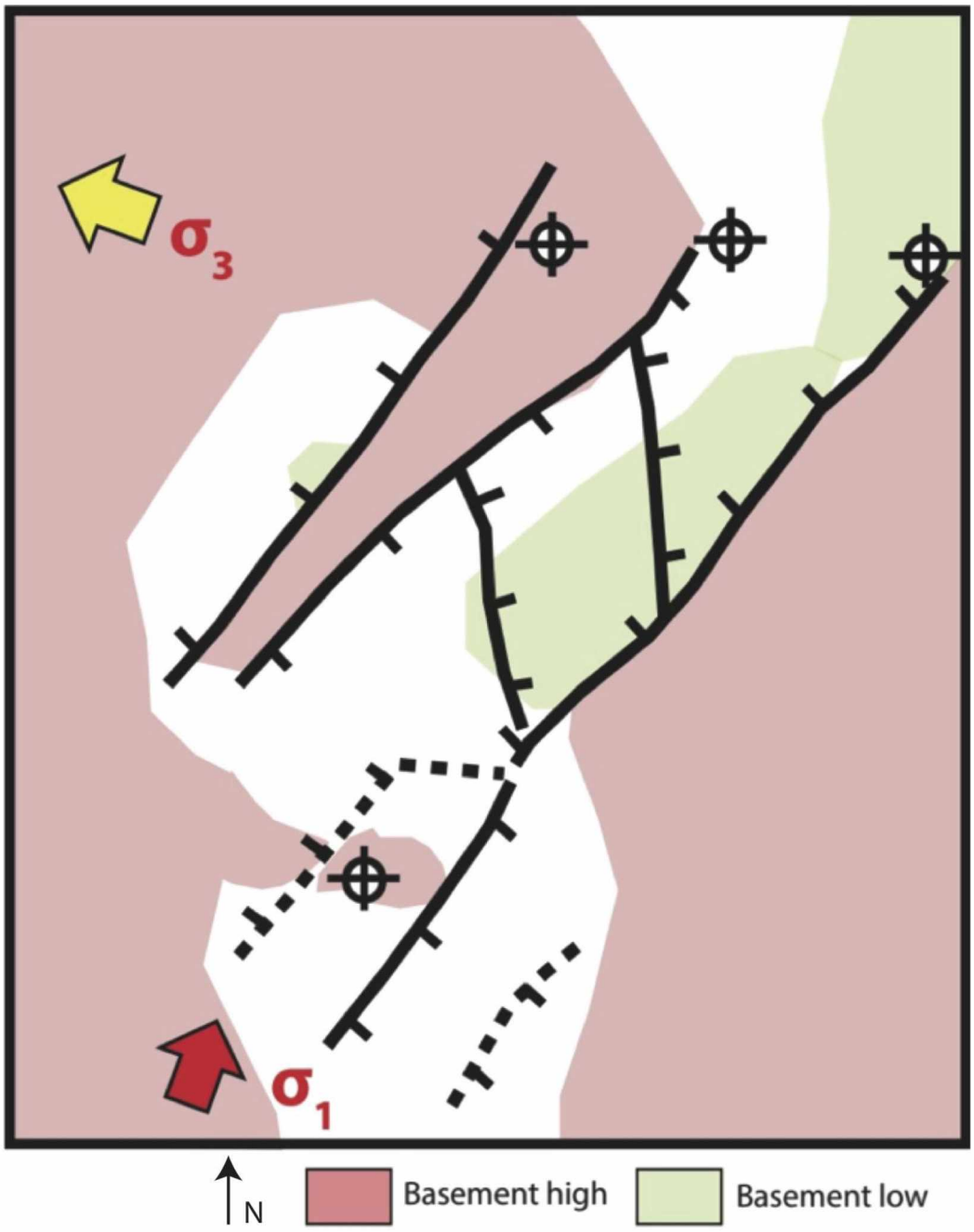

Figure 55: Model for fracture formation related to faulting in Interior Alaska and evolution of the Nenana basin: Late Paleocene time. Late Paleocene time is characterized by the onset of normal faulting in the Nenana basin. Both NE-SW and NW-SE oriented normal faults formed and are active during this phase. No measured fracture sets were observed that are attributed to this phase in basin evolution.

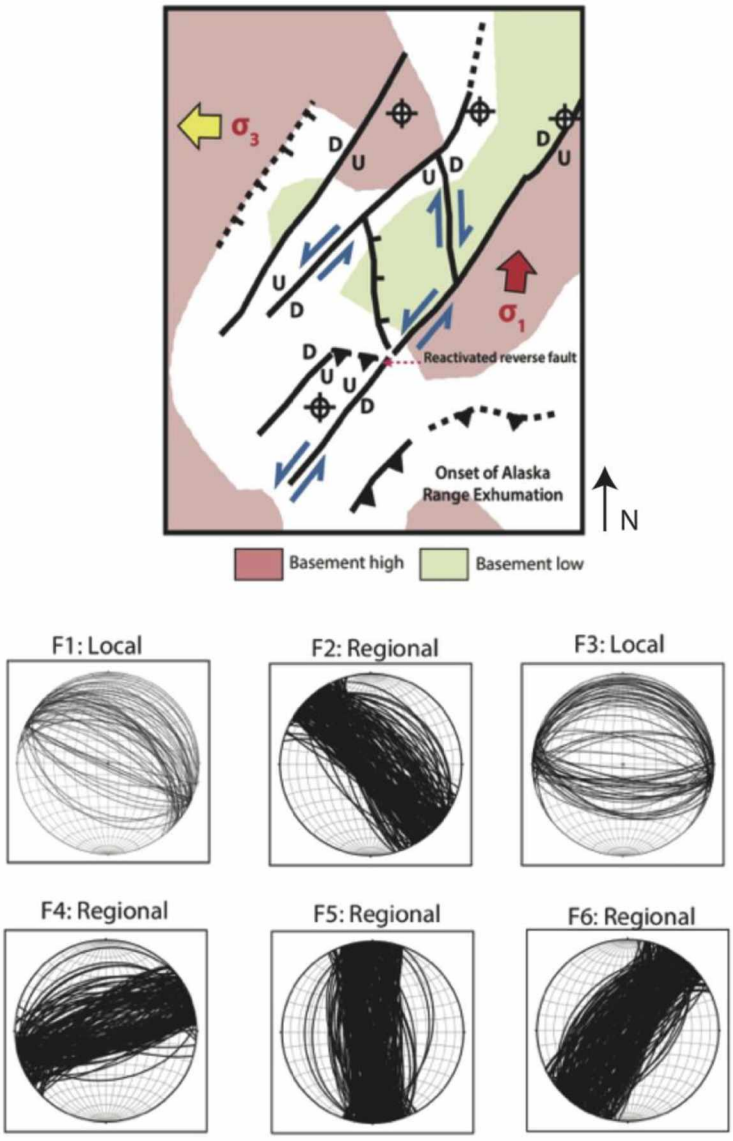

Figure 56: Model for fracture formation related to faulting in Interior Alaska and evolution of the Nenana basin: Late Miocene-Pliocene time
The Late Miocene to Pliocene time period is characterized as the onset of oblique faulting throughout the Nenana basin. Six fracture sets are attributed to this time in basin evolution. F1 and F3 are forming on a local scale in Domain I, while F2, F4, F5, F6 are forming on a regional scale.

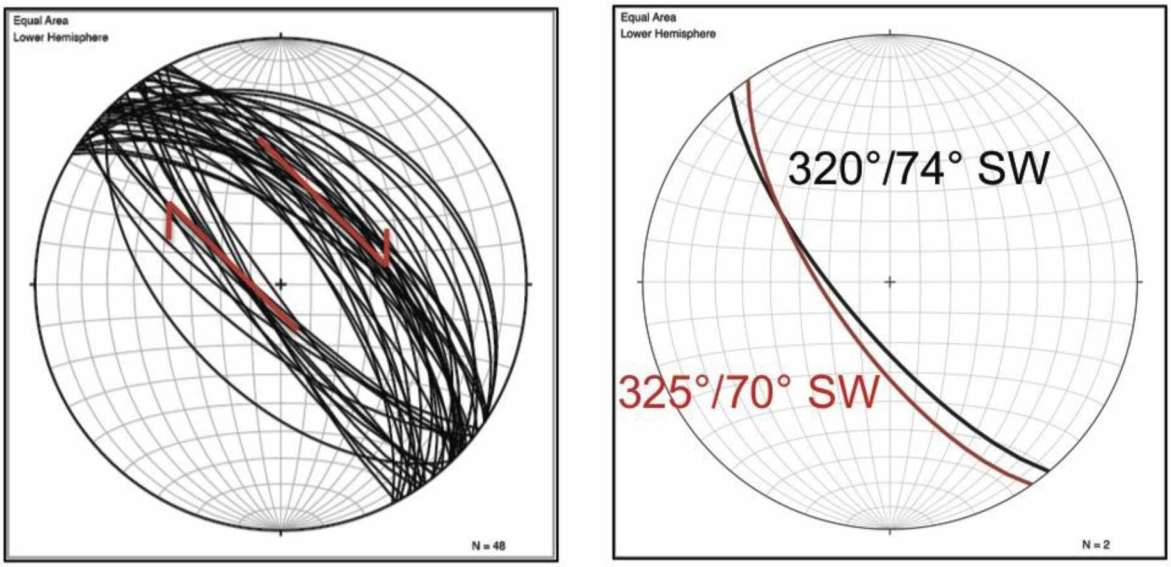

Figure 57: Formation of fracture set F2. Fracture set F2 and the NW-striking faults interior to and on the margin of the Nenana basin both share a similar orientation and right-lateral sense of shear. I propose that F2 fractures are related to normal oblique dip slip along the NW-striking faults with a right-lateral strike-slip component.

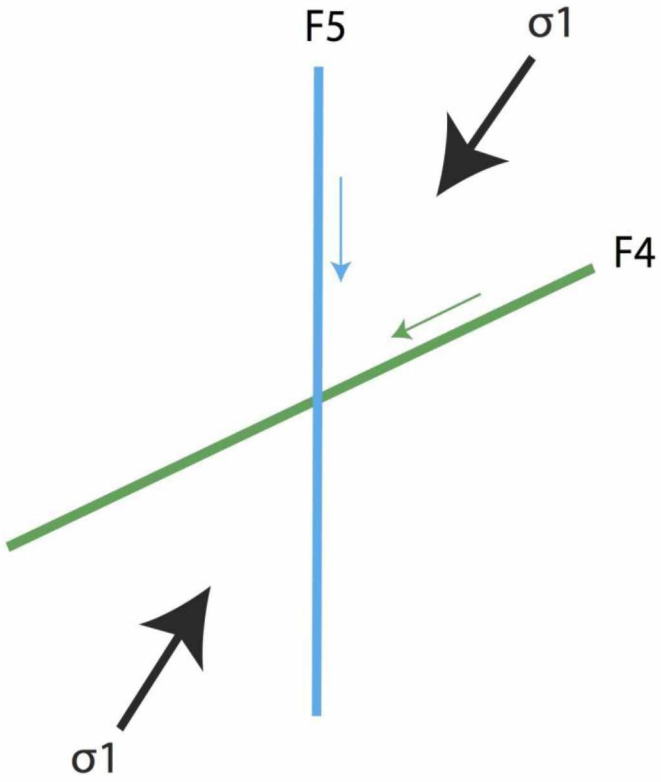

Figure 58: Formation of F4 and F5 fractures as conjugate shears. F4 and F5 formed as conjugate shear fractures associated with a NE-SW compressional stress. Both fracture sets have opposite senses of shear and match the orientation of structures that would form under this stress regime.

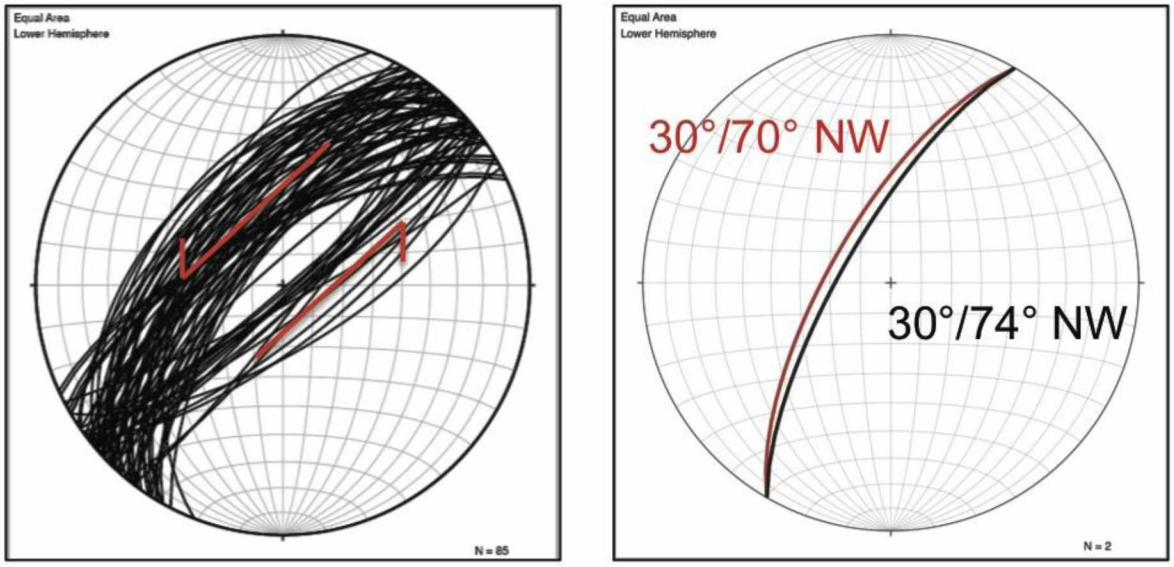

Figure 59: Formation of fracture set F6. Fracture set F6 and the NE-striking faults interior to and on the margin of the Nenana basin both share a similar orientation and a left-lateral sense of shear. I propose that F6 fractures are related to the normal oblique dip slip on these NE-striking faults with a left-lateral strike-slip component

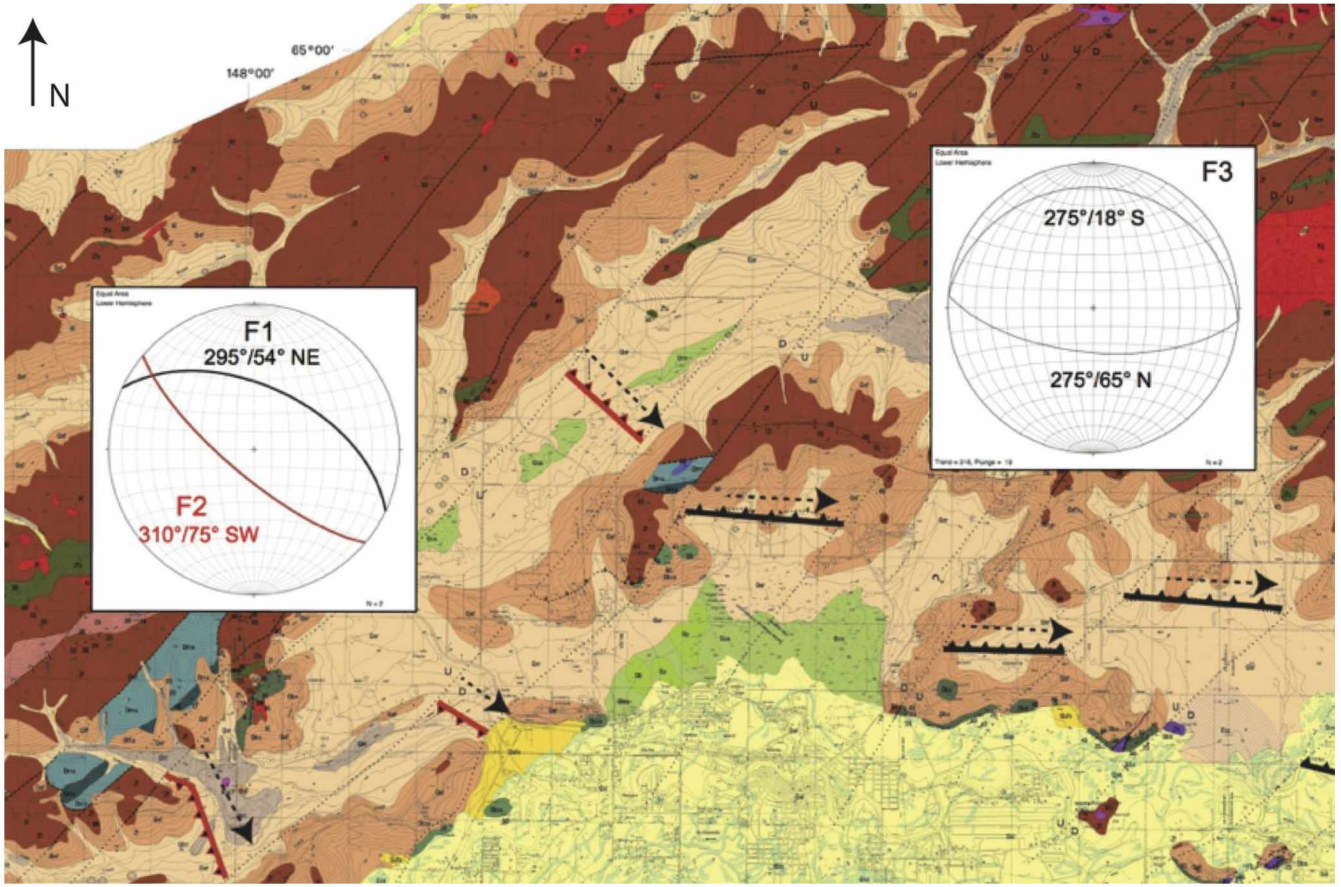

Figure 60: Local formation of fracture sets F1 and F3. Fracture sets F1 and F2 were observed only in a few locations in the Fairbanks area. I propose that F1 fractures are related to the reactivation of Cretaceous NW-striking proto-thrust faults (red faults) as oblique slip faults (thrust and minor right-lateral strike-slip). Similarly, F3 fractures are interpreted to have formed by reactivation of older NE-striking faults (black faults) as strike-slip faults in the Late Miocene. The interpreted right-lateral motion (black arrows) is consistent with the sense of shear observed in thin sections for F3 fractures. Map modified from Newberry et al. (1996).

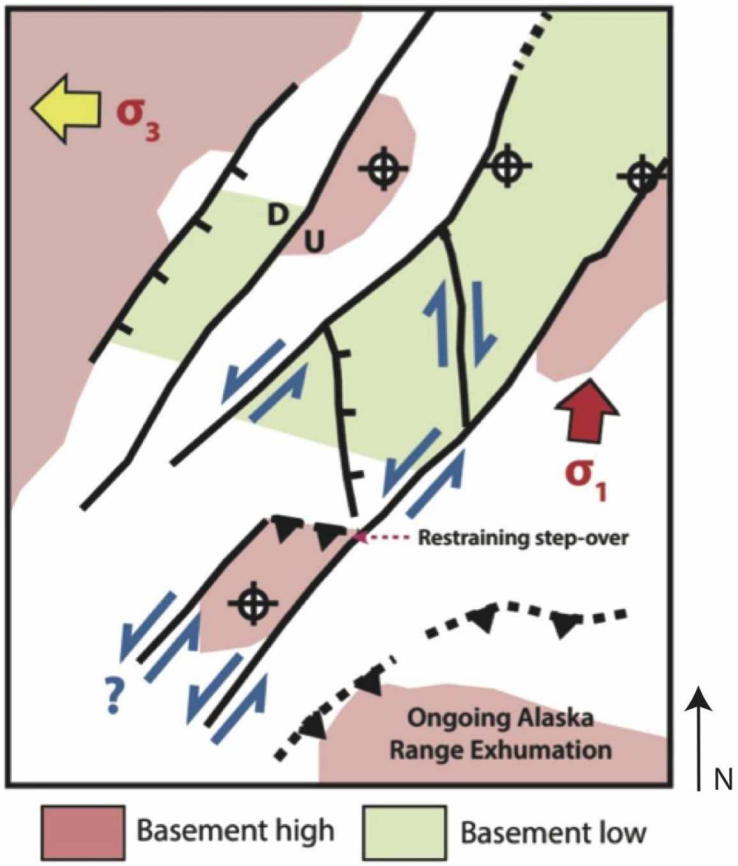

F6: Regional

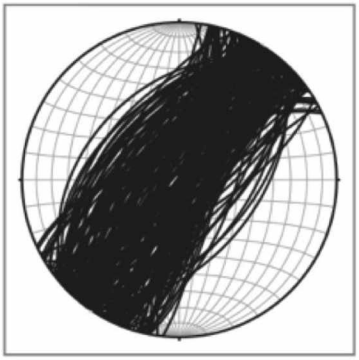

Figure 61: Model for fracture formation related to faulting in Interior Alaska and evolution of the Nenana basin: Pliocene-present day. During the Pliocene to the present day time period, the Nenana basin continued to grow in the NW-SE direction by oblique left-lateral strike slip and normal slip motion on existing faults and generation of new faults. F6 fractures share a similar orientation with these faults, post-date all other fracture sets, have lower temperature calcite twin geometries and are attributed to this period

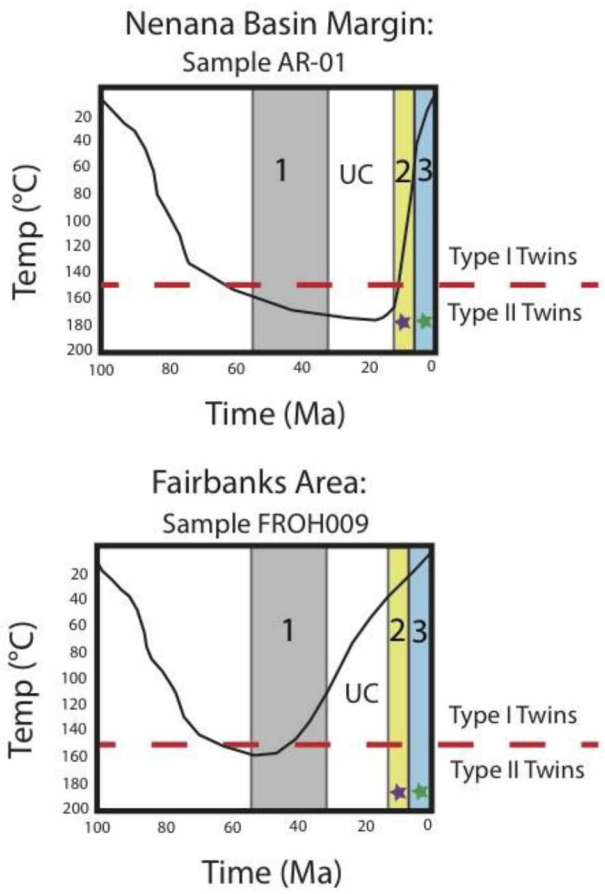

Figure 62: Synthesis of fracture history with available thermal and uplift data. Modeled apatite fission track data suggest two patterns of cooling occurred in Domain I. Younger ages (~40-7 Ma) occur near the margin of the Nenana basin (top); older cooling ages (~84.7-40 Ma) occur in the Fairbanks area. These curves, combined with constraints from analysis of the Nenana basin evolution (Dixit and Hanks, 2014) and calcite thermometry from fracture cements further constrain the timing of fracture sets.

1. Late Paleocene (pre-Healy Unconformity): No fracture formation occurs due to lack of strike slip faulting throughout the basin. Adjacent to the Nenana basin, burial is occurring during this time while the Fairbanks area is beginning to experience exhumation. No observed fractures are attributed to this period of time.
2. Late Miocene-Pliocene: All fracture sets are interpreted to have formed during this period. On the margin of the Nenana basin, the beginning stages of exhumation are occurring. Fractures formed during this time exhibit type II calcite twins. In the Fairbanks area, exhumation continues. Fracture filled during this time exhibit type I calcite twins.
3. Pliocene-Present Day: Only F6 fractures continue to form during this time. Exhumation is occurring in both areas; fracture cement exhibits type I calcite twins.

Numbers 1, 2 and 3 on graph represent time periods of basin evolution; UC= Unconformity; Purple Star= Formation of all sets in Domain I; Green Star= Formation of only F6

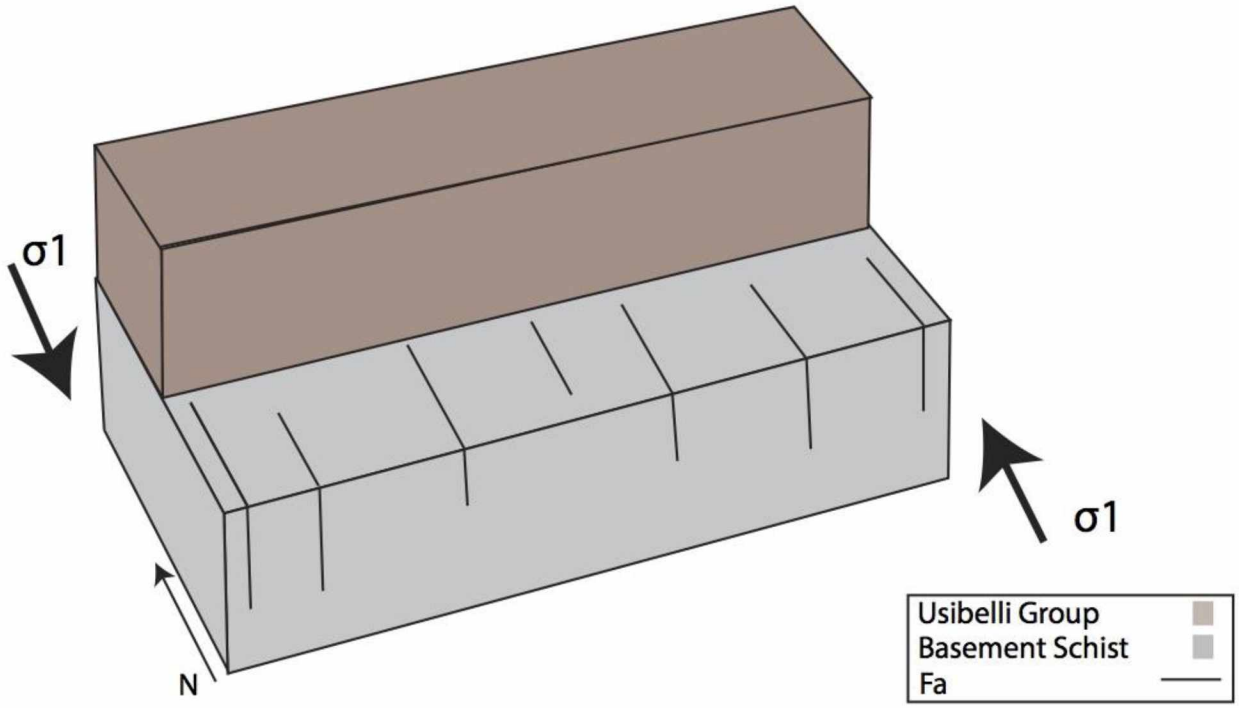

Figure 63: Model for fracture formation in Domain II: phase 1 (pre-Miocene time). Set Fa fractures form prior to the deformation of the Northern Foothills fold-and-thrust belt as a regional extensional fracture set parallel to the maximum compressive stress. Fa Fractures formed prior to deposition of the Usibelli Group sediments.

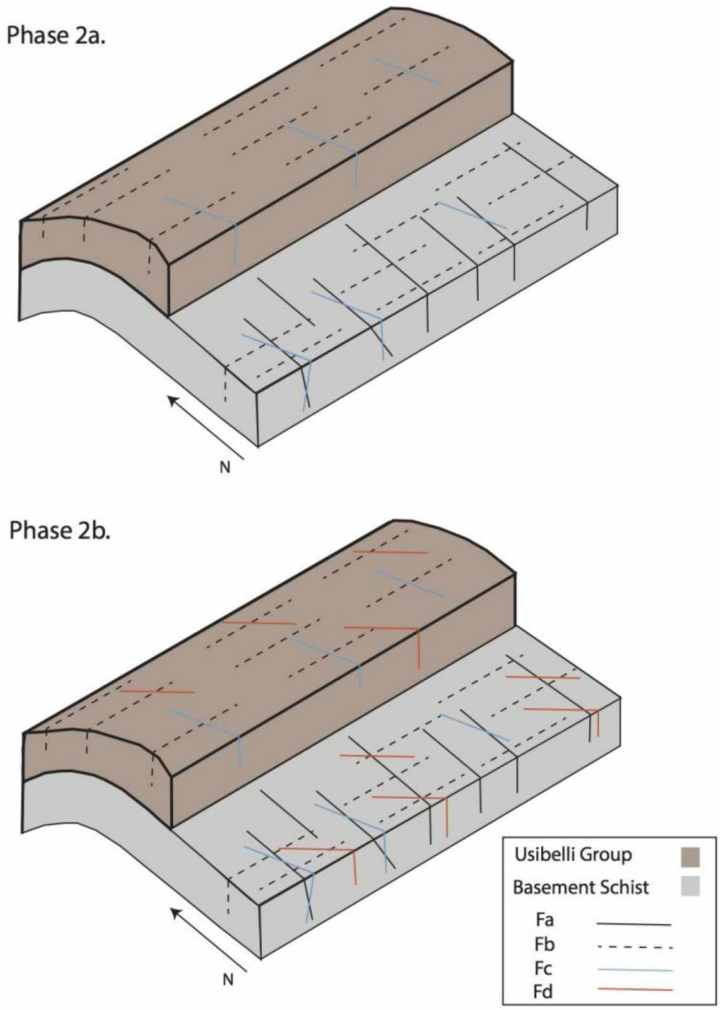

Figure 64: Model for fracture formation in Domain II: phase 2, Miocene time. Fractures formed during this phase occur in both the basement metamorphic rocks and overlying sediments of the Usibelli Group.

2a) Deformation of the northern hills fold-and-thrust belt begins with the formation of thrust faults and related folds. Set Fb fractures form orthogonal to the maximum compressive stress, parallel to the fold axes; Fc fractures form on the fold limbs as one fracture of a set of conjugate shear fractures. The NE-striking conjugate shear is not well-developed.

2b) Set Fd fractures form as on fracture of a set of conjugate shear fractures, with the corresponding NE-striking shear fracture poorly developed and not observed. Bemis and Wallace (2007) state that changes in orientation of the structures in the field area such as observed fracture sets Fc to Fd, can be due to variations in stress state during deformation due to changes in shortening; strike-slip motion along the E-W striking faults; local changes in lithologies (bed units); and/ or influence from pre-existing basement structures.

Table 1: Domain I (Fairbanks, Parks Highway, and Nenana): Summary of Fracture Sets and Their Characteristics

	Orientation	Fracture Characteristics		Sense of Motion (Slip Vector)	Average Density Fractures/Meter	Average Spacing (Meters)	Fracture Height (Meters)	Fracture Length (Meters)	Fracture Set Location		
		Outcrop	Thin Section						Fairbanks	Parks Highway	Nenana
1	 Orientation: 285-300°	-Shear fractures -Right-lateral shear -In schist and basalt	-Quartz with Secondary Cal. -Crystals are angled at 40°-50° in respect to the vein wall	Predominately Dip-Slip (Normal) (slip vector >45°, <80°)	Meta: 5.89 Basalt: 8.19	Meta: 0.27 Basalt: 0.28	Meta: 0.004-5.8 Basalt: 0.14-5.8	Meta: 0.0014-1.65 Basalt: 0.14-0.18			
2	 Orientation: 300-320°	-Shear fractures -Right-lateral shear -In schist	-Quartz with Secondary Cal. -Parallel to Strike: Right lateral Crystals are angled at 40°-50° -Parallel to Dip: Crystals are angled at 30° -Type I and II Calcite twins	Predominately Dip-Slip (Normal) (slip vector >40°, <80°)	Meta: 7.19 Basalt: N/A	Meta: 0.186 Basalt: N/A	Meta: 0.002-2.0 Basalt: N/A	Meta: 0.004-10.0 Basalt: N/A			
3	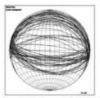 Orientation: 265-285°	-Shear fractures - Right-lateral shear -In schist and basalt	-Calcite veins -Parallel to Strike: Right lateral Crystals are angled 40°-60° -Parallel to Dip: Crystals are angled at 50°-70° -Type I and II Calcite twins	Predominately Dip-Slip (Normal) (slip vector >40°, <70°)	Meta: 4.91 Basalt: 2.36	Meta: 0.23 Basalt: 0.71	Meta: 0.056-0.19 Basalt: 0.09-9.1	Meta: 0.094-9.09 Basalt: 0.06-0.19			
4	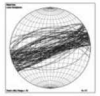 Orientation: 240-260°	-Shear fractures -Left-lateral shear -In schist and basalt	-Quartz and Calcite veins Parallel to Strike: Right-lateral Crystals are angled 65°-70° and at 40°-50 -Parallel to Dip: Crystals are angled at 50°-70° -Type I and II Calcite twins	Predominately Dip-Slip (Normal) (slip vector >45°, <80°)	Meta: 10.57 Basalt: N/A	Meta: 0.31 Basalt: N/A	Meta: 0.014-2.0 Basalt: N/A	Meta: 0.012-10.0 Basalt: N/A			
5	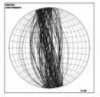 Orientation: 340-360°	-Shear fractures - Right-lateral shear - In schist and basalt	-Quartz and Calcite veins -Parallel to Strike: Right lateral shear -Type I and II Calcite twins	Predominately Strike-Slip (slip vector: N/A)	Meta: 7.22 Basalt: 3.53	Meta: 0.21 Basalt: 0.10	Meta: 0.002-4.0 Basalt: 0.32-0.55	Meta: 0.23-5.0 Basalt: N/A			
6	 Orientation: 190-210°	-Shear fractures -Left-lateral shear -In schist and basalt	-Quartz and Calcite veins -Parallel to Strike: left- lateral shear -Type I and II Calcite twins	Predominately Strike-Slip (slip vector: N/A)	Meta: 6.44 Basalt: 10.11	Meta: 0.29 Basalt: N/A	Meta: 0.002-2.76 Basalt: 0.16-2.05	Meta: 0.011-10.0 Basalt: 0.03-0.13			

Table 2: Domain II (Healy area): Summary of Fracture Sets and Their Characteristics

	Orientation	Fracture Characteristics		Average Density Fractures/Meter	Average Spacing (Meters)	Fracture Height (Meters)	Fracture Length (Meters)
		Outcrop	Thin Section				
A	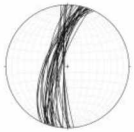 Orientation: 355-25°	-Joint fractures -No shear -In schist	-Quartz veins -crystals are perpendicular to vein wall	Meta: 11.87 Sed: N/A	Meta: 0.10 Sed: N/A	Meta: 0.004-.12 Sed: N/A	Meta: 0.06-0.33 Sed: N/A
B	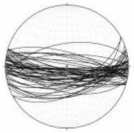 Orientation: 240-270°	-Shear fractures -Right-lateral shear -In schist and Sed. rocks	-Quartz with secondary calcite -Type II and II calcite twins -crystals are perpendicular to vein wall.	Meta: 11.48 Sed: 2.69	Meta: 0.12 Sed: 0.37	Meta: 0.004-0.49 Sed: 0.51-2.5	Meta: 0.013-1.83 Sed: 0.024-1.0
C	 Orientation: 325-350°	-Shear fractures -Left-lateral shear -In schist and Sed. rocks	-Quartz veins -crystals are perpendicular to vein wall	Meta: 8.79 Sed: 5.42	Meta: 0.15 Sed: 0.26	Meta: 0.002-1.94 Sed: 0.073-2.5	Meta: 0.012-2.17 Sed: 0.01-0.5
D	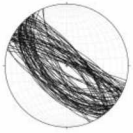 Orientation: 300-320°	-Shear fractures -Assumed left-lateral shear -In schist and Sed. rocks	No data	Meta: 13.64 Sed: 4.65	Meta: 0.064 Sed: 0.24	Meta: 0.003-0.23 Sed: 0.011-2.0	Meta: 0.032-1.38 Sed: 0.019-1.02

Table 3: Apatite Fission Track Data. From Frohman (2014)

Sample	Pooled Age	+/- 1 σ	Grains Counted	Mean Track Lengths	St. Dev (μ)	# Tracks
1338-17	7.8	6.5, 3.5	10	14.4	1.5	15
1338-01	38.2	39.6, 19.5	15	14	1.7	20
1338-02	28.4	4.1, 3.6	24			
1338-03	37	14.8, 20.6	16	13.9	1.6	64
1338-10	49.9	11.7, 9.5	24	14.2	1.4	125
1338-05	36.5	3.8, 3.4	32	14	1.8	152
1338-04	32.7	7.6, 6.2	16	14.6	1.3	138
1338-15	37.7	23.7, 14.6	2	14.7	1.3	10
1338-16	71.1	30.2, 21.2	2	14.4	0.7	17
1338-07	40.5	4.6, 4.1	34	14.4	1.5	158
1338-12	26	8.5, 6.4	6	14.4	1.5	20
1338-08	47.3	19.3, 13.7	28	14.9	6.8	78
1338-09	84.7	37.5, 26	34	14.2	1	16
1338-13	68	31.9, 21.7	21	15.2	1.1	20

Table 4: AFT Interpretations. From Frohman (2014)

Sample	Onset of Rapid Cooling (Ma)	Cooling Rate	Exhumation Rate m/Ma
1338-17	16	23.7	740.56
1338-01	58	6.18	193.08
1338-02	52	4.66	145.73
1338-03	56	3.75	117.23
1338-10	63	10.95	342.3
1338-05	60	3.51	109.8
1338-04	42	10.18	630.73
1338-15	55	7.96	248.72
1338-16	79	9.4	293.7
1338-07	51	5.8	181.13
1338-12	47	8.31	259.64
1338-08	65	4.26	133.01
1338-09	96	6.62	206.83
1338-13	75	9.35	292.34

APPENDIX A: Natural Fracture Data

1. Fairbanks, Parks Highway, and Nenana Area Fracture Orientations:

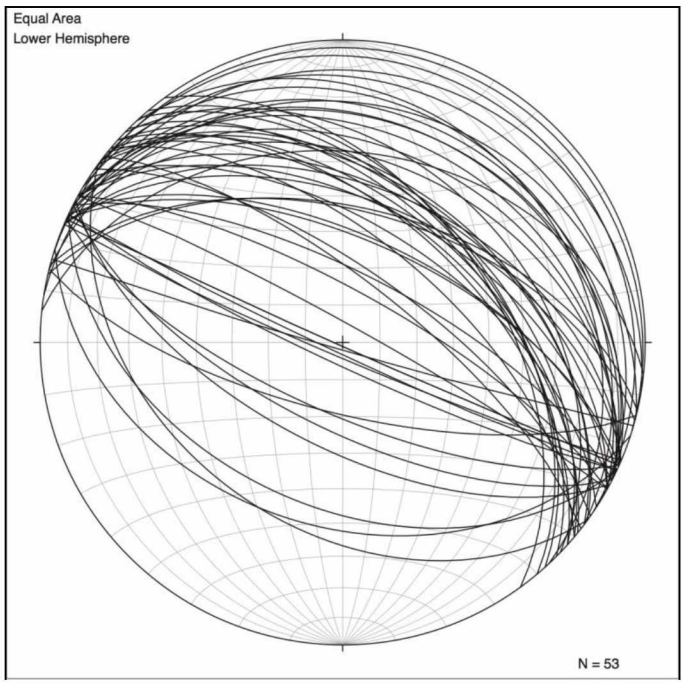

Figure A.1: Stereonet of fracture set F1.

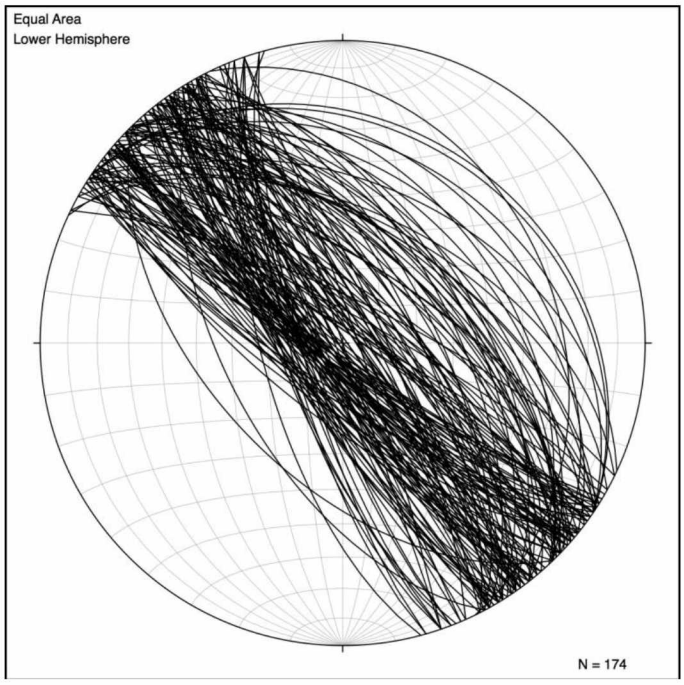

A.2: Stereonet of fracture set F2 (all field locations combined).

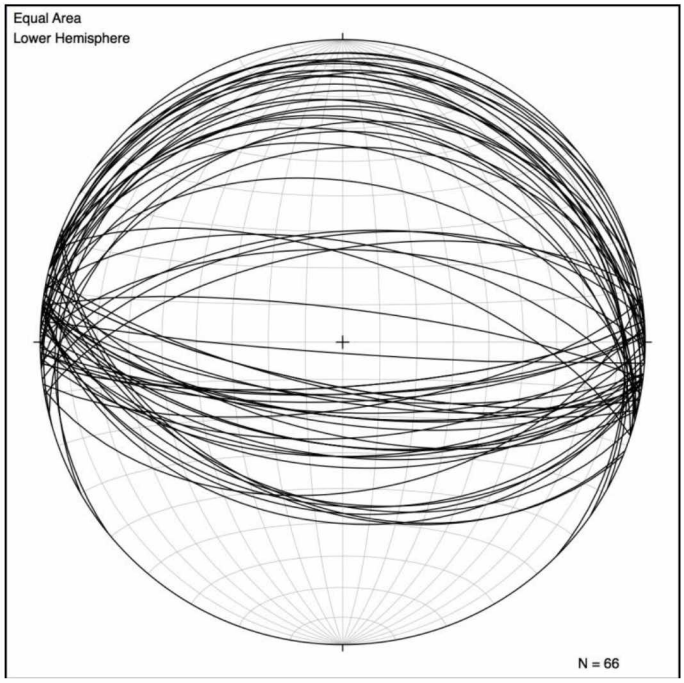

Figure A.3: Stereonet of fracture set F3.

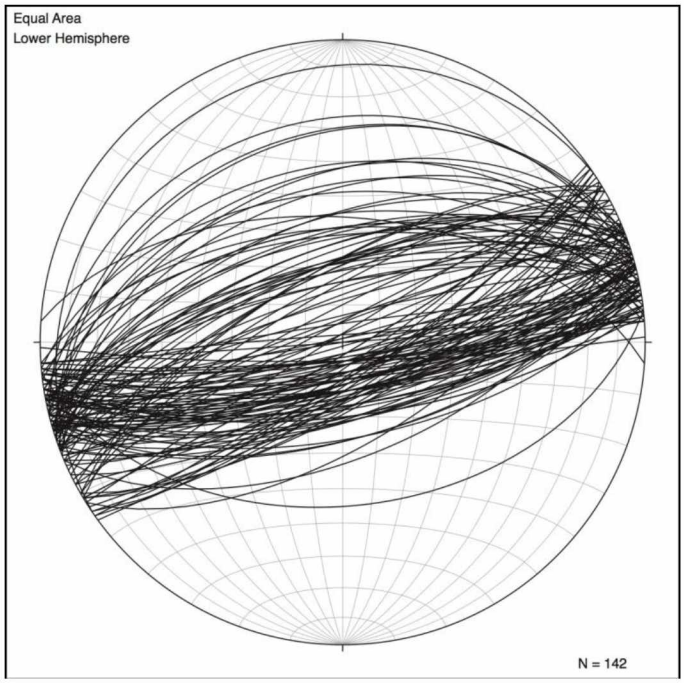

Figure A.4: Stereonet of fracture set F4 (all field locations combined).

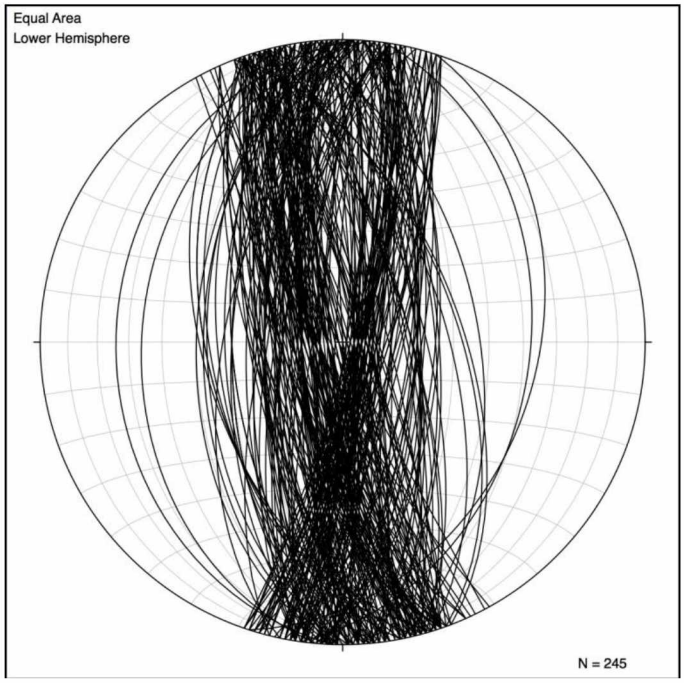

Figure A.5: Stereonet of fracture set F5 (all field locations combined).

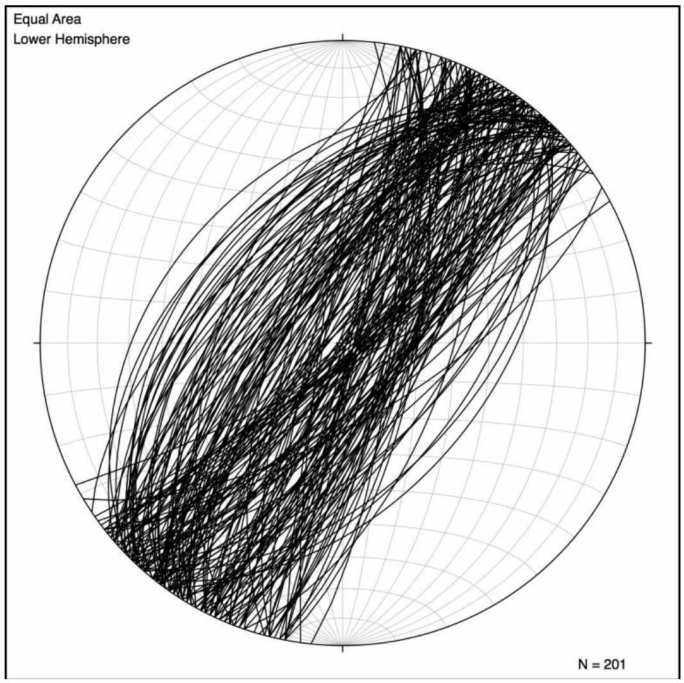

Figure A.6: Stereonet of fracture set F6 (all field locations combined).

2. Locations of Fracture Sets by Field Area:

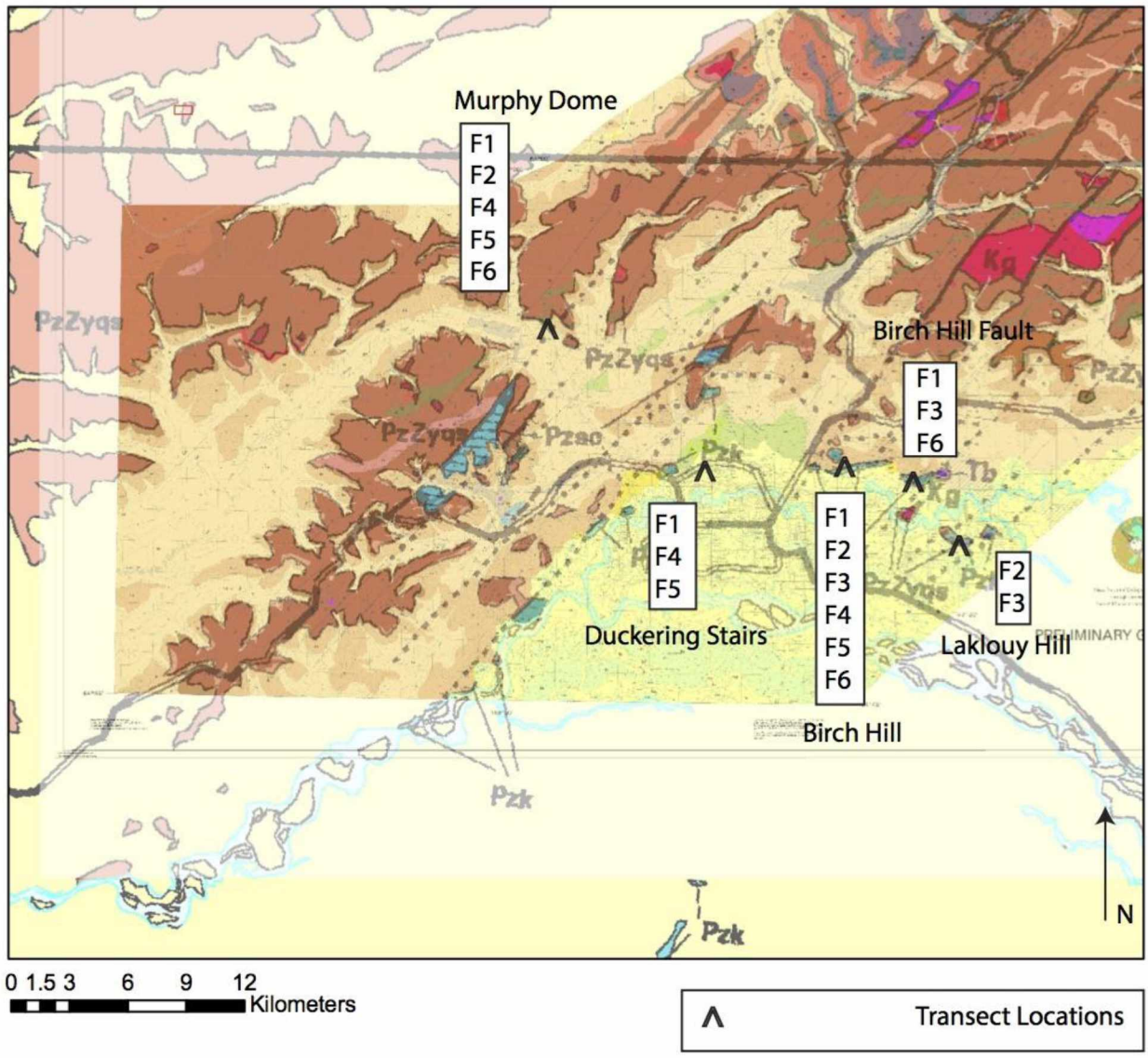

Figure A.7: Location of Fairbanks fracture transects.

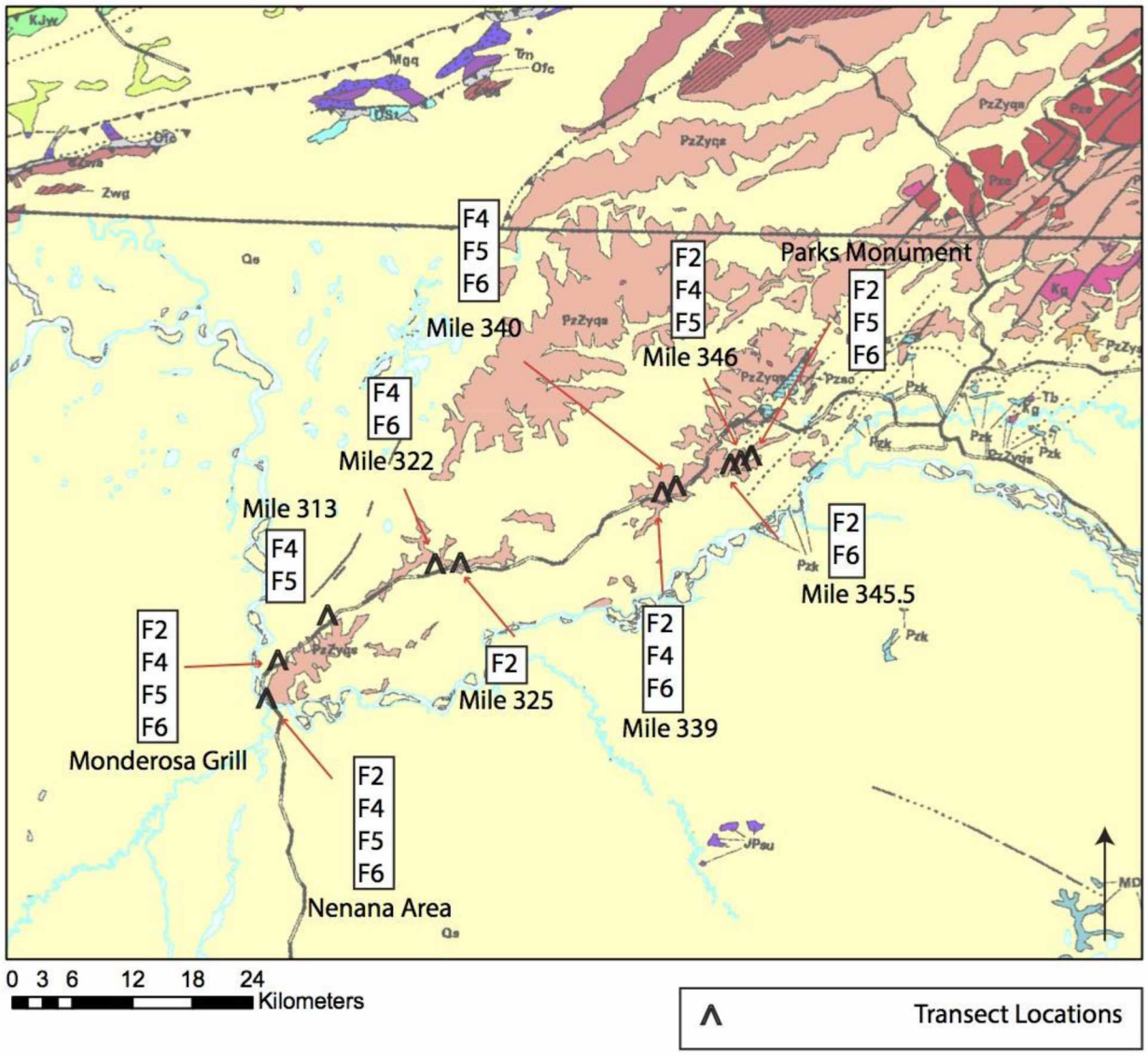

Figure A.8: Location of Parks Highway and Nenana area fracture transects.

3. Healy Area Fracture Orientations:

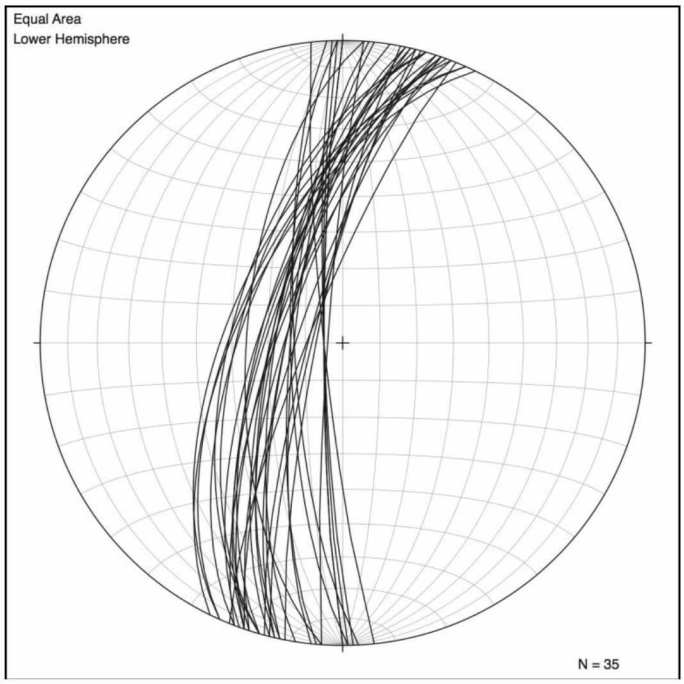

Figure A.9 Stereonet of fracture set Fa.

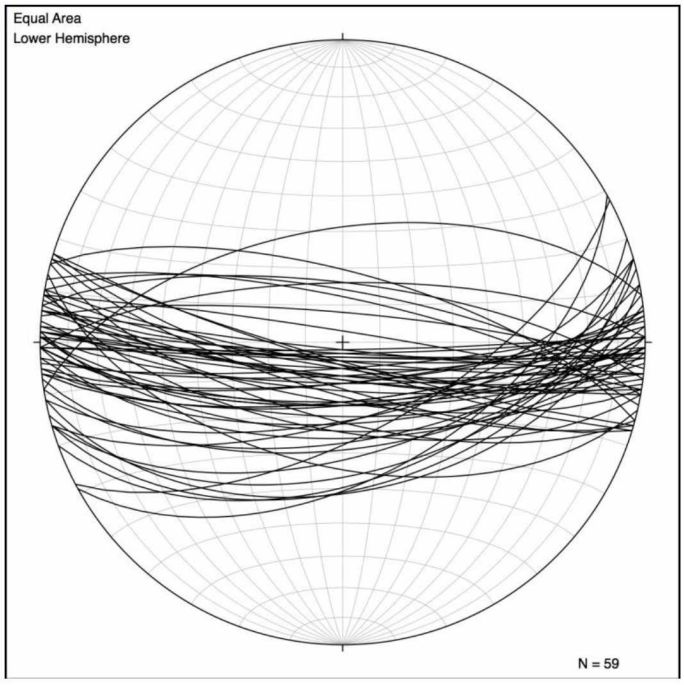

Figure A.10: Stereonet of fracture set Fb.

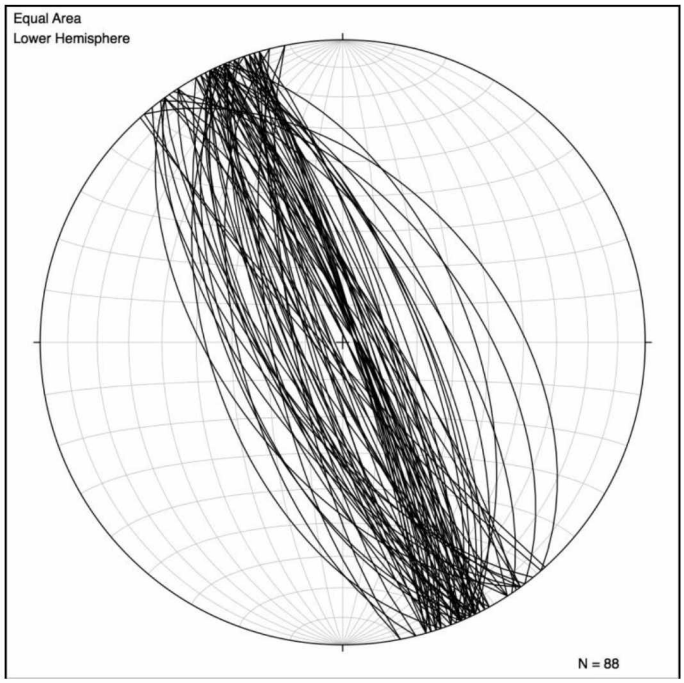

Figure A.11: Stereonet of fracture set Fc.

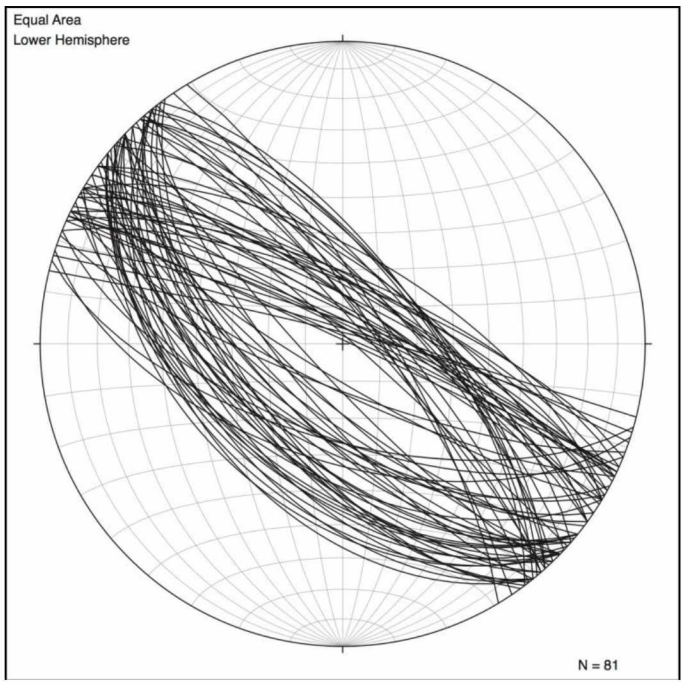

Figure A.12: Stereonet of fracture set Fd.

4. Locations of Fracture Sets by Field Area:

Healy Area:

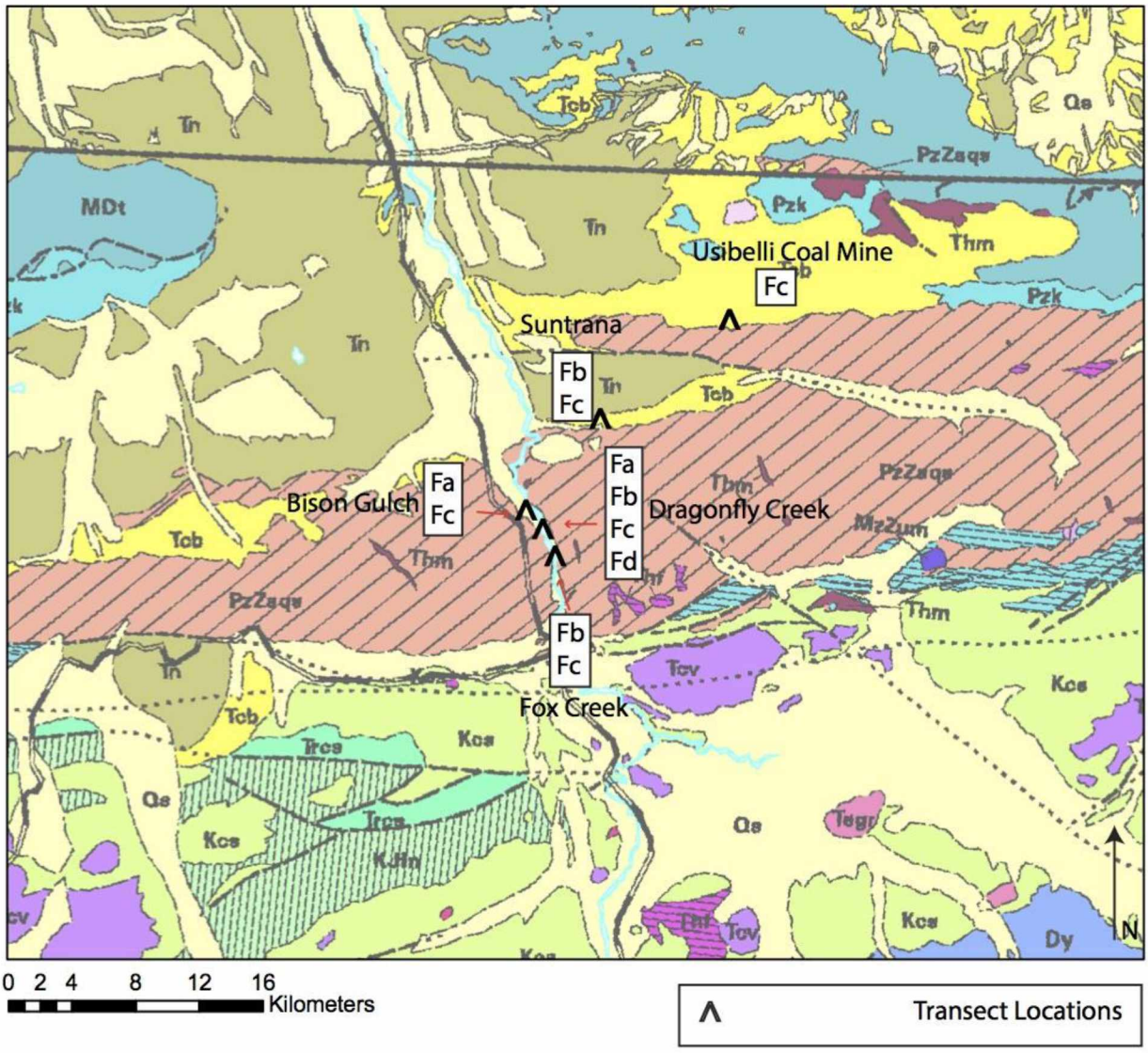

Figure A.13: Location of Healy area transects.

5. Field location descriptions

Table A.1: Waypoint Descriptions, Fairbanks Area

1) Lakloey Hill	Field area contains outcrops of both metamorphic basement and basalt. The contact between the two is a normal fault. Fracture measurements were taken from the schist. The outcrop was not in great condition but enough fractures were recorded to obtain data necessary for density, fracture spacing, height, and length measurements. Fractures were distributed as fibrous calcite veins with large apertures. One fracture set was recorded at this waypoint
2) Birch Hill Fault	Located on Fort Wainwright in Fairbanks, this field area contains a large oblique normal fault with basement schist and basalt outcrops. Slickensides are present on the basalt in the field, showing both a normal and strike-slip component. Fractures were taken from both the metamorphic schist and basalt. The outcropping schist was not in great condition due to the fault zone. The basalt had significant fractures and were recorded for the project. Fractures appeared to have been filled in the schist but were no longer due to the condition of the outcrop and were unfilled in the basalt. Four fracture sets were recorded at this waypoint. Outcrops were polished surfaces and could not get angle of bedding.
3) Birch Hill	Large phyllitic schist outcrop located on Fort Wainwright containing e-w striking folds. Fractures were recorded in the schist and were represented as both unfilled and filled quartz-calcite veins. Unfilled fractures in this area had remnant fill on fracture faces. 4 fracture sets were recorded at this field location
4) UAF Campus: Duckering Stairs	Friable basement schist outcrop located on the University of Alaska Fairbanks' campus. Fractures were both unfilled and filled quartz veins at this location. Three fracture sets were recorded at this location along one transect. Bedding was dipping at 25 degrees to the south. Outcrop was in good condition with only a portion of the transect covered by erosional debris.
5) Murphy Dome Road	Metamorphic outcrop with large marble vein 1 m in thickness running through schist. Bedding of schist is dipping at 35-45 degrees to the south-southeast. Fractures in the outcrop are both unfilled and filled. Oxidized en echelon quartz and calcite veins are present in outcrop, while unfilled fractures show signs of previous cement.

Table A.2: Waypoint Descriptions, Parks Highway and Nenana Areas

1) Park's Monument	Highly fractured schist with extensive horizontal and vertical joint fractures. Fractures are unfilled, but appear to have remnant cement with traces of mineralization on oxidized fracture faces. Four fracture sets were measured in outcrop in this location.
Mile 346	Schist outcrop that was poorly exposed alongside the Parks Highway. The majority of outcrop is slumped and large boulders are broken off and lying below the road cut. Outcrop bedding is dipping 30 degrees to the southeast. Two unfilled fracture sets were measured at this location with remnant mineralization of fracture faces.
Mile 345.5	Large schist outcrop located off of the Parks Highway with interbedded phyllite. Schist bedding dipping at 12 degrees to the southwest. Very minor quartz veins present in outcrop. Three fracture sets were measured at this waypoint.
Mile 340	Friable schist out crop with interbedded phyllite. Outcrop is mostly covered with erosional debris. Bedding is dipping at 13 degrees to the southwest. Fractures faces are heavily oxidized and unfilled. Four fracture sets were measured at this location.
Mile 339	Large schist outcrop that is mostly covered and was not highly fractured dipping at 84 degrees southeast. Bedding of schist is dipping at 36 degrees to the northeast. Most fractures are unfilled and contain remnant mineralization on fracture faces. Four fracture sets were measured at this waypoint.
Mile 325	Faulted quartzose schist outcrop located off the Parks Highway. Large fold is also visible in outcrop trending at 346 degrees and plunging at 28 degrees to the northwest. Bedding of schist dipping at 4 degrees to the southwest. Three fracture sets were measured at this waypoint.
Mile 323	Schist outcrop with bedding dipping to the southwest at 36 degrees. Outcrop was in poor condition and not highly fractured. One fracture set was recorded.

Mile 322	Schist outcrop in poor condition with bedding dipping 16 degrees to the northeast. Outcrop is slumped in some places and mostly covered by erosional debris. Due to the condition of the outcrop only one fracture set was measured at this location.
Mile 313	Poorly exposed, slumped outcrop off of the Parks Highway. Bedding of schist is dipping at 34 degrees to the east. Two unfilled fracture sets were recorded at this waypoint with some remnant mineralization along fracture faces.
Monderosa Grill	Large road cut located near Nenana, Alaska. Basement oxidized schist and pelitic quartzite with large granite crystals are present at this waypoint. Four fracture sets were recorded at this location, all of them were filled or contained remnant filled. Bedding dip varies from 24-35 degrees to the south and west. En echelon fractures as well as slickenfibres on fracture faces present throughout outcrop.
Nenana Outcrop (Basin Margin)	Many locations along this large outcrop were visited to collect data. Rocks range from schist in varying conditions to folded and faulted quartzite. A total of 4 fracture sets were measured at this location, all of them being filled or containing remnant fill of calcite or quartz. Bedding at this outcrop varies, from 29-42 degrees dipping to the northeast and west depending on the location along the outcrop.

Table A.3: Waypoint Descriptions, Healy Area

Usibelli Coal Mine	Unfilled coal cleats measured on a coal seam at the Usibelli coal mine located in Healy, Alaska. Bedding angle was immeasurable and the coal tended to be highly oxidized in parts of the exposed seam. One fracture set was measured at this location.
Suntrana	Basement schist and Usibelli Group outcrops were present at this location. Quartz-filled fractures in the schist as well as unfilled fractures in the Usibelli Group were measured. Schist was heavily folded with quartz lenses and filled fractures. Basement rocks were fiable and consectuvie fractures were hard to locate. Fractures were measured in oxidized sandstone, interbedded siltstone and coal beds, and coal seams throughout this field area with beds dipping at 10-25 degrees to the northeast-northwest. Fractures in sedimentary rocks were very extensive. A total of 3 fracture sets were measured at the suntrana section.
Bison Gulch	Outcrops consisted of chlorite-rich basement schist that were folded. Outcrops were heavily fractured and fracture sets consisted of quartz-calcite fill veins. Bedding of outcrop was dipping at 21 degrees to the east. Two fracture sets were measured at this location
Fox Creek	Heavily folded basement schist carved by water erosion was present at this location. Bedding was dipping at 10-15 degrees to the east. Fractures were commonly seen as quartz quartz veins in outcrop. In some locations, fractures were poorly exposed but two overall fracture sets were measured.
Dragonfly Creek	Outcrop was friable basement schist with bedding dipping from 7-10 degrees to the northeast-northwest. Outcrop was in poor condition with oxidized fracture faces showing signs of remnant mineralization. Four fracture sets were measured at this field site.

6. Fracture Transects

KEY:

Distance from origin: Distance from start of measuring tape

Aperture: The width of the fracture opening measured in millimeters

Fill:

1) Cal. for calcite fill; Oxd. when fill is oxidized
2) Qtz. For quartz; Oxd. when fill is oxidized
3) Rem. for remnant fill
4) Open, for when fracture is open
5)

Height: Vertical extent of the fracture

Width: The length of the fracture

Ind.: Indeterminate, missing, not exposed.

Fairbanks Transects:

Table A.4: Murphy Dome Road 1a

Fracture	Distance from Origin (cm)	Strike	Dip	Length (cm)	Height (cm)	Aperture (mm)	Type of Fill
1	9.4	274	21NW	IND	19.6	1-3	Rem.
2	39.8	284	9NW	IND	38.7	1-4	Rem.
3	48.7	279	16NW	IND	15.4	1	Rem.
4	50.6	274	8NW	IND	28.3	1-3	Rem.
5	60.2	271	5 NW	IND	29.1	1-2	Rem.
6	74.2	284	27NW	IND	9	0.5-1	Rem.
7	81.2	284	36NW	IND	21.8	0.5-1	Rem.
8	87.9	288	32NW	IND	15.2	0.5-1	Rem.
9	92.3	265	36NW	IND	26.2	0.5-1	Rem.
10	121.2	265	11NW	8.1	24.5	1-6	Rem.
11	135.2	254	5NW	IND	17.1	1-FF	Rem.
12	159.4	269	31NW	IND	24.7	1	Rem.
13	177.8	285	28NW	IND	15.2	0.5-1	Rem.
14	187.8	272	24NW	1.9	4.7	1	Rem.
15	196.4	256	29NW	IND	27.6	1-2	Rem.
16	218.6	288	14NW	3.2	9.8	0.5-1	Rem.
17	223.2	287	22NW	1.8	9.6	0.5-1	Rem.
18	227.2	266	18NW	2.3	9.4	0.5-1	Rem.

Table A.5: Murphy Dome Road 1b

Fracture	Distance from Origin (cm)	Strike	Dip	Length (cm)	Height (cm)	Aperture (mm)	Type of Fill
1	11.9	231	9NW	2.6	21.1	FF	Rem.
2	14.6	240	15NW	IND	35.1	1-2	Rem.
3	23	313	11NW	4.6	52.3	1-5	Rem.
4	43.4	305	14NW	IND	25.8	1	Rem.
5	99.8	269	23NW	IND	33.5	1	Rem.
6	112.4	299	15NW	IND	30.4	1-2	Rem.

Table A.6: Murphy Dome Road 2

Fracture	Distance from Origin (cm)	Strike	Dip	Length (cm)	Height (cm)	Aperture (mm)	Type of Fill
1	12	331	57N	59.7	10.2	FF	Rem.
2	32.4	354	40N	30.8	7.2	FF	Rem.
3	38.4	341	42N	34.1	1.6	FF	Open
4	43.4	337	55N	33.4	7.9	FF	Rem.
5	50.4	354	61NE	43.6	6.4	FF	Rem.
6	66.2	341	64N	30.7	2.1	FF	Rem.
7	70.6	329	55N	17.4	1.2	FF	Qtz.
8	74.2	334	69N	21.8	1.4	FF	Rem.
9	76.8	323	62N	32.8	9.7	FF	Open
10	93.2	357	59N	44.2	1.1	FF	Rem.
11	94.6	323	43N	88.7	11.2	FF	Open
12	105.4	323	58N	75.7	7.7	FF	Rem.
13	114.2	310	59N	15.3	8.3	FF	Open
14	118.6	309	85N	9.2	15.7	FF	Rem.
15	127.4	2	89N	41.2	1.4	FF	Rem.
16	130.2	336	84N	44.9	8.5	FF	Oxd. Qtz.
17	146.1	354	84N	24.6	7.2	FF	Rem.
18	155.2	340	77N	24.6	9.2	FF	Open

Table A.7: Murphy Dome Road 3

Fracture	Distance from Origin (cm)	Strike	Dip	Length (cm)	Height (cm)	Aperture (mm)	Type of Fill
1	6.3	195	IND	14.3	4.4	0.5-1	Open
2	7.8	194	46W	17.8	4.4	0.5-1	Oxd. Qtz.
3	11.6	192	75W	35.7	7.6	FF	Qtz.
4	22.2	187	81W	54.9	2.1	1-FF	Qtz.
5	24.4	189	IND	54.3	IND	0.5-1	Qtz.
6	38	188	IND	24.3	4.7	0.5-1	Qtz.
7	43.8	190	602	11.2	0.9	0.5-1	Qtz.
8	62.3	187	79W	16.8	2.6	0.5	Open
9	72.3	185	81W	57.3	0.5	0.5-1	Qtz.
10	89.2	192	IND	44.6	10.7	0.5-1	Qtz.
11	90.6	194	IND	28.4	IND	0.5-1	Oxd. Qtz.
12	96	185	89W	59.8	16.1	0.5-FF	Oxd. Qtz.
13	100.4	188	IND	34.2	IND	0.5-1	Oxd. Qtz.
14	103.8	183	85W	51.8	17.6	0.5-1	Qtz.
15	106.1	184	85W	7.4	2.9	FF	Oxd. Qtz.
16	113.2	189	85W	26.7	4.3	1	Oxd. Qtz.
17	114.3	186	74W	11.2	4.2	1	Qtz.
18	116.2	185	82W	5.9	5.8	0.5	Qtz.
19	120.6	182	IND	8.2	5.8	0.5	Qtz.
20	122.2	180	81W	8.6	5.8	0.5-1	Oxd. Qtz.
21	124.6	181	87W	54.2	24.6	0.5	Oxd. Qtz.
22	129.9	190	84W	13.6	8.6	0.5	Oxd. Qtz.
23	136.8	191	83W	27.4	7.2	0.5	Oxd. Qtz.
24	140.3	184	86W	9.7	IND	0.5	Oxd. Qtz.

Table A.8: Murphy Dome Road 4

Fracture	Distance from Origin (cm)	Strike	Dip	Length (cm)	Height (cm)	Aperture (mm)	Type of Fill
1	0.0	283	53NE	6.6	3	FF	Rem.
2	19.6	293	51NE	12.6	0.6	FF	Rem.
3	27.2	294	39NE	27.3	6	FF	Rem.
4	29.9	299	31NE	12.3	6.4	0.5-1	Oxd. Qtz.
5	40.1	296	35NE	12.7	6.8	0.5-1	Oxd. Qtz.
6	54.7	306	45NE	58.7	6.2	FF-2.3	Oxd. Qtz.
7	58.6	293	47NE	44.4	8.7	0.5-2	Oxd. Qtz.
8	63.4	297	27NE	21.6	2.1	0.5-1	Qtz.
9	69.8	314	38NE	26.2	3.8	0.5-1	Oxd. Qtz.
10	78.8	315	50NE	55.6	5.1	2-3	Oxd. Qtz.
11	82.3	312	47NE	11	4.7	0.5	Oxd. Qtz.
12	88.9	301	44NE	22.3	3.1	FF	Rem.
13	100.4	299	47NE	5.7	0.8	FF	Rem.
14	119.6	277	81NE	16.8	6.5	FF	Rem.
15	145.2	308	73NE	28.7	5.8	FF	Oxd. Qtz.

Table A.9: Murphy Dome Road 5a

Fracture	Distance from Origin (cm)	Strike	Dip	Length (cm)	Height (cm)	Aperture (mm)	Type of Fill
1	24	80	86SE	71.2	4.3	0.5-1	Qtz.
2	57	79	86SE	68.3	3.5	1	Open
3	61.8	80	87SE	61.3	1.4	1-2	Oxd. Qtz.

Table A.10: Murphy Dome Road 5b

Fracture	Distance from Origin (cm)	Strike	Dip	Length (cm)	Height (cm)	Aperture (mm)	Type of Fill
1	24.6	70	71SE	38.7	4.2	0.5-1	Rem.
2	36.1	61	66SE	19.2	5.9	0.5	Open
3	46.4	67	86SE	39.3	8.2	FF	Open
4	50.8	69	87SE	66.3	4.2	0.5	Partial
5	89.2	77	86SE	54.6	5.1	0.5	Open

Table A.11: Duckering Stairs, UAF Campus 1

Fracture	Distance from Origin (cm)	Strike	Dip	Length (cm)	Height (cm)	Aperture (mm)	Type of Fill
1	15.7	304	15N	IND	123.2	4-20	Rem.
2	79.5	307	22N	IND	48.3	4-23	Rem.
3	10.8	297	24N	IND	40.3	1-36	Rem.
4	164.5	322	76S	IND	29.2	1-2	Rem.
5	229.5	310	51S	IND	40.4	1	Rem.
6	238.5	62	75NW	IND	31.9	1-4	Oxd. Cal.
7	249.5	81	49S	IND	35.2	1-3	Open
8	259.6	74	57N	IND	22.6	2-3	Oxd. Cal.
9	263.6	65	62NE	IND	31.9	2-3	Oxd. Cal.
10	273.8	82	54N	IND	56.8	3-10	Rem.
11	279	88	76S	IND	10.3	2-3	Rem.
12	289.8	111	84S	IND	7.5	1	Rem.
13	337	76	57S	IND	38	1-2	Rem.
14	396.5	285	54N	IND	11.2	1-2	Rem.
15	415.7	292	84S	IND	49.3	1-10	Rem.
16	507.4	310	50N	IND	40.2	2-5	Rem.
17	527.6	317	22N	IND	82.3	2-20	Rem.
18	559	305	5N	IND	58.7	1-3	Rem.

Table A.12: Duckering Stairs, UAF Campus 2

Fracture	Distance from Origin (cm)	Strike	Dip	Length (cm)	Height (cm)	Aperture (mm)	Type of Fill
1	2	250	70N	IND	38.7	1-2	Rem.
2	15.2	260	70N	IND	52.3	1-2	Rem.
3	19.2	263	70N	IND	42.3	1-2	Rem.
4	70.5	287	3N	IND	250	1-10	Rem.
5	135.3	321	30N	IND	47	1-12	Rem.

Table A.13: Laklouy Hill 1

Fracture	Distance from Origin (cm)	Strike	Dip	Length (cm)	Height (cm)	Aperture (mm)	Type of Fill
1	12.2	30	78E	14.2	13.2	11	Cal.
2	17.8	24	81E	13.2	IND	1-3	Cal.
3	20.6	28	80E	16.9	7.4	1-7	Cal.
4	50.2	25	82E	21.7	11.8	11	Cal.
5	110.2	21	78E	35.2	13.1	42	Open

Table A.14: Laklouy Hill 2

Fracture	Distance from Origin (cm)	Strike	Dip	Length (cm)	Height (cm)	Aperture (mm)	Type of Fill
1	Random	15	76E	IND	7.1	1-8	Cal.
2	Random	12	83E	IND	8.1	1-3	Cal.
3	Random	2	86E	14.3	5.6	3	Cal.
4	Random	23	85E	14.3	4.8	2-3	Cal.

Table A.15: Birch Hill Fault #1

Fracture	Distance from Origin (cm)	Strike	Dip	Length (cm)	Height (cm)	Aperture (mm)	Type of Fill
1	10.2	299	85NW	IND	27.3	1-3	Rem.
2	15.1	276	37NW	IND	17.6	1	Rem.
3	25.8	279	74SW	IND	40.1	1-3	Rem.
4	39.2	96	75SW	IND	26.3	1-2	Rem.
5	41.4	103	65SW	IND	89.3	1-2	Rem.
6	46.2	248	54NW	5.3	30.6	2-3	Rem.
7	73.2	137	54SW	IND	23.3	1-2	Rem.
8	85.2	129	89SW	IND	17.2	1	Rem.
9	110.4	124	79SW	5.6	17.4	0.5-7	Rem.
10	115	149	81SW	4.4	74.6	2-3	Rem.
11	153	94	56SW	IND	47.8	1-12	Rem.
12	189.4	56	34SW	IND	55.4	1-2	Rem.
21	218.9	126	63SW	19.2	26.1	1-3	Rem.
14	335.0	135	43SW	IND	90.9	1-2	Rem.
15	344.6	100	63NW	IND	14.2	1	Rem.
16	357.6	108	67NW	IND	28.2	2-3	Rem.
17	367.6	280	46SW	IND	18.3	1	Rem.
18	396.2	277	43SW	IND	58	1-6	Rem.
19	422.3	292	45SW	IND	54.7	1-2	Rem.
20	431.4	286	46SW	IND	53.2	1	Rem.
21	464.6	79	88SW	IND	31.2	1	Rem.
22	469.3	96	45SW	IND	49.3	1-4	Rem.
23	485.6	111	44SW	IND	14.5	12	Rem.
24	496.6	316	73N	IND	14.4	1	Rem.
25	529.6	97	40SW	IND	101.3	2-3	Rem.

Table A.16: Birch Hill Fault 2

Fracture	Distance from Origin (cm)	Strike	Dip	Length (cm)	Height (cm)	Aperture (mm)	Type of Fill
1	15.8	69	87S	IND	31.6	1	Rem.
2	30.6	295	61N	IND	104.7	1-5	Rem.
3	32.2	297	71NE	IND	30.2	1	Rem.
4	35.6	311	44NE	IND	9.4	1	Rem.
5	42.6	93	59S	IND	142.5	1-4	Rem.
6	44.6	298	62S	IND	20.4	1-2	Rem.
7	64.4	117	67S	IND	98.8	1-5	Partial
8	73.2	91	65N	IND	15.8	2	Rem.
9	80	115	45S	IND	205.3	1-5	Rem.
10	90.6	115	87S	IND	132.1	1-5	Rem.
11	106.6	284	22N	IND	17.8	0.5	Rem.
12	107.8	108	39S	IND	58.7	1	Rem.
13	114.2	294	62N	IND	23.2	0.5	Rem.
14	131.4	279	11N	IND	16.8	0.5	Rem.
15	133.2	114	89S	IND	56.4	0.5	Rem.
16	162.2	124	7N	IND	29.2	0.5	Rem.
17	181.8	106	88S	2.9	76.7	1-2	Rem.
18	217.2	113	86S	IND	90.2	2-4	Rem.
19	219.4	126	39S	9.6	49.7	1-2	Rem.
20	235.4	114	89S	8.2	126.6	1-9	Rem.
21	240.9	115	84S	9.4	87.4	1	Rem.
22	259.4	97	70S	18.2	15m	1-30	Rem.
23	272.3	94	87S	14.3	20.4	0.5-1	Rem.
24	300.3	114	71S	12.7	51.4	0.5-1	Rem.
25	303.2	104	71S	11.6	15.6	1-2	Rem.

Table A.17: Birch Hill 1

Fracture	Distance from Origin (cm)	Strike	Dip	Length (cm)	Height (cm)	Aperture (mm)	Type of Fill
1	.2	144	48NE	16.3	84.3	0.5-FF	Rem.
2	10.3	114	27NE	IND	21.8	0.5-11	Rem.
3	23.6	144	85SW	9.9	24.3	4-FF	Rem.
4	43.2	138	66NE	IND	12.7	1	Rem.
5	53.6	148	69SW	IND	13.2	1-2	Rem.
6	70.8	129	53NE	IND	36.8	2	Rem.
7	86.6	138	78SW	26.9	26.8	FF	Rem.
8	106.2	123	58NE	8.1	11.9	FF	Rem.
9	125.4	137	82SW	IND	9.5	2-3	Rem.
10	144.6	164	89SW	45.8	14.6	1-44	Rem.
11	187.2	98	68SW	7.6	8.6	44	Rem.
12	207.6	98	62SW	59.8	90.6	44	Rem.
13	243.2	31	79E	12.8	22.1	0.5-FF	Rem.
14	255.2	138	48NE	107.2	28.7	FF	Rem.
15	277.3	183	86SW	107.2	27.4	1-FF	Rem.
16	279.2	132	54NE	107.2	25.4	FF	Rem.
17	290.2	170	90	134.6	71.2	2-FF	Rem.
18	309.8	140	47NE	2000	36.7	1-5	Rem.
19	341.2	172	87NE	45.2	9.6	FF	Rem.
20	345.2	136	79NE	40.4	12.6	1-2	Rem.
21	374.5	159	68NE	16.7	3.2	1-2	Rem.

Table A.18: Birch Hill 2

Fracture	Distance from Origin (cm)	Strike	Dip	Length (cm)	Height (cm)	Aperture (mm)	Type of Fill
1	19.4	310	62NW	IND	3.6	0.5	Rem.
2	30.4	299	52NW	IND	4.1	0.5	Rem.
3	36	97	59S	2.2	8.7	1	Rem.
4	49.8	63	63SE	2.3	12.6	0.5-5	Rem.
5	66.8	98	62S	IND	5.8	0.5	Rem.
6	75.6	97	62S	19.4	42.2	1-3	Rem.
7	83.4	249	46NW	8.2	4.2	FF	Rem.
8	93.2	225	66NW	IND	5.2	9	Rem.
9	99.2	247	63SE	20.8	30.7	1-2	Rem.
10	100.4	73	66SE	IND	2.8	1	Rem.
11	107.2	229	70NW	4.3	5.8	1	Rem.
12	121.8	103	77S	IND	14.8	1	Rem.
13	142.4	69	65SE	IND	13.2	1	Rem.
14	144.8	335	49N	1.5	4.8	0.5-1	Rem.
15	147.2	343	56NE	IND	14.1	1	Rem.
16	148.6	344	63NE	2.2	14.1	1	Rem.
17	149	347	75NE	IND	9.7	1-2	Rem.
18	152.4	184	71E	2.1	11.2	FF	Rem.
19	156.8	263	61NW	5.3	10.2	FF	Rem.
20	166.2	347	78NE	5.8	26.7	1-5	Rem.
21	177	327	55NE	IND	28.5	1-2	Rem.
22	178.2	185	85SW	9.2	27.2	1-4	Rem.
23	181.4	165	81SW	IND	26.3	1-FF	Rem.
24	191.2	19	84NE	IND	17.8	1-4	Rem.
25	219	77	84E	IND	18.8	1-10	Rem.

Table A.19: Birch Hill 3a

Fracture	Distance from Origin (cm)	Strike	Dip	Length (cm)	Height (cm)	Aperture (mm)	Type of Fill
1	0	299	76N	IND	31.6	5	Rem.
2	14.2	246	86NW	100	36.3	1-5	Rem.
3	32.3	17	61W	17.8	48.3	2-20	Rem.
4	37.8	244	76NW	24.3	182.3	1-34	Rem.
5	45.6	56	84W	IND	32.3	1-14	Rem.
6	77.2	49	30W	14.6	49.4	1-2	Rem.
7	106.2	194	75E	20.7	49.6	1-3	Rem.
8	98	211	86W	IND	2.5	0.5	Rem.

Table A.20 Birch Hill 3b

Fracture	Distance from Origin (cm)	Strike	Dip	Length (cm)	Height (cm)	Aperture (mm)	Type of Fill
1	14.5	236	71NW	IND	7.1	2	Rem.
2	19.8	251	74NW	IND	21.3	1	Rem.
3	29.4	101	78S	IND	21.5	1-4	Rem.
4	44.3	96	70S	3.2	47.2	1-3	Rem.
5	77.6	343	44NW	IND	14.2	1-2	Rem.
6	109.2	216	66W	IND	13.2	1-2	Rem.
7	127.2	11	50E	IND	50.9	1	Rem.
8	132.2	15	51E	IND	16.9	1-2	Rem.
9	143.6	56	62SE	IND	11.6	2-4	Rem.
10	163.4	350	75E	IND	17.4	1-10	Rem.
11	167	335	89E	IND	21.3	1-20	Rem.

Table A.21: Birch Hill 4a

Fracture	Distance from Origin (cm)	Strike	Dip	Length (cm)	Height (cm)	Aperture (mm)	Type of Fill
1	11.2	351	62NE	51.1	1.2	1	Rem.
2	18.4	337	61NE	30.2	2.4	FF	Rem.
3	30.2	346	62NE	91.8	4.6	FF	Rem.
4	36.8	355	57NE	84.2	17.6	FF	Rem.
5	48.4	345	81NE	40.9	13.1	FF	Rem.
6	75.2	357	76NE	73.6	6.1	FF	Oxd. Qtz.
7	104.2	348	59NE	56.6	3.1	FF	Oxd. Qtz.
8	109.1	344	84NE	54.6	4.5	FF	Oxd. Qtz.
9	115.1	342	72NE	48.2	0.9	FF	Oxd. Qtz.
10	135.0	353	75NE	17.9	1.6	FF	Oxd. Qtz.
11	136.5	354	79NE	8.3	1.5	FF	Oxd. Qtz.
12	142.4	346	76NE	17.2	0.4	1	Oxd. Qtz.
13	145.8	341	73NE	61.4	0.9	FF	Oxd. Qtz.
14	156.5	336	71NE	49.2	0.5	1	Oxd. Qtz.
15	170.5	353	86NE	36.2	1.9	FF	Oxd. Qtz.
16	186.5	352	86NE	28.2	0.3	FF	Oxd. Qtz.
17	191.7	354	85NE	26.4	2.1	0.5-1	Oxd. Qtz.
18	201.6	178	84SW	49.6	1.3	FF	Oxd. Qtz.
19	205.7	356	88NE	22.5	0.3	FF	Oxd. Qtz.
20	217.4	358	86NE	26.9	0.4	FF	Oxd. Qtz.

Table A.22: Birch Hill 4b

Fracture	Distance from Origin (cm)	Strike	Dip	Length (cm)	Height (cm)	Aperture (mm)	Type of Fill
1	13.5	82	72SE	38.3	0.4	1	Oxd. Qtz.
2	24	86	78SE	123.2	2.2	1	Oxd. Qtz.
3	49.6	88	74SE	100	1.2	1	Oxd. Qtz.
4	72	90	59SE	164.6	1.0	1	Oxd. Qtz.
5	87.9	92	71SE	76	0.8	1	Oxd. Qtz.
6	133.2	266	60NW	9.2	0.6	FF	Oxd. Qtz.
7	162.2	260	65NW	126.2	4.3	FF	Oxd. Qtz.
8	214.8	89	76SE	123.4	1.3	FF	Oxd. Qtz.
9	265.4	86	78SE	35.3	2.2	FF	Oxd. Qtz.
10	276.4	87	64SE	16.7	0.6	1	Oxd. Qtz.

Table A.23: Birch Hill 4c

Fracture	Distance from Origin (cm)	Strike	Dip	Length (cm)	Height (cm)	Aperture (mm)	Type of Fill
1	12.2	204	70W	33.8	6.1	2	Oxd. Qtz.
2	104.8	196	56W	48.1	1.2	1	Oxd. Qtz.
3	150.4	206	55W	33.6	0.9	1-2	Open
4	162.1	209	34W	18.7	1	1-2	Oxd. Qtz.
5	173.2	205	39W	17.4	0.3	1	Oxd. Qtz.
6	180.1	203	59W	12.8	0.7	FF	Oxd. Qtz.
7	194.8	104	58W	39.7	1	0.5-1	Oxd. Qtz.
8	203	195	57W	22.3	1.7	0.5-1	Oxd. Qtz.
9	211.4	187	62W	200	2	FF	Oxd. Qtz.
10	231.2	183	60W	37.9	1.6	FF	Oxd. Qtz.

Parks Highway Transects:

Table A.24: Parks Monument 1

Fracture	Distance from Origin (cm)	Strike	Dip	Length (cm)	Height (cm)	Aperture (mm)	Type of Fill
1	11.6	50	90	39.5	23.8	2-3	IND
2	24.1	20	78E	37.9	61	2-3	IND
3	17.8	15	86E	32.6	23.4	0.5-1	IND
4	38.2	355	83E	31.4	52.3	7	IND
5	43.2	43	84E	IND	85.2	0.5-1	IND
6	47.4	355	74E	IND	32.8	0.5-1	IND
7	55.4	359	83E	IND	89.3	0.5-5	IND
8	84.8	14	82W	9.4	64.7	0.5-2	IND
9	87.8	37	75W	11.2	68.9	0.5-3	IND
10	94.2	74	82E	15.4	135.3	0.5-20	IND
11	113.2	19	76E	9.3	45.6	0.5-FF	IND
12	125.2	24	74E	8.6	82.3	0.5-FF	IND
13	141.6	32	74E	11	74.6	0.5-FF	IND
14	144.8	44	76E	11.8	103	0.5-FF	IND
15	155.6	14	77E	8.4	49.4	1-FF	IND
16	165.1	22	85W	14.3	17.3	0.5-FF	IND
17	192.4	22	73E	21.6	97.5	1-FF	IND
18	210.6	42	76E	57.3	55.7	FF	IND
19	223.4	27	73E	4.9	154.6	0.5-FF	IND
20	239.2	26	82E	4.2	152.3	0.5-FF	IND
21	258.6	30	84E	3.2	147.3	1-8	IND
22	286.8	35	83W	IND	42.6	2-5	IND
23	300.4	23	85E	IND	45.2	0.5-6	IND
24	327	37	74E	IND	115.7	1-9	IND
25	337.4	38	74E	IND	177.6	0.5-12	IND

Table A.25: Parks Monument 2a

Fracture	Distance from Origin (cm)	Strike	Dip	Length (cm)	Height (cm)	Aperture (mm)	Type of Fill
1	17.6	59	74SE	46.4	108.6	1-4	IND
2	44.4	15	87SE	5.4	54.5	1-6	IND
3	55.4	62	81SE	15.6	267.4	1-FF	IND
4	58.6	63	81NW	59.7	267.4	1-FF	IND
5	61.4	58	88NW	76.3	267.4	1-FF	IND
6	65.2	62	85NW	103.4	267.4	1-FF	IND
7	72.8	24	73SE	IND	16.7	1-4	IND
8	77.6	53	78NW	IND	48.8	0.5-2	IND
9	105.4	58	63SE	IND	37.9	0.5-1	IND
10	132.2	122	78SE	IND	28.3	13	IND
11	144.3	136	73SE	15.7	28.6	12	IND
12	146.4	38	86SE	14.6	44.7	FF	IND
13	150.1	131	90	IND	24.3	1-17	IND
14	161.6	55	84SE	IND	13.6	0.5-4	IND
15	163.4	194	76NW	IND	14.2	1-FF	IND
16	177	59	76	61.3	224.3	FF	IND
17	186.2	186	77	IND	33.2	11	IND
18	203.2	69	66	78.6	137.2	0.5-FF	IND
19	230.2	29	76	38.7	51.4	1-FF	IND
20	241.3	193	82	90.2	53.2	FF	IND
21	242.2	72	78	22.8	28.2	FF	IND
22	247.3	30	75	50.7	32.4	FF	IND
23	250.2	104	68	61.9	38.2	FF	IND
24	268.4	31	84	IND	25.2	0.5-1	IND
25	282.3	53	67	9.5	118.6	0.5-FF	IND

Table A.26: Parks Monument 2b

Fracture	Distance from Origin (cm)	Strike	Dip	Length (cm)	Height (cm)	Aperture (mm)	Type of Fill
1	9.8	110	86S	82.7	3.8	FF	IND
2	18.8	105	87S	32.8	2.5	0.5-1	IND
3	20.4	104	89S	47.2	2.4	0.5-1	IND
4	29	109	84S	250	5.6	FF	IND
5	34.2	103	86S	50.8	7.2	1-FF	IND
6	46	106	86S	300	21.2	FF	IND
7	67.2	111	80S	70.1	3.3	1	IND
8	69.4	104	79S	57.4	7.6	1	IND
9	77.8	107	76S	19.4	2.3	0.5-1	IND
10	80.6	106	75N	200	10	FF	IND
11	85	105	86S	21.3	8.8	FF	IND
12	89.6	104	89S	55.6	11.7	FF	IND
13	95.4	103	88S	70.6	10.6	FF	IND
14	100.6	287	68N	250	14.3	FF	IND
15	137.2	112	84S	150	2.5	1-FF	IND
16	149.6	284	76N	84.6	6	0.5-FF	IND
17	153.2	282	85N	200	7.1	0.5-1	IND
18	154.8	107	83S	37.4	7.1	0.5-1	IND
19	163.8	100	86S	92.4	1.6	0.5-1	IND
20	172.2	101	88S	200	15.7	FF	IND

Table A.27: Park's Monument 3

Fracture	Distance from Origin (cm)	Strike	Dip	Length (cm)	Height (cm)	Aperture (mm)	Type of Fill
1	15.6	25	75E	IND	28.6	0.5-1	IND
2	19.4	30	74E	9.1	110.6	1-2	IND
3	21.6	181	52W	5.5	11.3	0.5	IND
4	34	32	70E	IND	29.3	1	IND
5	44.2	35	70E	IND	28.4	0.5-1	IND
6	48.8	205	82W	6.2	39.8	0.5-1	IND
7	63.2	37	83E	IND	16.3	0.5	Rem. Cal.
8	65.2	28	68E	IND	18.6	0.5	Rem. Cal.
9	100.2	202	84E	3.6	37.6	0.5-1	IND
10	102.6	24	58E	IND	73.4	0.5-1	IND
11	144	182	50W	10.4	28.6	0.5-1	IND
12	156.6	28	85E	6.3	79.6	1-2	IND
13	160.2	27	87E	5.4	148.4	1-2	IND
14	161.6	199	84W	8.3	48.2	1	IND
15	176.8	37	74E	30.2	154.3	1	IND
16	178.6	26	86E	31.2	46.5	1-2	IND
17	186.2	28	79E	29.1	30.8	1-3	IND
18	194.2	25	75E	28.7	53.4	1-2	IND
19	201.2	174	75W	28.4	32.8	1-2	IND
20	206.2	29	81E	IND	21.3	1	IND
21	215	23	71E	IND	34.7	0.5	Rem. Cal.
22	218.4	20	87E	IND	23.2	0.5-1	Rem. Cal.
23	239.6	37	87E	35.4	86.4	1-3	IND
24	244.2	201	89W	IND	26.3	0.5	IND
25	251	35	76E	74.2	134.3	1-10	IND

Table A.28: Mile 346 1

Fracture	Distance from Origin (cm)	Strike	Dip	Length (cm)	Height (cm)	Aperture (mm)	Type of Fill
1	9.8	144	84SW	19.6	3.6	0.5-1	IND
2	10.6	143	86SW	14.9	3.2	0.5-1	IND
3	15	140	89SW	14.6	3.5	1-2	Rem. Qtz
4	22.6	144	83SW	18.7	4.2	0.5-1	IND
5	29.2	145	82SW	13.3	3.4	FF	IND
6	35.4	145	84SW	27.5	18.6	2-4	Rem. Qtz.
7	40.2	320	78N	21.2	0.8	0.5	Oxi. Qtz.
8	43.2	326	78N	12.2	6.8	0.5	IND
9	55.6	331	79N	36.1	22.2	1-3	IND
10	88.8	320	74N	16.1	16.8	1-2	IND
11	157	282	73N	25.3	15.6	FF	IND
12	178.9	256	47NW	17	5.9	FF	IND
13	188.2	314	69N	8.2	3.1	2	IND
14	204.2	322	64N	2.2	3.4	1-2	IND

Table A.29: Mile 346 2

Fracture	Distance from Origin (cm)	Strike	Dip	Length (cm)	Height (cm)	Aperture (mm)	Type of Fill
1	14.2	12	85E	18.7	0.4	0.5-FF	IND
2	15.3	5	65E	17.3	0.4	0.5-FF	IND
3	18.2	359	86E	17.3	0.3	0.5	IND
4	19.1	1	87E	12.7	IND	0.5	IND
5	20.2	357	83E	13.4	IND	0.5	IND
6	21.6	3	86E	20.7	IND	0.5	IND
7	22.8	4	68E	15.2	6	0.5	IND
8	24.4	4	64E	8.4	1.8	0.5	IND
9	25.9	10	71E	13.7	0.7	0.5	IND
10	26.8	11	69E	11.2	1.1	0.5	IND

Table A.30: Mile 346 3

Fracture	Distance from Origin (cm)	Strike	Dip	Length (cm)	Height (cm)	Aperture (mm)	Type of Fill
1	13.2	183	72W	6.2	16.1	1-3	IND
2	18.8	182	64W	5.3	20.6	1-4	IND
3	24.2	189	77W	IND	9.1	1	IND
4	36.4	186	74W	5	12.1	FF	IND
5	56.2	11	88E	15.1	28.3	1-3	IND
6	73.4	171	67W	13.3	37.2	FF	IND
7	78.2	11	86E	IND	23.2	1-4	IND
8	81.4	212	80W	IND	23.1	1-4	IND
9	105.2	12	87E	40.3	57.4	1-3	IND
10	137.2	187	78W	13.9	23	FF	IND
11	145.1	215	73W	20.7	16.7	1-FF	IND
12	164.2	24	89E	16.2	12.8	FF	IND
13	182.4	344	84NE	IND	13.1	1-4	IND
14	187.1	11	78E	IND	12.7	1-2	IND
15	190.6	34	86E	IND	12.6	1-2	IND
16	199.2	17	86E	IND	12.8	1-3	IND
17	211.8	26	89E	IND	12.3	FF	IND
18	239.2	189	70W	IND	11.4	0.5-1	IND
19	250.4	189	72W	IND	11.9	0.5	IND
20	269.7	188	74W	IND	11.6	1	IND
21	287.2	14	89E	IND	8.2	1-2	IND
22	293.4	189	74E	17.1	25.8	1-FF	IND
23	306.4	12	71E	20.1	21.6	1-FF	IND
24	318.6	26	83E	12.4	15.3	FF	IND

Table A.31: Mile 345.5 1

Fracture	Distance from Origin (cm)	Strike	Dip	Length (cm)	Height (cm)	Aperture (mm)	Type of Fill
1	2.3	116	84SW	13.9	15.8	FF	IND
2	22.3	149	75NE	4.6	4.2	FF	IND
3	39.8	168	78SW	3.2	14.1	0.5-1	IND
4	45.5	349	86NE	2.4	0.6	FF	IND
5	60.8	352	70NE	0.4	1.6	FF	IND
6	62.9	348	74NE	8.5	5.6	FF	IND
7	77.6	356	69NE	19.2	6.9	0.5-1	IND
8	80.2	355	70NE	19.1	16.9	0.5-1	IND
9	87.8	4	71NE	13.4	15.8	0.5-1	IND
10	94.5	173	81SW	14.4	15.1	1-2	IND
11	98.1	4	70NE	7.1	3.4	FF	IND
12	101.0	161	83SW	6.1	19.2	0.5-1	IND
13	95	165	80SW	6.5	8.9	0.5-1	IND
14	110.4	346	86NE	5.2	21.6	0.5-1	IND
15	111.2	341	81NE	4.6	8.6	0.5-1	IND
16	115	340	82NE	5.8	11.1	0.5-1	IND
17	124.1	169	82SW	16.1	19.2	1	IND
18	125.4	164	81SW	12.9	13.9	1	IND
19	126.4	167	83SW	3.9	3.1	0.5-1	IND
20	131	156	85SW	17.4	28.1	0.5	IND
21	142.4	166	84SW	13.9	21.5	0.5-FF	IND
22	152.8	164	86SW	16.4	31.2	0.5-1	IND
23	157.2	157	88SW	7.1	10.9	0.5	IND
24	161.5	343	88SW	8	6.6	0.5	IND
25	167.8	345	89NE	13.9	27.2	0.5	IND
26	173.2	166	86SW	5.3	26.2	0.5	IND
27	186.4	344	72NE	8.2	27.6	0.5	IND

Table A.32: Mile 345.5 2

Fracture	Distance from Origin (cm)	Strike	Dip	Length (cm)	Height (cm)	Aperture (mm)	Type of Fill
1	9.4	256	83NW	55.2	3.2	FF	IND
2	19.1	249	85NW	39.2	3.9	FF	IND
3	21.9	259	74NW	5.3	1.4	FF	IND
4	29.8	252	68NW	60.8	5.6	FF	IND
5	42.8	56	77SE	9.5	0.6	FF	IND
6	44.6	55	79SE	9.6	0.5	FF	IND
7	45	54	82E	12.9	1.1	FF	IND
8	45.8	59	87SE	17.2	4.2	FF	IND
9	47.2	240	76NW	54.7	7.1	FF	IND
10	50.4	57	80NW	13.9	1.3	FF	IND
11	77.2	59	87SE	13.4	14.2	FF	IND
12	77.8	348	84SE	19.1	8.2	FF	IND
13	79.8	236	62NW	32.1	16.2	FF	IND
14	87	48	88SE	29.1	19.6	FF	Rem. Qtz.
15	95.8	249	69NW	30.6	11.8	FF	IND
16	100.1	251	64NW	11.6	2.6	FF	IND
17	107.2	259	69NW	18.4	14.6	FF	IND
18	164.4	47	85SE	20.6	9.1	FF	IND
19	173.2	56	80SE	54.2	2.1	FF	IND
20	181.2	46	86SE	100	10.2	FF	IND

Table A.33: Mile 340 1

Fracture	Distance from Origin (cm)	Strike	Dip	Length (cm)	Height (cm)	Aperture (mm)	Type of Fill
1	14.2	290	79N	30.8	9.2	1-FF	IND
2	18.8	285	76N	44.7	10.3	1-FF	IND
3	29.6	304	87NE	90.4	27.6	1-3	IND
4	34.2	306	87NE	39.2	26.3	0.5-2	IND
5	35.2	315	81NE	7.3	6.4	0.5-1	IND
6	36	314	83NE	14.8	5.9	0.5-FF	IND
7	38.4	131	82S	12.7	10.4	1-FF	IND
8	43.2	134	84S	23.6	14.2	0.5-1	IND
9	46.1	130	89S	26.4	22.1	0.5-2	IND
10	48.8	151	84S	16.2	16.4	0.5-1	IND
11	62.8	182	73SW	10.3	5.4	0.5	IND
12	70.6	149	87SW	27.4	27.8	0.5	IND
13	83.2	168	89SW	9.1	19.3	0.5	IND
14	84.3	191	85SW	6.2	11.1	0.5-FF	IND
15	90.6	296	54N	8.3	10.3	FF	IND
16	107.2	299	56NW	43.4	27.2	1-FF	IND
17	109.4	134	75S	10.9	18.3	0.5-2	IND
18	116.3	151	87S	25.1	17.1	0.5	IND
19	129.4	149	89S	16.9	17.4	0.5-FF	IND
20	142.4	161	77S	20.4	20.1	0.5-FF	IND
21	154.6	314	64N	16.8	8.3	0.5	IND
22	164.2	328	87N	52.6	28.7	1-FF	IND
23	171.2	341	84N	39.3	15.2	0.5-FF	IND
24	180.4	356	69N	34	29.6	0.5-FF	IND
25	190.2	19	61S	14.2	23.2	FF	IND

Table A.34: Mile 340 2

Fracture	Distance from Origin (cm)	Strike	Dip	Length (cm)	Height (cm)	Aperture (mm)	Type of Fill
1	10.8	77	87SE	32.8	12.1	FF	Oxidized
2	18.1	86	88N	18.3	14.1	FF	Oxidized
3	30.2	259	89N	20.4	8.9	FF	Oxidized
4	63.9	81	80SE	42.7	6.1	FF	Oxidized
5	64.6	84	82SE	19.8	4.6	FF	Oxidized
6	88.2	74	89SE	34.2	11.1	FF	Oxidized
7	92.1	78	84SE	31.9	10.7	FF	Oxidized
8	92.5	70	85SE	49.5	13.8	FF	Oxidized
9	95.6	247	88N	19.9	7.8	FF	Oxidized
10	116.2	68	84SE	24.1	1.9	FF	Oxidized
11	119.6	74	79SE	54.5	4.1	FF	Oxidized

Table A.35: Mile 340 3

Fracture	Distance from Origin (cm)	Strike	Dip	Length (cm)	Height (cm)	Aperture (mm)	Type of Fill
1	23.2	222	87W	25.2	5.1	FF	Oxidized
2	31.2	221	86W	13.9	6.8	FF	Oxidized
3	37.4	46	78E	13.1	2.2	FF	Oxidized
4	35.2	43	89E	11.9	1.7	FF	Oxidized
5	42.1	45	74E	7.9	1.3	FF	Oxidized
6	44.6	44	75E	14	2.1	FF	Oxidized
7	75.2	228	87W	34.8	5.6	FF	Oxidized
8	94.6	52	74E	5.1	8.2	FF	Oxidized

Table A.36: Mile 339 1

Fracture	Distance from Origin (cm)	Strike	Dip	Length (cm)	Height (cm)	Aperture (mm)	Type of Fill
1	0	147	74SW	32.3	56.2	FF	IND
2	1.2	153	77SW	8.4	19.6	FF	IND
3	73.6	169	54SW	IND	77.4	0.5-2	IND
4	108.2	182	26SW	2.1	91.5	2-5	IND
5	156	349	53NE	IND	41.2	1-2	IND
6	156.4	166	53SW	4.0	33.2	1-2	IND
7	189.2	185	34SW	1.4	66.2	1-4	IND
8	257.6	166	81SW	5.1	68.1	1-3	IND
9	226.8	166	53SW	IND	45.4	1-2	IND
10	265.2	334	30NE	IND	145.4	1-10	IND
11	269.8	179	53SW	IND	51.8	0.5-1	IND
12	279	174	56SW	7.2	12.5	FF	IND
13	305.4	168	66SW	IND	55.7	0.5-1	IND
14	377.2	161	66SW	3.1	22.9	1-2	IND
15	484.3	178	58SW	21.4	25.8	2-7	IND

Table A.37: Mile 339 2

Fracture	Distance from Origin (cm)	Strike	Dip	Length (cm)	Height (cm)	Aperture (mm)	Type of Fill
1	13.2	311	76NE	40.8	14.3	1-4	IND
2	32.4	163	86SW	36.4	39.7	1-3	IND
3	117.4	173	84SW	10.3	45.3	0.5-1	IND
4	152.6	151	89SW	32.1	13.4	1-FF	IND
5	159.2	218	89NW	15.8	12.8	0.5-1	IND
6	166.2	215	89NW	15.9	11.1	0.5-1	IND
7	176.2	217	90	10.2	9.8	0.5-1	IND
8	185.6	207	90	9.8	9.8	0.5-1	IND

Table A.38: Mile 339 3

Fracture	Distance from Origin (cm)	Strike	Dip	Length (cm)	Height (cm)	Aperture (mm)	Type of Fill
1	10.2	74	73S	232.6	91.3	FF	Oxidized
2	13.1	76	70S	22.6	2.3	FF	Oxidized
3	42.3	67	76S	78.2	36.7	FF	Oxidized
4	48.2	69	73S	34.6	7.2	FF	Oxidized
5	84.2	75	76S	26.4	31.8	FF	Oxidized
6	125.4	82	86S	30.4	2.3	FF	Oxidized
7	158.2	86	85S	16.7	4.3	FF	Oxidized
8	202.1	73	84S	9.8	25.2	FF	Oxidized
9	253.1	64	75S	37.2	19.6	FF	Oxidized
10	273.4	72	79S	11.9	3.9	FF	Oxidized
11	312.6	67	59S	75.4	44.6	FF	Oxidized
12	341	66	78S	10.6	5.1	FF	Oxidized

Table A.39: Mile 339 4

Fracture	Distance from Origin (cm)	Strike	Dip	Length (cm)	Height (cm)	Aperture (mm)	Type of Fill
1	10	74	79S	250	57.8	FF	IND
2	102.4	68	85S	47.3	56.1	FF	IND
3	247.4	73	87S	194.6	49.7	FF	IND
4	409.6	76	79S	400	82.3	FF	IND
5	493.6	83	81S	34.1	17.9	FF	IND
6	584.6	85	84S	107.6	49.7	FF	IND

Table A.40: Mile 339 5:

Fracture	Distance from Origin (cm)	Strike	Dip	Length (cm)	Height (cm)	Aperture (mm)	Type of Fill
1	9.4	130	88SW	35.4	5.3	FF	Oxidized
2	45.4	148	74SW	66.1	57.2	1-2	Oxidized
3	79.6	149	78SW	18.2	21.6	1-2	Oxidized
4	146.4	131	85SW	18.6	27.2	FF	Oxidized
5	211.2	129	74SW	77.9	47.2	FF	Oxidized
6	299.2	128	82SW	7.1	10.2	FF	Oxidized
7	319.2	132	87SW	11.1	8.4	1-2	Oxidized
8	474.2	141	82SW	80.2	77.4	FF	Oxidized
9	505.4	142	78SW	20.2	31.6	FF-2	Oxidized
10	525.8	138	86SW	24.1	65.2	1-3	Oxidized
11	533.2	141	81SW	15.2	17.1	1-2	Oxidized
12	537.2	131	86SW	12.6	34.4	1-2	Oxidized
13	546.2	309	81NW	13.1	11.2	FF	Oxidized
14	555.2	316	83NW	33.7	46.3	FF	Oxidized
15	562.5	139	82SW	21.6	34.5	FF	Oxidized
16	674.2	134	83SW	100	200	1-FF	Oxidized

Table A.41: Mile 325

Fracture	Distance from Origin (cm)	Strike	Dip	Length (cm)	Height (cm)	Aperture (mm)	Type of Fill
1	0	161	77S	4.9	7.9	FF	IND
2	14.2	167	78S	4.7	8.7	1-2	IND
3	16.1	174	79S	9.2	7.1	FF	IND
4	19.2	177	72S	8.1	9.2	FF	IND
5	43.1	195	71SW	15.1	17.6	1-2	IND
6	51.8	181	69SW	1.2	14.7	1	IND
7	70	188	79SW	8.2	11.3	1-2	IND
8	83.9	341	84NE	7.1	16.7	FF	IND
9	89.4	328	72NE	14.1	22.6	1	IND
10	99.1	181	86S	14.3	31.2	1-2	IND
11	103.4	179	74S	16.4	29.1	1-2	IND
12	110.5	183	84SW	12.1	21.1	1-2	IND
13	112.6	3	88NE	4.6	14.6	1-2	IND
14	123.7	349	87NE	1.9	11.6	FF	IND
15	127.5	148	76S	13.1	13.4	FF	IND
16	131.9	181	83S	9.8	11.3	1-2	IND
17	143.8	172	85NE	5.6	9.8	1	IND
18	149.8	178	79S	2.3	7.8	0.5-1	IND
19	165.8	171	68S	2.2	10.7	1-2	IND
20	171.4	159	80S	2	8.6	1-2	IND
21	193	179	82S	6.5	12.3	0.5-1	IND
22	197.7	172	86S	4.9	3.4	FF	IND
23	207.3	1	84NE	24.2	35.2	FF	IND
24	216.5	142	86S	16.5	20.6	FF	IND
25	224.2	183	66S	4.9	19.8	0.5-1	IND
26	225.5	184	84S	4.6	6.2	FF	IND

Table A.42: Mile 323 1

Fracture	Distance from Origin (cm)	Strike	Dip	Length (cm)	Height (cm)	Aperture (mm)	Type of Fill
1	9.4	197	88W	IND	29.8	1-2	IND
2	74.8	66	65E	8.2	21.5	FF	Oxidized
3	120.6	76	51E	6.3	11.4	FF	IND
4	126.2	68	49E	10.9	16.5	FF	IND
5	189.2	86	60E	21.4	10.3	FF	IND
6	204.8	46	71E	33.6	23.9	1	IND
7	262.4	213	57W	28.7	29.6	1	IND
8	273	53	50E	9.5	9.2	FF	IND

Table A.43: Mile 323 2

Fracture	Distance from Origin (cm)	Strike	Dip	Length (cm)	Height (cm)	Aperture (mm)	Type of Fill
1	19.6	331	84SW	6.1	64.2	1-2	IND
2	43.4	161	74SW	IND	8.7	1	IND
3	45.4	159	81SW	17.6	22.9	1	IND
4	143.2	304	86NE	127.6	163.6	FF	IND
5	191.4	324	85NE	3.2	25.4	FF	IND
6	196.7	328	81NE	IND	33.1	1	IND
7	312.2	307	85NE	1.2	17.1	1	IND
8	334.5	329	84NE	6.4	8.7	0.5-1	IND
9	339.2	331	86NE	3.6	10.4	FF	IND
10	341.6	321	81NE	4.1	16.4	FF	IND
11	357.2	332	86NE	12.6	104.2	FF	IND
12	358.4	323	87NE	4.7	19.7	1-2	IND
13	426.4	164	76SW	54.6	200	1-2	IND
14	445.2	333	82NE	3.6	97.6	1	IND
15	504.8	164	76SW	IND	38.7	1-2	IND
16	540.4	157	84SW	25.8	24.6	1-FF	IND
17	542.4	158	73SW	23.1	41.2	1-3	IND
18	590.2	150	83SW	IND	30.6	1	IND
19	598.4	325	82NE	IND	37.3	1	IND
20	639.4	322	87NE	IND	11.3	1	IND
21	673.2	164	79SW	11.6	61.2	1-3	IND
22	696.3	145	86NE	IND	40.3	1-2	IND

Table A.44: Mile 321 1

Fracture	Distance from Origin (cm)	Strike	Dip	Length (cm)	Height (cm)	Aperture (mm)	Type of Fill
1	0	152	58S	66.2	57.4	FF	IND
2	31.6	296	78N	18.7	13.2	FF	IND
3	105.2	124	76S	79.2	59.6	FF	IND
4	163.4	123	76S	20.8	50.7	FF	IND
5	205.4	125	84S	17.2	18.1	FF	IND
6	222.3	303	75N	37.6	31.2	FF	IND
7	242.3	129	86S	116.3	39.2	FF	IND
8	283.2	299	82N	16.9	6.3	FF	IND
9	308.6	300	86N	82.3	39.2	FF	IND
10	357.3	306	84N	32.1	40.6	FF	IND

Table A.45: Mile 321 2

Fracture	Distance from Origin (cm)	Strike	Dip	Length (cm)	Height (cm)	Aperture (mm)	Type of Fill
1	10.8	188	84NW	2.3	9.3	FF	IND
2	89.6	21	78E	2.6	31.8	1-2	IND
3	103.4	208	86NW	IND	8.1	1-2	IND
4	130.8	14	76E	1.3	6.1	FF	IND
5	174.6	20	81E	3.6	32.1	FF	IND
6	194.4	12	74E	1.3	16.4	1-2	IND
7	197.8	14	78E	2.4	14.6	1-2	IND
8	199.2	16	72E	1.4	13.7	1-2	IND
9	202.1	11	70E	IND	7.4	0.5-1	IND
10	213.2	25	81E	3.6	15.8	1-3	IND
11	228.6	204	79NW	9.8	11.2	FF	IND

Table A.46: Mile 313 1

Fracture	Distance from Origin (cm)	Strike	Dip	Length (cm)	Height (cm)	Aperture (mm)	Type of Fill
1	9.8	122	86S	34.7	14.2	FF	IND
2	17.4	121	84S	66.9	12.8	FF	IND
3	21.2	126	86S	13.2	2.7	FF	IND
4	70.2	124	87S	174.6	4.1	FF	IND
5	116.2	134	83S	31.6	3.2	FF	IND
6	137.4	138	84S	20.2	2.3	FF	IND
7	162.1	134	76S	15.3	7.6	FF	IND
8	175	129	86S	7.4	1.2	FF	IND
9	181.4	122	84S	18.3	0.4	FF	IND
10	197.1	125	82S	9.2	0.4	FF	IND
11	196.7	124	86S	38.2	1.9	FF	IND
12	260.1	131	82S	91.7	6.1	FF	IND
13	269.2	132	84S	38.7	0.5	FF	IND
14	301.5	130	83S	26.4	1.3	FF	IND
15	305.7	121	84S	22.6	2.3	FF	IND
16	310.6	123	87S	17.2	4.3	FF	IND

Table A.47: Mile 313 2

Fracture	Distance from Origin (cm)	Strike	Dip	Length (cm)	Height (cm)	Aperture (mm)	Type of Fill
1	12.2	35	84E	49	1.2	1	IND
2	25.9	41	86E	41.9	1.1	0.5-1	IND
3	36.2	41	75E	40.8	1.8	1-2	IND
4	55.4	44	52W	79.2	1.4	1-2	IND
5	58.2	45	79E	60.1	2.1	FF	IND
6	71.5	42	50W	29.1	0.6	1-2	IND
7	79	45	40W	35.6	2.9	0.5-1	IND

Table A.48: Mile 313 3

Fracture	Distance from Origin (cm)	Strike	Dip	Length (cm)	Height (cm)	Aperture (mm)	Type of Fill
1	10	36	69W	6.9	0.8	FF	IND
2	12.9	37	71W	21.6	2.1	FF	IND
3	29.6	39	72E	29.9	3.2	FF	IND
4	54.5	36	54W	28.4	1.1	1-2	IND
5	62	41	85E	35.2	1.3	FF	IND

Table A.49: Monderosa Grill 1

Fracture	Distance from Origin (cm)	Strike	Dip	Length (cm)	Height (cm)	Aperture (mm)	Type of Fill
1	10.2	336	79NE	IND	22.7	0.5-1	IND
2	26.2	324	89NE	2.0	23.4	0.5-1	IND
3	51.2	159	74SW	5.3	20.3	1-FF	IND
4	58.3	84	45S	6.4	42.4	2-FF	IND
5	59.2	326	89N	3.6	22.6	FF	IND
6	65	182	70SW	35.2	57.4	1-FF	IND
7	97.2	161	79SW	IND	49.4	0.5-1	IND
8	110.3	165	68SW	2.9	31.4	1-FF	IND
9	137.2	341	90	22.1	39.4	FF	IND
10	145.4	254	89NW	25.3	42.3	1-FF	IND
11	152.2	352	82SW	16.6	28.2	FF	IND
12	160.3	71	75NE	17.6	26.2	1-FF	IND
13	168.8	357	90	60.2	43.7	FF	IND
14	211.2	253	69NW	46.7	55.8	FF	IND
15	252.3	151	70SW	52.6	55.7	FF	IND
16	273.2	250	84NW	14.7	5.7	FF	IND
17	274.1	261	90	16.8	9.6	FF	IND
18	301.8	266	90	10.1	5.8	FF	IND
19	325.2	325	72NE	3.2	31.1	1-2	IND
20	371.6	354	70NE	IND	43.8	1-2	IND
21	399.8	260	86SE	IND	21.8	1-2	IND
22	432.2	106	78S	IND	8.2	1	Qtz.
23	434.8	99	80S	5.1	22.1	FF	Qtz.
24	453	354	69N	IND	13.1	1-2	IND
25	470.2	345	68	11.8	13.4	FF	IND

Table A.50: Monderosa Grill 2

Fracture	Distance from Origin (cm)	Strike	Dip	Length (cm)	Height (cm)	Aperture (mm)	Type of Fill
1	0	225	73S	58.7	IND	1-3	Qtz.
2	9.4	235	69S	154.2	IND	1-5	Qtz.
3	13.8	212	76N	33.4	IND	1	Qtz.
4	23.6	229	86S	23.1	IND	0.5-FF	Qtz.
5	27.2	234	77S	110/4	IND	1-3	Qtz.
6	32.2	238	86N	8.8	IND	1	Qtz.
7	35.2	237	77S	6.7	IND	0.5-1	Qtz.
8	36.1	237	76S	15.4	IND	1-1.5	Qtz.
9	36.4	237	82S	12.8	IND	0.5-1	Qtz.
10	53.6	253	83S	5.3	IND	1	Qtz.
11	53.8	255	77S	8.2	IND	1	Qtz.
12	54.8	256	79S	26.7	IND	0.5-1	Qtz.
13	62	242	69S	23.1	IND	1-2	Qtz.
14	63.4	234	68S	16.7	IND	0.5-1	Qtz.
15	65	231	68S	39.4	IND	1-2	Qtz.
16	68.5	247	69S	31.7	IND	1-2	Qtz.
17	73.5	235	68S	25.5	IND	0.5-2	Qtz.
18	75	249	78S	5.9	IND	0.5-1	Qtz.
19	77.4	236	74S	24.5	IND	1-4	Qtz.
20	78.4	231	63S	22.8	IND	1-4	Qtz.
21	82	226	64S	34.2	IND	1-4	Qtz.
22	86.4	226	68S	40.2	IND	1-5	Qtz.
23	89.2	224	69S	18.4	IND	1-4	Qtz.
24	91	226	68S	24.3	IND	1-4	Qtz.

Table A.51: Monderosa Grill 3a

Fracture	Distance from Origin (cm)	Strike	Dip	Length (cm)	Height (cm)	Aperture (mm)	Type of Fill
1	2.3	166	84SE	96.4	57.2	FF	IND
2	49.2	167	88SE	94.8	61.2	1-2	IND
3	75.2	162	89SE	19.2	41.6	1-2	IND
4	96.1	168	82SE	20.2	34.6	FF	IND
5	105.6	169	83SE	22.9	24.6	FF	IND
6	116.9	166	76NW	85.1	24.2	FF	IND
7	131.6	175	74NW	35.7	6.2	FF	IND
8	135.4	342	84NW	6.4	0.4	FF	IND
9	137.8	346	83NW	27.2	0.9	1-FF	IND
10	140.7	162	83SE	6.8	0.8	FF	IND
11	149.2	168	77SE	72.6	22.6	FF	IND
12	163.1	171	81SE	59.4	10.7	FF	IND
13	160.5	170	82SE	128.3	72.6	FF	IND
14	207.4	168	89NW	50.1	33.6	0.5-1	IND
15	213.2	174	87SE	85.7	37.2	FF	IND

Table A.52: Monderosa Grill 3b

Fracture	Distance from Origin (cm)	Strike	Dip	Length (cm)	Height (cm)	Aperture (mm)	Type of Fill
1	2	213	75W	72.4	31.2	FF	IND
2	55.2	215	74W	11.6	8.2	FF	IND
3	94.2	214	81W	27.1	11.2	FF	IND
4	95.4	219	84W	26.2	5.1	FF	IND
5	100.6	217	72W	15.1	8.2	FF	IND
6	109.6	214	76W	21.2	5.2	FF	IND
7	112.8	219	87E	13.6	2.9	FF	IND
8	124.2	216	69E	4.3	7.3	FF	IND
9	127.2	207	73W	36.8	7.6	FF	IND
10	112.6	208	84W	36.9	10.2	FF	IND
11	116.1	202	79E	15.2	6.4	FF	IND
12	136.4	211	78W	26.8	6.8	FF	IND
13	143.6	207	71W	13.6	5.2	FF	IND
14	155.9	210	69W	9.8	4.6	FF	IND
15	160.2	206	81W	31.6	7.8	FF	IND

Nenana Area Transects:

Table A.53: Nenana 1a

Fracture	Distance from Origin (cm)	Strike	Dip	Length (cm)	Height (cm)	Aperture (mm)	Type of Fill
1	5	67	IND	8	IND	0.5	Cal.
2	8	69	32NW	32	IND	1	Cal.
3	12	70	IND	7.5	IND	0.5	Cal.
4	24	60	IND	29	IND	1	Cal.
5	27	70	IND	36	IND	0.5	Cal.
6	28.3	70	IND	27	IND	1	Cal.
7	29.7	70	IND	20	IND	1	Cal.
8	29	70	IND	18	IND	1	Cal.
9	29.5	70	IND	17	IND	1	Cal.
10	31	70	IND	94	IND	5	Cal.
11	40.5	70	IND	16	IND	0.5	Cal.
12	43.5	70	IND	77	IND	1	Cal.
13	45	70	IND	47	IND	1	Cal.
14	51.5	70	IND	25	IND	1	Cal.
15	52	50	IND	19	IND	1	Cal.
16	61	65	IND	10	IND	1	Cal.
17	65	35	IND	29	IND	1	Cal.
18	76	70	IND	24	IND	1-2	Cal.
19	83	72	IND	32	IND	3	Cal.
20	88.5	75	IND	60	IND	0.5	Cal.
21	90.5	70	IND	24	IND	0.5	Cal.
22	93.5	78	IND	23	IND	3	Cal.
23	95.3	80	IND	4	IND	1	Cal.
24	96	35	IND	10	IND	0.5-1	Cal.
25	98	75	IND	163	IND	2	Cal.
26	101	10	IND	107	IND	1-4	Cal.

Table A.54: Nenana 1b

Fracture	Distance from Origin (cm)	Strike	Dip	Length (cm)	Height (cm)	Aperture (mm)	Type of Fill
1	10.6	259	44	10.6	4.7	0.5-1	Cal.
2	19.1	251	31	9.3	5.1	0.5-1	Cal.
3	22.6	69	32	33.1	5.2	1-2	Cal.
4	25.9	61	IND	4.7	IND	0.5	Cal.
5	28.4	56	11	19.6	3.4	0.5-1	Cal.
6	39.5	64	IND	14.6	4.1	0.5	Cal.
7	40	65	IND	17.6	IND	0.5	Cal.
8	40.8	64	IND	32.8	IND	0.5	Cal.
9	42	67	IND	21.6	IND	0.5	Cal.
10	42.7	65	IND	18.2	IND	0.5	Cal.
11	43.8	64	IND	18.7	IND	0.5	Cal.
12	44.5	70	49	85.7	5	FF	Cal.
13	48.4	59	IND	3.8	IND	0.5	Cal.
14	54.2	67	IND	11.1	IND	0.5	Cal.
15	57.3	73	43	100.2	4.3	1-2	Cal.
16	58.9	68	44	45.2	2.9	1	Cal.
17	65.8	69	56	43.1	2.2	1	Cal.
18	66.7	72	56	62.4	IND	0.5	Cal.
19	74.6	73	IND	13.5	IND	0.5	Cal.
20	81	76	IND	166.5	IND	FF	Cal.

Table A.55: Nenana 1c

Fracture	Distance from Origin (cm)	Strike	Dip	Length (cm)	Height (cm)	Aperture (mm)	Type of Fill
1	0	199	81E	200	56.2	1-3	Cal.
2	31.2	189	82E	26.7	13.4	FF	Cal.
3	52.8	187	80E	123.7	29.2	1-3	Cal.
4	83.4	192	58W	33.2	1.2	1-2	Cal.
5	125.8	188	38E	106.8	63.2	1-2	Cal.
6	130.2	189	82E	26.2	1.2	1	Cal.
7	132.4	187	79W	46.1	1.6	1-2	Cal.
8	142.1	198	36E	16.2	2.1	FF	Cal.
9	161.4	177	84W	82.4	26.2	1-2	Cal.
10	175.8	174	71W	58.4	6.2	1	Cal.
11	188.5	190	76E	22.1	5.8	1-3	Cal.
12	195	175	64E	26.5	3.8	FF	Cal.
13	207.6	191	84E	13.6	16.8	FF	Cal.
14	209.4	186	87E	8.7	7.6	1	Cal.
15	215.6	176	81W	13.8	3.9	FF	Cal.

Table A.56: Nenana 2

Fracture	Distance from Origin (cm)	Strike	Dip	Length (cm)	Height (cm)	Aperture (mm)	Type of Fill
1	3.2	76	77NW	65.3	IND	1	Cal.
2	7.5	75	69SE	10.2	IND	1	Cal.
3	17.6	76	82NW	146	IND	1-1.5	Cal.
4	20.7	78	70SE	20.6	IND	1	Cal.
5	24.7	75	75NW	137.5	IND	1	Cal.
6	40.3	75	64SE	59	IND	1-1.5	Cal.
7	46.5	75	79SE	122.4	IND	1-1.5	Cal.
8	52.6	80	77NW	48	IND	1	Cal.
9	57	78	69SE	76.7	IND	1.5	Cal.
10	67.3	80	82NW	36.5	IND	0.5	Cal.
11	73	125	70SE	5.1	IND	0.5	Cal.
12	74.5	83	75NW	157	IND	1-7	Cal.
13	80	119	64SE	244	IND	1-2	Cal.
14	84	80	79SE	163	IND	1	Cal.
15	87	120	77NW	97.6	IND	1	Cal.
16	91.5	74	69SE	78	IND	1-15	Cal.
17	93	105	82NW	54	IND	0.5-1	Cal.
18	94.6	83	70SE	30.3	IND	0.5	Cal.
19	101.7	75	75NW	68	IND	0.5-1	Cal.
20	121	73	64SE	66	IND	0.5-1	Cal.
21	128.4	124	79SE	66.2	IND	1-1.5	Cal.
22	128.8	74	77NW	66.5	IND	1-1.5	Cal.
23	132	70	69SE	127	IND	1	Cal.
24	138	75	82NW	74.3	IND	1	Cal.
25	144.3	79	70SE	155.2	IND	0.5-1	Cal.

Table A.57: Nenana 3a

Fracture	Distance from Origin (cm)	Strike	Dip	Length (cm)	Height (cm)	Aperture (mm)	Type of Fill
1	4.3	80	73SE	75	IND	1	Rem. Cal.
2	21.2	78	80SE	56.3	IND	2	Cal.
3	26.4	35	77SE	62	IND	1-3	Cal.
4	43.7	85	77SE	117.6	IND	1	Rem. Cal.
5	60.7	83	85SE	124.6	IND	2-6	Cal.
6	69.3	85	73SE	15	IND	1	Rem. Cal.
7	72.4	60	80SE	15.4	IND	1-2	Cal.
8	76.1	84	77SE	149.3	IND	1-3	Cal.
9	17.2	42	77SE	77.3	IND	1-2	Rem. Cal.
10	79.3	79	85SE	177.3	IND	1-4	Cal.
11	86.3	84	73SE	55.4	IND	1-2	Rem. Cal.
12	91.6	81	80SE	82.3	IND	1-2	Cal.
13	105.6	79	77SE	54.2	IND	1	Cal.
14	115.3	125	77SE	170.3	IND	1-5	Rem. Cal.
15	117.1	89	85SE	31.6	IND	0.5-1	Cal.
16	122.3	132	73SE	162.4	IND	1-2	Rem. Cal.
17	129.1	81	80SE	24.6	IND	1	Cal.
18	137.2	79	77SE	177.2	IND	1-5	Cal.
19	141.9	81	77SE	122.1	IND	1-2	Rem. Cal.
20	144.6	81	85SE	134.7	IND	1-13	Cal.
21	146.7	79	73SE	177.5	IND	1-13	Rem. Cal.
22	151.9	112	80SE	59.6	IND	1	Cal.
23	154.4	81	77SE	26.3	IND	0.5-1	Cal.
24	164.6	139	77SE	307.5	IND	1-12	Rem. Cal.
25	168.5	77	85SE	30.3	IND	0.5-1	Cal.

Table A.58: Nenana 3b

Fracture	Distance from Origin (cm)	Strike	Dip	Length (cm)	Height (cm)	Aperture (mm)	Type of Fill
1	15.6	333	71NE	37.3	0.6	1	Oxi. Cal.
2	37.3	329	57NE	187.6	0.8	0.5	Oxi. Cal.
3	184.3	336	IND	74.1	IND	1	Oxi. Cal.
4	235.4	328	76NE	157.6	IND	0.5-1	Oxi. Cal.
5	245.8	329	IND	25.2	IND	0.5	Oxi. Cal.
6	261.5	327	68	92.1	0.3	0.5-1	Oxi. Cal.
7	291.4	321	IND	37.5	IND	0.5-1	Oxi. Cal.
8	318.9	325	IND	54.5	IND	0.5-1	Oxi. Cal.
9	344	322	58	500	1.2	1	Oxi. Cal.
10	405.9	321	IND	72.9	IND	0.5-1	Oxi. Cal.
11	448.9	316	57	300	0.6	1-2	Oxi. Cal.
12	455.6	314	IND	88.6	IND	1-2	Oxi. Cal.
13	474.2	309	IND	119.6	IND	0.5	Oxi. Cal.
14	486.5	317	53	300	0.6	1-2	Oxi. Cal.
15	531.8	316	64	350	0.5	1-2	Oxi. Cal.
16	541.5	315	IND	48.7	0.3	0.5	Oxi. Cal.
17	553.6	331	61	26.3	0.2	0.5	Oxi. Cal.
18	595	315	67	67	0.7	1	Oxi. Cal.
19	613.8	312	IND	33.2	IND	0.5-1	Oxi. Cal.
20	628.8	327	IND	45.8	IND	0.5	Oxi. Cal.

Table A.59: Nenana 3c

Fracture	Distance from Origin (cm)	Strike	Dip	Length (cm)	Height (cm)	Aperture (mm)	Type of Fill
1	0	35	IND	110.3	IND	1-4	Oxd. Cal.
2	10.6	33	62W	300	2.1	1-3	Oxd. Cal.
3	35.2	36	IND	44.2	IND	1	Oxd. Cal.
4	49.3	34	IND	32.3	IND	1-2	Oxd. Cal.
5	85.5	46	IND	29.2	IND	0.5-1	Oxd. Cal.
6	106.9	39	49W	70.2	0.9	1-2	Oxd. Cal.
7	144.9	41	61W	86.3	0.4	1	Oxd. Cal.
8	180.4	37	IND	115	IND	1-2	Oxd. Cal.
9	209.3	42	53W	137.2	1.3	1-3	Oxd. Cal.
10	265.3	36	54W	9.1	0.3	0.5-1	Oxd. Cal.

Table A.60: Nenana 3d

Fracture	Distance from Origin (cm)	Strike	Dip	Length (cm)	Height (cm)	Aperture (mm)	Type of Fill
1	10.4	152	89SW	186.7	2.1	FF	Oxd. Cal.
2	20.2	345	78NE	18.2	0.3	FF	Oxd. Cal.
3	61	339	58NE	186.4	24.6	FF	Oxd. Cal.
4	81.6	347	73NE	32.3	0.4	FF	Oxd. Cal.
5	88.2	346	72NE	66.9	0.2	0.5-1	Oxd. Cal.
6	94.1	163	77SW	116.3	IND	0.5-1	Oxd. Cal.
7	125.8	161	89SW	77.6	IND	0.5-1	Oxd. Cal.
8	144.9	353	81NE	143.2	1.2	FF	Oxd. Cal.
9	149.2	167	IND	137.6	IND	1	Oxd. Cal.
10	170.6	352	IND	51.4	IND	0.5-1	Oxd. Cal.
11	187.7	155	83SW	38.7	0.5	0.5-1	Oxd. Cal.
12	194.8	343	72NE	31.2	0.4	FF	Oxd. Cal.
13	202.4	355	65NE	50.6	2.6	FF	Oxd. Cal.
14	238.2	171	72SW	36.4	1.1	FF	Oxd. Cal.
15	256.8	340	59NE	42.1	0.4	FF	Oxd. Cal.
16	269.4	343	62NE	16.2	1.3	FF	Oxd. Cal.
17	290.8	161	74SW	26.4	0.6	FF	Oxd. Cal.
18	312.5	164	80SW	66.2	1.2	FF	Oxd. Cal.
19	330.3	357	87NE	124.2	1.1	0.5-1	Oxd. Cal.
20	456.2	8	84SW	123.4	2.3	1	Oxd. Cal.
21	468.2	186	67SW	172.3	0.8	1-FF	Oxd. Cal.
22	492.4	172	77SW	94.2	1.4	1	Oxd. Cal.
23	513.6	356	81NE	27.5	0.6	0.5	Oxd. Cal.
24	612.3	358	77NE	165.2	2.1	1-3	Oxd. Cal.
25	652.4	164	65SW	250	2.3	1-3	Oxd. Cal.

Table A.61: Nenana 4a

Fracture	Distance from Origin (cm)	Strike	Dip	Length (cm)	Height (cm)	Aperture (mm)	Type of Fill
1	12.1	334	87SW	17.6	9.6	2-8	IND
2	50.3	341	86SW	82.4	69.7	2-18	IND
3	83.9	344	82SW	IND	39	0.5-6	IND
4	106.3	336	84SW	IND	25.3	0.5	IND
5	108.8	339	86NE	51	214.3	2-35	IND
6	120.7	353	86SW	IND	43.8	11-32	IND
7	129.8	347	79SW	IND	48.2	2-7	IND
8	132.4	339	84SW	IND	20.2	1-3	IND
9	147.3	349	84SW	IND	21.2	1	IND
10	151.3	350	87SW	IND	44.6	FF	IND
11	160.8	80	72NE	IND	44.6	FF	IND
12	163.6	295	46SW	IND	36.2	1-9	IND
13	184.6	336	77SW	IND	22.8	2-4	IND
14	187.7	331	83SW	IND	21.6	0.5-2	IND
15	213.2	341	80SW	23.2	46.8	2-4	IND
16	232.8	310	78SW	29.7	96.3	2-7	IND
17	267.8	329	81SW	42.8	150.6	3-6	IND
18	289.2	305	79SW	34.5	91.6	0.5-7	IND
19	322.5	347	90	35.4	89.1	1	IND
20	428.2	310	84SW	1200	IND	1-30	IND
21	450.6	44	61W	131.2	14.5	1	IND

Table A.62: Nenana 4b

Fracture	Distance from Origin (cm)	Strike	Dip	Length (cm)	Height (cm)	Aperture (mm)	Type of Fill
1	12.4	209	69NW	2.3	10.8	1-2	IND
2	15	241	69NW	2.6	8.2	FF	IND
3	18.1	207	75NW	13.9	40.6	1-3	IND
4	21.2	194	69NW	16.9	11.1	1-FF	Cal.
5	39.6	185	80E	14.5	66.5	1	IND
6	50.2	222	74NW	23.2	11.3	0.5-1	Cal.
7	73.9	219	68NW	7.1	12.8	0.5-1	IND
8	83.2	49	77E	IND	5.3	1	IND
9	85.8	223	67NW	IND	9.8	1	Cal.
10	87.6	239	69NW	10.2	12.4	0.5	IND
11	91	235	75NW	5.4	12.8	1	Cal.
12	99.6	229	74NW	2.3	14.6	1-2	Cal.
13	101.5	233	68NW	2.2	3.9	0.5	Cal.
14	102.2	235	55NW	2	5.5	1	Cal.
15	105.1	231	71NW	IND	6.9	1	Cal.
16	108	52	86E	2.1	14.2	3-4	Cal.
17	109.6	44	87E	IND	7.1	1	Cal.
18	116	50	89E	23.2	11.1	1	Cal.
19	135.6	51	74E	9.1	13.8	FF	Cal.
20	149.8	256	62NW	9.9	12.7	FF	IND
21	164.2	82	85E	2.2	7.8	FF	IND
22	173.6	62	84E	1.1	8.5	FF	IND
23	182.3	48	87E	9.3	20.6	FF	IND

Table A.63: Nenana 5

Fracture	Distance from Origin (cm)	Strike	Dip	Length (cm)	Height (cm)	Aperture (mm)	Type of Fill
1	24.6	44	90	IND	32.2	2-7	IND
2	30.4	49	76	IND	21.4	5-35	IND
3	46.7	44	72	IND	17.3	1-2	IND
4	47.3	352	74	IND	12.6	1-7	Cal.
5	63.6	46	43	IND	110.5	1-16	IND
6	67.6	47	76	IND	28.7	3-9	IND
7	77.8	345	50	29.1	10.3	1-3	IND
8	85.3	341	87	22.5	38.4	2-5	IND
9	102.9	335	64	IND	29.6	1-3	IND
10	124.7	345	75	IND	9.4	0.5-1	Cal.
11	152.3	312	63	IND	9.7	1	Cal.
12	174.7	353	72	IND	9.8	1-7	IND
13	195	352	80	IND	88.6	0.5	IND
14	214.5	44	59	IND	22.5	1-40	IND
15	227.6	44	69	IND	25.9	1-14	IND
16	242.2	60	87	IND	25.1	5-11	IND
17	250.3	45	82	IND	17.2	2-10	IND
18	260.1	51	53	IND	18.3	2-5	IND
19	297.5	44	76	IND	27.3	5-22	IND
20	307.5	47	66	IND	74.3	3-15	IND
21	313.3	64	89	IND	24.2	1-1.5	IND
22	363.2	49	81	IND	18.5	0.5-1	IND
23	388.7	55	86	IND	64.6	1-7	IND
24	447.0	355	86	IND	24.6	1-2	IND

Table A.64: Nenana 6a

Fracture	Distance from Origin (cm)	Strike	Dip	Length (cm)	Height (cm)	Aperture (mm)	Type of Fill
1	11.3	245	71W	19.6	22.1	1	IND
2	15.2	240	70W	23.6	13.2	1	IND
3	24.1	232	71W	26.1	15.6	1-FF	IND
4	30.6	232	72W	34.4	11.8	FF	IND
5	73.2	244	71W	14.3	IND	0.5-FF	IND
6	86.4	55	85E	94.2	3.4	1-2	IND
7	90.9	54	79E	44.6	IND	1	IND
8	103.4	53	86E	89.2	IND	1	IND
9	112.4	52	85E	51.9	2.3	1	IND
10	148.2	229	47W	200	4.9	1-2	IND
11	153.2	52	71W	21.3	3.6	0.5-1	IND
12	157.9	223	56E	41.3	2.1	0.5-1	IND
13	174.2	51	88E	1000	41.3	1-5	IND
14	200	39	80E	33	6.7	0.5	IND
15	244.6	212	60W	67.3	8.2	FF	IND
16	245.2	226	59W	55.6	35.2	1-2	IND
17	249.6	224	74W	IND	27.3	1-2	IND
18	260.3	47	83E	IND	24.3	1-2	IND
19	268.2	48	86E	IND	24.3	1-2	IND
20	278.2	212	76W	57.2	27.5	1-2	IND
21	285.8	37	83E	59.4	28.4	1	IND
22	309.2	25	89E	35.1	28.7	1-3	IND
23	320.4	28	79E	68.5	31.2	FF	IND
24	326.8	239	70W	1000	32.4	1-2	IND
25	282.4	59	69E	26.7	17.4	1-3	IND

Table A.65: Nenana 6b

Fracture	Distance from Origin (cm)	Strike	Dip	Length (cm)	Height (cm)	Aperture (mm)	Type of Fill
1	0	305	55NE	153.6	IND	1-4	IND
2	20.6	322	76NE	117.2	2.4	1-2	IND
3	29.6	143	74SW	23.8	3.1	FF	IND
4	76	323	75NE	98.2	3.6	1-4	IND
5	86.8	355	82NE	74.2	4.1	1	IND
6	119	337	84NE	76.2	6.4	1-2	IND
7	262.4	332	69NE	75.3	11.6	1-FF	IND
8	186.7	312	81NE	100	14.3	FF	IND
9	210.4	135	82SW	57.3	11.6	1-5	IND
10	227	10	76NE	IND	IND	IND	IND

Table A.66: Nenana 6c

Fracture	Distance from Origin (cm)	Strike	Dip	Length (cm)	Height (cm)	Aperture (mm)	Type of Fill
1	0	309	69N	34.6	IND	3	IND
2	13	308	70S	200	IND	1-5	IND
3	41.1	314	60N	48.6	IND	1	IND
4	79.6	304	58N	123.4	IND	1-3	IND
5	92.1	302	68N	56.4	IND	1-3	IND
6	136.4	110	87S	350	IND	1-2	IND
7	261.2	312	62N	350	IND	1-2	IND
8	290.8	304	30N	250	IND	1-3	IND
9	306.1	304	28N	91	IND	1-4	IND
10	321.6	303	68N	1000	16.3	FF	IND
11	374.4	311	64N	1000	16.3	FF	IND
12	458.6	304	36N	26.4	IND	0.5-1	IND
13	501.2	313	60N	115	IND	1-2	IND
14	551.6	322	45N	1000	IND	1-10	IND
15	606.8	316	56N	600	IND	1-2	IND
16	623	316	49N	IND	IND	IND	IND
17	628.9	314	38N	600	IND	1-4	IND
18	707.2	303	58N	650	IND	1-2	IND
19	727.2	309	44N	600	IND	1-3	IND
20	758.3	307	59N	1000	61	FF	IND

Table A.67: Nenana 6d

Fracture	Distance from Origin (cm)	Strike	Dip	Length (cm)	Height (cm)	Aperture (mm)	Type of Fill
1	0	160	69W	223	36.3	1-FF	IND
2	33.2	179	IND	65	IND	1	IND
3	88.7	175	IND	101.2	IND	1-2	IND
4	101.7	173	IND	103.4	IND	1-2	IND
5	129.4	175	IND	120.3	IND	1-2	IND
6	167.2	177	79W	78	12.3	1	IND
7	169	174	IND	58.3	IND	1	IND
8	181.4	178	IND	68.3	IND	1-2	IND
9	205	181	IND	103.2	IND	1-2	IND
10	234	181	IND	60.1	IND	1	IND
11	295.4	180	IND	94.2	IND	1	IND
12	340.4	181	60W	50.2	IND	1	IND
13	350	176	IND	37.6	IND	1	IND
14	397.4	184	IND	69.2	IND	1	IND
15	434.3	182	IND	78.6	IND	1-2	IND

Table A.68: Nenana 7a

Fracture	Distance from Origin (cm)	Strike	Dip	Length (cm)	Height (cm)	Aperture (mm)	Type of Fill
1	11.6	8	81E	IND	IND	1-2	Cal.
2	12.2	9	84E	IND	IND	1-2	Cal.
3	26	7	84E	IND	IND	1-2	Cal.
4	27.1	11	85E	IND	IND	1-2	Cal.
5	33	16	85E	IND	IND	1-2	Cal.
6	37	17	78E	IND	IND	1-2	Cal.
7	42.1	18	78E	IND	IND	1-2	Cal.
8	59.4	12	83E	IND	IND	1-2	Cal.
9	69	11	85E	IND	IND	1-2	Cal.
10	70.4	15	85E	IND	IND	1-2	Cal.
11	74.4	16	86E	IND	IND	1-2	Cal.
12	75.6	18	87E	IND	IND	1-2	Cal.
13	97.8	15	85E	IND	IND	1-2	Cal.
14	105.4	11	82E	IND	IND	1-2	Cal.
15	112.2	14	85E	IND	IND	1-2	Cal.
16	115.2	17	83E	IND	IND	0.5	IND
17	123.8	19	79E	IND	IND	0.5	0.5
18	137.2	12	86E	IND	IND	0.5	0.5
19	139.8	15	88E	IND	IND	0.5	0.5
20	202	8	77E	IND	IND	0.5	0.5
21	214.8	16	75E	IND	IND	0.5	0.5
22	217.5	18	86E	IND	IND	0.5	0.5
23	222.1	12	85E	IND	IND	0.5	0.5

Table A.69: Nenana 7b

Fracture	Distance from Origin (cm)	Strike	Dip	Length (cm)	Height (cm)	Aperture (mm)	Type of Fill
1	13.4	229	65W	80.3	27.5	FF	Cal.
2	19.2	217	78W	29.2	3.6	0.5-1	Cal.
3	23.4	218	75W	18.1	2.1	0.5-1	Cal.
4	29.6	216	70W	45.2	2.1	0.5-1	Cal.
5	35.4	217	76W	27.4	1.8	0.5-1	Cal.
6	38.2	212	66W	15.8	1.8	0.5-1	Cal.
7	45.8	216	59W	22.1	16.3	0.5	Cal.
8	46.4	211	73W	34.3	2.6	0.5-1	Cal.
9	60	213	79W	41.2	2.3	0.5-1	Cal.
10	63.5	209	57W	16.4	6.5	0.5-1	Cal.
11	67.9	217	54W	44.7	11	0.5-1	Cal.
12	82.4	218	63W	16.2	0.4	0.5-1	Cal.
13	94.8	226	47W	19.6	1.2	0.5-1	Cal.
14	104.9	225	66W	29.7	3.6	0.5-1	Cal.
15	120.4	201	57W	500	IND	FF	Cal.
16	129.6	221	IND	20.2	IND	0.5-1	Cal.
17	150.1	236	58W	35.4	7.2	FF	Cal.
18	165.2	224	64W	49.4	8.3	FF	Cal.
19	167.8	223	69W	64.8	18.6	FF	Cal.
20	174.3	230	72W	115.2	40.6	FF	Cal.
21	209.6	210	63W	CONT	40.6	0.5-1	Cal.
22	226.4	224	52W	CONT	40.6	0.5-1	Cal.
23	265.6	229	69W	CONT	40.6	0.5-1	Cal.
24	364.6	223	77W	CONT	40.6	0.5-1	Cal.
25	387.9	229	83W	CONT	40.6	0.5-1	Cal.

Table A.70: Nenana 8a

Fracture	Distance from Origin (cm)	Strike	Dip	Length (cm)	Height (cm)	Aperture (mm)	Type of Fill
1	13.3	227	IND	50.3	IND	1	Cal.
2	27.1	224	IND	24.3	IND	1	Cal.
3	33.6	222	IND	33.6	IND	1-2	Cal.
4	42	223	54NW	43.4	1.4	1	Cal.
5	49.6	219	46NW	18.7	2.0	1	Cal.
6	60.2	221	79NW	131.6	18.6	1-2	Cal.
7	72.2	226	59NW	34.4	0.7	1	Cal.
8	83.7	211	76NW	27.2	20.3	1	Cal.
9	92.2	218	IND	21.6	IND	1	Cal.
10	98.1	221	IND	14.3	IND	1	Cal.
11	99	225	IND	14.1	IND	1	Cal.
12	100.8	231	64NW	19.6	2.3	1	Cal.
13	104.6	227	IND	28.2	IND	1-1.5	Cal.
14	107.9	228	56NW	20.1	3.9	1-1.5	Cal.
15	110.4	216	60NW	5.6	8.3	1	Cal.
16	111.2	222	IND	8.7	IND	0.5-1	Cal.
17	115.4	229	IND	26.7	IND	0.5-1	Cal.
18	120.5	226	59NW	28.4	2.3	0.5-1	Cal.
19	131.4	215	64NW	187.6	17.4	1-2	Cal.
20	153.8	227	61NW	29.4	5.1	FF	Cal.
21	156.4	224	IND	24.1	IND	0.5-1	Cal.
22	177.4	226	71NW	37.3	5.3	0.5-1	Cal.

Table A.71: Nenana 8b

Fracture	Distance from Origin (cm)	Strike	Dip	Length (cm)	Height (cm)	Aperture (mm)	Type of Fill
1	0	141	81S	61.3	70.3	1-2	Cal.
2	135	148	IND	62.7	IND	0.5-1	Cal.
3	187.3	324	72N	86.1	1.7	FF	Cal.
4	270	131	81S	113.2	13.6	FF	Cal.
5	304.5	132	83S	92.1	29.4	FF	Cal.
6	319.4	332	66N	48	2.3	FF	Cal.
7	401.2	126	77S	107.6	18.7	0.5-1	Cal.
8	405.3	316	74N	19.6	5.9	FF	Cal.
9	432.4	144	87S	14.7	4.6	FF	Cal.
10	494.3	319	61N	46.4	6.7	FF	Cal.
11	508.6	136	54S	20.3	4.1	FF	Cal.
12	526.2	325	76N	107.5	11.2	FF	Cal.
13	544.6	131	84S	30.2	5.4	FF	Cal.
14	625.8	146	76S	65.7	19.8	FF	Cal.
15	676.4	152	82S	121.4	20.3	FF	Cal.
16	725.4	145	80S	45.2	6.1	FF	Cal.
17	756.4	139	75S	52.1	6.1	FF	Cal.
18	832.2	326	54N	211.4	47.2	FF	Cal.
19	940.6	141	80S	42.3	33.6	FF	Cal.
20	992.6	150	81S	75.4	49.1	FF	Cal.

Table A.72: Nenana 8c

Fracture	Distance from Origin (cm)	Strike	Dip	Length (cm)	Height (cm)	Aperture (mm)	Type of Fill
1	13.8	9	85E	114.6	0.5	0.5-1	Cal.
2	31.2	6	70E	138.3	0.3	0.5-1	Cal.
3	60.4	8	83E	39.2	18.3	0.5-1	Cal.
4	62.1	9	86E	43.6	0.3	0.5-1	Cal.
5	124.9	359	87E	37.8	23.6	0.5-1	Cal.
6	135.2	16	85E	2.5	14.6	0.5-1	Cal.
7	141.4	6	87E	21.4	0.4	0.5-1	Cal.
8	191.4	5	84E	79.3	0.4	0.5-1	Cal.
9	208.2	11	87E	24.4	0.4	0.5-1	Cal.
10	249.1	10	89E	46	29.3	1-2	Cal.
11	297.6	12	86E	95.2	29.4	1-2	Cal.
12	342.4	14	87E	20.6	11.4	FF	IND

Table A.73: Nenana 8d

Fracture	Distance from Origin (cm)	Strike	Dip	Length (cm)	Height (cm)	Aperture (mm)	Type of Fill
1	10.4	23	85E	116.4	14.2	FF	Cal.
2	24.2	29	86E	101.5	31.6	FF	Cal.
3	49.8	2	82E	44.1	34.6	FF	Cal.
4	73.2	9	89E	10.3	95.2	FF	Cal.
5	81.4	11	87E	16.4	1.7	FF	Cal.
6	119.8	7	88E	19.2	7.1	FF	Cal.
7	136.6	10	81E	20.8	1.9	FF	Cal.
8	154.6	8	72E	20.9	2.1	FF	Cal.
9	167.7	2	86E	21.2	5.3	FF	Cal.
10	172.2	17	76E	14.6	14.2	FF	Cal.
11	188.2	19	85E	18.2	7.1	1-2	Cal.
12	196.4	13	74E	29.1	35.2	FF	Cal.
13	216.1	4	89E	8.1	36.1	FF	Cal.

Table A.74: Nenana 9

Fracture	Distance from Origin (cm)	Strike	Dip	Length (cm)	Height (cm)	Aperture (mm)	Type of Fill
1	0	166	84SW	100	300	FF	Cal.
2	42	182	82SW	6.8	100.3	FF	Cal.
3	44.2	184	77SW	26.7	34.6	FF	Cal.
4	64.2	162	74SW	7.8	157.6	1-2	Cal.
5	165.5	177	76SW	12.7	58.6	1-4	Cal.
6	180.4	165	69SW	10.6	300	1-3	Cal.
7	196.4	164	72SW	9.2	71.8	FF	Cal.
8	200.4	161	68SW	10.1	43.6	FF	Cal.
9	207.8	162	75SW	13.1	75.2	FF	Cal.
10	210.2	160	80SW	4.3	27.8	FF	Cal.
11	249.8	176	82SW	IND	300	3-4	Cal.
12	293	169	86SW	IND	97.6	1-2	IND
13	366.8	168	88SW	12.8	78.6	1-2	IND
14	389	156	74SW	5.3	46.8	1-2	IND
15	442.6	174	67SW	6.2	88.2	1-2	IND
16	465.4	162	74SW	9.2	220.6	1-4	IND
17	542.6	177	78SW	26.7	142.7	FF	Cal.
18	554.2	179	72SW	16.2	38.2	1-2	Cal.
19	599.6	164	74SW	2.3	47.8	1-3	IND
20	638.2	165	82SW	6.7	123.4	1-5	IND
21	696.2	171	78SW	IND	94.6	1-5	IND
22	793.4	166	73SW	12.1	143.6	2-6	Cal.
23	904.2	174	85SW	21.6	400	4-10	IND

Healy Area Transects:

Table A.75: Suntrana 1a

Fracture	Distance from Origin (cm)	Strike	Dip	Length (cm)	Height (cm)	Aperture (mm)	Type of Fill
1	11	74	50S	12.7	3.8	1-2	Qtz.
2	12.1	62	65S	IND	6.8	1	Qtz.
3	15.4	61	53S	11.8	4.1	1	Qtz.
4	34.6	76	54S	3.7	3.4	1-2	Qtz.
5	35.6	83	61S	3.5	4.9	2-5	Qtz.
6	39.4	87	68S	6.8	8.4	5	Qtz.
7	40.4	74	69S	IND	1.2	0.5-1	Qtz.
8	41.2	70	52S	3.9	1.4	1	Qtz.
9	42.8	79	49S	9.5	5.9	1-2	Qtz.

Table A.76: Suntrana 1b

Fracture	Distance from Origin (cm)	Strike	Dip	Length (cm)	Height (cm)	Aperture (mm)	Type of Fill
1	17.4	74	59	IND	2.7	1-2	Qtz.
2	19.2	84	74	6.4	2.1	5	Qtz.
3	23.4	85	73	7.0	1.3	1-2	Qtz.
4	24.8	99	74	1.3	4.1	2-3	Qtz.
5	27.2	99	83	6.6	7.2	1-6	Qtz.
6	39.2	100	66	7.6	3.5	4-6	Qtz.
7	41.8	91	70	3.9	91	2-4	Qtz.
8	44	89	64	15.9	7.9	FF	Qtz.

Table A.77: Suntrana 2

Fracture	Distance from Origin (cm)	Strike	Dip	Length (cm)	Height (cm)	Aperture (mm)	Type of Fill
1	33.8	129	57SW	26.2	84.3	FF	Open
2	59.2	134	47SW	56.2	114.7	FF	Open
3	102.6	141	46SW	7.5	96.2	1-2	Open
4	113.4	146	62SW	IND	39.7	0.5-1	Open
5	161.2	157	81SW	IND	28.8	0.5-1	Open
6	172.4	158	78SW	IND	19.2	.5	Open
7	222.3	144	63SW	6.8	70.4	1-3	Open
8	349	143	61SW	15.3	128.2	1-7	Open
9	357.2	137	81SW	IND	119.3	1	Open
10	361.4	129	51SW	49.3	26.2	FF	Open
11	362.9	129	53SW	IND	13.9	1	Open
12	364.6	134	52SW	2.3	29.3	0.5-1	Open
13	394.9	139	60SW	20.8	90.2	FF	Open
14	397.2	141	60SW	20.8	83.3	1-2	Open
15	409.6	147	76SW	IND	40.3	0.5-1	Open
16	420.6	141	74	IND	29.2	1-2	Open
17	498.2	148	57	4.7	57.2	1-5	Open
18	586.2	146	82	4.2	30.9	FF	Open
19	605.3	132	49	12.1	36.2	1-10	Open
20	614.9	139	63	5.4	53.2	3-5	Open
21	617.5	134	68	3.4	103.4	0.5-4	Open
22	796.6	141	54	30.1	45.2	1-2	Open
23	800	142	59	22.8	50.2	1-2	Open
24	845.2	149	61	23.4	102.1	FF	Open
25	876.2	154	57	16.2	80.9	1-2	Open

Table A.78: Suntrana 3a

Fracture	Distance from Origin (cm)	Strike	Dip	Length (cm)	Height (cm)	Aperture (mm)	Type of Fill
1	13.5	111	78S	23.5	8.4	1-3	Open
2	82.3	121	55S	23.2	10.1	1-3	Open
3	110.4	120	65S	26.7	13.2	1-3	Open
4	118.9	118	62S	26.2	11.1	1-2	Open
5	122.3	108	58S	27.1	14.2	1-2	Open
6	129.4	106	64S	20.3	13.1	1	Open
7	135.6	112	65S	22.1	9.7	1	Open
8	144.4	124	66S	48.3	20.4	1	Open
9	146.9	129	75S	30.4	21.2	1	Open
10	160.4	127	71S	30.9	15.2	1	Open
11	164.6	134	76S	31.3	18.4	1	Open
12	187.2	131	64S	28.2	6.8	1	Open
13	194.2	133	45S	34.5	9.1	1	Open
14	200	126	68S	32.1	9.6	1-2	Open
15	225.8	134	71S	44.3	8.7	FF	Open
16	239.2	131	60	29.2	24.1	1-2	Open
17	245.8	116	78	30.2	26.1	FF	Open
18	304	136	68	21.4	32.4	1	Open
19	312.1	134	57	IND	19.6	1-2	Open
20	315.6	130	60	IND	19.7	1-2	Open
21	350.4	136	58	10.2	16.8	FF	Open
22	367.4	129	52	23.4	43.6	FF	Open

Table A.79: Suntrana 3b

Fracture	Distance from Origin (cm)	Strike	Dip	Length (cm)	Height (cm)	Aperture (mm)	Type of Fill
1	0	154	75SW	10.1	16.2	1-4	Open
2	16.3	159	76SW	21.2	15.2	FF	Open
3	29.6	164	85SW	16.3	14.2	FF	Open
4	69	150	IND	18.7	IND	FF	Open
5	154	169	84NE	12.3	23	FF	Open
6	179.6	166	86NE	6.8	14.9	FF	Open
7	186	344	86NE	12.9	16.8	FF	Open
8	186.8	337	89NE	14.4	17.6	FF	Open
9	198.6	341	86NE	11.5	7.1	1	Open
10	201.6	334	89NE	6.6	13.1	1-2	Open
11	207.4	344	82NE	5.4	17.3	FF	Open
12	209.4	343	86NE	21.6	22.2	1-2	Open
13	218.2	345	87NE	27.8	25.3	FF	Open
14	223.4	342	86NE	24.6	28.3	FF	Open
15	227.3	346	88NE	28.3	11.7	1	Open
16	231	343	88NE	24.2	17.3	FF	Open
17	247.2	344	86NE	8.7	24.3	FF	Open
18	251.3	337	87NE	14.2	3.9	1	Open
19	254.2	341	83NE	29.4	6.1	1	Open
20	255.6	334	86NE	26.4	4.9	1	Open
21	264.8	332	89NE	25.2	7.4	FF	Open
22	273.4	343	84NE	26.2	9.7	FF	Open
23	276.4	339	87NE	12.4	0.4	1	Open
24	279.4	335	82NE	21.4	3.6	FF	Open

Table A.80: Suntrana 4a

Fracture	Distance from Origin (cm)	Strike	Dip	Length (cm)	Height (cm)	Aperture (mm)	Type of Fill
1	10.4	204	77W	IND	32.1	0.5-1	Open
2	27.2	208	72W	IND	30.2	0.5-1	Open
3	41.2	218	63W	3.4	79.4	0.5-1	Open
4	84.2	215	72W	57.4	80.2	0.5-1	Open
5	142.3	217	56W	3.8	104.3	0.5-1	Open
6	164.2	207	31E	0.9	24.9	0.5-1	Open
7	171.2	206	43W	IND	24.6	0.5-1	Open
8	181.4	210	54W	4.6	41.4	0.5-1	Open
9	189.6	221	58W	1.9	18.1	0.5-1	Open
10	205.6	219	63W	IND	46.5	0.5-1	Open
11	237.4	223	62W	IND	43.5	0.5-1	Open
12	240.6	221	72W	IND	43.9	0.5-1	Open

Table A.81: Suntrana 4b

Fracture	Distance from Origin (cm)	Strike	Dip	Length (cm)	Height (cm)	Aperture (mm)	Type of Fill
1	0	194	20E	16.5	250	1	Open
2	8.2	12	31E	6.7	150	1	Open
3	10.8	14	36E	3.6	17.2	1	Open
4	14.4	16	42E	6.8	25.6	1	Open
5	30.2	17	11E	8.6	20.1	1	Open
6	17.4	17	30E	4.6	20.7	1	Open

Table A.82: Suntrana 4c

Fracture	Distance from Origin (cm)	Strike	Dip	Length (cm)	Height (cm)	Aperture (mm)	Type of Fill
1	0	351	76E	IND	350	1-2	Open
2	79.6	5	65E	IND	350	1-2	Open
3	126.2	356	76E	IND	124.6	1-2	Open
4	235.4	16	62E	IND	350	1-2	Open

Table A.83: Suntrana 5

Fracture	Distance from Origin (cm)	Strike	Dip	Length (cm)	Height (cm)	Aperture (mm)	Type of Fill
1	0	103	56SE	7.7	113.2	1-2	Open
2	24.4	280	84SE	IND	50.6	1-2	Open
3	55.8	106	76SE	2.4	78.6	1-2	Open
4	77.2	105	69SE	100	250	1-2	Open
5	120.2	121	81SE	50	200	1-2	Open
6	149.3	139	85SE	50	200	1-4	Open
7	185.7	107	78SE	5.7	71.2	FF	Open
8	214.2	154	74SE	3.6	80.2	1-4	Open
9	247.4	141	68SE	14.8	94.2	FF	Open
10	267.1	157	84SE	7.8	23.2	FF	Open
11	274.6	151	86SE	7.6	67.1	1-3	Open
12	290.4	164	81SE	7.9	51.7	FF	Open
13	311.6	166	78SE	3	200	1-4	Open
14	330.4	157	87SE	13.6	113.4	FF	Open
15	380.4	152	83SE	26.7	60.8	FF	Open

Table A.84: Suntrana 6a

Fracture	Distance from Origin (cm)	Strike	Dip	Length (cm)	Height (cm)	Aperture (mm)	Type of Fill
1	20.2	301	66NE	IND	107.2	1-2	Open
2	46.4	306	70NE	IND	128.4	1-2	Open
3	57.2	294	72NE	2.6	90.3	1-2	Open
4	69.3	292	74NE	IND	110.2	1-2	Open
5	113.6	301	86NE	9.2	157.6	FF	Open
6	132.1	295	84SE	IND	166.3	1-2	Open
7	142.3	116	86NE	7.1	78.4	1-2	Open
8	169.8	311	70NE	IND	174.6	1-2	Open
9	178.6	304	79NE	IND	62.1	1-2	Open
10	181.6	300	76NE	2.6	124.6	FF	Open
11	203.4	119	73NE	IND	200	1-2	Open
12	216.2	116	82NE	IND	173.6	1-2	Open
13	230.4	115	85NE	IND	156.2	1-2	Open
14	247.6	299	81NE	IND	186.3	1-2	Open
15	271.2	287	86NE	IND	126.8	1-2	Open
16	298	286	87NE	IND	186.4	1-2	Open
17	313.6	289	84NE	IND	78.6	1-2	Open
18	330.1	295	84NE	IND	106.2	1-2	Open
19	342.3	295	89NE	IND	54.2	1-2	Open
20	358.2	114	88NE	6.2	139.6	1-2	Open
21	387.1	302	82NE	6.7	200	1-2	Open
22	407.4	296	74NE	IND	126.4	1-2	Open
23	438.4	297	78NE	2.6	87.2	1-2	Open
24	464.8	121	75NE	IND	93.2	1-2	Open
25	488.9	124	79NE	1.9	111.2	1-2	Open

Table A.85: Suntrana 6b

Fracture	Distance from Origin (cm)	Strike	Dip	Length (cm)	Height (cm)	Aperture (mm)	Type of Fill
1	166.2	155	60SW	IND	200	1-2	Open
2	206.2	144	57SW	IND	250	1-2	Open
3	234	161	54SW	IND	124.2	1-2	Open

Table A.86: Usibelli Coal Mine

Fracture	Distance from Origin (cm)	Strike	Dip	Length (cm)	Height (cm)	Aperture (mm)	Type of Fill
1	9.4	157	78W	3.2	23.4	1-2	Open
2	30.2	336	78E	9.1	74.1	0.5-14	Open
3	43.8	351	79E	2.1	16.4	0.5	Open
4	57.8	239	73E	4.1	15.3	0.5	Open
5	82.2	169	82W	13.4	115.3	3-5	Open
6	100.2	167	74W	4.1	49.7	1-3	Open
7	117.2	16	77W	2.3	16.2	1	Open
8	134.2	173	70W	1.6	7.3	FF	Open
9	142.2	351	75E	1.9	14.2	FF	Open
10	159	174	84W	1	16.7	1	Open
11	185.6	164	78W	29.7	85.7	FF	Open
12	255	344	71E	24.2	41.2	FF	Open
13	260.2	168	87W	21.8	69.2	FF	Open
14	267.4	173	82W	1.3	29.7	1	Open
15	282.8	173	82W	2.1	64.5	1	Open
16	290.6	172	80W	1.2	27.4	0.5	Open
17	293.2	169	79W	2.2	35.2	1-2	Open
18	296.2	174	75W	2.4	57.2	1-3	Open
19	319.2	359	84E	5.2	37.2	FF	Open
20	322	357	70E	7.1	42.3	1-3	Open
21	338.2	342	74E	5.2	32.7	FF	Open
22	355.4	172	75W	22.7	57.2	FF	Open
23	412.3	345	82E	16.7	97.4	FF	Open
24	414.6	346	75E	19.4	101.2	FF	Open
25	437.8	173	80W	4.5	26.2	1-2	Open
26	449.6	355	79E	10.8	118.4	1-3	Open

Table A.87: Bison Gulch 1

Fracture	Distance from Origin (cm)	Strike	Dip	Length (cm)	Height (cm)	Aperture (mm)	Type of Fill
1	1.2	334	81NE	78.4	13.3	FF	Rem.
2	13.4	147	70SW	11.4	4.1	1-3	Rem.
3	40.4	337	82NE	207.4	76.2	1-4	Rem.
4	42.3	331	87NE	5.9	1.1	FF	Rem.
5	44.2	324	87NE	31.8	5.6	FF	Rem.
6	59.2	153	83SW	52.8	27.3	FF	Rem.
7	62.4	155	79SW	87.3	21.4	FF	Rem.
8	65.4	334	80NE	15.4	1.6	FF	Rem.
9	75.4	151	69SW	20.4	4.2	FF	Rem.
10	78.2	154	70SW	16.4	2.1	FF	Rem.
11	81.9	147	79SW	40.2	2.9	FF	Rem.
12	93.2	332	79NE	21.8	2.3	1	Rem.
13	112.4	335	69NE	13.6	2.7	FF	Rem.
14	115	334	85NE	28.7	6.8	1-2	Rem.
15	118.7	157	79SW	39.2	7.4	1-2	Rem.
16	123	160	71SW	48.1	19.6	FF	Rem.
17	134	143	70SW	12.2	2.6	1-2	Rem.
18	136.8	144	73SW	50.8	4.2	FF	Rem.
19	149	335	86NE	45.8	2.4	FF	Rem.
20	154.1	154	84SW	19.6	4.2	FF	Rem.
21	158.2	158	74SW	97.3	4.7	FF	Rem.
22	166.2	154	69SW	20.4	4.3	FF	Rem.

Table A.88: Bison Gulch 2a

Fracture	Distance from Origin (cm)	Strike	Dip	Length (cm)	Height (cm)	Aperture (mm)	Type of Fill
1	10.6	204	59W	5.1	2.2	FF	Rem.
2	35.8	206	62W	7.3	0.4	1	Rem.
3	36.4	196	60W	33.6	3.7	FF	Rem.
4	46.8	199	72W	5.8	3.9	1	Rem.
5	51.4	193	72W	4.3	1.7	FF	Rem.
6	57	194	1W	1.8	5.2	0.5	Rem.
7	59.2	196	62W	1.7	4.3	FF	Rem.
8	61.8	202	81W	4.8	1.6	FF	Rem.
9	69.1	199	70W	1.2	3	0.5	Rem.
10	74.2	200	68W	2.4	4	0.5-1	Rem.
11	85.2	198	69W	7.8	3.9	FF	Rem.
12	92.4	184	64W	35.2	62.3	1	Rem.
13	116.1	201	73W	26.2	1.8	FF	Rem.
14	134.8	198	75W	25.2	12.1	0.5	Rem.
15	166.4	196	68W	20.8	7.2	0.5-1	Rem.
16	187.2	192	71W	20.7	5.8	0.5-1	Rem.
17	203.4	204	61W	39.4	16.2	FF	Rem.
18	210.8	201	63W	29.3	8.3	FF	Rem.

Table A.89: Bison Gulch 2b

Fracture	Distance from Origin (cm)	Strike	Dip	Length (cm)	Height (cm)	Aperture (mm)	Type of Fill
1	14.4	319	81NE	15.2	2.8	FF	Oxi. Qtz.
2	25	142	82NE	37.6	2.9	FF	Oxi. Qtz.
3	30.8	318	84NE	30.3	8.2	FF	Oxi. Qtz.
4	33.2	312	88NE	137.6	11.4	FF	Oxi. Qtz.
5	40.8	329	78NE	6.2	1.8	FF	Oxi. Qtz.
6	46.5	319	78NE	18.7	2.8	FF	Oxi. Qtz.
7	53.2	316	74NE	44.2	3.8	FF	Oxi. Qtz.
8	59.8	321	69NE	30.1	3.9	FF	Oxi. Qtz.
9	64	313	74NE	36.6	4.2	FF	Oxi. Qtz.
10	71.2	232	68NE	11.1	1.2	FF	Oxi. Qtz.

Table A.90: Bison Gulch 2c

Fracture	Distance from Origin (cm)	Strike	Dip	Length (cm)	Height (cm)	Aperture (mm)	Type of Fill
1	10.4	306	79NE	23.6	0.8	0.5	IND
2	31.2	318	68NE	15.1	2.8	0.5	IND
3	59.2	318	71NE	49.2	12.4	FF	IND
4	64.2	320	68NE	42.3	5.1	FF	IND
5	69.4	326	81NE	23.2	7.6	FF	IND
6	85.2	306	75NE	33.1	4.2	FF	IND

Table A.91: Lower Dragonfly Creek 1

Fracture	Distance from Origin (cm)	Strike	Dip	Length (cm)	Height (cm)	Aperture (mm)	Type of Fill
1	0	325	79NE	217	194	FF	IND
2	24.4	343	86NE	5.3	23	FF	IND
3	29.2	167	86NE	7.2	3.1	0.5-1	IND
4	30.4	161	85NE	4.6	2.4	FF	IND
5	34.2	164	86NE	1.4	2.3	FF	IND
6	56.6	161	81NE	12.5	0.5	FF	IND
7	58.2	162	83NE	19.3	1.2	0.5-1	IND
8	69	169	71SW	10.8	1.3	FF	IND
9	70.6	157	86NE	20.8	1.4	FF	IND
10	80.4	163	82SW	33.2	3.2	0.5-1	IND
11	93.4	163	87NE	34.2	15.6	0.5-1	IND
12	98.3	164	78NE	15.6	4.3	0.5-1	IND
13	103.2	156	88SW	7.6	6.5	FF	IND
14	108.6	164	87NE	49.2	8.7	0.5-1	IND
15	115.2	171	80SW	3.6	2.9	0.5-1	IND
16	115.6	173	85SW	7.2	0.4	FF	IND
17	128.6	167	88NE	6	1.3	FF	IND
18	141.6	159	78NE	14.2	3.2	0.5-1	IND

Table A.92: Lower Dragonfly Creek 2

Fracture	Distance from Origin (cm)	Strike	Dip	Length (cm)	Height (cm)	Aperture (mm)	Type of Fill
1	9.8	149	81SW	26.2	2.4	FF	IND
2	13.4	146	77SW	7.6	1.4	FF	IND
3	18.2	137	85SW	19.2	1.2	FF	IND
4	20.4	137	80SW	42.6	2.4	FF	IND
5	25.4	138	83SW	40.2	2.3	FF	IND
6	40	143	81SW	28.6	2.9	FF	IND
7	59.4	126	82SW	46.2	4.9	FF	IND
8	73	136	84SW	37.4	0.9	FF	IND
9	74.2	132	85SW	54.1	4.1	FF	IND
10	76.2	133	84SW	27.2	1.6	FF	IND
11	83.2	138	82SW	32.1	7.5	FF	IND
12	84.3	129	84SW	44.6	7.6	FF	IND
13	90.3	143	81SW	37.2	5.4	FF	IND
14	91.3	124	83SW	83.3	14.2	FF	IND
15	107.8	138	81SW	10.1	0.6	FF	IND
16	108.6	144	86SW	9.2	0.3	0.5	IND
17	109.6	159	86SW	10.4	1.3	FF	IND
18	109.8	165	83SW	3.2	0.4	FF	IND
19	123	159	86SW	5.1	1.5	FF	IND
20	134	152	79SW	57.2	5.1	0.5-1	IND
21	138.4	154	83SW	8.9	2.7	0.5	IND
22	147.6	141	87SW	37.9	3.8	FF	IND
23	156	142	81SW	20.6	1.2	0.5-1	IND
24	156.8	149	77SW	15.2	7.8	FF	IND
25	160.6	138	75SW	35.2	16.8	FF	IND
26	170	148	74SW	45.2	22.8	FF	IND

Table A.93: Lower Dragonfly Creek 3

Fracture	Distance from Origin (cm)	Strike	Dip	Length (cm)	Height (cm)	Aperture (mm)	Type of Fill
1	18	87	81SE	12.6	0.7	FF	IND
2	21.2	85	79SE	11.6	0.8	FF	IND
3	24.8	93	81SE	11.2	1.8	FF	IND
4	29.2	97	80SE	12.5	2.3	FF	IND
5	37	96	81SE	8.4	0.4	FF	IND
6	39.8	94	77SE	8.3	0.4	FF	IND
7	41.8	92	83SE	8.8	2.1	FF	IND
8	45.2	91	86SE	7.9	2	FF	IND
9	48	92	66SE	14.8	1.6	FF	IND
10	54.2	96	85SE	10	1.7	FF	IND
11	55.2	98	80SE	16.1	0.6	FF	IND
12	67	104	71NW	11.6	1.3	FF	IND
13	83.7	89	74SE	11.3	4.1	FF	IND
14	90	81	59NW	4.4	4.7	FF	IND
15	113	91	73SE	12.6	0.5	FF	IND
16	126.4	81	63SE	27.3	9.2	FF	IND
17	170.6	79	69SE	43.2	9.7	FF	IND

Table A.94: Lower Dragonfly Creek 4a

Fracture	Distance from Origin (cm)	Strike	Dip	Length (cm)	Height (cm)	Aperture (mm)	Type of Fill
1	9.8	184	86W	17.9	7.6	0.5-1	IND
2	26.6	185	76W	6	2.3	0.5	IND
3	29	180	85W	21.6	1.7	FF	IND
4	34.2	179	76W	12.3	2.9	0.5	IND
5	39.2	179	85W	19.7	4.8	FF	IND
6	50.4	178	85W	12.1	3.2	FF	IND

Table A.95: Lower Dragonfly Creek 4b

Fracture	Distance from Origin (cm)	Strike	Dip	Length (cm)	Height (cm)	Aperture (mm)	Type of Fill
1	33.2	192	75W	29	7	FF	IND
2	44.6	199	78W	20.2	2	FF	IND
3	49.4	194	82W	33.2	2.1	0.5	IND
4	59.1	191	83W	20.4	4.2	FF	IND
5	61.4	186	77W	33.2	10.1	FF	IND
6	78.8	193	75W	21.5	10.8	0.5	IND
7	85	195	81W	6.6	0.4	FF	IND
8	90	189	72W	32.6	11.7	0.5-1	IND
9	109.2	177	77W	7	1.1	FF	IND
10	112.1	180	85W	6.9	2.5	0.5	IND
11	126.2	174	85W	11.7	4	FF	IND

Table A.96: Fox Creek 1a

Fracture	Distance from Origin (cm)	Strike	Dip	Length (cm)	Height (cm)	Aperture (mm)	Type of Fill
1	10.6	92	85S	67.9	21.2	5	Oxi. Qtz.
2	61	89	88S	68	3.2	1	Oxi. Qtz.
3	125.2	93	87S	15.9	14.2	Ff	Oxi. Qtz.
4	143.2	89	73S	27.2	5.6	Ff	Oxi. Qtz.
5	154.2	89	83S	91.3	49.2	2-6	Oxi. Qtz.
6	168.2	107	84S	10.2	1.2	2	Oxi. Qtz.
7	183.8	92	86S	57.8	13.4	4-7	Oxi. Qtz.
8	205.4	96	88S	29.1	3.2	2-3	Oxi. Qtz.
9	219.6	86	83S	183.2	47.2	1-3	Oxi. Qtz.

Table A.97: Fox Creek 1b

Fracture	Distance from Origin (cm)	Strike	Dip	Length (cm)	Height (cm)	Aperture (mm)	Type of Fill
1	12.6	84	74S	79.6	1	1-2	Oxi. Qtz.
2	14.5	91	79S	65.2	1.3	1-3	Oxi. Qtz.
3	28.8	89	87S	90.7	1.9	2-5	Oxi. Qtz.
4	65	106	85S	55.4	0.8	3	Oxi. Qtz.
5	80.5	84	79S	141.5	4.6	2	Oxi. Qtz.

Table A.98: Fox Creek 1c

Fracture	Distance from Origin (cm)	Strike	Dip	Length (cm)	Height (cm)	Aperture (mm)	Type of Fill
1	15.8	324	83N	37.2	90	0.5-1	Oxi. Qtz.
2	55.4	138	86S	14.7	37.1	0.5-1	Oxi. Qtz.
3	108.6	172	84W	28.6	65.4	0.5-1	Oxi. Qtz.
4	134	173	55W	19.1	3.2	0.5-1	Oxi. Qtz.
5	181	157	61W	65.7	21.2	1-2	Oxi. Qtz.
6	218.2	161	87W	11.8	2.1	FF	Oxi. Qtz.
7	245.6	156	67W	101.4	79.3	1-4	Oxi. Qtz.
8	262.2	147	87W	40.8	2.5	FF	Oxi. Qtz.
9	292.1	144	64W	9.1	3.6	FF	Oxi. Qtz.
10	351.2	326	86NE	6.9	1.4	0.5-1	Oxi. Qtz.
11	368.7	33	86NE	60.8	5.2	FF	Oxi. Qtz.
12	378.2	147	78NE	14.2	2.3	0.5-1	Oxi. Qtz.

Table A.99: Fox Creek 1d

Fracture	Distance from Origin (cm)	Strike	Dip	Length (cm)	Height (cm)	Aperture (mm)	Type of Fill
1	14.5	166	62W	35.5	0.6	1-2	Oxi. Qtz.
2	15.4	157	76W	20.9	1.1	0.5-1	Oxi. Qtz.
3	36.4	143	IND	40.8	IND	1-2	Oxi. Qtz.
4	74.2	323	55NE	20.2	13.1	1	Oxi. Qtz.
5	94.2	337	56NE	17.9	10.2	1	Oxi. Qtz.
6	104.6	319	47NE	9.3	16.2	1-2	Oxi. Qtz.
7	119.1	334	63NE	14.1	15.2	1	Oxi. Qtz.
8	126.8	342	76NE	41.8	13.2	FF	Oxi. Qtz.

Table A.100: Fox Creek 1e

Fracture	Distance from Origin (cm)	Strike	Dip	Length (cm)	Height (cm)	Aperture (mm)	Type of Fill
1	12.1	269	74NW	12.1	27.2	2	Qtz.
2	14	279	87NW	14	21.7	1-2	Qtz.
3	31.2	280	76NW	31.2	6.2	0.5-1	Qtz.
4	32.3	275	82NW	40	17.2	1-2	Qtz.
5	40	277	74NW	32.3	3.6	1-2	Qtz.
6	46.9	282	78NW	46.9	21.6	1-3	Qtz.

Table A.101: Fox Creek 2

Fracture	Distance from Origin (cm)	Strike	Dip	Length (cm)	Height (cm)	Aperture (mm)	Type of Fill
1	10.8	322	68NE	66.8	51.4	2-5	Oxi. Qtz.
2	40.6	346	53NE	3.2	1.9	FF	Oxi. Qtz.
3	47.1	343	59NE	16.9	3.1	FF	Oxi. Qtz.
4	56.5	337	69NE	86.2	3.6	1-2	Oxi. Qtz.
5	83.2	334	68NE	25.6	1.1	FF	Oxi. Qtz.
6	95.2	343	76NE	21.1	0.4	0.5-1	Oxi. Qtz.
7	114.5	353	72NE	18.5	1.4	0.5-1	Oxi. Qtz.
8	126.2	356	71NE	42.8	12.2	1-3	Oxi. Qtz.
9	137	349	66NE	91.6	81.6	1-3	Oxi. Qtz.
10	153.2	162	84SW	10.2	10.6	FF	Oxi. Qtz.
11	155.4	165	85SW	7	1	FF	Oxi. Qtz.
12	169.8	338	70NE	19	4.6	0.5-1	Oxi. Qtz.
13	177.1	343	73NE	29.5	7.6	0.5-1	Oxi. Qtz.
14	189	339	74NE	10.2	0.8	1	Oxi. Qtz.
15	224.1	348	78NE	49.2	30.3	1-2	Oxi. Qtz.

APPENDIX B: Natural Fracture Statistics

1. Fracture Characteristics

To further understand how the fracture sets change along the margin of the basin, fracture characteristics were analyzed to determine the variation in density, spacing, height, and length. For density and spacing data, box and whisker plots were generated to graphically depict how the fracture sets compare with one another for each of the separate field areas. Since only visual heights and lengths were measured in the field, histograms were generated to show statistical variation amongst sets. For this study, only basement metamorphic rocks were analyzed because there was enough statistical data. Whereas in igneous and sedimentary rocks, fracture data were more limited.

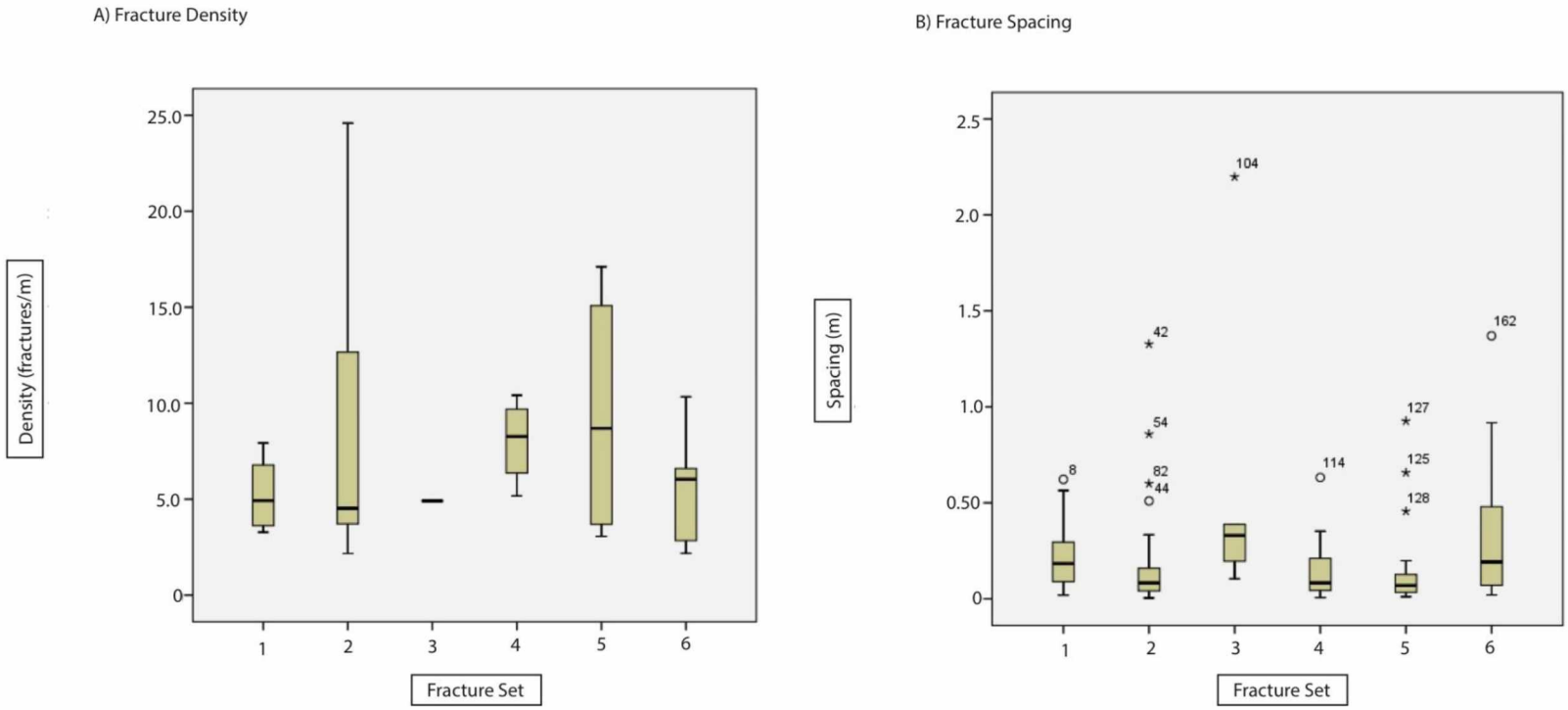

Figure B.1: Fairbanks fracture density and spacing (metamorphic rocks). Box and whisker plots for the mean density and spacing values in the Fairbanks area. For density values, only 5 fracture sets had enough data to create plots. Both spacing and density charts show the fracture sets have similar average values. Statistical outliers are shown as asterisks and circles.

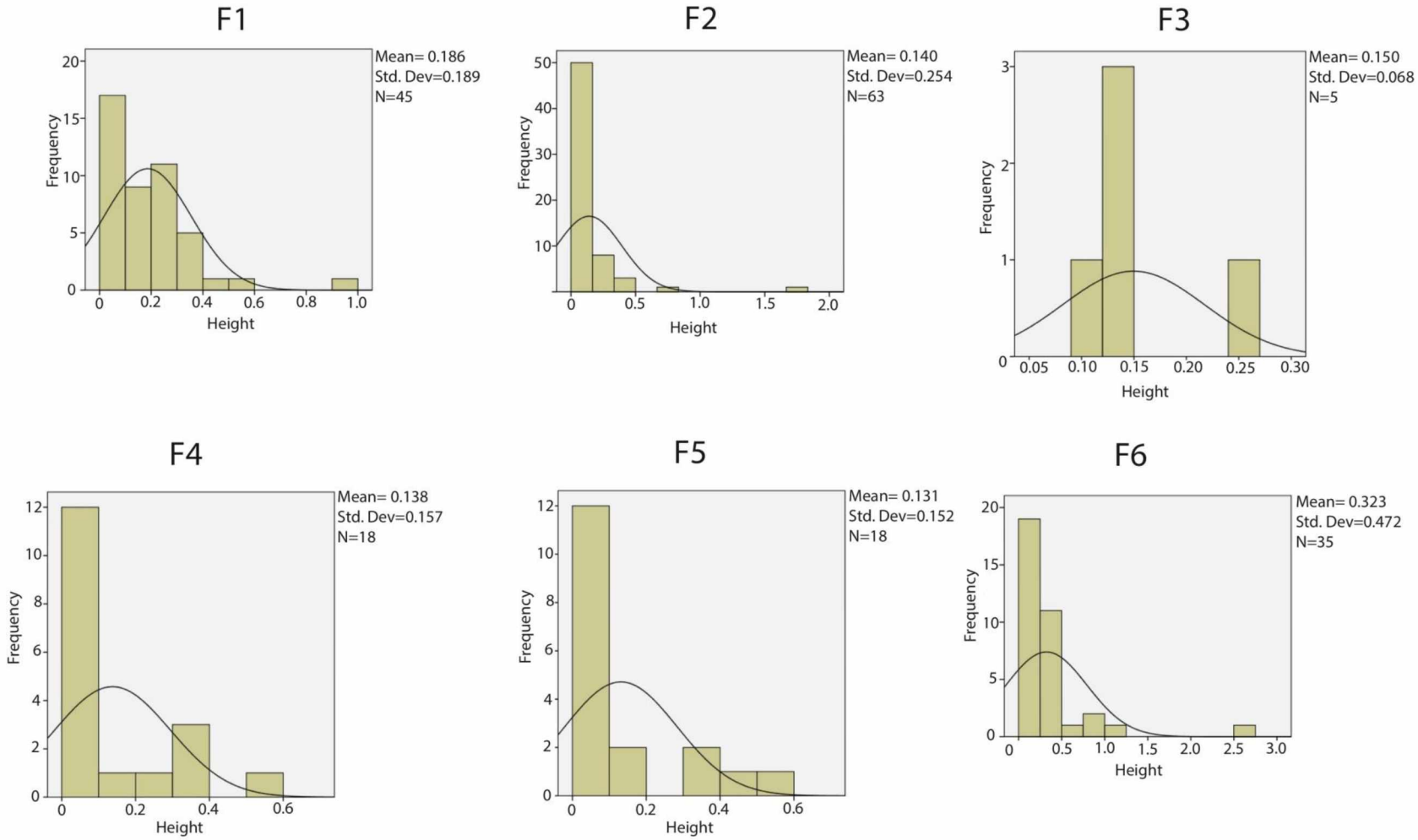

Figure B.2: Fairbanks fracture height (metamorphic rocks). Histograms for the fracture height values in the Fairbanks area. Normal distribution curve is shown on each graph. Fracture heights for all sets range greatly from .09 m-9.1m.

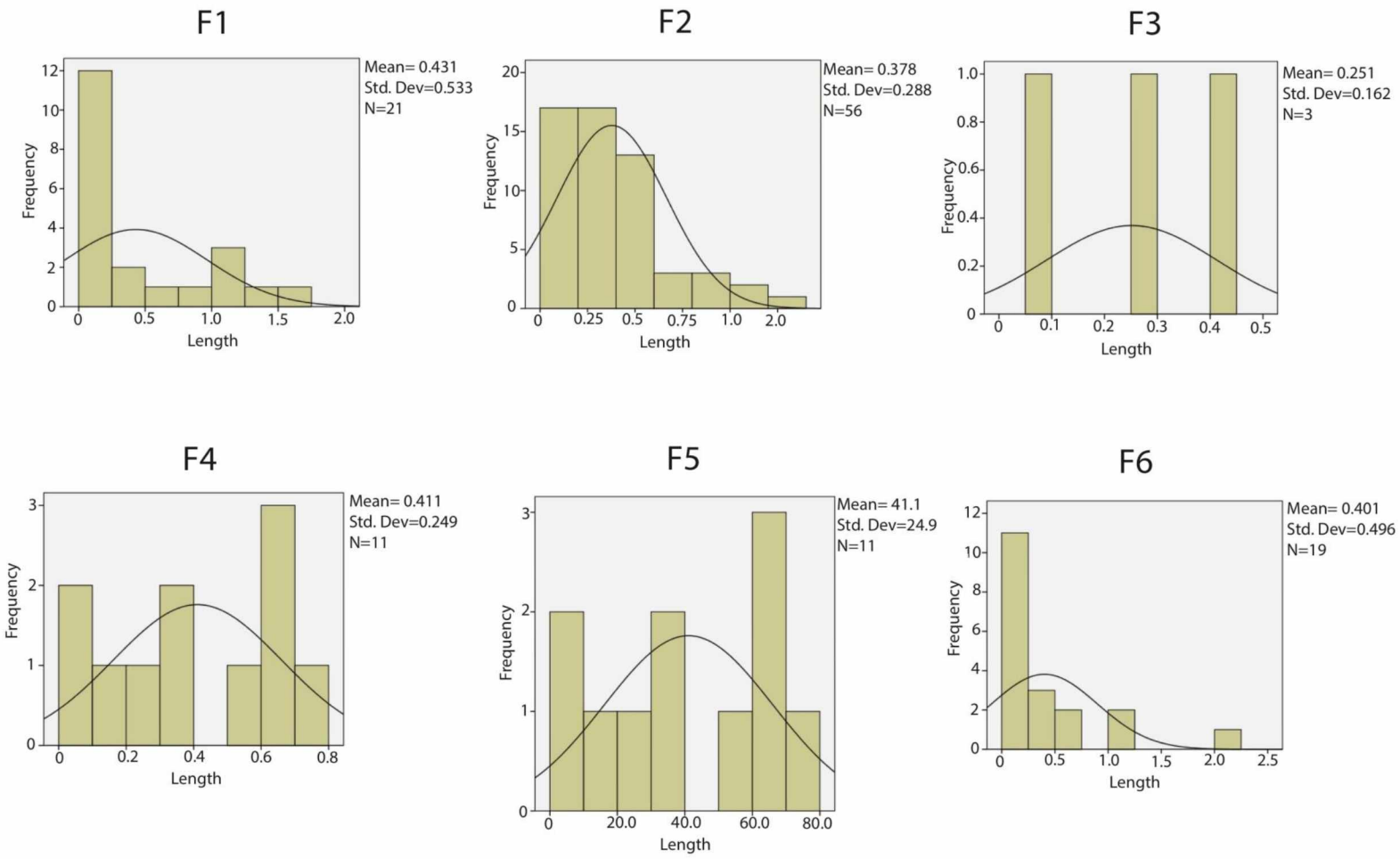

Figure B.3: Fairbanks fracture length histograms (metamorphic rocks). Histograms for the fracture length values in the Fairbanks area. Normal distribution curve is shown on each graph. Fracture length for all sets ranges from 06 m–0.18 m.

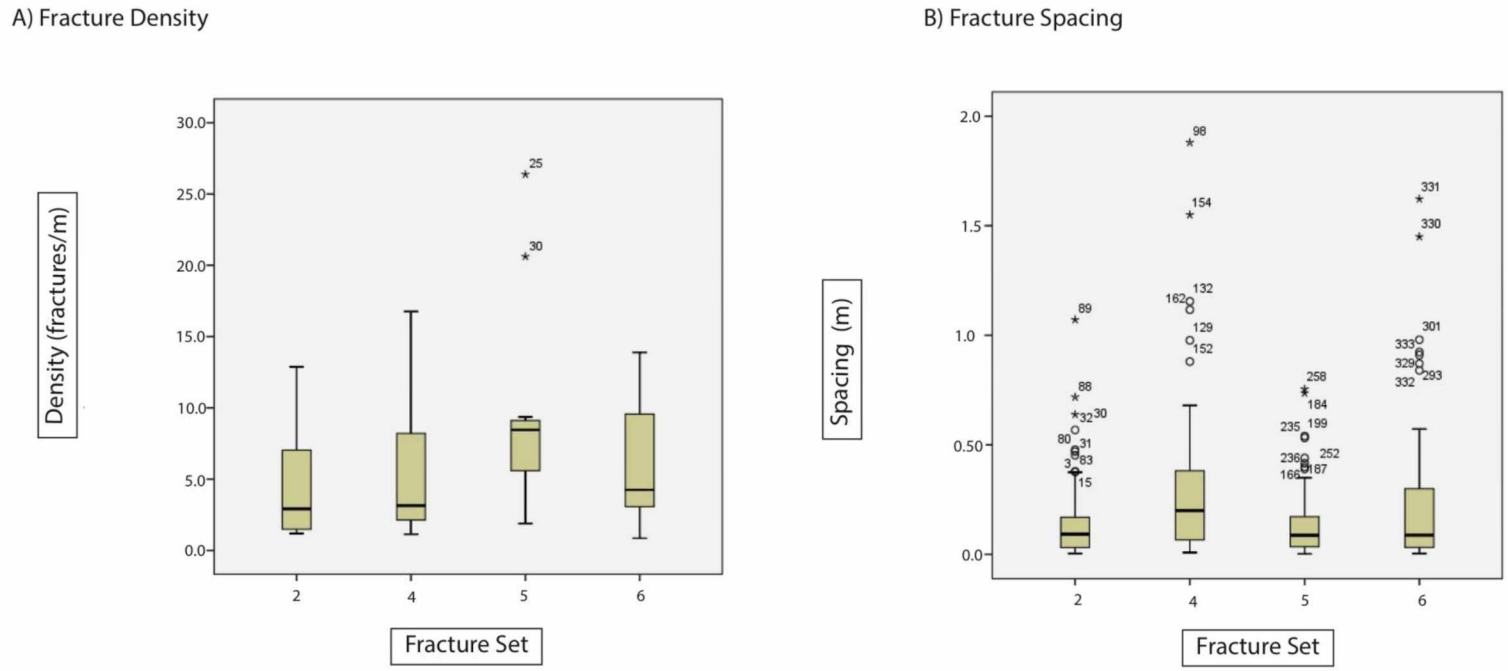

Figure B.4: Parks Highway fracture density and spacing. Box and whisker plots for the mean density and spacing values in the Fairbanks area. Density and spacing show similar average values. Statistical outliers are shown as asterisks and circles.

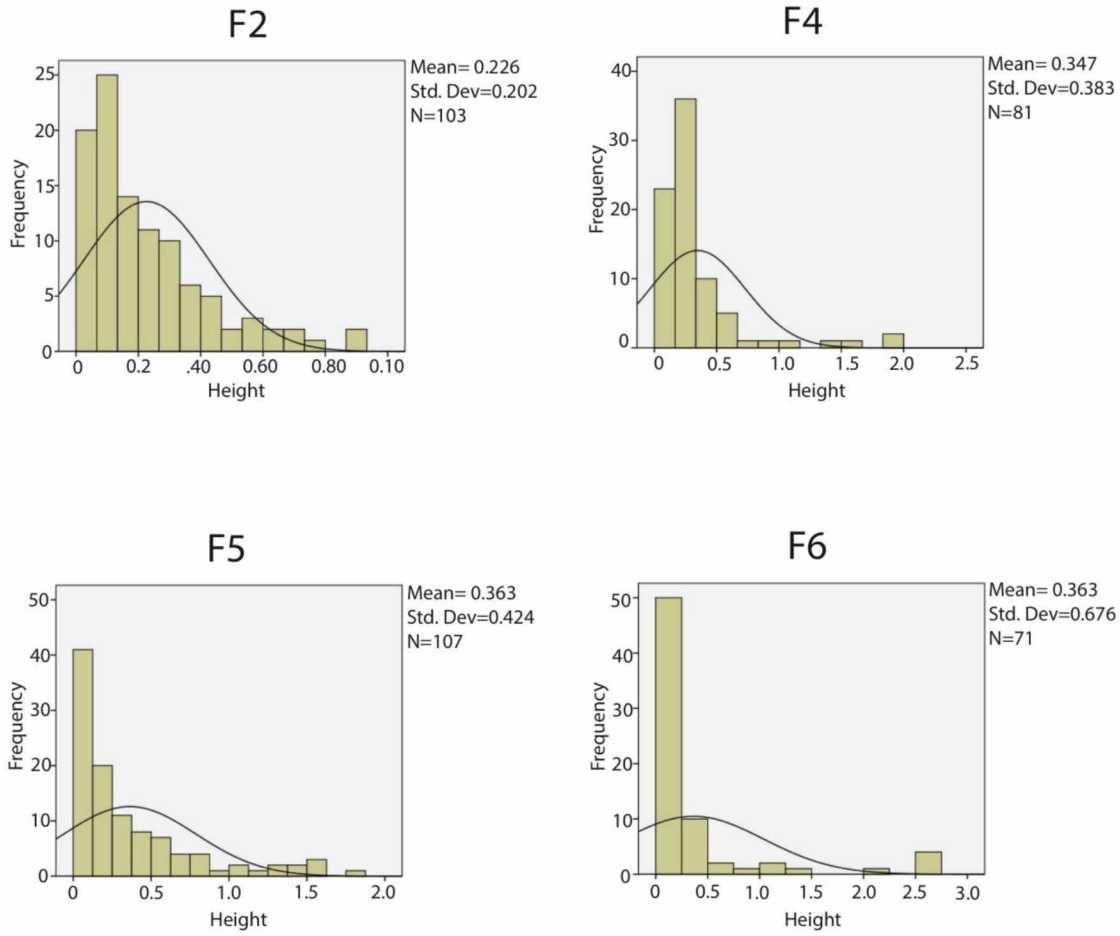

Figure B.5: Parks Highway fracture height. Histograms for the fracture height values in the Parks Highway Area. Normal distribution curve is shown on each graph. Fracture heights for all sets range greatly from .002 m-2.76m.

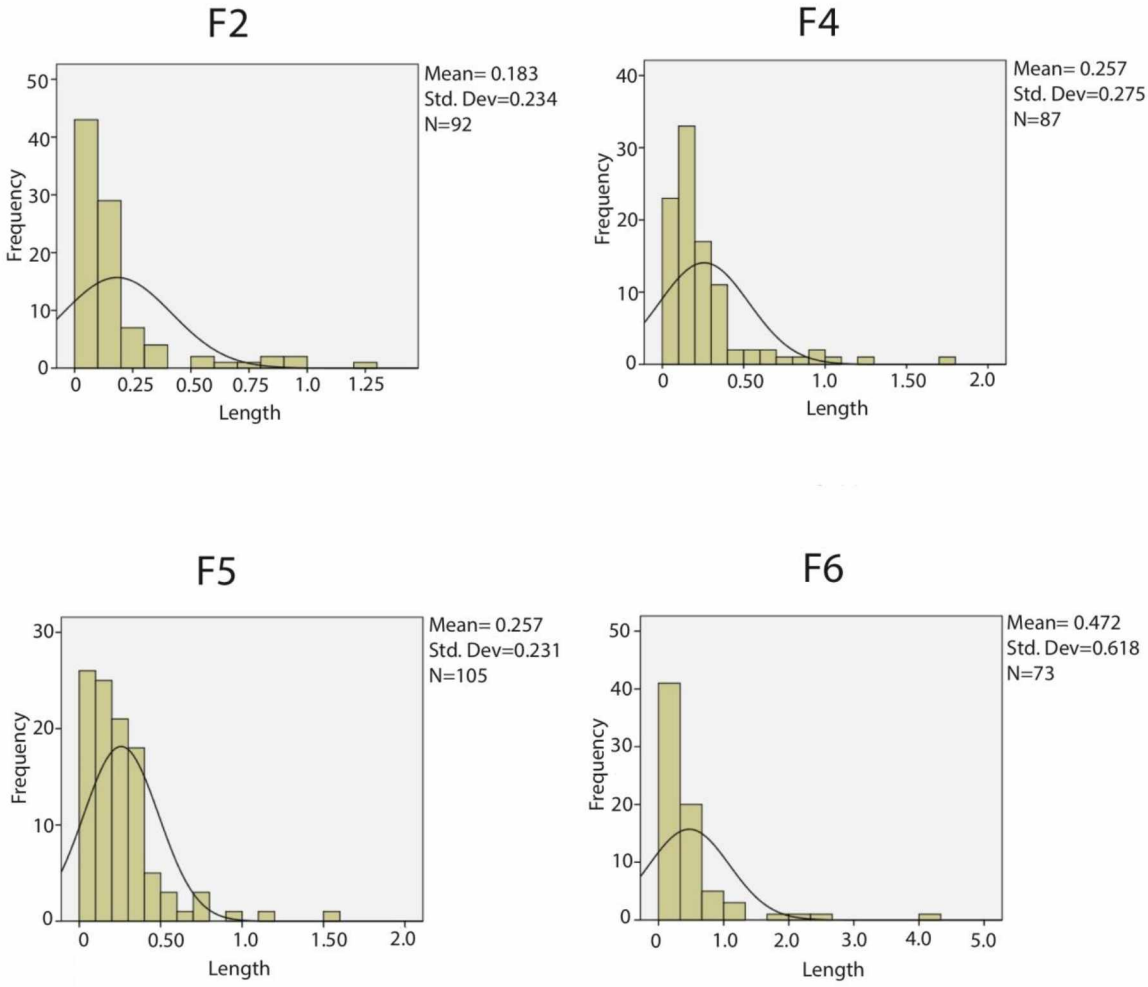

Figure B.6: Parks Highway fracture length. Histograms for the fracture length values in the Parks Highway area. Normal distribution curve is shown on each graph. Fracture lengths for all sets range greatly, but average values are below .5m.

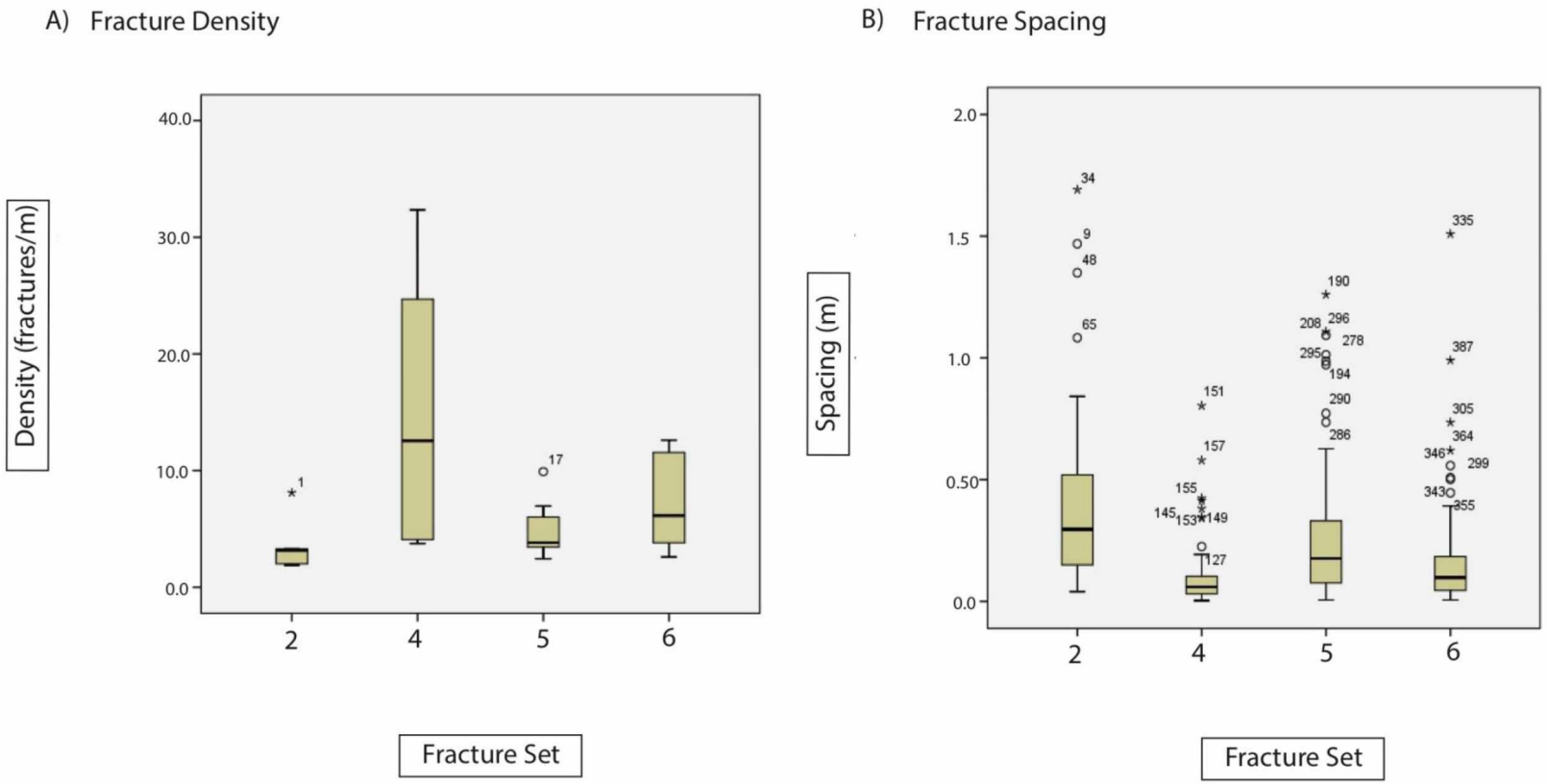

Figure B.7: Nenana area fracture density and spacing. Box and whisker plots for the mean density and spacing values for the Nenana field area. Apart from F4, all fracture sets show similar values for density. For fracture spacing, all sets show similar average values. Statistical outliers are shown as asterisks and circles.

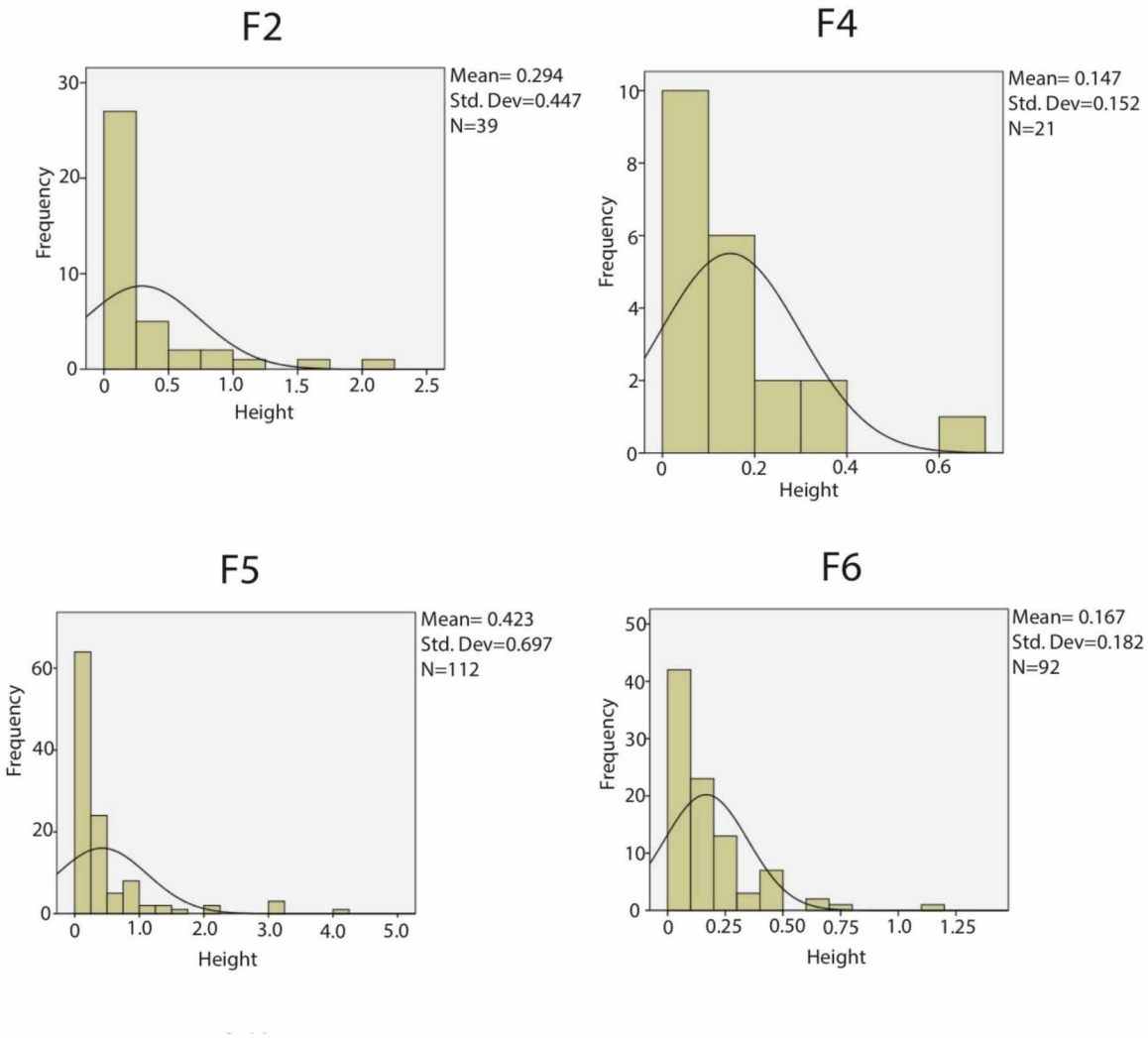

Figure B.8: Nenana area fracture height. Histograms for the fracture height values in the Nenana Area. Normal distribution curve is shown on each graph. Fracture heights for all sets range greatly from .002 m-4m, but average values are lower than .5m.

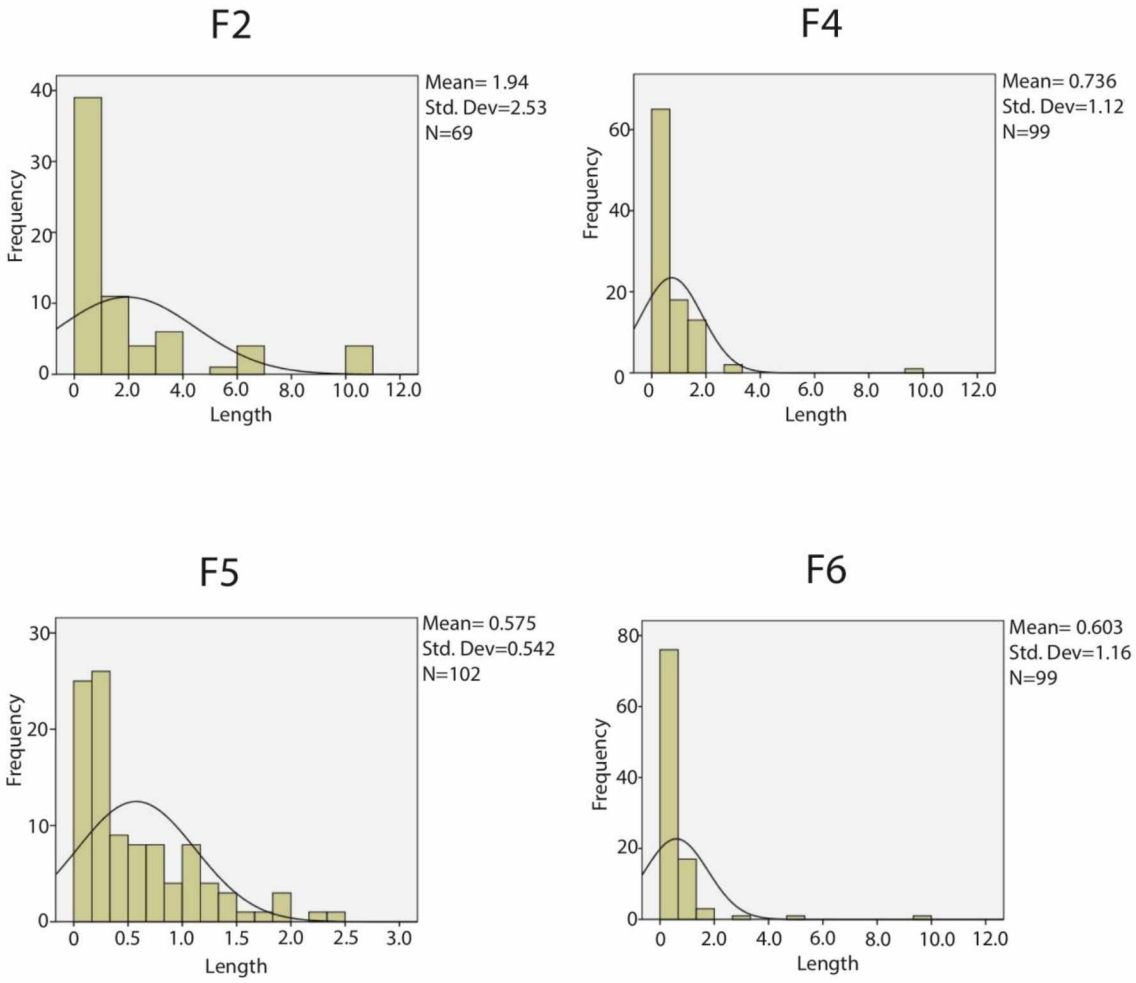

Figure B.9: Nenana area fracture length. Histograms for the fracture length values in the Nenana Area. Normal distribution curve is shown on each graph. Fracture lengths for all sets range greatly from .011 m-10m.

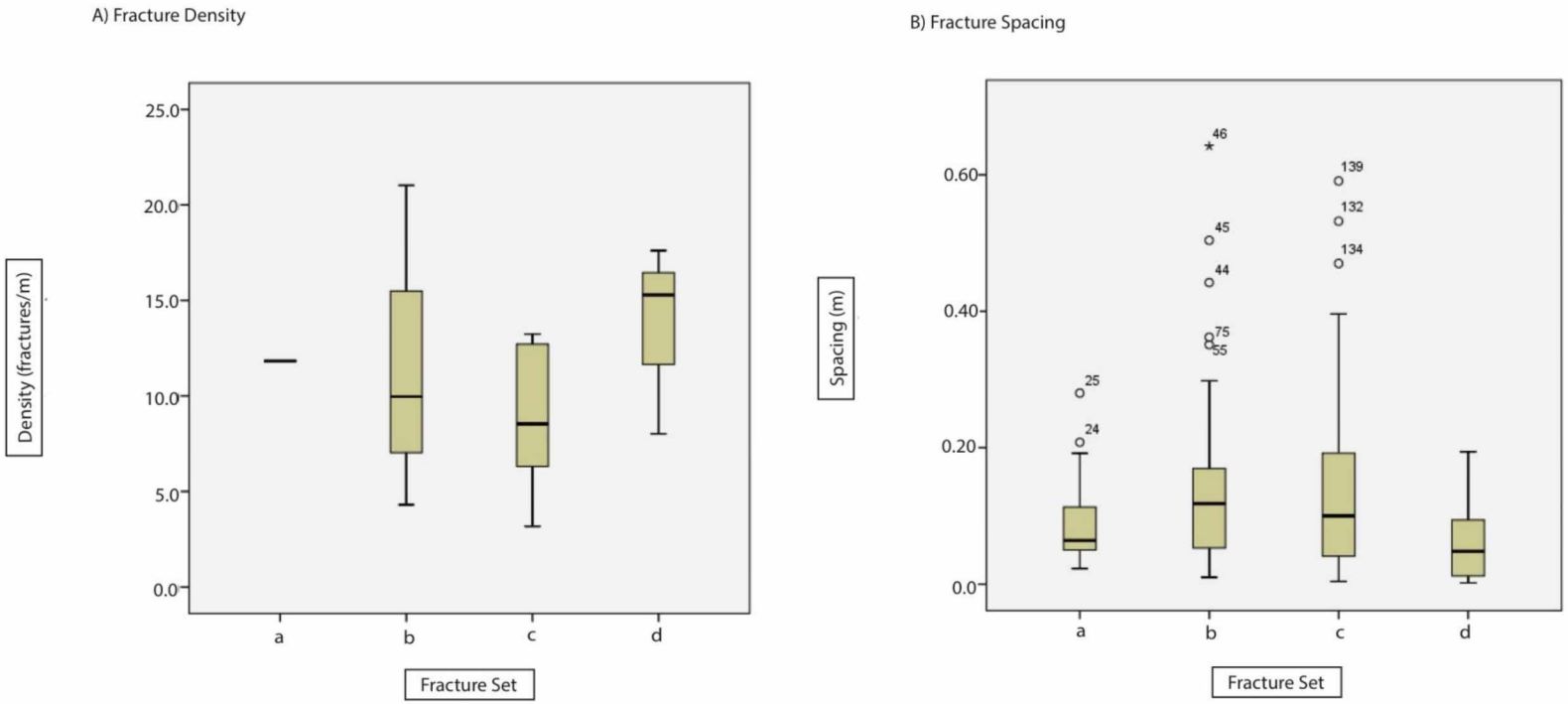

Figure B.10: Healy area fracture density and spacing (metamorphic rocks). Box and whisker plots for the mean density and spacing values in metamorphic rocks throughout the Healy area. For density values, only three sets had enough data to create box and whisker plots. Average values for density range from around 9 fractures/m to just under 14 fractures/m. Fracture spacing data show similar mean values. Statistical outliers are shown as asterisks and circles.

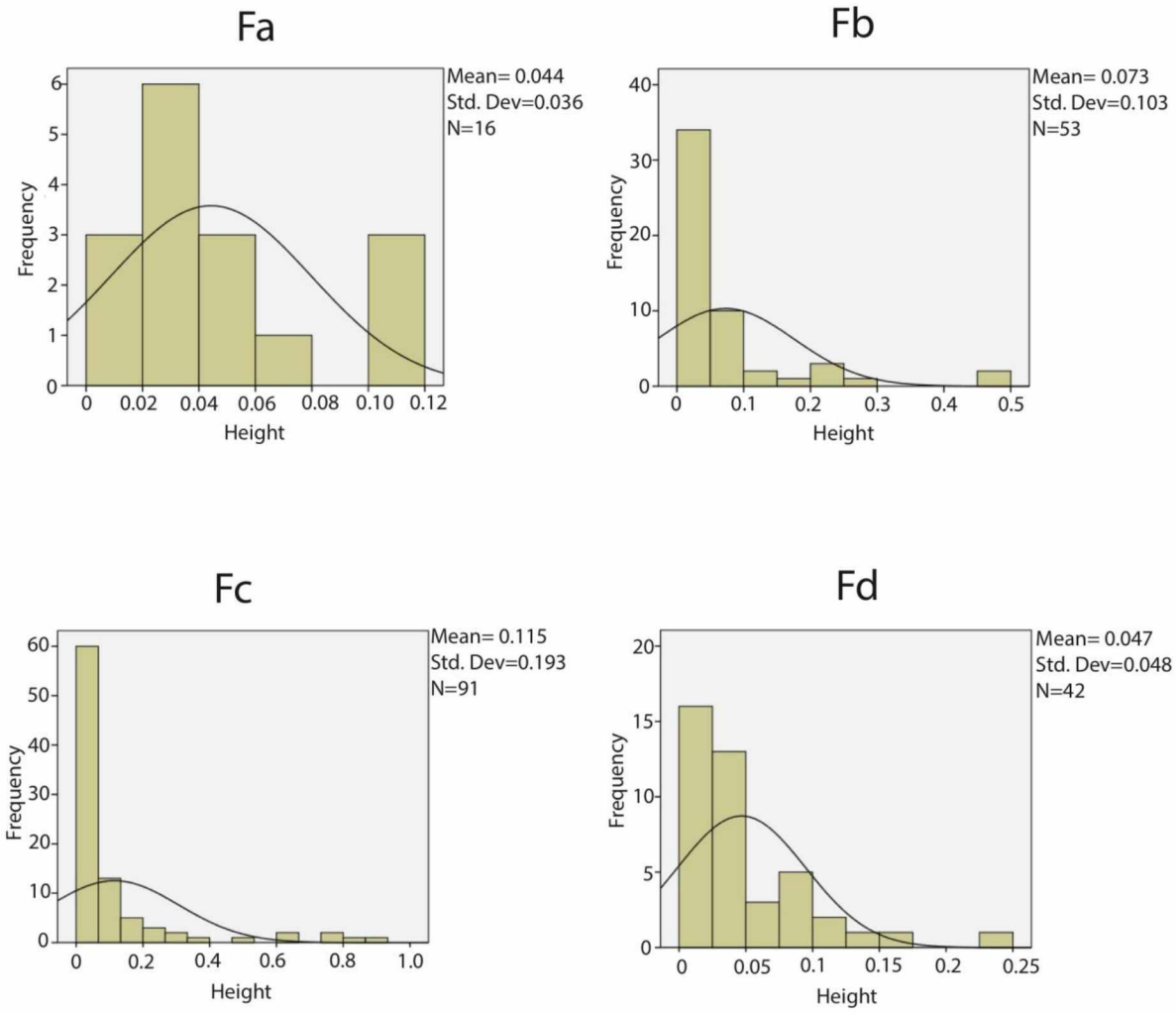

Figure B.11: Healy area fracture height. Histograms for the fracture height values in the Healy Area. Normal distribution curve is shown on each graph. Fracture heights for all sets range greatly from .002 m-1.94m.

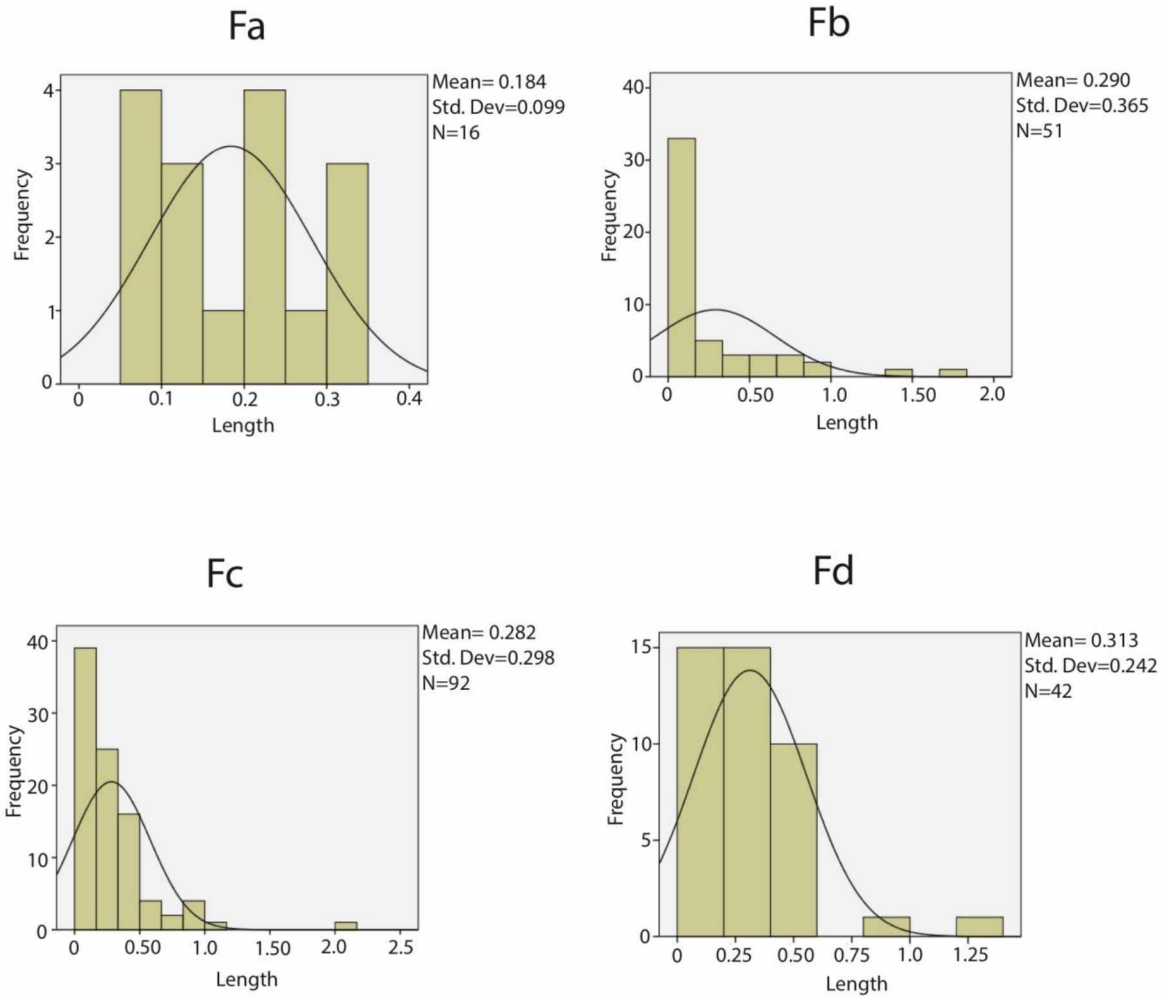

Figure B.12: Healy area fracture length. Histograms for the fracture length values in the Healy Area. Normal distribution curve is shown on each graph. Fracture lengths for all sets range greatly from .012 m-2.17m.

2. Statistically Comparing Common Fracture Sets Found in Separate Field Areas

Fractures of the same orientation, vein fill, and shear indicators are present across field locations in the Fairbanks, Parks Highway and Nenana areas. In order to statistically prove if they are the same set, one-way analysis of variance (anova test) and post hoc tests (Tukey HSD test) were applied to the fracture density and spacing data of these common sets. The anova test was applied to see if there is a statistical difference in the values for density and spacing. The Tukey post hoc test was then applied to see which fracture sets can be statistically distinguished from each other. For example, the Tukey HSD test is applied to see which of the F4 sets from the three field areas is different from the other mean values for F4. This test was only significant if the sets of data showed statistical variation from each other. For both tests, if the significant values are less than .05, they are statistically different; if they are greater than .05, the values are not statistically different.

Fracture Set 2

Between the three areas, the fracture densities significant values are greater than .05, signifying that there is no significant statistical difference between the three pools of data (Figs. B.13-B.14). As for fracture spacing, data from the Fairbanks and Parks Highway area show no significant difference, but the comparison between the other locations show that statistically the sets are different.

Fracture Set 4

The density anova test shows that the three sets are statistically different with a significant value of .046 (Figs. B.15-B.16). Comparing each set's data, the results of the Tukey HSD test for the density data shows that the only sets that are different are those from the Nenana area and Parks Highway area. For fracture spacing, the anova test revealed that the sets are statistically different,

whereas the results from the post hoc test show that sets from the Fairbanks and Nenana area are not statistically different but the other comparisons are different.

Fracture Set 5

The results from the anova test for fracture density shows that the sets are not statistically different (Figs. B.17-B.18*)*. Both tests for fracture spacing show that the sets are statistically different with exception to a significant value from the Tukey HSD test that shows that the sets from the Fairbanks and Parks Highway area are not statistically different.

Fracture Set 6

For density, the results from both tests show that there is no statistical difference in the densities across the three field areas. All the significant values are greater than .05 and show that the values not statistically different (Figs. B.19-B.20). As for fracture spacing, the results from the anova test shows that the three sets are statistically different. The results from the post hoc test (Tukey HSD) show that the sets from the Fairbanks and Nenana areas are the only sets that are significantly different from each other.

Summary of Statistical Results

The data above is not perfect, but for each fracture set at least one of either the spacing or density tests shows some type of comparison across the focus areas. The statistical tests were performed to see if the fracture sets are related statistically and some are strongly related but because some tests do not show comparison does not mean that they are different sets. I believe that these fracture sets should be considered the same sets. The statistical differences from above could be due to sample size, outcrop conditions, or from differences in the proximity to the basin.

A)

Descriptives

Density

	N	Mean	Std. Deviation	Std. Error	95% Confidence Interval for Mean		Minimum	Maximum
					Lower Bound	Upper Bound		
1	7	9.315201775	8.202970726	3.100431507	1.728719176	16.90168437	2.174858634	24.59016393
2	10	4.700991777	3.960891132	1.252543754	1.867540952	7.534442602	1.195219124	12.87553648
3	6	4.575893218	3.133692311	1.279324529	1.287284822	7.864501614	1.889644747	8.960573477
Total	23	6.072682153	5.640299714	1.176083790	3.633633655	8.511730650	1.195219124	24.59016393

B)

Means Plots

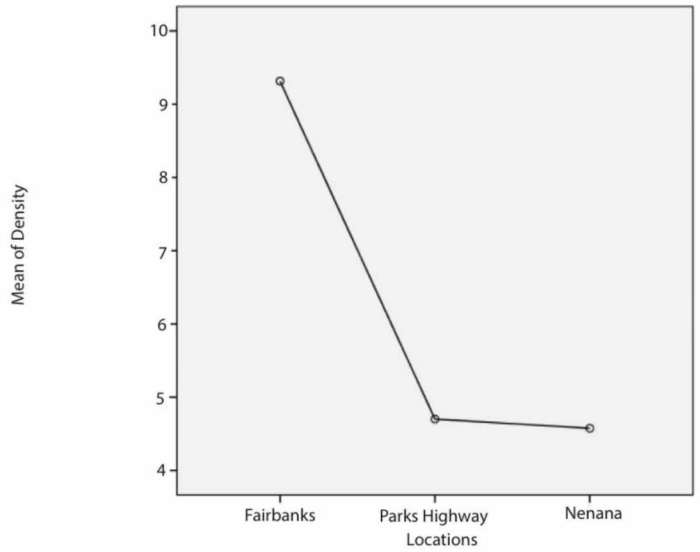

C)

ANOVA

Density

	Sum of Squares	df	Mean Square	F	Sig.
Between Groups	105.855	2	52.928	1.782	.194
Within Groups	594.030	20	29.702		
Total	699.886	22			

D)

Multiple Comparisons

Dependent Variable: Density

Tukey HSD

(I) V2	(J) V2	Mean Difference (I-J)	Std. Error	Sig.	95% Confidence Interval	
					Lower Bound	Upper Bound
1	2	4.614209998	2.685745098	.223	-2.18067651	11.40909650
	3	4.739308557	3.032050163	.284	-2.93172350	12.41034061
2	1	-4.61421000	2.685745098	.223	-11.4090965	2.180676508
	3	.1250985596	2.814321557	.999	-6.99508406	7.245281179
3	1	-4.73930856	3.032050163	.284	-12.4103406	2.931723496
	2	-.125098560	2.814321557	.999	-7.24528118	6.995084060

Figure B.13: Comparison of mean fracture density across field locations (F2).

A) Descriptives table: 1=Fairbanks, 2=Parks Highway area, 3= Nenana Area
B) Means of fracture density plotted
C) Results of the one-way analysis of variance test (anova) between sample locations for F2. The significant value is greater than .05 signifying that there is no statistical difference in fracture density between the three sample locations.
D) Tukey HSD Post Hoc test table showing that the significant value is greater than .05 in all circumstances signifying that there is no statistical difference in fracture density between the three sample locations.

A)

Descriptives

Spacing

	N	Mean	Std. Deviation	Std. Error	95% Confidence Interval for Mean		Minimum	Maximum
					Lower Bound	Upper Bound		
1	58	.1502758621	.2186827224	.0287144482	.0927761713	.2077755528	.0040000000	1.327000000
2	89	.1506966292	.1806860917	.0191526874	.1126346876	.1887585708	.0040000000	1.071000000
3	66	.3930909091	.3436150676	.0422960910	.3086197824	.4775620358	.0400000000	1.691000000
Total	213	.2256901408	.2743207353	.0187961471	.1886388560	.2627414257	.0040000000	1.691000000

B)

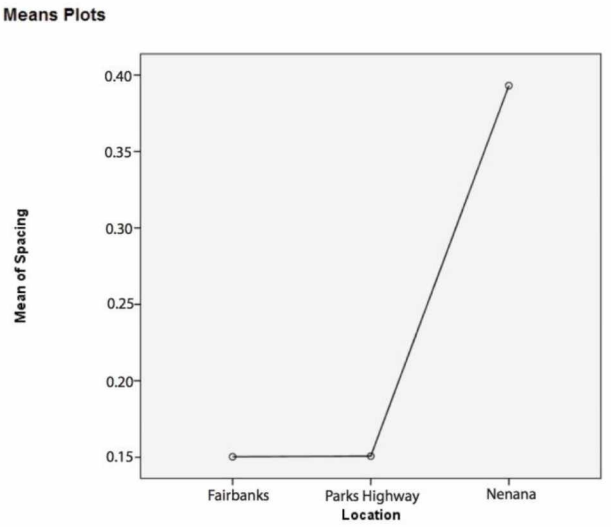

C)

ANOVA

Spacing

	Sum of Squares	df	Mean Square	F	Sig.
Between Groups	2.680	2	1.340	21.200	.000
Within Groups	13.273	210	.063		
Total	15.953	212			

D)

Multiple Comparisons

Dependent Variable: Spacing

Tukey HSD

(I) Location	(J) Location	Mean Difference (I-J)	Std. Error	Sig.	95% Confidence Interval	
					Lower Bound	Upper Bound
1	2	-.000420767	.0424260226	1.000	-.100565384	.0997238496
	3	-.242815047*	.0452488483	.000	-.349622810	-.136007284
2	1	.0004207671	.0424260226	1.000	-.099723850	.1005653838
	3	-.242394280*	.0408396047	.000	-.338794232	-.145994328
3	1	.242815047*	.0452488483	.000	.1360072840	.3496228101
	2	.242394280*	.0408396047	.000	.1459943275	.3387942323

*. The mean difference is significant at the 0.05 level.

Figure B.14: Comparison of mean fracture spacing across field locations (F2).

A) Descriptives table: 1=Fairbanks, 2=Parks Highway area, 3= Nenana Area
B) Means of fracture spacing plotted
C) Results of the one-way analysis of variance test (anova) between sample locations for F2. The significant value is less than .05 signifying that there is a statistical difference in fracture spacing between the three sample locations.
D) Tukey HSD Post Hoc showing that the significant value is greater than .05 between the Fairbanks and Parks Highway area signifying that there is no statistical difference in fracture spacing between the two sample locations. The Nenana area values in comparison to the Fairbanks and Parks Highway values show a difference in variance and show no common bounds.

A)

Descriptives

Density

	N	Mean	Std. Deviation	Std. Error	95% Confidence Interval for Mean		Minimum	Maximum
					Lower Bound	Upper Bound		
1	4	8.028157609	2.235315203	1.117657601	4.471272305	11.58504291	5.167958656	10.41666667
2	12	5.430510775	5.107794578	1.474493287	2.185172931	8.675848618	1.131221719	16.75977654
3	6	15.00561550	11.44997240	4.674431657	2.989606390	27.02162461	3.755054882	32.35294118
Total	22	8.514202396	7.944359881	1.693743218	4.991870552	12.03653424	1.131221719	32.35294118

B)

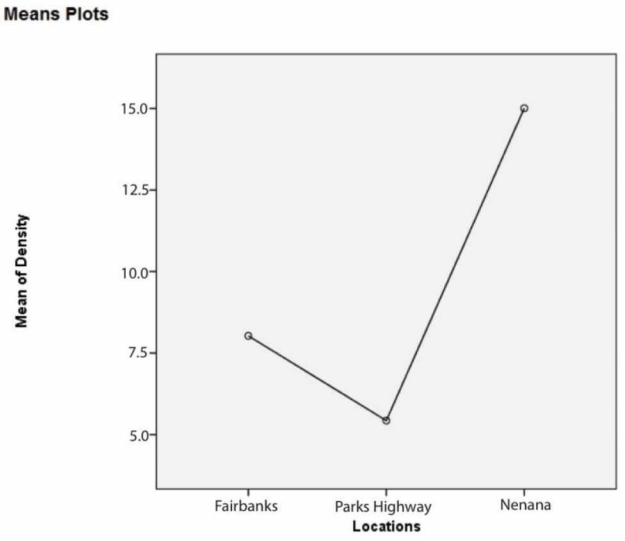

C)

ANOVA

Density

	Sum of Squares	df	Mean Square	F	Sig.
Between Groups	367.885	2	183.943	3.650	.046
Within Groups	957.484	19	50.394		
Total	1325.370	21			

D)

Multiple Comparisons

Dependent Variable: Density

Tukey HSD

(I) Locations	(J) Locations	Mean Difference (I-J)	Std. Error	Sig.	95% Confidence Interval	
					Lower Bound	Upper Bound
1	2	2.597646835	4.098533031	.804	-7.81447178	13.00976545
	3	-6.97745789	4.582299233	.303	-18.6185604	4.663644617
2	1	-2.59764683	4.098533031	.804	-13.0097654	7.814471780
	3	-9.57510472*	3.549433723	.036	-18.5922640	-.557945496
3	1	6.977457889	4.582299233	.303	-4.66364462	18.61856040
	2	9.57510472*	3.549433723	.036	.5579454964	18.59226395

*. The mean difference is significant at the 0.05 level.

Figure B.15: Comparison of mean fracture density across field locations (F4).

A) Descriptives table: 1=Fairbanks, 2=Parks Highway area, 3= Nenana Area
B) Means of fracture density plotted
C) Results of the one-way analysis of variance test (anova) between sample locations for F4. The significant value is greater than .05 signifying that there is no statistical difference in fracture density between the three sample locations.
D) Tukey HSD Post Hoc test table showing that the significant value is less than .05 between the Parks Highway and Nenana area signifying that there is a statistical difference in fracture density between the two sample locations. Other comparisons resulted in significant values greater than .05, meaning that there is no statistical difference.

A)

Descriptives

Spacing

	N	Mean	Std. Deviation	Std. Error	95% Confidence Interval for Mean		Minimum	Maximum
					Lower Bound	Upper Bound		
1	18	.1446111111	.1614143878	.0380457361	.0643416245	.2248805977	.0060000000	.6320000000
2	73	.3023972603	.3549591033	.0415448207	.2195791739	.3852153466	.0080000000	1.880000000
3	91	.0951758242	.1265970505	.0132709768	.0688107124	.1215409360	.0030000000	.8040000000
Total	182	.1831813187	.2651605270	.0196550059	.1443989053	.2219637321	.0030000000	1.880000000

B)

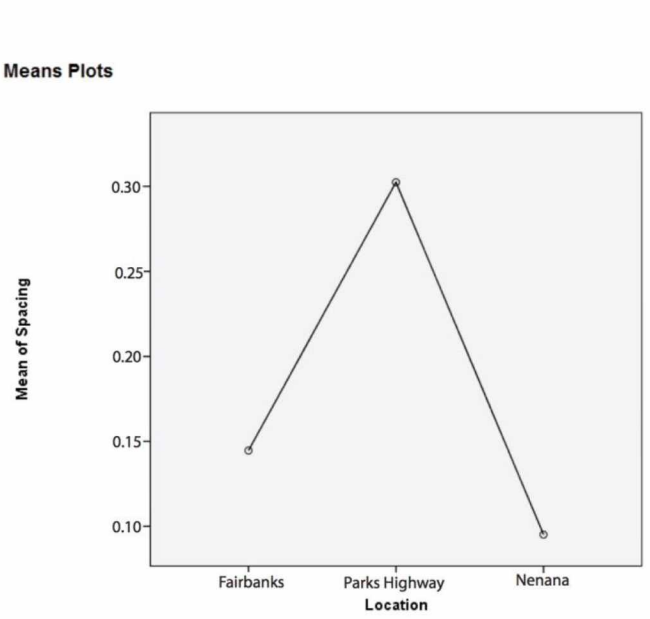

C)

ANOVA

Spacing

	Sum of Squares	df	Mean Square	F	Sig.
Between Groups	1.769	2	.885	14.450	.000
Within Groups	10.957	179	.061		
Total	12.726	181			

D)

Multiple Comparisons

Dependent Variable: Spacing

Tukey HSD

(I) Location	(J) Location	Mean Difference (I-J)	Std. Error	Sig.	95% Confidence Interval	
					Lower Bound	Upper Bound
1	2	-.157786149*	.0651093468	.043	-.311663896	-.003908403
	3	.0494352869	.0638229134	.719	-.101402136	.2002727099
2	1	.157786149*	.0651093468	.043	.0039084028	.3116638955
	3	.207221436*	.0388740799	.000	.1153474411	.2990954311
3	1	-.049435287	.0638229134	.719	-.200272710	.1014021360
	2	-.207221436*	.0388740799	.000	-.299095431	-.115347441

*. The mean difference is significant at the 0.05 level.

Figure B.16: Comparison of mean fracture spacing across field locations (F4).

A) Descriptives table: 1=Fairbanks, 2=Parks Highway area, 3= Nenana Area
B) Means of fracture spacing plotted
C) Results of the one-way analysis of variance test (anova) between sample locations for F4. The significant value is less than .05 signifying that there is a statistical difference in fracture spacing between the three sample locations.
D) Tukey HSD Post Hoc test table showing that the significant value is less than .05 between all locations besides the Fairbanks and Nenana areas, signifying that there is a statistical difference between fracture spacing at most locations.

A)

Descriptives

Density

	N	Mean	Std. Deviation	Std. Error	95% Confidence Interval for Mean		Minimum	Maximum
					Lower Bound	Upper Bound		
1	4	9.384040816	6.796874645	3.398437323	-1.43130349	20.19938512	3.061224490	17.10620100
2	11	9.720224311	7.341915328	2.213670762	4.787858480	14.65259014	1.888574127	26.37362637
3	9	4.777154913	2.437876148	.8126253825	2.903237420	6.651072405	2.437703142	9.909521758
Total	24	7.810542704	6.107756734	1.246740623	5.231463227	10.38962218	1.888574127	26.37362637

B)

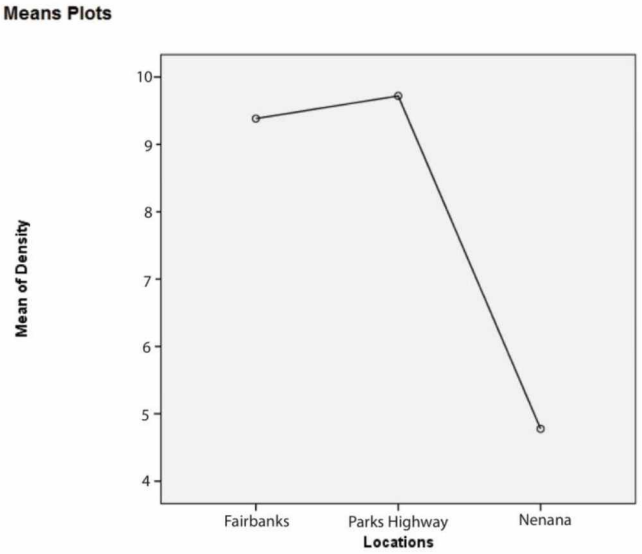

C)

ANOVA

Density

	Sum of Squares	df	Mean Square	F	Sig.
Between Groups	132.832	2	66.416	1.923	.171
Within Groups	725.176	21	34.532		
Total	858.008	23			

D)

Multiple Comparisons

Dependent Variable: Density

Tukey HSD

(I) Locations	(J) Locations	Mean Difference (I-J)	Std. Error	Sig.	95% Confidence Interval	
					Lower Bound	Upper Bound
1	2	-.336183495	3.431083190	.995	-8.98447011	8.312103125
	3	4.606885903	3.531281853	.408	-4.29395850	13.50773030
2	1	.3361834947	3.431083190	.995	-8.31210313	8.984470115
	3	4.943069398	2.641249071	.172	-1.71438475	11.60052354
3	1	-4.60688590	3.531281853	.408	-13.5077303	4.293958496
	2	-4.94306940	2.641249071	.172	-11.6005235	1.714384746

Figure B.17: Comparison of mean fracture density across field locations (F5).

A) Descriptives table: 1=Fairbanks, 2=Parks Highway area, 3= Nenana Area
B) Means of fracture density plotted
C) Results of the one-way analysis of variance test (anova) between sample locations for F5. The significant value is greater than .05 signifying that there is no statistical difference in fracture density between the three sample locations.
D) Tukey HSD Post Hoc test table showing that the significant value is greater than .05 in all circumstances signifying that there is no statistical difference in fracture density between the three sample locations.

A)

Descriptives

Spacing

	N	Mean	Std. Deviation	Std. Error	95% Confidence Interval for Mean		Minimum	Maximum
					Lower Bound	Upper Bound		
1	36	.1249722222	.1862143904	.0310357317	.0619663372	.1879781073	.0110000000	.9260000000
2	118	.1282711864	.1377002604	.0126763365	.1031663663	.1533760066	.0020000000	.7540000000
3	139	.2445251799	.2426066277	.0205776256	.2038369679	.2852133918	.0060000000	1.260000000
Total	293	.1830170648	.2073590866	.0121140472	.1591751493	.2068589804	.0020000000	1.260000000

B)

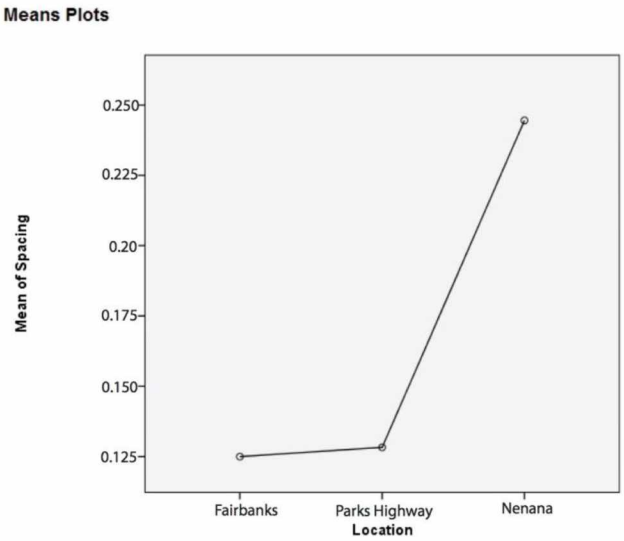

C)

ANOVA

Spacing

	Sum of Squares	df	Mean Square	F	Sig.
Between Groups	1.001	2	.500	12.560	.000
Within Groups	11.555	290	.040		
Total	12.555	292			

D)

Multiple Comparisons

Dependent Variable: Spacing

Tukey HSD

(I) Location	(J) Location	Mean Difference (I-J)	Std. Error	Sig.	95% Confidence Interval	
					Lower Bound	Upper Bound
1	2	-.003298964	.0380053998	.996	-.092832520	.0862345915
	3	-.119552958*	.0373282451	.004	-.207491264	-.031614651
2	1	.0032989642	.0380053998	.996	-.086234591	.0928325199
	3	-.116253993*	.0249859207	.000	-.175116111	-.057391876
3	1	.119552958*	.0373282451	.004	.0316146508	.2074912645
	2	.116253993*	.0249859207	.000	.0573918756	.1751161112

*. The mean difference is significant at the 0.05 level.

Figure B.18: Comparison of mean fracture spacing across field locations (F5).

A) Descriptives table: 1=Fairbanks, 2=Parks Highway area, 3= Nenana Area
B) Means of fracture spacing plotted
C) Results of the one-way analysis of variance test (anova) between sample locations for F5. The significant value is greater than .05 signifying that there is no statistical difference in fracture spacing between the three sample locations.
D) Tukey HSD Post Hoc test table showing that the significant value is greater than .05 between the Parks Highway and Nenana area signifying that there is a statistical difference in fracture spacing between the two sample locations. Other comparisons resulted in significant values less than .05, meaning that there is a statistical difference between sample locations.

A)

Descriptives

Density

	N	Mean	Std. Deviation	Std. Error	95% Confidence Interval for Mean		Minimum	Maximum
					Lower Bound	Upper Bound		
1	9	6.366974737	3.623981594	1.207993865	3.581335889	9.152613584	2.178649237	13.24503311
2	7	6.325794904	4.729203773	1.787471012	1.952010902	10.69957891	.8552856654	13.88888889
3	8	7.282147953	4.057270249	1.434461653	3.890185140	10.67411077	2.590673575	12.61656610
Total	24	6.660021691	3.951551231	.8066070173	4.991427946	8.328615436	.8552856654	13.88888889

B)

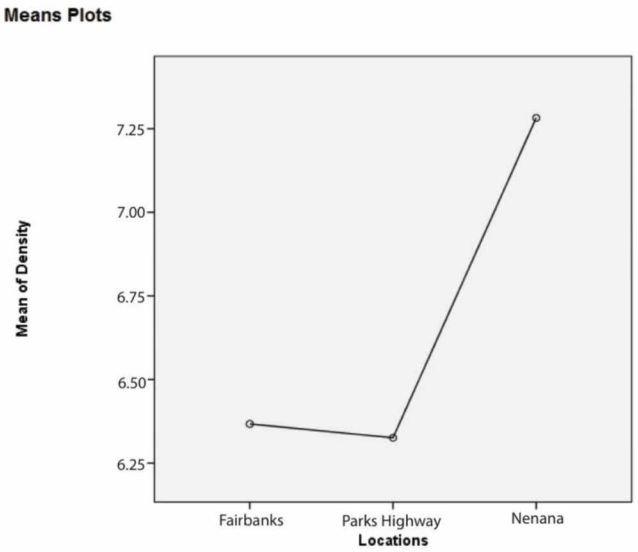

C)

ANOVA

Density

	Sum of Squares	df	Mean Square	F	Sig.
Between Groups	4.651	2	2.326	.138	.872
Within Groups	354.488	21	16.880		
Total	359.139	23			

D)

Multiple Comparisons

Dependent Variable: Density

Tukey HSD

(I) Locations	(J) Locations	Mean Difference (I-J)	Std. Error	Sig.	95% Confidence Interval	
					Lower Bound	Upper Bound
1	2	.0411798325	2.070527427	1.000	-5.17773025	5.260089911
	3	-.915173216	1.996408837	.891	-5.94726217	4.116915741
2	1	-.041179833	2.070527427	1.000	-5.26008991	5.177730246
	3	-.956353049	2.126389833	.895	-6.31606825	4.403362156
3	1	.9151732161	1.996408837	.891	-4.11691574	5.947262173
	2	.9563530486	2.126389833	.895	-4.40336216	6.316068253

Figure B.19: Comparison of mean fracture density across field locations (F6).

A) Descriptives table: 1=Fairbanks, 2=Parks Highway area, 3= Nenana Area
B) Means of fracture density plotted
C) Results of the one-way analysis of variance test (anova) between sample locations for F6. The significant value is greater than .05 signifying that there is no statistical difference in fracture density between the three sample locations.
D) Tukey HSD Post Hoc test table showing that the significant value is greater than .05 in all circumstances signifying that there is no statistical difference in fracture density between the three sample locations.

A)

Descriptives

Spacing

	N	Mean	Std. Deviation	Std. Error	95% Confidence Interval for Mean		Minimum	Maximum
					Lower Bound	Upper Bound		
1	29	.2924137931	.3220382095	.0598009942	.1699170095	.4149105767	.0200000000	1.370000000
2	63	.2439206349	.3457573875	.0435613363	.1568427645	.3309985053	.0040000000	1.622000000
3	113	.1577433628	.2039432160	.0191853639	.1197300235	.1957567022	.0060000000	1.509000000
Total	205	.2032780488	.2760274492	.0192785933	.1652672004	.2412888972	.0040000000	1.622000000

B)

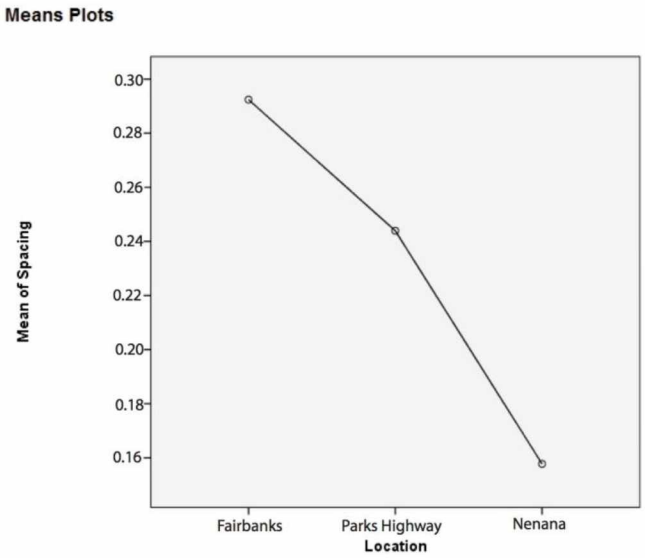

C)

ANOVA

Spacing

	Sum of Squares	df	Mean Square	F	Sig.
Between Groups	.569	2	.284	3.836	.023
Within Groups	14.974	202	.074		
Total	15.543	204			

D)

Multiple Comparisons

Dependent Variable: Spacing

Tukey HSD

(I) Location	(J) Location	Mean Difference (I-J)	Std. Error	Sig.	95% Confidence Interval	
					Lower Bound	Upper Bound
1	2	.0484931582	.0610971758	.707	-.095764617	.1927509336
	3	.134670430*	.0566764248	.048	.0008505792	.2684902813
2	1	-.048493158	.0610971758	.707	-.192750934	.0957646172
	3	.0861772721	.0428098132	.112	-.014901842	.1872563864
3	1	-.134670430*	.0566764248	.048	-.268490281	-.000850579
	2	-.086177272	.0428098132	.112	-.187256386	.0149018423

*. The mean difference is significant at the 0.05 level.

Figure B.20: Comparison of mean fracture spacing across field locations (F6).

A) Descriptives table: 1=Fairbanks, 2=Parks Highway area, 3= Nenana Area
B) Means of fracture spacing plotted
C) Results of the one-way analysis of variance test (anova) between sample locations for F6. The significant value is less than .05 signifying that there is a statistical difference in fracture spacing between the three sample locations.
D) Tukey HSD Post Hoc test table showing that the significant value is greater than .05 in all circumstances besides the comparison of sets in the Fairbanks and Nenana areas. This can be interpreted as little statistical variance between F6 at the three locations.

APPENDIX C: Apatite Fission Track Models

Apatite fission track samples were collected by Rachel Frohman, Nilesh Dixit, and myself. Modeling of samples was performed in HeFty by Paul O'Sullivan (AtoZinc) and incorporated in Frohman (2014) and in this thesis.

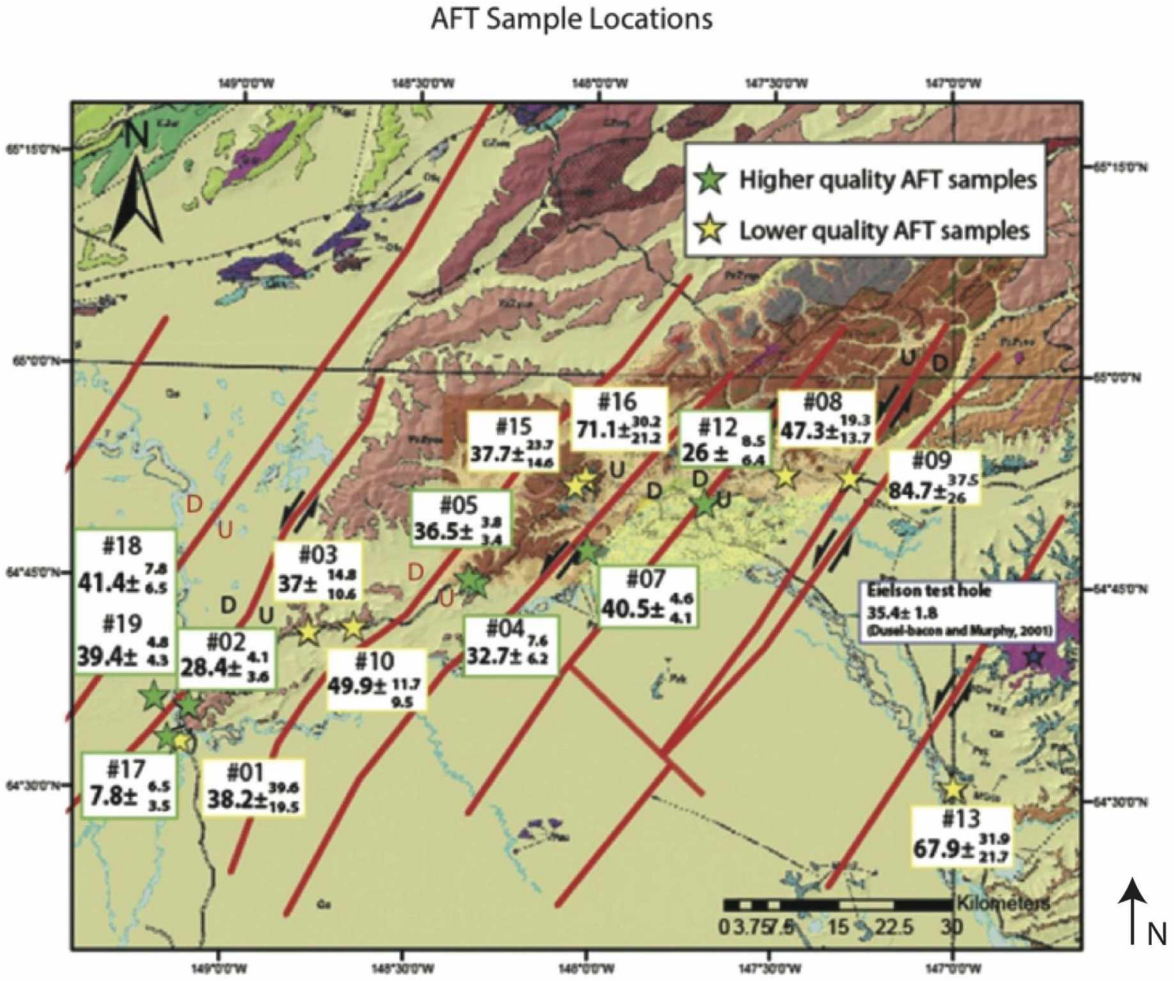

Figure C.1: Location of AFT samples (Frohman, 2014)

AFT Models (Frohman, 2014):

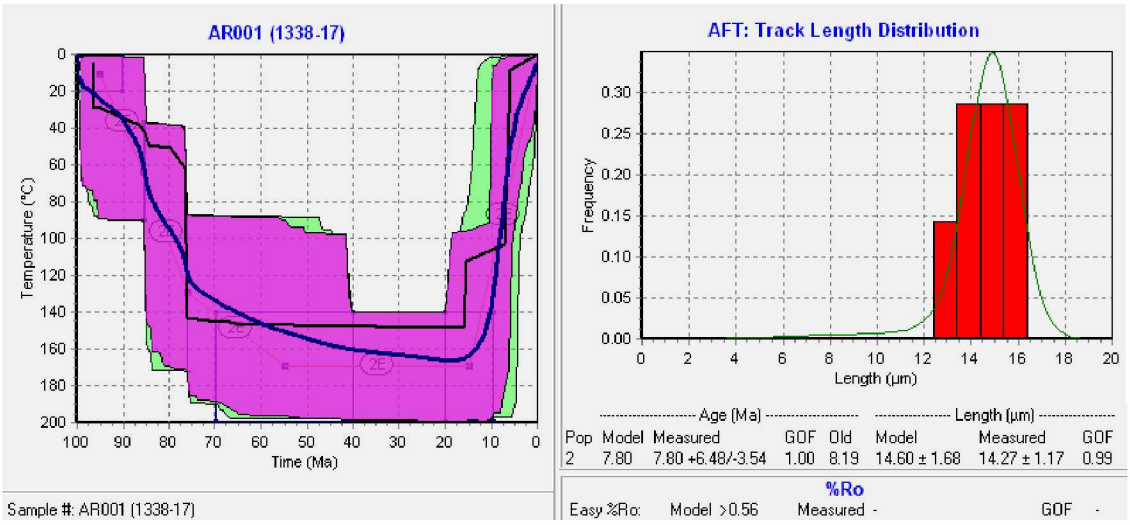

Figure C.2: Model for AFT sample 1338-17

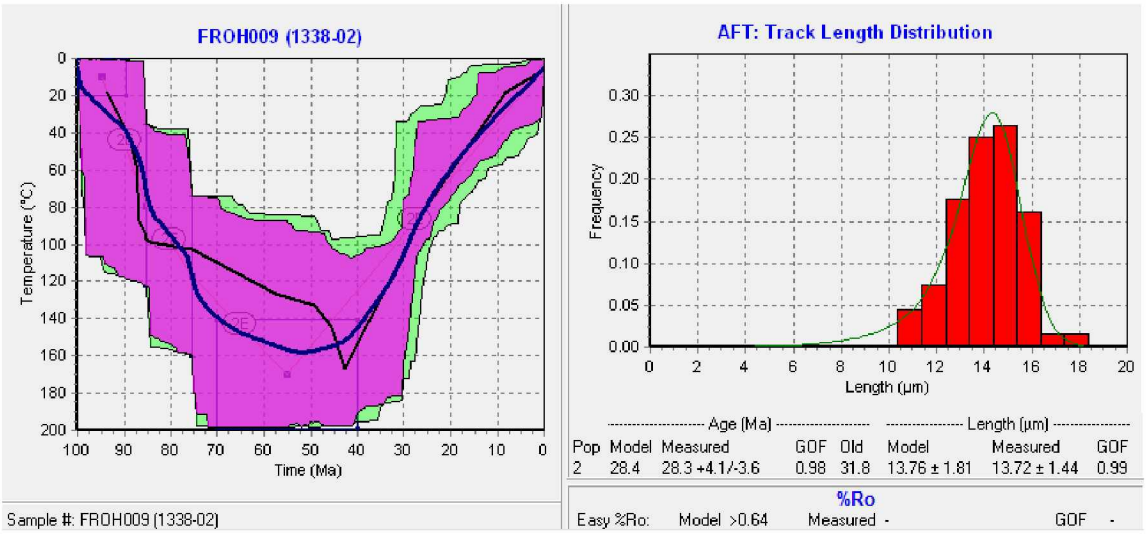

Figure C.3: Model for AFT sample 1338-02

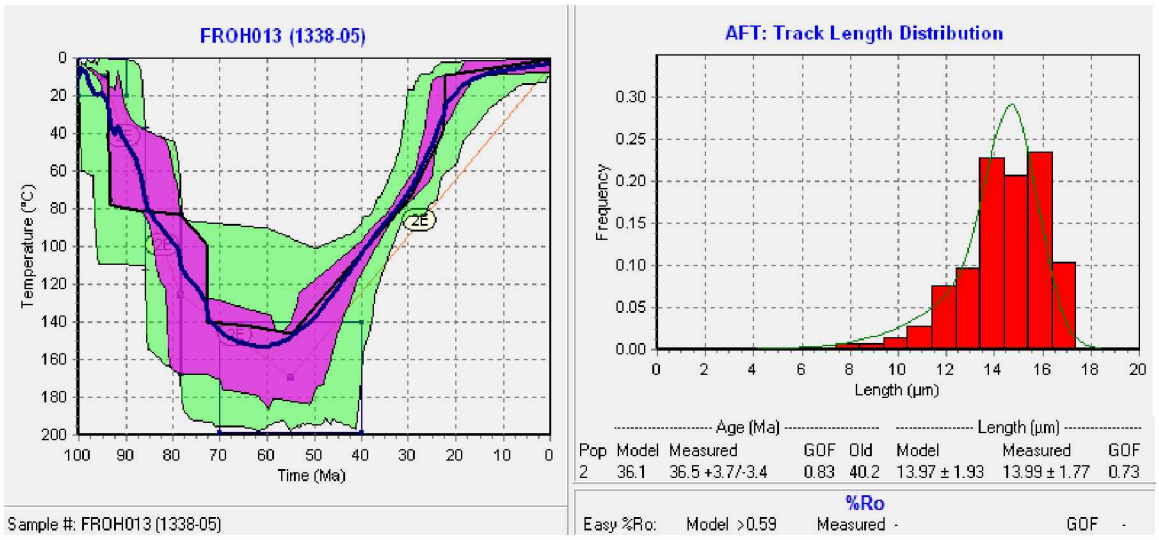

Figure C.4: Model for AFT sample 1338-05

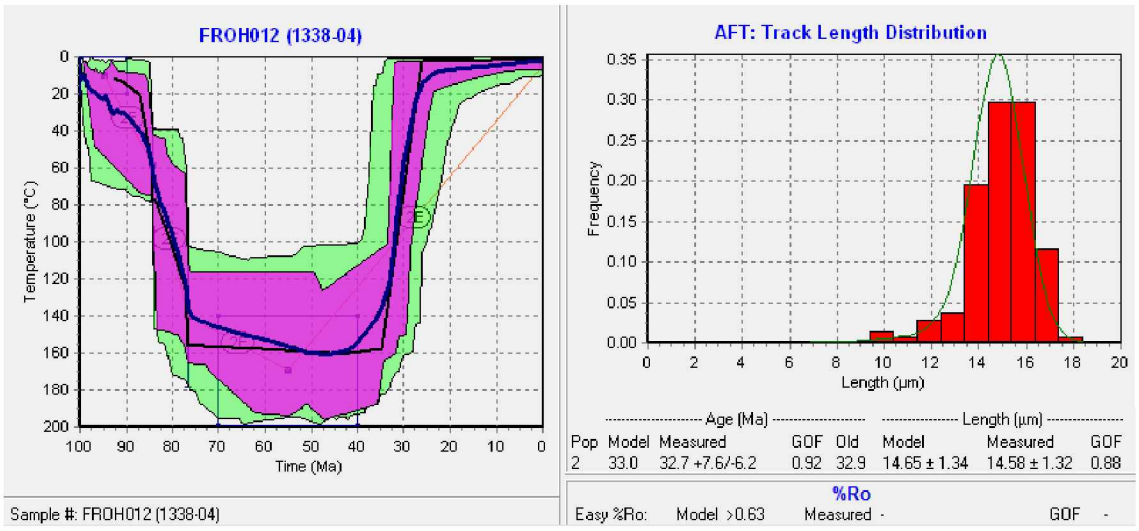

Figure C.5: Model for AFT sample 1338-04

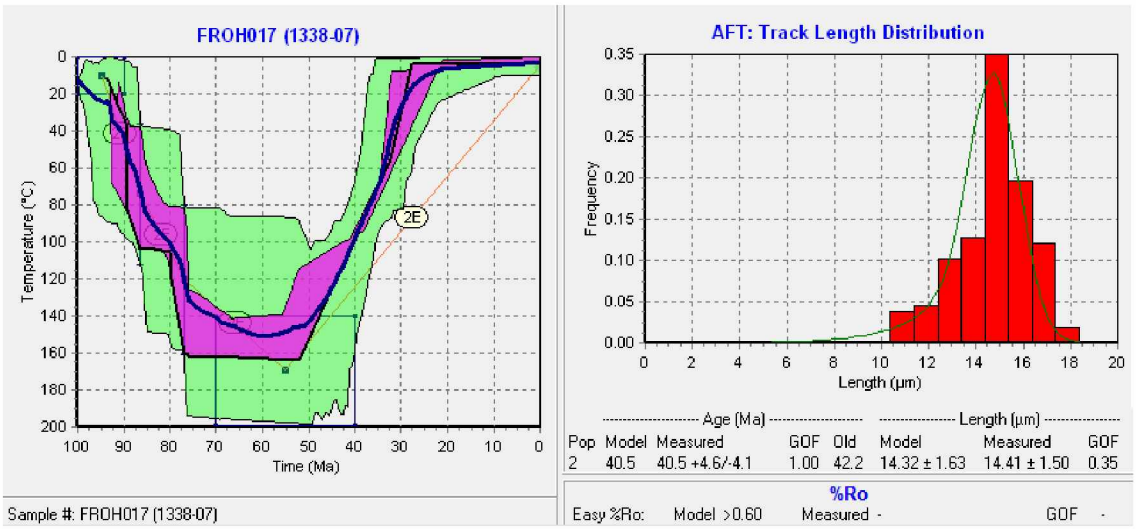

Figure C.6: Model for AFT sample 1338-07

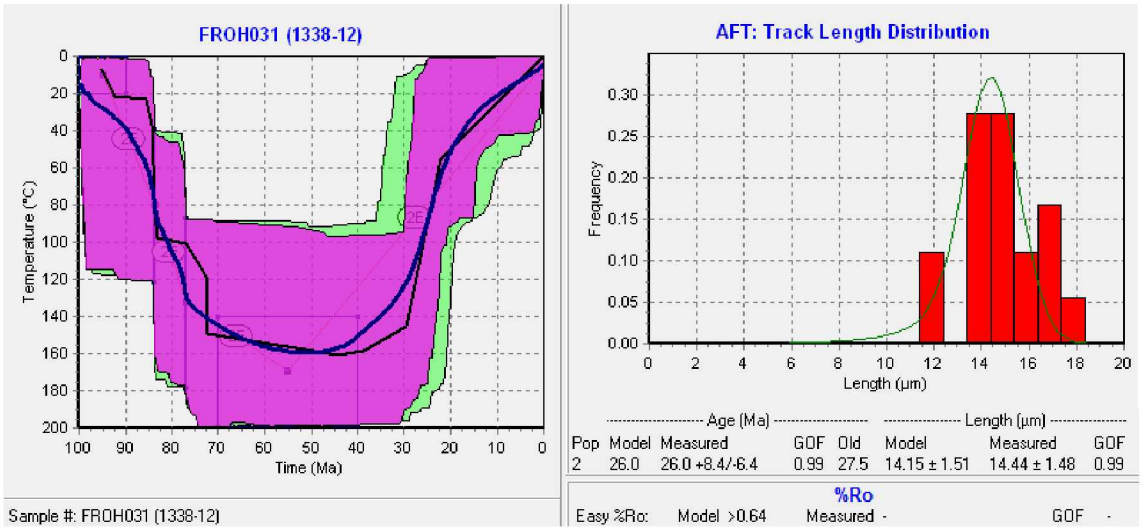

Figure C.7: Model for AFT sample 1338-12

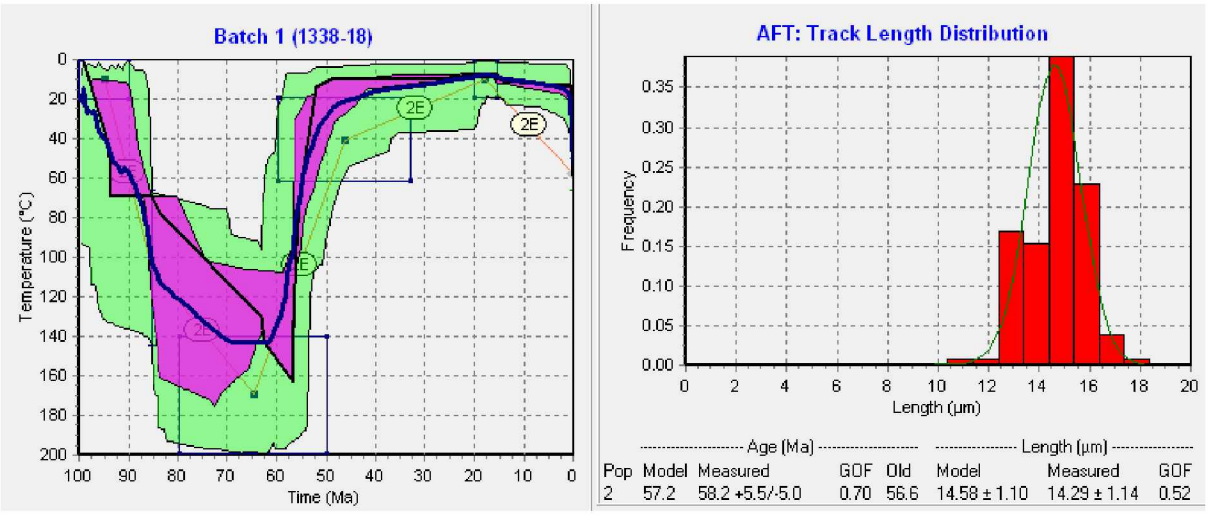

Figure C.8: Model for AFT sample 1338-18

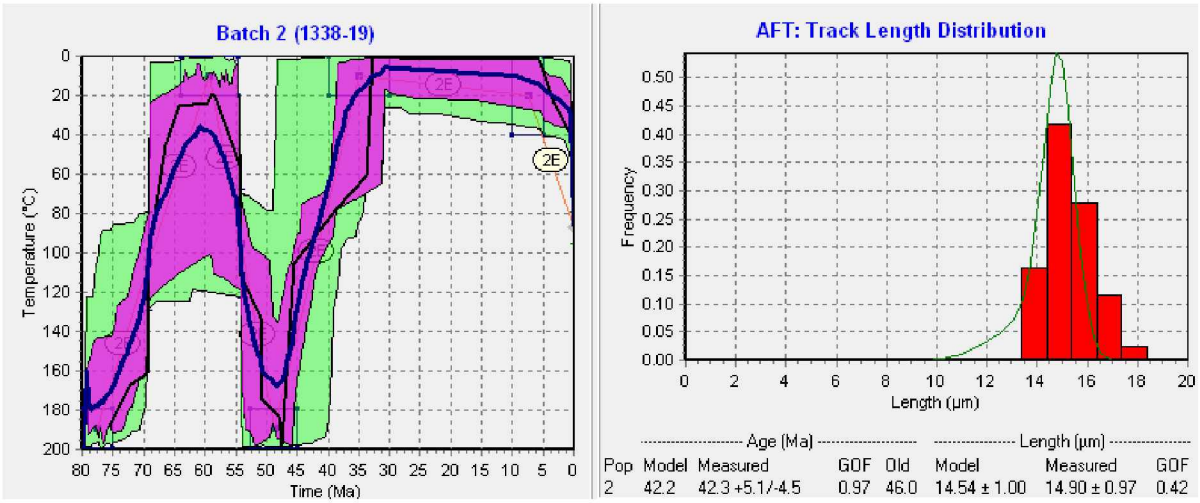

Figure C.9: Model for AFT sample 1338-19

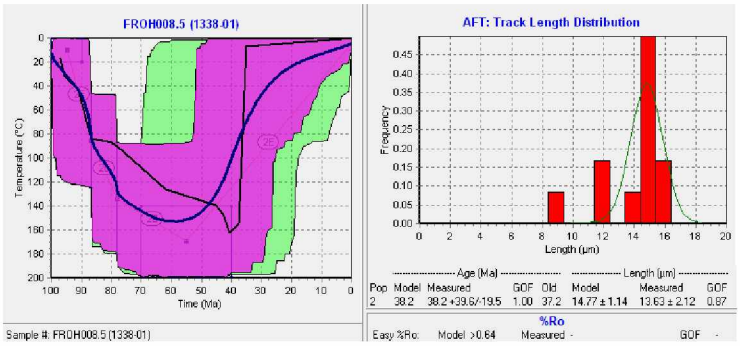

Figure C.10: Model 1 for AFT sample 1338-01

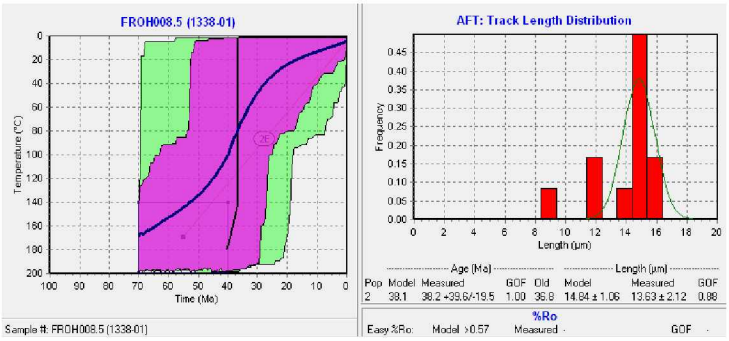

Figure C.11: Model 2 for AFT sample 1338-01

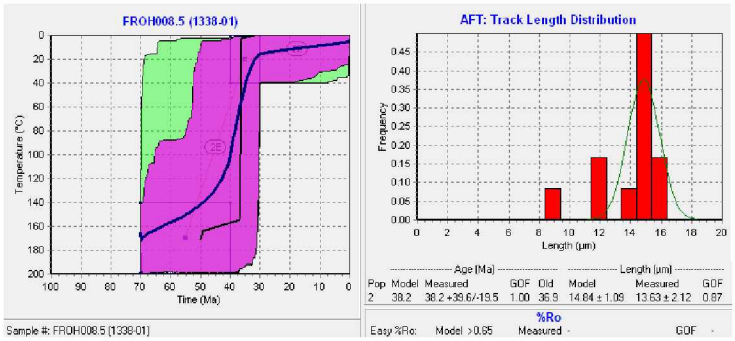

Figure C.12: Model 3 for AFT sample 1338-01

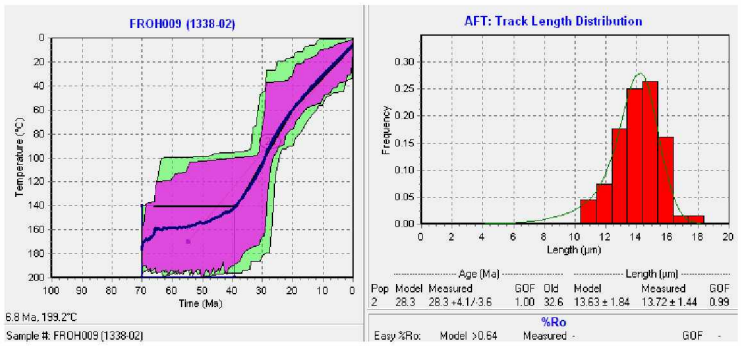

Figure C.13: Model 2 for AFT sample 1338-02

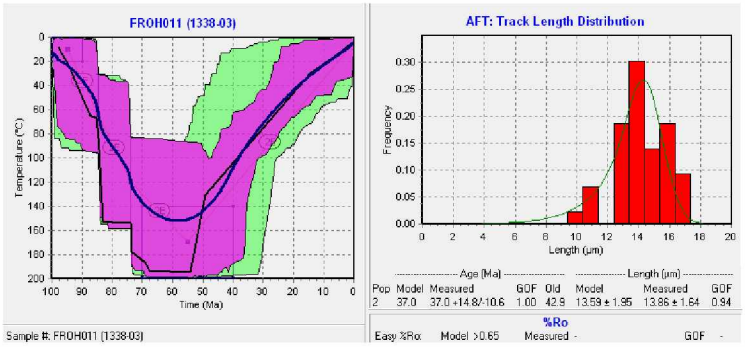

Figure C.14: Model 3 for AFT sample 1338-03

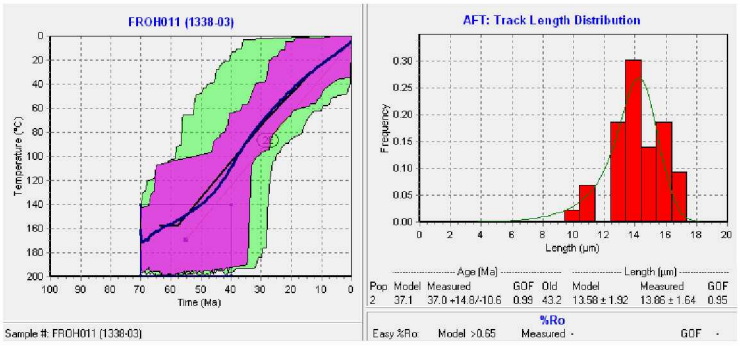

Figure C.15: Model 2 for AFT sample 1338-03

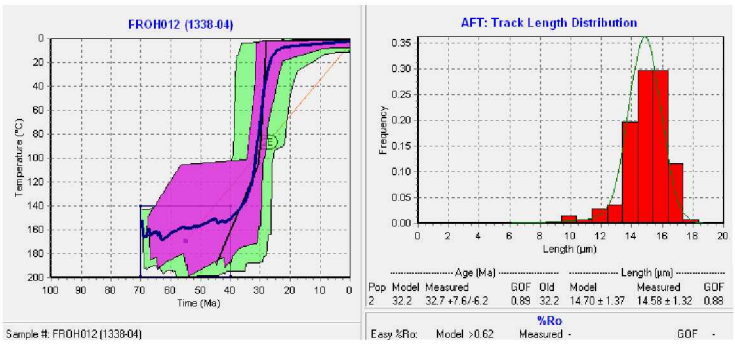

Figure C.16: Model 2 for AFT sample 1338-04

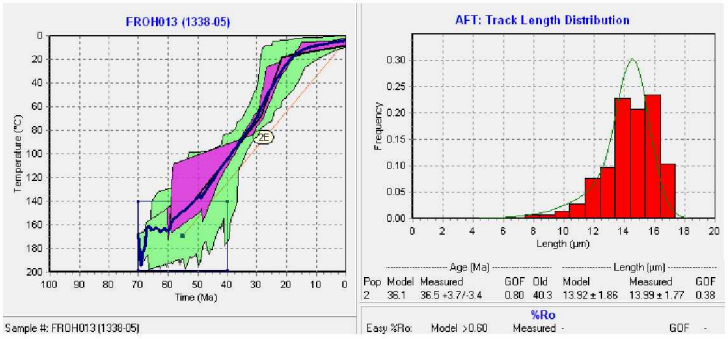

Figure C.17: Model 2 for AFT sample 1338-05

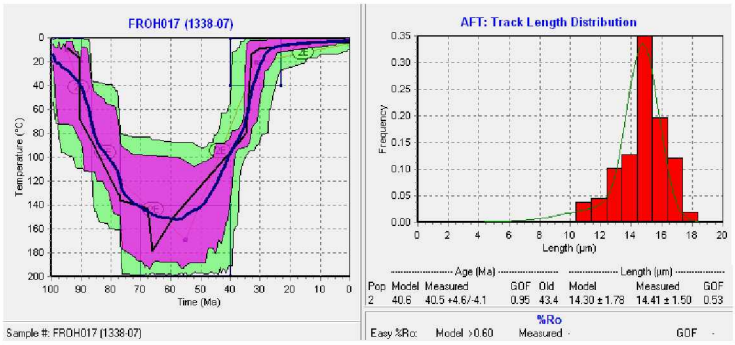

Figure C.18: Model 2 for AFT sample 1338-07

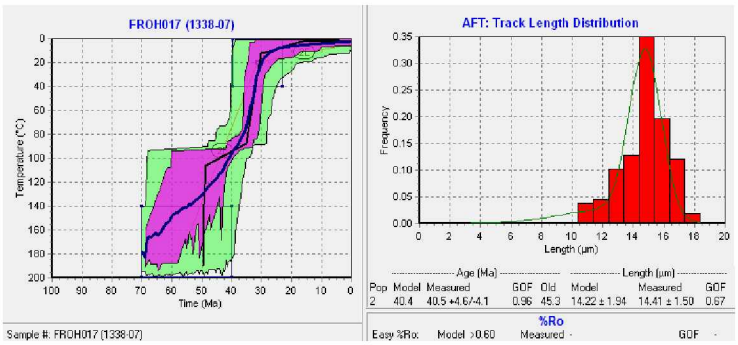

Figure C.19: Model 3 for AFT sample 1338-07

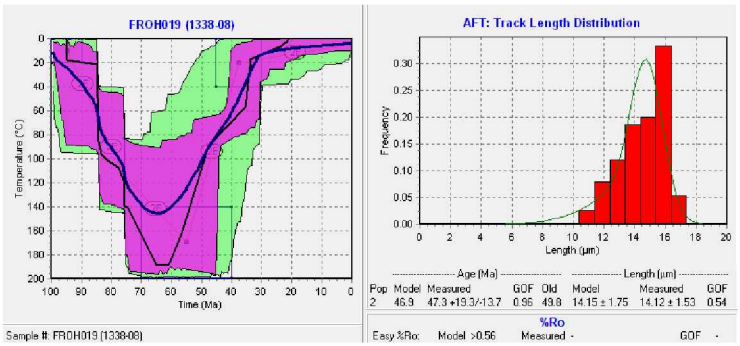

Figure C.20: Model 1 for AFT sample 1338-08

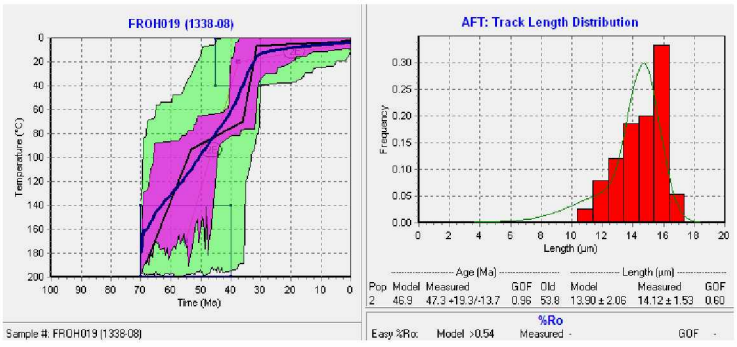

Figure C.21: Model 2 for AFT sample 1338-08

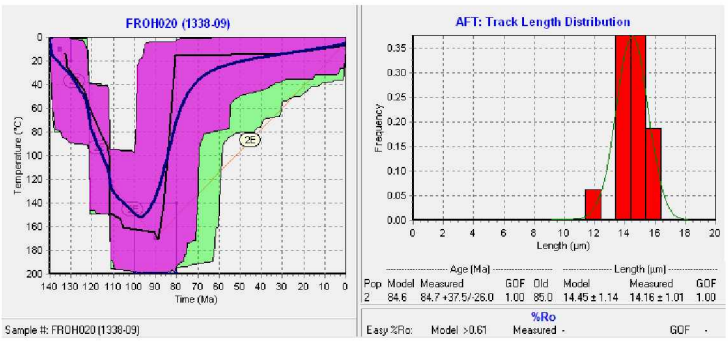

Figure C.22: Model 1 for AFT sample 1338-09

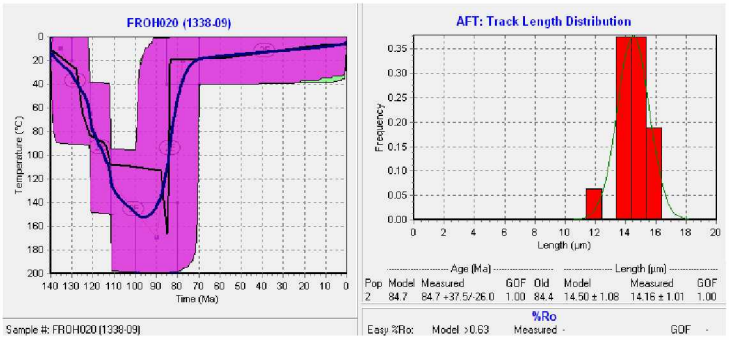

Figure C.23: Model 2 for AFT sample 1338-09

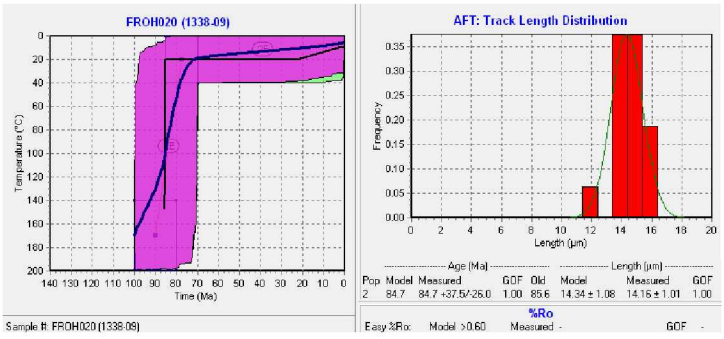

Figure C.24: Model 3 for AFT sample 1338-09

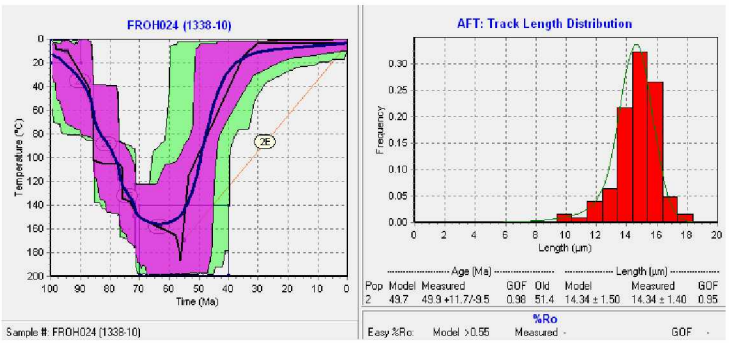

Figure C.25: Model 1 for AFT sample 1338-10

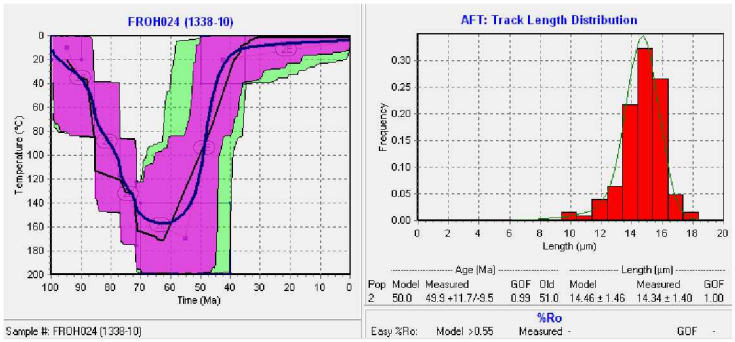

Figure C.26: Model 2 for AFT sample 1338-10

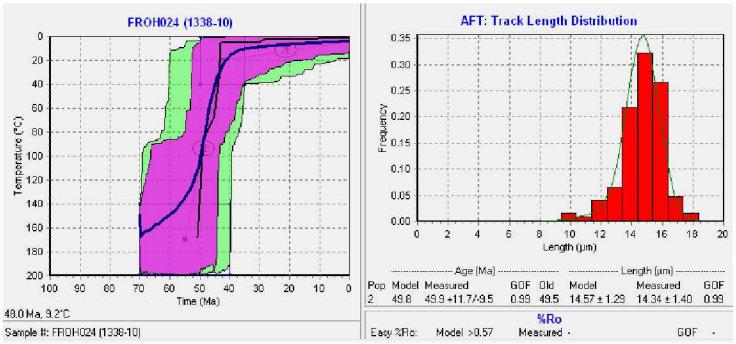

Figure C.27: Model 3 for AFT sample 1338-10

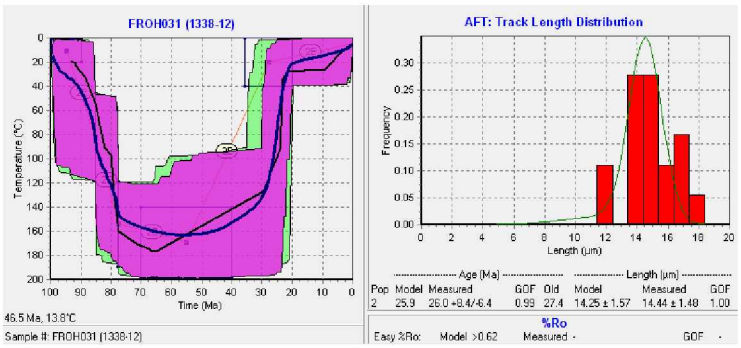

Figure C.28: Model 2 for AFT sample 1338-12

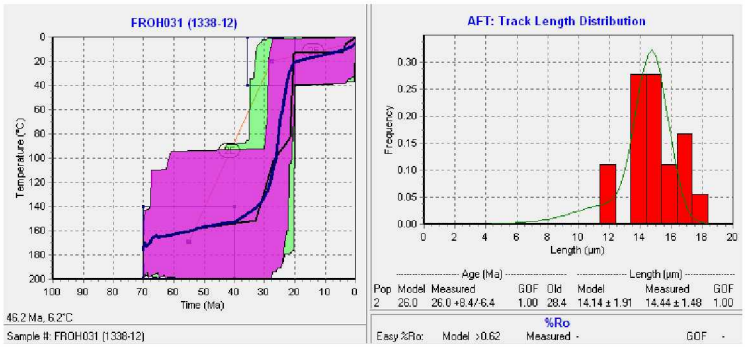

Figure C.29: Model 3 for AFT sample 1338-12

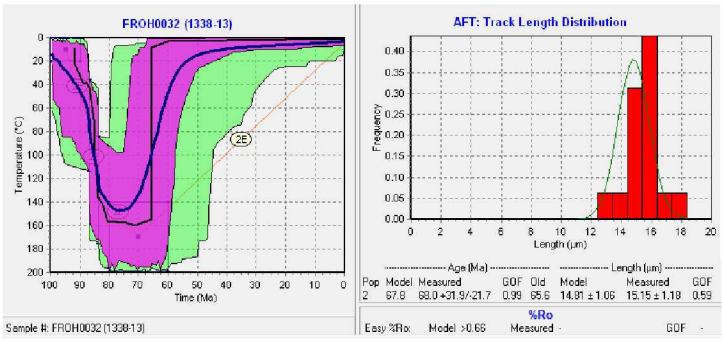

Figure C.30: Model 1 for AFT sample 1338-13

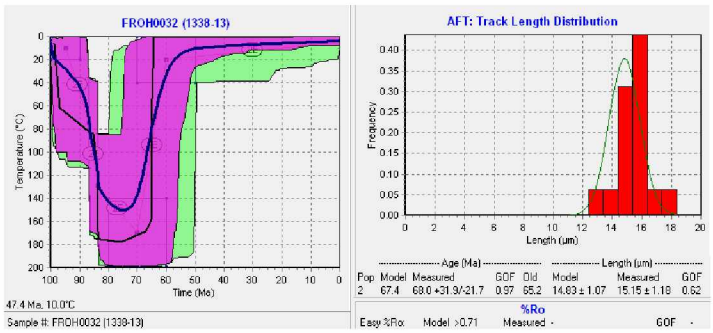

Figure C.31: Model 2 for AFT sample 1338-13

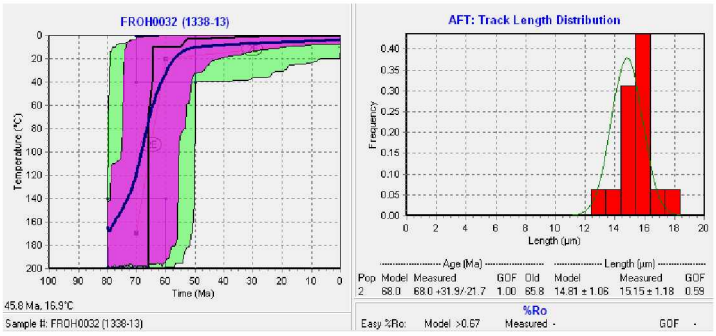

Figure C.32: Model 3 for AFT sample 1338-13

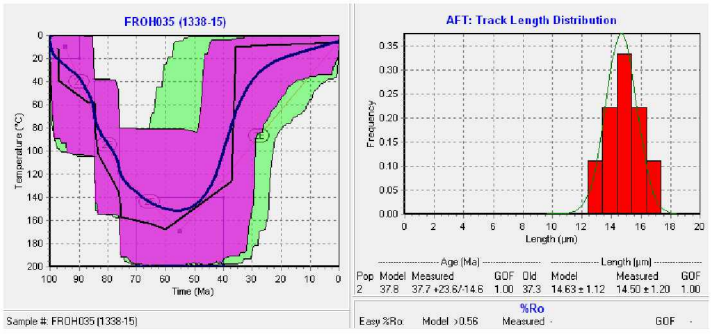

Figure C.33: Model 1 for AFT sample 1338-15

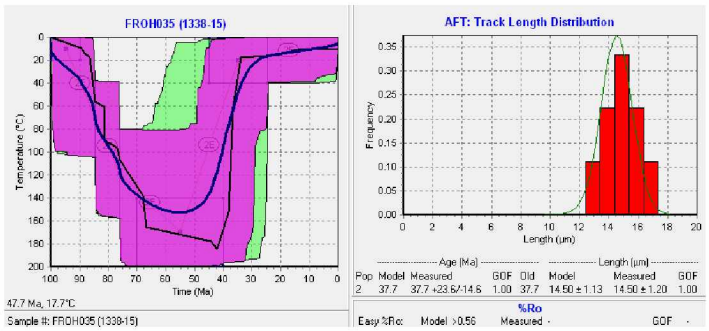

Figure C.34: Model 2 for AFT sample 1338-15

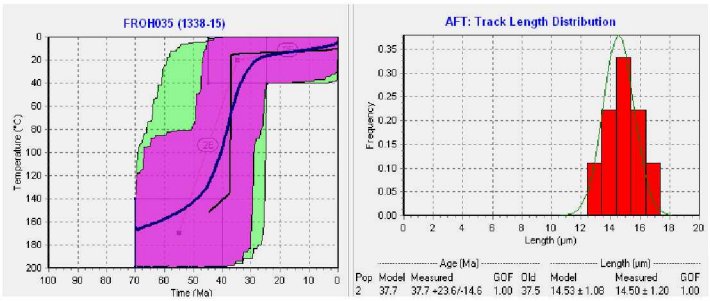

Figure C.35: Model 3 for AFT sample 1338-15

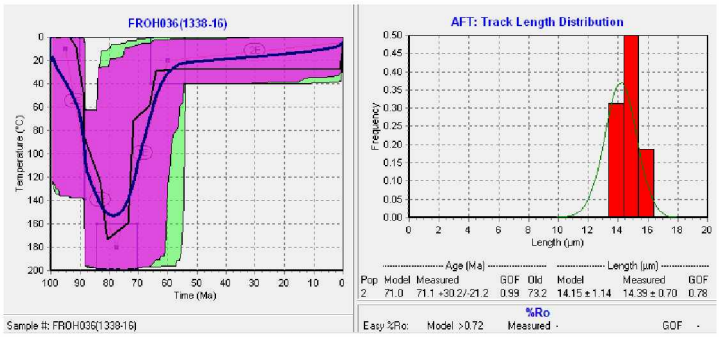

Figure C.36: Model 1 for AFT sample 1338-16

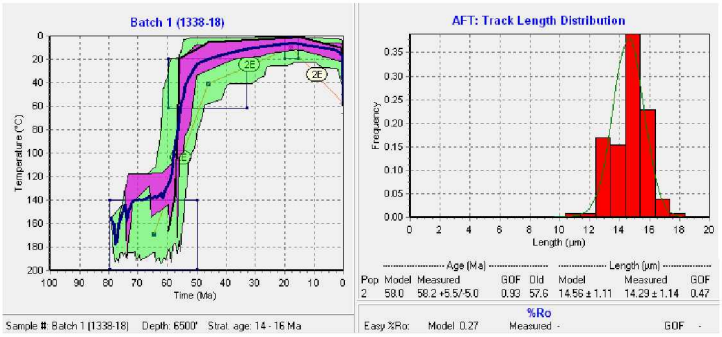

Figure C.37: Model 2 for AFT sample 1338-18

APPENDIX D: Additional Tested Conceptual Models

Other conceptual models for fracture formation were tested and are described below. Fracture sets F4, F5, and F6 were tested to see if they are riedel shears related to a NE-striking pure strike-slip fault, oblique fault (normal with left-lateral shear sense), and a pure dip-slip fault. In addition, fracture sets F4 and F5 were tested to see if they are riedel shears related to the evolution of the NW-striking faults interior to the Nenana basin.

Scenario 1. Fracture sets F4, F5, and F6 formed as riedel shears related to the Minto Fault and other northeast-striking faults

In this scenario, F4, F5, and F6 are all riedel shears related to the Minto fault (NE-striking fault). I chose these fracture sets due to their differing shear senses, orientations, and for being regional sets. Fracture set F5 has an antithetic shear sense while F4 and F6 have a synthetic left-lateral shear sense with respect to the Minto fault. This scenario was tested by evaluating if the orientations and shear movement of the individual fracture sets are geometrically consistent with riedel shears associated with either pure strike-slip, pure dip-slip or oblique-slip movement on the Minto fault. Unfortunately, the orientations and sense of shear of F4, F5, and F6 could not be explained by a riedel shear model using any of these slip directions.

Scenario 1.1: Riedel Shears formed due to a pure left-lateral strike-slip faulting on the Minto fault

In a typical left-lateral riedel shear model, R shears are oriented ~15° counterclockwise from the fault, R' shears are oriented 75° counterclockwise from the fault, and P shears are oriented 15° clockwise from the fault (Fig. D.1a). These modeled sets (R, R', and P shears) were chosen because they are the dominant fractures that form in a riedel shear model. If the Minto fault is the master fault, the corresponding R shears would strike ~25°, R' shears would be oriented ~325°,

and the P shears would be oriented ~55°. R and P shears would be synthetic to the master fault (left-lateral), while R' shears would have antithetic right-lateral shear sense to the Minto fault.

However, no observed fractures have either the correct orientations or the correct sense of shear to have formed in this manner (Fig. D.1b).

Scenario 1.2: Riedel shears formed due to pure dip-slip faulting

Since the traditional riedel shear model for left-lateral faults does not fit with the fracture orientations that were measured in outcrop, a riedel shear model was evaluated that assumed pure dip-slip motion associated with the Minto fault. The model was constructed by (Fig. 2):

A) Rotating ideal riedel shears and fault to match the Minto fault orientation

B) Rotating fracture sets 20° to match dip of Minto fault (70° W)

C) Rotating ideal riedel shears 90° along the pole of the Minto fault (130°)

However after rotating the sets, results show that neither the orientations nor shear sense of the fracture sets are consistent with the ideal riedel shears that could form on a pure dip-slip fault (Fig. 2).

Scenario 1.3: Fractures are riedel shears formed in an oblique fault system

This hypothesis is that select fractures form as riedel shears during a period of oblique slip on the Minto fault. The traditional riedel shears for a left-lateral strike slip fault were plotted on a stereonet and then rotated to determine the orientations of the same riedel shears if motion on the fault was oblique. The initial stereonet projection was generated with a vertical fault and fractures and first rotated horizontally (around the strike of the fault) to account for the dip of the Minto fault (70° W). Next, the fractures were rotated along the pole of the Minto fault to try and replicate the measured fractures in the field. In order to do so, the orientation of the slip vector of the Minto fault had to be estimated. 20°, 40°, and 60° were all used as inputs for rake. These varying angles

were chosen because the extent of oblique slip along the Minto fault is unknown. At higher angles of estimation, the orientations of the fracture sets began to appear more like the fractures measured in outcrop.

Even though the fracture sets begin to appear more like the orientations measured in the field, the result of the tests show that the fractures still do not fit into the rotation model (Fig. D.3). Dips of fracture sets and various dips of the Minto fault were also tried in the model with similar negative results.

The conclusion to all of these tests is that the fracture sets cannot be placed into a simple riedel shear model for the Minto fault.

Origin of fracture set F2 in scenario 1:

Fracture set F2 is related to the NW-striking oblique faults active in Late Miocene time. Fracture set F2 is parallel to the fault orientation. In addition, the right-lateral shear sense observed on F2 matches the projected shear sense for the NW-striking faults.

Scenario 2: F4 and F5 as riedel shears related to northwest-striking faults

In this scenario, F4 and F5 fractures are R and R' shears formed as oblique motion was activated along the NW-striking oblique faults in the Late Miocene-Pliocene time (Fig. D.4). I propose that the left-lateral strike-slip on the NE-striking faults during the Late Miocene may have reactivated the NW-striking faults as antithetic shears with a right-lateral shear motion and F4 and F5 fracture sets as riedel shears (Fig. D.4). Fracture set F4 is antithetic to the NW-striking faults with a left-lateral shear sense while fracture set F5 is synthetic. The orientations and shear sense of fracture sets F4 and F5 in relation to the NW-striking faults match an ideal riedel shear model.

Origin of fracture set F2 and F6 in scenario 2:

Similar to scenario 1, F2 and F6 are parallel to the dominant fault orientations and can be related to the oblique component along the dominant fault trends (NE-striking and NW-striking).

Deficiencies of Scenario 2:

The extent, density, and shear sense of the NW-striking faults are poorly understood, but they coincide with the orientation of subsidiary extensional faults in a NE-trending shear zone governed by the dominant left-lateral NE-striking faults interior to and on the margin of the basin.

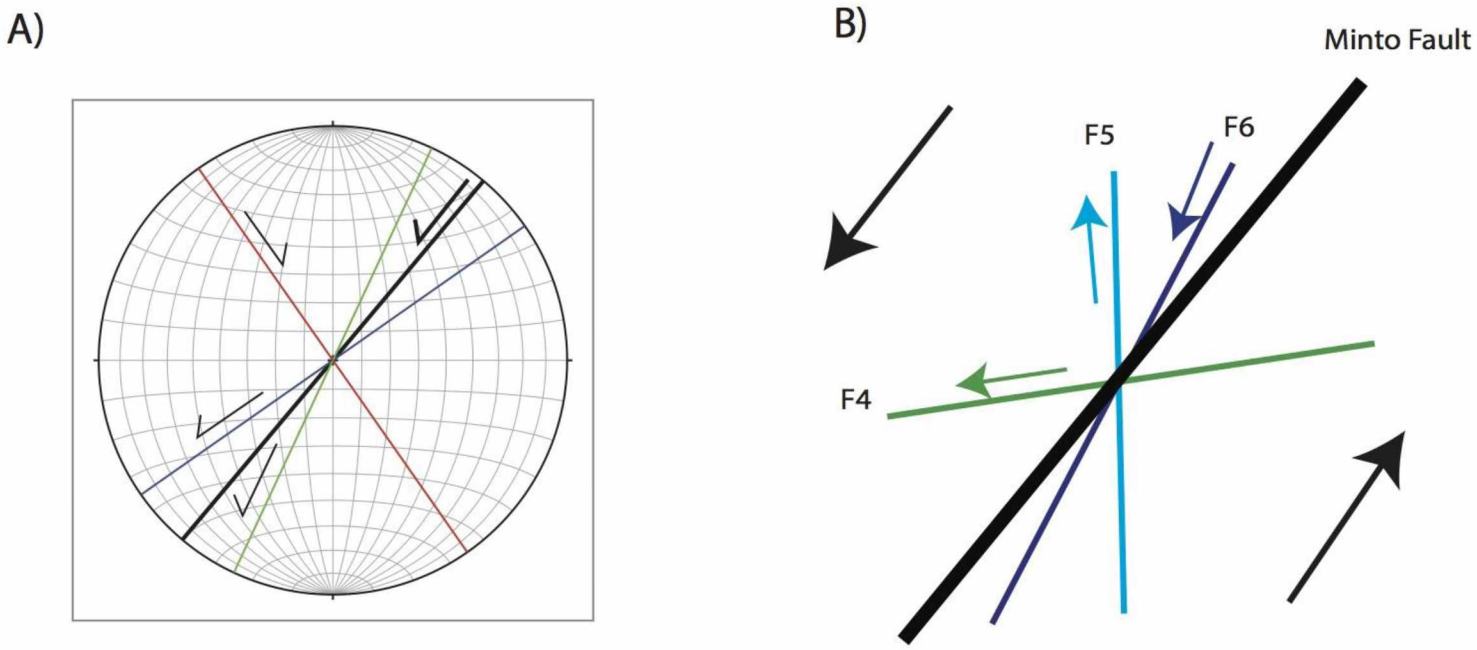

Figure D.1: F4, F5, and F6 as riedel shears for a pure strike-slip fault
A) Stereonet projection of ideal riedel shears around the Minto fault.
B) Fracture sets are related to the left-lateral strike slip motion on the Minto fault. Neither the orientations nor shear senses of observed fracture sets match the ideal model for a pure strike slip fault.

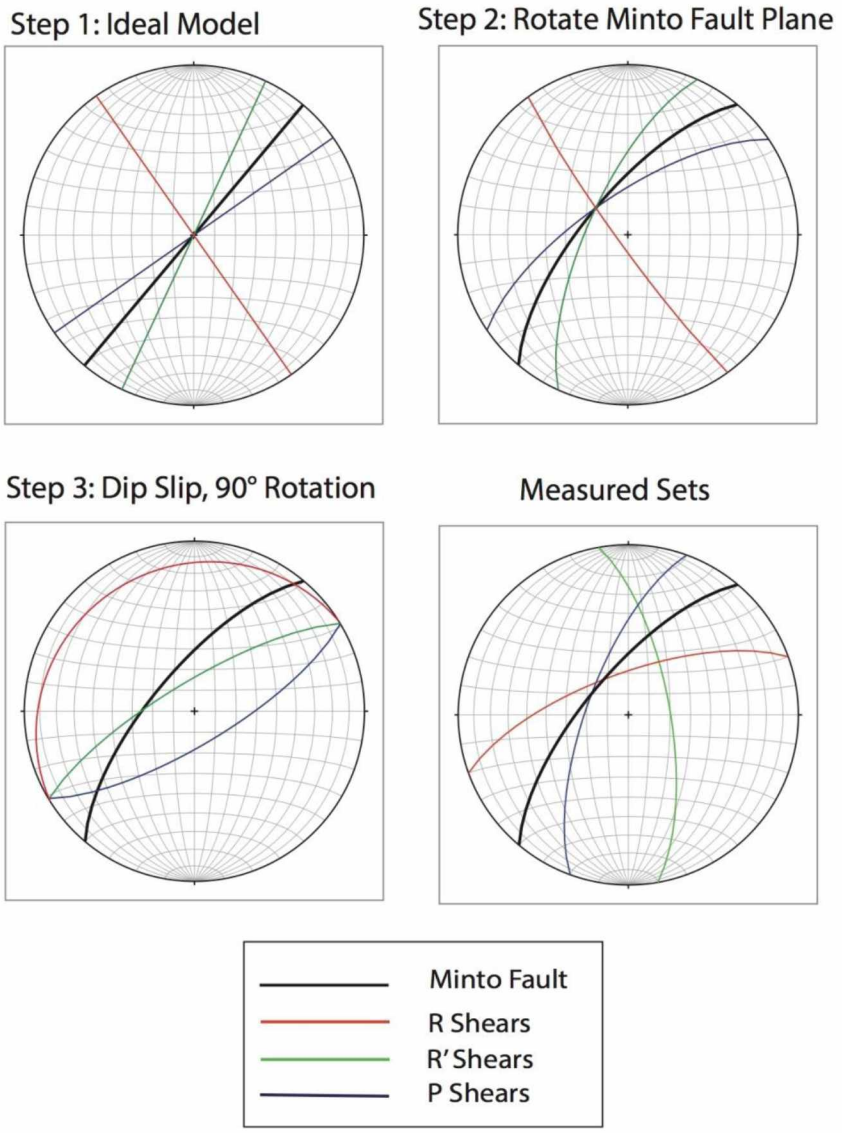

Figure D.2: Fractures as revised riedel shears, dip slip faulting. For this scenario, F4 (red), F5 (green) and F6 (blue) are used. This model for a pure dip slip was constructed by:
Step 1: Rotating ideal riedel shears and fault to match the Minto fault orientation
Step 4: Rotating fracture sets 20° to match dip of Minto fault
Step 3: Rotating ideal riedel shears 90° along the pole of the Minto fault (130°)
Neither the orientations nor shear senses of observed fracture sets match the ideal model for a pure dip slip fault.

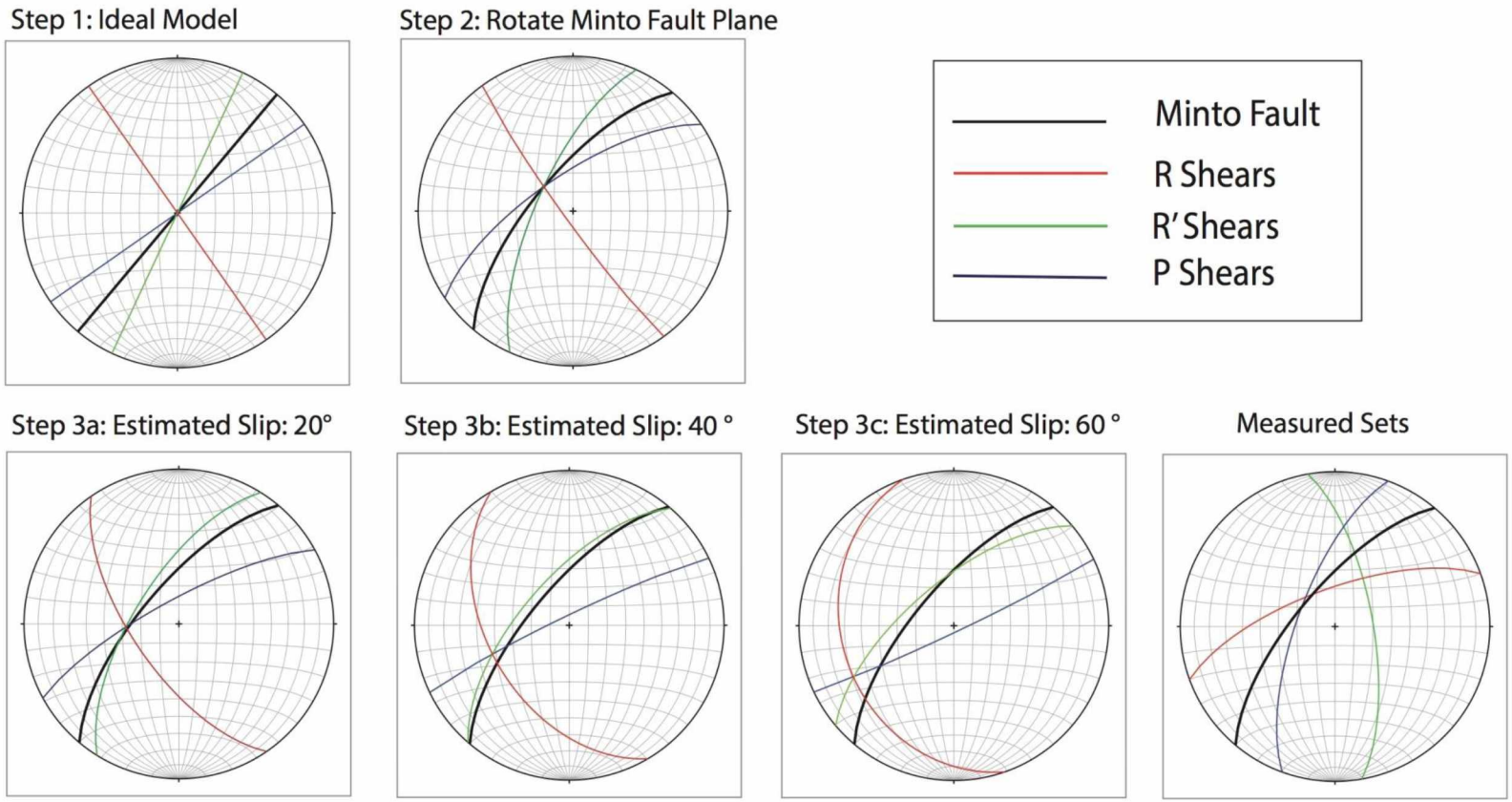

Figure D.3: Fractures as revised riedel shears, rotational model.
Step 1: Ideal riedel shear model with vertical fracture sets and fault.
Step 2: Rotate fracture sets 20° horizontally to account for the dip of the Minto fault (70°)
Step 3: The fracture sets were then rotated along the pole of the Minto fault at varying amounts of angles (20°, 40° and 60°) to represent the rake of the fault.
However, neither the orientations nor shear senses of observed fracture sets match the ideal model for an oblique fault.

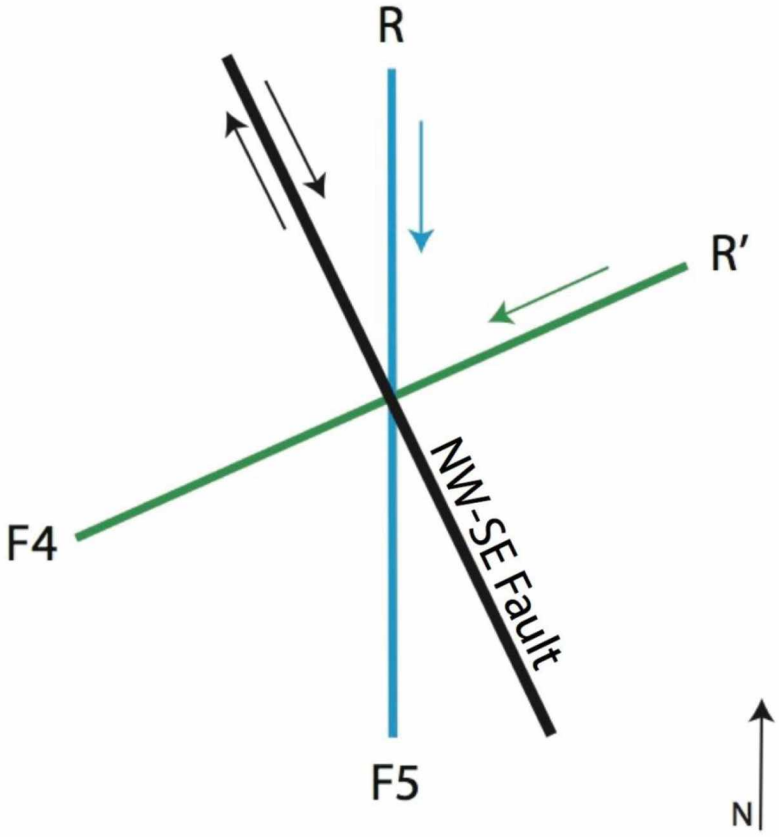

Figure D.4: Fractures as riedel shears (F4+F5). A second interpretation for F4 and F5 is that they are related to the shear along the NW-SE striking faults in the basin as riedel shears. This would occur as oblique faulting is activated in the basin during phase II. F4 would be considered the R' shears while F5 would be considered the R shears due to their sense of slip in respect to the shear along the master fault.